

University of California
Santa Barbara

Integrated Quantum Photonics with III-V Semiconductors

A dissertation submitted in partial satisfaction
of the requirements for the degree

Doctor of Philosophy
in
Materials

by

Trevor John Steiner

Committee in charge:

Professor John Bowers, Co-Chair
Professor Galan Moody, Co-Chair
Professor Chris Palmstrøm
Professor Chris G. Van de Walle

March 2024

The Dissertation of Trevor John Steiner is approved.

Professor Chris Palmstrøm

Professor Chris G. Van de Walle

Professor Galan Moody, Committee Co-Chair

Professor John Bowers, Committee Co-Chair

February 2024

Integrated Quantum Photonics with III-V Semiconductors

Copyright © 2024

by

Trevor John Steiner

To my dog, Luna

Acknowledgements

During the past four and a half years, I have had the privilege to work with many great scientists, colleagues, and mentors. First, I would like to thank my advisors Prof. Galan Moody and Prof. John Bowers for their outstanding support, mentorship, and advice during my time at UCSB. I would also like to thank Prof. Russell Holmes from the University of Minnesota who inspired me to pursue a doctorate degree through his interest and excitement for research. I also appreciate all of the collaborators who have helped me along the way — particularly, my colleagues at Purdue University, Oak Ridge National Lab, SRI International, University of Pavia, and University of Toronto.

I feel grateful to have so many friends that have helped me through the highs and lows of graduate school. A special thanks to my friends from Minnesota who have helped to keep me sane with weekend game nights, Zoom calls, and trips over the years. Even though we are thousands of miles away, I constantly feel your support. To my roommates, Jake and Elias, thank you for forcing me out of my room after a long day in lab to watch a show, go surfing, or rock climb. Even though I was sometimes reluctant to join, it was always worth it. To my other friends, I appreciate all of the game nights, BBQs, potlucks, and holiday celebrations we have had. Last, but certainly not least, I am so thankful for such a loving family. Mom, Dad, Tristan, Cassie, Vani, and Luna, I could not have asked for a better family.

Curriculum Vitæ

Trevor John Steiner

Education

- 2024 Ph.D. in Materials (Expected), University of California, Santa Barbara.
- 2019 Bachelor of Materials Science and Engineering, University of Minnesota, Twin Cities.

Professional Employment

- 3/2024 Senior Layout Engineer, IonQ, College Park, MD
- 9/2019 - 3/2024 Graduate Student Researcher, Materials Department, University of California, Santa Barbara, CA
- 6/2020 - 9/2020 Intern, Hewlett Packard Enterprise, Goleta, CA
- 4/2017 - 9/2019 Intern, Minnesota Department of Transportation, Materials and Road Research, Maplewood, MN

Selected Awards

1. Institute of Energy Efficiency Excellence in Research Fellowship, August 2023
2. Heeger Fellowship Award, February 2023
3. NSF Quantum Foundry Fellowship, January 2020
4. Sergio Marchionne Student Award, June 2020
5. University of Minnesota College of Science and Engineering Dean's List

Publications

1. **Steiner, T. J.**, Shen, M., Castro, J. E., Bowers, J. E., & Moody, G. (2023). Continuous Entanglement Distribution from an AlGaAs-on-Insulator Microcomb for Quantum Communications. *Optica Quantum* 1, 55-62 (2023).
2. **Steiner, T. J.**, Castro, J. E., Le, K., Duan, L., Peters, J., McDonald, C., Lewis, N., Thiel, L., Bowers, J. E., & Moody, G. (2023). Integrated Tunable Bell State Generator and Hong-Ou-Mandel Experiment on AlGaAsOI. 2023 Conference on Lasers and Electro-Optics (CLEO), 12.
3. Castro, J. E., **Steiner, T. J.**, Chang, L., Pintus, P., Bowers, J. E., & Moody, G. (2022). Expanding the Quantum Photonic Toolbox with Low-Loss AlGaAs-on-Insulator. 2022 Conference on Lasers and Electro-Optics (CLEO), 12.

4. Castro, J. E., **Steiner, T. J.**, Thiel, L., Dinkelacker, A., McDonald, C., Pintus, P., Chang, L., Bowers, J. E., & Moody, G. (2022). Expanding the Quantum Photonic Toolbox in AlGaAsOI. *APL Photonics*, 7(9), 096103.
5. **Steiner, T. J.**, Castro, J. E., Chang, L., Bowers, J. E., & Moody, G. (2022). Pushing the limits on chip-scale quantum light generation for sensing and precision metrology. *Optical and Quantum Sensing and Precision Metrology II*, 12016, 120160J.
6. Zhou, Q., Anaclet, B., **Steiner, T.**, Kotiuga, M., & Darancet, P. (2021). Tuning the Electronic Structure of Two-Dimensional Materials through Molecular Assembly. *APS March Meeting Abstracts*, 2021, J48.007.
7. Zhou, Q., Anaclet, B., **Steiner, T.**, Kotiuga, M., & Darancet, P. (2021). Engineering the Electronic Structure of Two-Dimensional Materials with Near-Field Electrostatic Effects of Self-Assembled Organic Layers. *arXiv:2109.09990*
8. **Steiner, T. J.**, Castro, J. E., Chang, L., Dang, Q., Xie, W., Norman, J., Bowers, J. E. & Moody, G. (2021). Ultra-bright entangled-photon pair generation from an AlGaAs-on-insulator microring resonator. *PRX Quantum*, 2(1), 010337.
9. Castro, J. E., **Steiner, T. J.**, Chang, L., Dang, Q., Xie, W., Li, C., Norman, J., Bowers, J. E., & Moody, G. (2021). Time-energy Entangled Photon Pairs Generated via SFWM in an AlGaAsOI Ring Resonator. *Optical Fiber Communication Conference (OFC)*, M3B.1.
10. **Steiner, T. J.**, Castro, J. E., Chang, L., Dang, Q., Xie, W., Li, C., Norman, J., Bowers, J. E., & Moody, G. (2021). Entangled Photon Pair Generation from an AlGaAs-on-Insulator Microring Resonator. *Conference on Lasers and Electro-Optics*, FTh1O.4.
11. Moody, G., Chang, L., **Steiner, T. J.**, & Bowers, J. E. (2020). Chip-Scale Nonlinear Photonics for Quantum Light Generation. *AVS Quantum Science*, 2(4), 041702.
12. Bangsund, J. S., Fielitz, T. R., **Steiner, T. J.**, Shi, K., Van Sambeek, J. R., Clark, C. P., & Holmes, R. J. (2019). Formation of aligned periodic patterns during the crystallization of organic semiconductor thin films. *Nature Materials*.
13. **Steiner, T.**, & Holmes, R. J. (2019). Epitaxy and Pattern Formation in Crystalline Organic Semiconductor Thin Films. *University of Minnesota Undergraduate Honors Thesis*.
14. **Steiner, T.**, Hoegh, K., Teshale, E. Z., & Dai, S. (2020). Method for Assessment of Modeling Quality for Asphalt Dielectric Constant to Density Calibration. *Journal of Transportation Engineering, Part B: Pavements*, 146(3), 04020054.
15. Hoegh, K., **Steiner, T.**, Zegeye Teshale, E., & Dai, S. (2020). Coreless Asphalt Pavement Compaction Assessment - MnDOT Case Studies. *Transportation Research Record*.

16. Hoegh, K., Dai, S., **Steiner, T.**, & Khazanovich, L. (2018). Enhanced model for continuous dielectric-based asphalt compaction evaluation. *Transportation Research Record*.

Presentations

1. Nonlinear Integrated Photonics for Quantum Communications and Computing. *Invited Talk*. IEEE Quantum Computing: Devices, Cryogenic Electronics and Packaging Workshop, October 2023. Milpitas, CA.
2. AlGaAsOI Integrated Quantum Photonics (Poster). International Summer School on Integrated Quantum Photonics, July 2023. Bristol, UK.
3. Nonlinear Integrated Photonics for Quantum Communications and Computing. *Invited Talk*. Orca Computing Seminar, June 2023. Virtual.
4. Integrated Tunable Bell State Generator and Hong-Ou-Mandel Experiment on AlGaAsOI. Conference on Lasers and Electro-Optics (CLEO), May 2023. San Jose, CA.
5. Entanglement-Enhanced Precision Metrology and Sensing with Integrated Photonics. *Invited Talk*. SPIE Photonics West, January 2023. San Francisco, CA.
6. AlGaAsOI Photonics and Low-Loss Links for High-Speed Entanglement-Based Quantum Key Distribution. Conference on Lasers and Electro-Optics (CLEO), May 2022. San Jose, CA.
7. Pushing the limits on chip-scale quantum light generation for sensing and precision metrology. *Invited Talk*. SPIE Photonics West, January 2022. San Francisco, CA.
8. Entangled Photon Pair Generation from an AlGaAs-on-Insulator Microring Resonator. Conference on Lasers and Electro-Optics (CLEO), May 2021. Virtual Conference.
9. Nonlinear Quantum Light Generation. OSA Quantum 2.0 Conference, September 2020. Virtual Conference.
10. Tuning the Wavelength of Spontaneously Formed Gratings in an Organic Small Molecule. University of Minnesota Undergraduate Research Symposium Spring 2018, Minneapolis, MN
11. Crystallinity of Homoepitaxial and Heteroepitaxial Layers in Organic Thin Films. University of Minnesota Undergraduate Research Symposium Spring 2017. Minneapolis, MN.
12. Tuning the Electronic Structure of Two-dimensional Materials through Molecular Assembly. 2018 Northwestern University REU Closing Symposium. Evanston, IL.
13. Analysis of Rolling Density Meter Data. 2017 Minnesota Department of Transportation Peer Exchange. Maplewood, MN.

Abstract

Integrated Quantum Photonics with III-V Semiconductors

by

Trevor John Steiner

The exploration of quantum technologies presents a promising avenue to achieve new functionalities and capabilities not possible with classical systems, which could revolutionize computing, information transfer and storage, encryption and security, sensing, and enhance our understanding of many natural phenomena. Among many quantum platforms, quantum photonics—the science and engineering of encoding and manipulating quantum information with photons—offers advantages due to the ability to maintain robust quantum coherence at room temperature, achieve scalability through semiconductor processing, minimize undesirable environmental interactions, and encode quantum states in many different degrees of freedom of a photon.

State-of-the-art quantum photonic platforms are based on silicon waveguides, which benefit from the decades of research on silicon semiconductor processing but are limited by the weak optical nonlinearity, small electronic bandgap, and lack of a strong Pockels effect. Here, integrated quantum photonics with nonlinear III-V semiconductors, namely InGaP and AlGaAs, is explored to demonstrate ultrabright sources of quantum light, efficient entanglement distribution, and two-photon interference from nominally indistinguishable photon-pair sources. We demonstrate a novel, ultra-low-loss AlGaAs-on-insulator platform capable of generating time-energy entangled photons through spontaneous four wave mixing in a $Q > 1$ million microring resonator with nearly 1,000-fold improvement in brightness compared to existing sources. The waveguide-integrated sources exhibit internal generation rates greater than 10 million pairs per second below

50 μW pump power, emit in a wavelength ranges spanning 1400 nm to 1700 nm, produce heralded single photons with $> 99\%$ purity, and violate Bells inequality by more than 40 standard deviations with visibility $> 97\%$. After developing an efficient source of quantum light, we demonstrate the fundamental building blocks required for chip-scale quantum photonic circuitry including chip-to-fiber couplers, waveguide crossers, optical filters, interferometers, and spectral pulse shapers all with comparable performance to the silicon and silicon nitride quantum photonic platforms.

Using the bright source of quantum light, we demonstrate the most efficient time-bin quantum key distribution protocol to date with 8 kbps sifted key rates using less than 110 μW of input power while maintaining error rates below 10% and sufficient two-photon visibility to ensure security of the channel. As a proof of principle, a quantum key is distributed across 12 km of deployed fiber on the UCSB campus and used to transmit a 21 kB image with $< 9\%$ error. Finally, preliminary chip-scale quantum photonic circuits are developed to demultiplex qubits and perform the Hong-Ou-Mandel two-photon interference experiment on an integrated photonic chip. This circuit utilizes beamsplitters, optical filters, interferometers, and efficient ring-based quantum light sources as a foundation for larger circuits and experiments in the near future. Additionally, the III-V semiconductor material platforms offer exciting potential for engineering other quantum states of light, including squeezed vacuum states and broadband entangled-photon pairs spanning visible to telecommunications wavelengths. This work demonstrates the benefits of III-V semiconductor materials for nonlinear quantum photonic circuits that can surpass the capabilities possible with state-of-the-art silicon photonics.

Contents

Curriculum Vitae	vi
Abstract	ix
List of Figures	xiii
List of Tables	xxiv
1 Introduction	1
1.1 Thesis Outline	2
1.2 Permissions and Attributions	5
Bibliography	6
2 Background	7
2.1 Quantum Computation and Information	8
2.2 Integrated Photonics	24
2.3 Nonlinear Photonics	44
Bibliography	55
3 Quantum Light Sources	62
3.1 Photon Pair Sources	64
3.2 Squeezed Light Sources	100
3.3 Conclusion and Outlook	106
Bibliography	109
4 AlGaAsOI Integrated Quantum Photonics Toolbox	115
4.1 Fiber to Chip Coupling Strategies	116
4.2 Waveguide Routing	126
4.3 Beamsplitters	131

4.4	Optical Filters	137
4.5	Conclusion and Outlook	152
Bibliography		154
5	Quantum Key Distribution	158
5.1	Introduction	158
5.2	QKD Using AlGaAsOI microcombs	171
5.3	QKD Source Characterization	179
5.4	Time Bin Quantum Key Distribution	187
5.5	Deployed Fiber QKD	191
5.6	Conclusion and Outlook	193
Bibliography		197
6	Integrated Qubit Demultiplexing and Hong-Ou-Mandel Interference	202
6.1	Qubit Demultiplexing	203
6.2	Integrated Hong-Ou-Mandel Interferometer	206
6.3	Conclusion and Outlook	221
Bibliography		225
7	Conclusion and Outlook	227
Bibliography		230
A1	Example Singles Scan	231
A2	Example Coincidence Measurement	232
A3	CAR Measurement	233
A4	Additional HOM Measurement	234
A5	Device List for Experiments	236

List of Figures

2.1	Examples of photonic degrees of freedoms used as qubits. Time-bin qubits are the superposition of photons in an early or late time window. Path encoding involves photons existing in a state between two paths (commonly waveguides). Frequency-bin qubits are the result of photons existing in a superposition of two different frequencies of light. Polarization qubits involve the superposition of horizontal or vertical polarization. In the center of the picture, the Bloch sphere is illustrated which represents the possible pure qubit states which lie on the surface of the sphere.	14
2.2	The Hong Ou Mandel effect involves two photons impinging on a 50/50 beamsplitter. Classically, the photons can exit in any of the four possible output port configurations. If the photons are indistinguishable, a quantum interference effect causes the two photons to always exit the same port.	22
2.3	a) Real component of refractive index versus wavelength for bulk AlGaAs and InGaP. b) AlGaAs on insulator waveguide structure shown via false-colored SEM image. The AlGaAs core is surrounded by $1\mu\text{m}$ thick SiO_2 cladding. c) TE mode profile for a 600nm wide, 400nm thick $\text{Al}_{0.2}\text{Ga}_{0.8}\text{AsOI}$ waveguide. d) TE mode profile for a $10\mu\text{m}$ bend, showing the mode get pushed toward the right waveguide wall.	27
2.4	Ray optics picture of total internal reflectance for a waveguide. Light reflects at the interface between the two materials at an angle θ . The bottom panels show the different waveguide structures that can confine light.	28
2.5	Schematic of an add-drop and all-pass ring resonator. The relevant coupling and transmission coefficients for an all-pass ring resonator are shown in the central panel. The different coupling regimes are illustrated in the simulated transmission spectra of an all-pass ring resonator that is 10x undercoupled, critically coupled, and 10x overcoupled.	38

2.6	a) Schematic of a pulley coupler designed to couple light from a bus waveguide to a ring resonator. b) Mode profiles of the two TE supermodes of a 520 nm wide $\text{Al}_{0.2}\text{Ga}_{0.8}\text{As}$ bus waveguide coupling to a 600 nm wide ring waveguide with a 400 nm gap and a radius of 30 μm solved via Lumerical EME. c) Linear plot showing the electric field profile across the two coupled modes at the center of the waveguide.	42
3.1	Generation of entangled photon pairs using nonlinear materials. The energy conservation of $\chi^{(2)}$ SPDC and $\chi^{(3)}$ SFWM processes is indicated where one (two) pump photon annihilates to generate a signal and idler photon pair for SPDC (SFWM). The generated signal and idler frequencies are correlated as shown in the joint spectral intensity plots. For resonant excitation schemes, the resonance modes are correlated while off-resonant frequencies do not enter the resonator and thus do not generate photon pairs.	66
3.2	Microscope of 400 nm thick $\text{Al}_{0.2}\text{Ga}_{0.8}\text{AsOI}$ waveguide spirals with lengths from 3.1 cm to 4.2 cm.	72
3.3	Model of SFWM in a 400nm thick $\text{Al}_{0.2}\text{Ga}_{0.8}\text{AsOI}$ waveguide with a 800nm width. The different colors show varying waveguide lengths, and the x's indicate the full width at half maximum.	76
3.4	Phase matching for SPDC in InGaP waveguides. The pump light is TM polarized (dashed lines) while the generated light is TE polarized (solid). The different colors indicate different waveguide thicknesses, and the location where the TE and TM lines cross indicates the width where phase matching is achieved. On the right panel, this width is plotted as a function of the waveguide thickness for the straight waveguide (left panel) as well as for bent waveguides.	78
3.5	Dispersion of 400nm thick $\text{Al}_{0.2}\text{Ga}_{0.8}\text{As}$ waveguides with various widths. For 1.55 μm wavelength, the zero dispersion width is approximately 800nm.	79
3.6	Model of phase matching to show a waveguide geometry that can be used to generate visible-telecom entangled photon pairs. a) Frequency mismatch versus the waveguide width for different thicknesses of GaN waveguides. b) Entangled photon pair flux for a 500 nm thick, 725 nm wide GaN waveguide showing the generation of a signal at 775nm and idler at 1550nm.	81
3.7	The first set of devices used in the quantum experiments with AlGaAsOI were fabricated by Weiqiang Xie in Prof. Bowers group. Here, the quality factor of the devices screened for quantum experiments are shown. This plot lists the maximum quality factor found in a wavelength range from 1510 nm to 1600 nm.	85

3.8	a) Schematic illustration of entangled-photon pair generation from a photonic microring resonator. Pump photons (λ_p) are coupled into the waveguide bus and ring and are converted into signal (λ_s) and idler (λ_i) photons via spontaneous four-wave mixing (SFWM). b) Optical microscope image of a representative AlGaAsOI ring resonator pulley with 30 μm radius. c) Resonator transmission spectrum with signal (1572 nm) and idler (1542 nm) wavelengths two free-spectral ranges away from the pump (1557 nm) resonance. d) Resonator transmission spectrum of the pump resonance (blue-trace). A $Q = 1.24 \times 10^6$ is determined from the superimposed Lorentzian fit (red-trace).	90
3.9	Schematic of the experimental setup for a fiber-based folded Franson-type interferometer. The tunable CW laser diode is swept and held at the resonance wavelength of the microring resonator. The laser is sent through ASE rejection filters and coupled via lensed fiber onto and off of the photonic chip. The light is split into a short and long arm of an interferometer. A piezo-based phase shifter is used to modify the phase of the photons that travel through the long arm. The pump photons are removed via an FBG and filters on the signal and idler channels. The signal and idler channels are coupled to SNSPDs to determine the count rates.	91
3.10	(a) Corrected detected singles rates versus on-chip pump power. The difference in the generated singles rates is due to the difference in the filter loss in the two channels (19.4 dB for the idler and 13.6 dB for the signal). (b) On-chip pair generation rate versus on-chip pump power. The dashed line is a fit to the data, yielding a pair generation rate of 20×10^9 pairs $\text{sec}^{-1} \text{mW}^{-2}$ (c) Coincidence-to-accidental ratio (CAR) versus on-chip pair generation rate.	93
3.11	Example trace of the heralded g^2 for the second adjacent resonance with an on-chip power of 108 μW . The dip at zero time delay illustrates $>95\%$ single photon purity.	96
3.12	(a) Schematic illustration of the setup for the two-photon interference experiment using a fiber-based folded Franson interferometer. BPF = band-pass filter; [S] ([L]) denotes the short (long) interferometer path; SNSPD = superconducting nanowire single-photon detector. (b) Coincidence histograms for different interferometric phase $\phi_{s+i} = 0.4\pi$ and π , respectively. (c) Singles counts (top) measured with the interferometer setup simultaneously with the two-photon interference (bottom). Visibility of the raw (fitted) data yields 95% (97.1%).	97
3.13	Entangled photon pair brightness for various material platforms, illustrating the performance of the AlGaAsOI material platform.	99
3.14	Illustration of the uncertainty distribution for a coherent state $\Delta Q = \Delta P$ and a squeezed state $\Delta Q < \Delta P$ of light. The grey circle and blue ellipse illustrate the uncertainty of the particular state.	102

3.15	Squeezed light generated from an InGaP ring resonator source using the second-order nonlinear interaction when pumped at 775nm and light is generated at 1550nm. The plot shows the squeezing output as a function of the intrinsic quality factor of the 1550nm light and the pump power at 775nm. The source is an InGaP resonator with a $5\mu\text{m}$ radius, with 97.5% escape efficiency from the resonator, and loaded quality factor for the pump $Q_{775nm}=700,000$	104
3.16	Squeezed quadrature variance as a function of the pump power for different system efficiencies. The source is an AlGaAsOI microring resonator with $14\mu\text{m}$ radius, $Q = 500,000$, and $\gamma_{NL} = 300\text{ W}^{-1}\text{m}^{-1}$	105
4.1	a) Tunable AlGaAs-on-insulator (AlGaAsOI) microring resonator entangled-photon pair source. The AlGaAsOI platform enables the large-scale integration of active and passive quantum photonic components, including tunable lasers, nonlinear quantum light sources, filters and wavelength division multiplexing (WDM), superconducting nanowire single-photon detectors (SNSPDs), and microcontrollers. These components can be monolithically integrated for all-on-chip quantum photonic circuits, including b) quantum gates for optical computing, c) m -mode unitary operations for Boson sampling, and d) Bell-state measurements for chip-to-chip teleportation of quantum states.	117
4.2	a) Design of an inverse taper edge coupler with dimensions labeled. b) Flare taper design. c) Scanning electron microscope (SEM) image of an array of inverse taper edge couplers. d) Simulated mode overlap as a function of taper width for both the TE and TM modes. e) Mode conversion loss in a flare taper of $3\mu\text{m}$ width and inverse taper of 200 nm width as a function of the taper length for the fundamental TE mode. f) Misalignment sensitivity in the x- and y-axes for the flare and inverse taper designs for the TE mode. g) Heat map showing the mode overlap of various inverse taper widths and different wavelengths for the TE mode. The star shows an experimentally obtained value.	120
4.3	a) Schematic showing the operating principle of a grating coupler. b) Schematic illustrating a grating coupler in the AlGaAs platform. c) Simulated transmission efficiency as a function of wavelength for a fully etched AlGaAs grating coupler and one with a partial etch.	125

4.4	a) Schematic image of the simple waveguide crossing design. The relevant design variables are indicated on the image. b) Simulated mode profile for the optimized simple crossing design. The beating between the higher order modes and the fundamental mode results in a maximum electric field intensity in the center of the waveguide at the crossing, which minimizes the coupling to the vertical waveguide. c) Simulated transmission through the simple waveguide crossing as a function of the wavelength. d) Schematic image of the 13-width crossing design where a swarm optimization varies the width of the parabolic taper at 13 locations and minimizes the transmission loss. e) Simulated mode profile of the optimized 13-width crossing. f) Simulated transmission through the 13-width crossing design as a function of wavelength. g) Optical image of cascaded waveguide crossings for loss characterization. b) Normalized waveguide crossing transmission loss at a wavelength of 1550 nm using the cutback method. The orange trend line indicates an insertion loss of 0.23 dB/crossing.	127
4.5	a) Directional coupler with relevant design parameters labeled. b) The first TE supermode for a pair of two waveguides with 400 nm width and 400 nm height separated by a 300 nm gap. c) The second TE supermode. d) FDTD simulation of the power transferred to the lower waveguide of the directional coupler including the input/output sine bends.	133
4.6	a) Schematic illustration of a multimode interferometer with the relevant design parameters. b) Simulated mode profile of an $\text{Al}_{0.2}\text{Ga}_{0.8}\text{As}$ MMI depicting 3-dB coupling behavior with a length near $16.0 \mu\text{m}$. Here, the waveguide is tapered from $w_1 = 0.4 \mu\text{m}$ to $w_2 = 0.9 \mu\text{m}$ in over $L_t = 10 \mu\text{m}$. The core width is $2.1 \mu\text{m}$, and the length is $18.75 \mu\text{m}$	135
4.7	a) Optical image of an AlGaAs MZI with DCs and a $45 \mu\text{m}$ path imbalance. b,c) Transmission spectra of the 2-4 and 2-3 port combinations of an MZI with MMIs (b) and DCs (c). The MMIs have parameters matching the simulations in Figure 4.6. The directional couplers consist of 400 nm wide waveguides with a 300 nm coupling gap and a $20.8 \mu\text{m}$ coupling length. d) Extracted coupling coefficients for the DCs and MMIs in the MZIs indicating near-optimal 3-dB coupling.	140
4.8	a) Schematic of a double-resonator CROW filter with the relevant coupling and transmission coefficients labeled. b) Simulated transmission through the drop port of the coupled resonators. The plot shows the expected trend for two rings and three rings coupled in series. The rings here are designed using 400 nm thick $\text{Al}_{0.2}\text{Ga}_{0.8}\text{As}$ with waveguide widths of 690 nm and radii of $20 \mu\text{m}$. The loss is assumed to be 0.4 dB/cm and $\kappa_1^2 = \kappa_3^2 = 0.5$ and $\kappa_2^2 = 0.1$. c) Microscope image showing the fabricated CROW filter device.	143

4.9	a) Microscope image of a ring-assisted Mach-Zehnder interleaver device. b) Simulated transmission through the interleaver as a function of the coupling coefficient of the directional coupler on the input and output of the MZI. The device was designed with a $62 \mu\text{m}$ radius ring, $195 \mu\text{m}$ path imbalance, and waveguide widths of 600 nm . The waveguide to ring coupling was designed using a $140 \mu\text{m}$ coupling length with 275 nm gap. c) Experimental transmission scan showing 10 dB extinction for an interleaver device designed to match the simulation parameters.	145
4.10	Motivation for frequency-bin quantum information processing using electro-optic modulators and pulse shapers. A quantum frequency comb is generated using a microring resonator and sent through an integrated pulse shaper to apply phases to particular frequency modes. The output is mixed using a fast electro-optic modulator.	147
4.11	a) Microscope image of a 6 channel AlGaAsOI pulse shaper. Each ring had a $31 \mu\text{m}$ radius, 690 nm waveguide width, 350 nm coupling gap, and a coupling angle of 80 degrees. b) Tuning map of the top six rings showing >1 FSR tuning capability ($\sim 3.2 \mu\text{m}$ FSR). c) Thermal crosstalk measurement for the leftmost ring (ring 1) where the resonance location of ring 1 is monitored while the phase shifter in its drop arm is swept.	148
4.12	a) Manual alignment while tuning the channel 1 phase shifter. The black trace shows the transmission through the upload port and the blue trace shows the through port response. Since ring 1 is shifted due to thermal crosstalk, the upload port becomes misaligned while trying to do manual alignment. b) Optimizer result while tuning the phase shifter. The channels remain aligned as the phase shifter is tuned.	150
4.13	a) Experimental design using the pulse shaper to demultiplex signal and idler photon pairs from a ring resonator entangled photon pair source. A CW laser pumps the ring resonance near 1557 nm to generate a signal and idler photon at the adjacent resonances with 1 MHz and 0.5 MHz off-chip photon flux. This light is then coupled into the pulse shaper chip, and the channels are tuned to demultiplex the signal and idler photons. b) Signal photon counts (orange) and idler photon counts (blue) for 1000 seconds, showing robust alignment of the pulse shaper. The idler photon counts experience significant loss and thus are only on the 1 kHz level. c) Coincidence peak over the 1000 second integration showing the time-correlations of the photon pairs is preserved through the pulse shaper. . .	151

5.1	Progress on quantum computing and Shor’s factorization algorithm. Quantum annealers are not universal, and cannot implement Shor’s algorithm, however they can implement efficient optimization algorithms to factor large numbers, making them a contender to break RSA 2048 encryption. Results for quantum annealers are from D-Wave’s system which boasts up to 5000 qubits [9]. Universal quantum computers based on superconducting circuits are also advancing rapidly with up to 1121 qubits demonstrated on IBM’s latest quantum computer [10]. Advances in Shor’s algorithm have improved the resource requirements, now requiring only 20 million qubits for RSA 2048 [11].	162
5.2	BB84 Quantum Key Distribution Protocol	166
5.3	AlGaAsOI quantum optical microcomb enabling multi-user entanglement distribution. A microring resonator generates pairs of entangled photons across many spectral modes that can be distributed to various users over long distances using low-loss telecommunication optical fibers. The frequency comb spectrum shown is from the device characterized in this work and shows the ability to create a user network with more than 20 nodes with ultrabright entanglement generation requiring $< 100 \mu\text{W}$ on-chip power. In this illustration, Alice and Bob each receive a photon from one set of modes, and Charlie and David each receive a photon from a different set.	172
5.4	Filter characterization illustrating the insertion loss, extinction ratio, and filter bandwidth of one set of fixed-wavelength DWDMs. The transmission measurement is limited by the power meter sensitivity, with additional characterization showing $> 100 \text{ dB}$ extinction.	174
5.5	Experimental design for a three-detector time-bin QKD protocol. A tunable continuous wave (CW) laser source pumps the resonator source after passing through amplified spontaneous emission (ASE) filters. The pump light, along with the entangled photon pairs generated via spontaneous four wave mixing (SFWM) couple from the chip to lensed optical fibers and enter dense wavelength division demultiplexer (DWDM) filters. The signal photon travels to Bob’s measurement setup, and the idler photon travels to Alice. Alice and Bob establish visibility measurements in the X basis via locked Franson interferometry. Alice has a tunable phase shifter and sweeps the relative phase between the short and long path to show two-photon interference of the $\frac{1}{\sqrt{2}}(SS\rangle + \exp(i\phi) LL\rangle)$ state. In the Z basis, Alice uses a single superconducting nanowire single photon detector (SNSPD) and collects the single photon arrival times as well as an electronically delayed channel (black lines). Bob splits his signal photons into two paths using a fiber-based 3-dB splitter. Each path has an SNSPD, and Bob records detection events in either the ”0” time bin (short path) or ”1” time bin (long path). The table shows how a sifted key is established.	176

5.6	Characterization of the entangled photon pair source used for the QKD protocol. a) The frequency comb spectrum from the ring resonator source when pumped with sufficient pump power to generate a frequency comb visible using an optical spectrum analyzer. The blue stars indicate the adjacent resonance and the black triangles indicate the second nearest resonance. b) Collected raw single photon counts as a function of the on-chip pump power. c) Measured coincidence count rate as a function of on-chip power along with the coincidence-to-accidental ratio (CAR). d) Raw (without background subtraction) two-photon interference visibility as a function of the on-chip power. The visibility is largely limited by the pump leakage at higher powers. Figure 5.8 shows the visibility after background subtraction. e) Heralded single photon purity measurement as a function of power.	181
5.7	a) Coincidence histogram of the two-photon interference at 0.4π (blue) and π (black) relative phase between the long and the short path. b) Single photon flux as the relative phase is swept showing stable flux on both channels. c) Coincidence counts in the central peak as a function of the relative phase along with a sinusoidal fit of the data. The fit shows 74.9% uncorrected two-photon visibility and 91% visibility with background subtraction.	183
5.8	Visibility as a function of power for the adjacent and second nearest resonance with and without background subtraction. The red data points indicate the background subtracted results while the blue and black data points indicate the same data as shown in Figure 5.6d).	185
5.9	Example trace of the heralded g^2 for the second adjacent resonance with an on-chip power of $108 \mu\text{W}$. The dip at zero time delay illustrates $>95\%$ single photon purity.	186
5.10	a) Sifted key rate and bit error rate as a function of on-chip pump power. The pump power is limited to $<120 \mu\text{W}$ to maintain a visibility above 70.7%. The triangles indicate the adjacent resonance characterization, and the stars indicate the second nearest resonance. b) Sifted key rate and bit error rate of the second nearest resonance as a function of attenuation on Alice's path. The pump power is maintained at $\sim 90 \mu\text{W}$ while sweeping the voltage on a variable optical attenuator. The equivalent optical fiber distance is calculated and indicated on the top axis. c) Key rate stability measurement. Pumping with $\sim 65 \mu\text{W}$ of on-chip power, the source consistently outputs 2.5 kbps sifted key rate for up to 10,000 seconds (limited by the measurement time of the experiment).	187
5.11	The Shannon rate, $1 - 2H(x)$, of the QKD system as a function of the on-chip power. As the error rate approaches $\sim 11\%$, the Shannon rate goes to 0, and no secure key can be established. For the adjacent resonance, this occurs $\sim 70\mu\text{W}$, and for the second resonance this value is at $\sim 108\mu\text{W}$.	189

5.12	Illustration of the deployed fiber experiment conducted on the UCSB campus. Six loops of ~ 2 km fibers are in place between our research lab in Henley Hall and the campus police department building. The yellow lines indicate a rough estimate of the path of the deployed fibers which follow underneath the road connecting these parts of campus. The six independent loops allow for measurements to be completed at different deployed fiber lengths. a) The sifted key rate and error rate of the QKD protocol after sending Alice's photons through the deployed fiber path. b) The stability of the key rate and error rate at the longest deployed fiber distance of 12.3 km. The chip-to-fiber coupling drift is significant during this measurement, so a realignment is completed at the 5,300 second mark. Using the 12.3 km deployed fiber, the UCSB logo is transmitted and encrypted using the QKD protocol. The image is encrypted with a key transmitted at 600 bps and a 9 percent error rate without any error correction.	192
6.1	a) Experimental schematic of qubit demultiplexing utilizing an 3.2 nm FSR AlGaAs ring resonator source and a 13.0 nm FSR MZI (DC). b) Transmission spectra of a ring resonator and MZI tuned to a relative phase of zero and π radians. The signal, pump, and idler wavelengths are indicated. c) Normalized counts on the SNSPDs after demultiplexing as the MZI phase is swept from 0 to 2π radians.	205
6.2	a) Microscope image of the AlGaAsOI circuit for HOM and tunable Bell State generation. The ports on the output are labeled 1-4 on the right side of the image. The initial photon state is in $ \Phi^+\rangle$ (shown in the bottom left panel of the inset). After exiting the final interferometer, the unitary MZI operator transforms the initial state into either the $ \Psi^+\rangle$ or $ \Phi^-\rangle$ state when a 0 and π phase shift is applied, respectively.	208
6.3	Microscope image of the AlGaAsOI circuit for HOM interference. This image is the same as illustrated in Figure 6.2a), but now the different portions of the circuit are highlighted for the HOM interference experiment. Light enters from the left side of the circuit and goes into a symmetric MZI that acts as a tunable beamsplitter (BS) to distribute the input power equally to the two ring sources. The two ring resonators act as sources of entangled photon pairs. Next, two unbalanced MZIs demultiplex the signal and idler photon pairs into two paths. The signal photons exit ports 1 and 4 for heralding, and the idler photons enter the HOM interferometer to show two-photon quantum interference.	210

6.4	a) Transmission scan through ring 1 and exiting through the topmost port (port 1). b) Transmission scan through ring 2 and exiting through the bottommost port (port 4). c) Signal resonance scan for ring 1 showing 1.2×10^5 loaded quality factor. d) Pump resonance scan for ring 1 showing 1.1×10^5 loaded quality factor. e) Idler resonance scan for ring 1 showing 0.7×10^5 loaded quality factor. f) Signal resonance scan for ring 2 showing 0.9×10^5 loaded quality factor. g) Pump resonance scan for ring 2 showing 1.2×10^5 loaded quality factor. h) Idler resonance scan for ring 2 showing 1.4×10^5 loaded quality factor.	213
6.5	a) Tuning of the first tunable beamsplitter of the HOM circuit to adjust the power coupled into each of the two ring sources. b) Single photon counts and coincidence counts for various pump powers of the first ring source. c) Single photon counts and coincidence counts for various CW pump powers of the second ring source.	215
6.6	The demultiplexers are highlighted on a microscope image of the HOM circuit. a) Single photon counts as the power in the demultiplexer heater is swept. The left panel shows all four SNSPD channels, and the right panel shows just the photons exiting the top port (port 1). b) Same plot as <i>a</i> for the second demultiplexer.	216
6.7	a) Experimental setup to measure HOM interference using a tunable CW laser. The laser is filtered through tunable bandpass filters to remove ASE power at the signal and idler wavelengths before being coupled into the chip. The chip performs the HOM experiment when the rings both generate photon pairs simultaneously that can interfere on the final HOM interferometer. A fiber v-groove array couples light from all four output ports of the circuit. Ports 1 and 4 are sent through DWDMs aligned with the idler mode, and ports 2 and 3 are sent through the signal DWDMs. The photons are detected using SNSPDs and time correlations are measured using a time correlated single photon counting module. b) Example interference scan as the HOM interferometer phase heater power is swept.	219
6.8	a) Joint spectral intensity of a CW ring resonator entangled photon pair source. The main diagonal has width related to the spectral bandwidth of the pump source, and the antidiagonal is set by the lesser of spectral bandwidth of the phase-matching function or the transmission window. b) JSI of a pulsed laser showing the broadening along the main diagonal which results in a separable bi-photon state. c) Illustration of CW pumping with a signal and idler resonance. The pump mode is narrow relative to the resonance linewidth and can thus generate a variety of unique signal and idler frequencies. The green and orange lines in a) are shown in the schematic in c).	223

A1	Example singles scan for an on-chip power of -15.14 dBm (30.6 μ W). The scan begins with the laser set to an off-resonance wavelength (at 430 seconds). The laser is then swept to the resonance wavelength, reaching the resonance wavelength at approximately 630 seconds. The laser is held at this wavelength for 360 seconds to allow for the average singles rate to be determined.	231
A2	Example histogram showing the normalized coincidence counts (in counts per second) as a function of the time delay. The data is from the device characterized in Chapter 3 with record-high photon pair brightness. Here, -12.2 dBm of power into the ring generates over 1200 coincidences per second.	232
A3	Illustration of the CAR measurement. Here, data from the QKD protocol used in Chapter 5 is used to illustrate the CAR calculation. The coincidence peak is integrated over a roughly 1 ns window (corresponding to the FWHM) and shown in green to collect the total coincidence count rate. The accidental counts are recorded by integrating over the same time window away from the peak (shown in purple). Here, the total coincidence count rate is 861.3 counts per second, and the accidental counts are 105.7 counts per second, corresponding to a CAR of 8.15.	233
A4	a) Transmission scan of the 8th device of Crazy Coral wafer 3. The blue trace shows the output through port 1, and the orange trace shows the output through port 4. b) The single photon and coincidence count rates for the top ring source (ring 1) are shown as a function of the off-chip power. The source is so efficient that the SNSPDs latch and cannot collect data at the powers above -23 dBm off-chip (indicated by the black box). c) The second ring is characterized, showing 300,000 single photon counts per second and 400 coincidences per second. d) The fourfold coincidence data for the HOM experiment with this device, showing a raw visibility of 72 %.	235

List of Tables

2.1	Examples of degrees of freedom used for photonic qubit systems and their generation, manipulation, and detection schemes. SPD -single photon detector, WDM -wavelength division multiplexer, PBS -polarization beam-splitter	18
2.2	Comparison of nonlinearity, refractive index, bandgap, and scalability of nonlinear material platforms	54
3.1	All values are reported for microring resonators. The CAR, visibility, and $g_H^{(2)}(0)$ are shown for 1 MHz PGR. Brightness and PGR shown are normalized to 1 mW on-chip pump power. Data from this dissertation is highlighted in red.	98
4.1	Table comparing the AlGaAsOI platform with SOI and Si ₃ N ₄	152
5.1	Eavesdropper: BB84 quantum key distribution protocol with eavesdropping.	168
5.2	BBM92 entanglement-based quantum key distribution protocol.	170
5.3	System losses for the measurement of entangled photon pairs generated from a high-Q AlGaAsOI microring resonator.	173
5.4	Comparison of entanglement-based QKD protocols. The key rates are adjusted to reflect transmission without attenuation and are reported for a single set of photon pairs (i.e without multiplexing).	190

Chapter 1

Introduction

Quantum technologies are at the cusp of realizing useful systems that can facilitate computation, sensing, communication, and storage. Already, small-scale quantum systems have shown “supremacy” or “quantum advantage” by solving specialized tasks that are intractable on classical hardware [1–3]. Although these results are impressive, the systems are still dominated by noise and are more susceptible to errors than conventional computers [4]. These limitations, along with difficulty in maintaining low noise with an increasing number of quantum bits (qubits), have restricted the size and utility of quantum systems. System-level implementations have been completed on a number of quantum platforms, and it is still unclear which will be the best suited for scalable, fault-tolerant, quantum computing and information processing. Beyond the direct application of integrated photonics for optical quantum computing, quantum photonics systems will also play a pivotal role in the development of quantum technologies and networks. The low loss in free space and fiber optic cables along with minimal environmental decoherence make a photon an ideal carrier of quantum information. Thus, the transfer of quantum information between systems and users will likely utilize quantum photonic technologies. Regardless of which paths quantum technologies take in the future, quantum photon-

ics will be a crucial, core building block in large scale systems and for the transfer of quantum information across large distances. Thus, the study of methods to improve the efficiency of entanglement distribution, generation, and scalability in quantum photonic circuits is vital to future quantum technologies.

The decades of research on integrated photonics driven by semiconductor processing and telecommunications systems has pushed silicon photonics to a position of prominence in the field of quantum photonics. The scalability of silicon device fabrication is unrivaled, and silicon photonics has relatively low propagation loss and a moderate nonlinearity that can enable nonlinear quantum light generation. In this thesis, alternative material platforms with much larger nonlinearities are explored to demonstrate brighter, more efficient sources of entanglement and quantum light. Although the platforms are explored on their own, it is likely that integration with silicon-based photonics will be the best route to scaling quantum photonic systems — where the wealth of knowledge in silicon photonics can be leveraged with the efficient quantum light sources from other nonlinear materials.

1.1 Thesis Outline

This thesis is organized into five main chapters. It starts with an introduction and background chapter (Chapter 2) that introduces the foundational knowledge required to comprehend the work completed in this dissertation. A general overview of quantum computation and information is established through a discussion of bits and qubits, single qubit states, mixed states, photonic qubits, and multiple qubit states. Next, the concepts of entanglement and quantum interference are discussed. These sections are crucial to the final application-focused experiments performed in Chapter 5 and 6. The discussion will then continue by generally introducing integrated photonics through waveguide the-

ory and the critical figures of merit relevant to integrated photonic circuits. Since the quantum light sources in this work are mainly based on ring resonators, Chapter 2 will introduce ring resonator design and theory. A classical description of nonlinear optics using III-V materials is included to form the basis for the quantum picture developed in Chapter 3. The chapter ends with a discussion of various material platforms, highlighting some of the state-of-the-art materials used for integrated quantum photonic systems along with the advantages and disadvantages of each system.

Chapter 3 builds on the foundational theory of classical nonlinear optics to create a quantum framework that can be used to describe the creation of quantum states of light. The chapter will focus mainly on the creation of entangled photon pairs or heralded single photons (discrete variable quantum systems) with a brief discussion of squeezed light generation (continuous variable quantum systems). Preliminary results showing a 1000-fold improvement in the entangled photon pair brightness using AlGaAs-on-insulator (AlGaAsOI) microring resonators with high quality factors are shown to motivate the use of III-V material platforms for integrated quantum photonics. The full characterization of a ring resonator quantum light source is included to show that the photons are indeed entangled with $> 97\%$ visibility and have high purity $> 99\%$. The chapter ends with a discussion of modeling and simulations for squeezed light generation, showing the possibility of creating a 16 dB chip-scale squeezed light source.

Chapter 4 continues the development of the AlGaAsOI material platform by discussing the design and testing of critical components for the creation of integrated quantum photonic circuits. Here, fiber-to-chip couplers are designed using both edge coupling and vertical coupling strategies with less than 3 dB of loss per facet. Next, waveguide crossers, beamsplitters, and interferometers are designed with comparable performance to silicon and silicon nitride material platforms for quantum applications. The chapter ends with a discussion of optical filters, showing various designs and preliminary results for

interference-based filters, ring filters, photonic interleavers, and spectral pulse shapers. The pulse shaper is discussed in detail and used to demultiplex signal and idler photons from a quantum light source.

Chapter 5 moves on to the first applied demonstration using quantum light from the AlGaAsOI material platform. Photonic time-bin entangled qubits are distributed to two users and used to establish a quantum key for secure communications. The light source produces 8 kbps sifted key rates with less than 10% error rate. Using a variable attenuator to simulate fiber distance, > 100 bps sifted key rates with < 10 percent error are possible up to 92.5 km. This characterization is for one pair of entangled photon modes, and when the > 20 modes are multiplexed, key rates > 100 kbps are possible. To demonstrate the utility of the system, a secure key is established through 12.3 km of deployed standard telecommunications fiber on the UCSB campus and used to encrypt a 21 kB image with $< 9\%$ error. This initial demonstration shows that the source can be utilized with already established fiber networks to leverage the infrastructure established by the telecommunications industry.

Lastly, Chapter 6 discusses progress in advancing the AlGaAsOI platform with additional photonics componentry, including chip-scale demultiplexing where an interferometer is integrated with a ring resonator quantum light source to demultiplex the generated signal and idler entangled photon pairs. Next, the circuit is scaled up by integrating two ring resonator sources with demultiplexers and an interferometer to perform the Hong-Ou-Mandel experiment using a single photonic chip.

This thesis establishes a framework for quantum photonic integrated circuits using III-V semiconductor materials, with an emphasis on the AlGaAsOI and InGaPOI material platforms. The efficiency of quantum light sources with these highly nonlinear materials exceeds that which is possible with silicon or silicon nitride. The platforms have a plethora of other beneficial effects including second order nonlinearity which opens the possibility

for fast electro-optic modulation and tuning via the Pockels effect. The platforms are also inherently compatible with quantum dots sources that can pave the way for laser integrated sources of quantum light. The foundation established here is just the initial step toward larger integrated quantum photonic circuits, and the future of these platforms seems quite promising.

1.2 Permissions and Attributions

1. The content of Chapter 3 has previously appeared in the open access journal PRX Quantum [5]. It is reproduced here under the Creative Commons Attribution 4.0 International.
2. The content of Chapter 4 and Chapter 6 have previously appeared in the open access journal APL Photonics [6]. It is reproduced here under the Creative Commons CC BY license.
3. The content of Chapter 5 has previously appeared in the open access journal Optica Quantum [7]. It is reproduced here under the Optica Open Access Publishing Agreement.

Bibliography

- [1] F. Arute, K. Arya, R. Babbush, *et. al.*, *Quantum supremacy using a programmable superconducting processor*, *Nature* **574** (10, 2019) 505–510.
- [2] Y. Wu, W.-S. Bao, S. Cao, *et. al.*, *Strong quantum computational advantage using a superconducting quantum processor*, *Physics Review Letters* **127** (2021), no. 180501.
- [3] H. S. Zhong, H. Wang, Y. H. Deng, *et. al.*, *Quantum computational advantage using photons*, *Science* **370** (12, 2020) 1460–1463.
- [4] J. Preskill, *Quantum Computing in the NISQ era and beyond*, *Quantum* **2** (8, 2018) 79.
- [5] T. J. Steiner, J. E. Castro, L. Chang, *et. al.*, *Ultra-bright entangled-photon pair generation from an AlGaAs-on-insulator microring resonator*, *PRX Quantum* **2** (9, 2021) 010337.
- [6] J. E. Castro, T. J. Steiner, L. Thiel, *et. al.*, *Expanding the quantum photonic toolbox in AlGaAsOI*, *APL Photonics* **7** (9, 2022) 096103.
- [7] T. J. Steiner, M. Shen, J. E. Castro, *et. al.*, *Continuous entanglement distribution from an AlGaAs-on-insulator microcomb for quantum communications*, *Optica Quantum* **1** (12, 2023) 55–62.

Chapter 2

Background

In the early twentieth century, a series of classical physics crises necessitated the development of a new theoretical picture to describe naturally occurring phenomena and address some of the inconsistencies predicted by classical physics. For example, the “ultraviolet catastrophe” predicted infinite energies, and classical descriptions of atoms involved electrons spiraling into the nucleus [1]. Scientists spent many years trying to understand these aspects using their current models, but no clear answer was found. Instead, to address these lapses in classical theory, the basis of quantum mechanics was developed in the early 1920s, providing a new, mathematical framework for the construction of physical theories. Some of the major foundations of quantum mechanics that differentiate from classical physics include quantization, wave-particle duality, the uncertainty principle, superposition, and entanglement [2]. These aspects allow for a more complete understanding of the universe where quantities like energy, electric charge, and angular momentum are quantized (existing in discrete, indivisible units), and objects can exhibit both wave- and particle-like behavior. With this new understanding, many of the gaps in classical physics were addressed, and a revolution in science and technology began, not only allowing for the creation of critical components like transistors, but also beginning

a new field of study—quantum information processing, computation, communications, networking, and sensing.

In conjunction with the tremendous advances in quantum mechanics in the last couple of decades, the field of optics and photonics has seen a similarly rapid advancement. No longer is the study of light simply for free-space systems of mirrors and lenses, but now includes lasers, fiber optics, and other optical technologies to generate, control, and measure various properties of light. In a similar fashion to the advancement of electrical components from the semiconductor boom, the miniaturization and integration of photonic components over the past decades have resulted in efficient systems for optical communications that has become the most efficient method of high-speed data transmission and enabled the creation of a global communications network [3, 4]. Combining these two growing fields results in the field quantum photonics—the focus of this thesis. The developments in quantum photonics over the past few decades and an outlook toward the future of the field is outlined in Reference [5].

This chapter will provide some of the necessary background in quantum mechanics, integrated photonics, and quantum systems to help understand the motivation for many of the projects pursued in this dissertation. Although the work described in the following chapters is based solely on photonic-based systems, some general discussion of quantum technologies as well as motivation for the use of photonic-based technologies will be included.

2.1 Quantum Computation and Information

For decades, classical computing technologies have scaled with the commonly known Moore’s law, where the computational power doubles for a constant cost every two years. The improvements have largely been based on the miniaturization of the building blocks

of classical computers, namely transistors, and the improvement to semiconductor manufacturing to increase the density of components on a single chip. However, this trend has begun to falter as components have reached near fundamental limits in terms of size. As the devices approach the atomic scale, quantum mechanical effects start to interfere with the desired functionality, creating a bottleneck to future scaling of classical computers. One approach to continue advancing computing technologies is to shift the computing paradigm, moving to quantum computing technologies. Quantum computers have already been shown to more adequately address a particular subset of problems and tasks that appear to be intractable for classical technologies. Since quantum systems can exist in a superposition of states, it is possible to engineer the constructive and destructive interference of these states to lead to solutions more quickly than classical systems—potentially allowing for a more efficient way to address these tasks [6]. That being said, it is important to note that quantum computers rely on the measurement probabilities to indicate the optimal solution. Thus, although many solutions are explored simultaneously, the best solution is only found through numerous, repeated computing cycles to determine the most probable outcome, necessitating a reproducible, stable physical computing platform. It is also important to understand that although a quantum computer may be able to perform a particular set of useful tasks more efficiently than a classical computer, it is unlikely that a quantum computer will ever do *every* computation more efficiently. Algorithms like Shor’s algorithm for factoring large numbers and Grover’s algorithm for searching unsorted databases showcase the potential of quantum computing to solve problems exponentially faster than classical computers for specific tasks [6]. In addition to providing an alternate means to improve upon the functionality of classical computing, the study of quantum technologies can provide a route to revolutionize information transfer, encryption, and provide additional insight to the workings of many natural phenomenon.

One of the greatest challenges facing the expansion of quantum technologies is the creation of a platform that can generate, interact, and measure quantum states at (very) large scales. Famously, DiVincenzo developed a set of criteria that a quantum system must meet for useful quantum computing [7]:

- A scalable physical system with well-characterized qubits.
- The ability to initialize the state of a qubit to a simple fiducial state.
- Long decoherence times (much longer than the gate operation time).
- A universal set of quantum gates.
- Qubit-specific measurement capability.

In addition to this set of criteria for quantum computing systems, there are two extra characteristics needed for quantum communication systems.

- The ability to convert between stationary and flying qubits.
- The ability to transmit flying qubits between specified locations.

Although this list of criteria seems extensive, it is not without flaws. For example, the requirement of a scalable system might immediately discourage a lot of currently expensive or complex-to-fabricate technologies, but scalability can be engineered over time. The third and fourth criteria are also often in direct conflict. A system with long decoherence times has little to no interaction with the environment or other qubits, thus making two-qubit interactions and gates difficult to implement with high fidelity. From this list, it is clear that finding a technology that meets all of the requirements is challenging, especially with some of the requirements seeming to be in direct conflict. Nonetheless, there have been many promising demonstrations of small scale quantum computers in the past

few years that show the possibility to overcome these hurdles. A example is the demonstration at Google that showed “quantum supremacy” using a superconducting quantum processor in 2019 for a random circuit [8]. More recently, Professor Jianwei Pan’s group’s demonstrated quantum computational advantage via optical Boson sampling in 2020 [9]. These seminal experiments pave the way toward the implementation of quantum technologies on a large scale that can be used for more efficient algorithms, simulations, and information transfer. Along with these great developments, there has been a considerable amount of research using various platforms for quantum technologies, including electronic spins [10], optomechanical resonators [11], superconducting circuits [12], and trapped atoms and ions [13]. From a commercial perspective, the sheer magnitude of new quantum computing companies in a variety of platforms indicates the race for these various technologies to create a useful quantum computer. Companies like PsiQuantum utilize silicon photonics for discrete variable quantum computing, while companies like Xanadu pursue an alternative approach based on continuous-variable quantum computing using squeezed states of light [14]. Other teams at Google (as mentioned above) and IBM utilize superconducting qubits, and researchers at IonQ, QuEra, Atom Computing, and ColdQuanta use trapped ions and neutral atoms [15]. The breadth of research in quantum computing technologies is incredible and there is no clear leading technology yet, creating significant competition between platforms (in addition to the competition of teams within a single platform).

This thesis will focus on what is regarded as one of the more promising platforms, especially for quantum communications—encoding, manipulating, and detecting quantum information using photons, otherwise known as the field of quantum photonics. The aforementioned matter- and superconducting-based quantum systems typically require operation in ultra-high vacuum or at millikelvin operating temperatures to prevent interactions between the quantum system and the environment. Photons are unique in

their ability to generate and distribute entangled quantum states across long distances in free space or fiber networks at room temperature whilst retaining a high degree of coherence. Useful quantum computers and communication systems will look much more like data centers than a single computing unit; as such, they must be networked. Photons thus have an advantage, since computing and networking can utilize the same physical hardware, methods, encoding, and framework. Additionally, photons allow for the encoding of quantum information across numerous degrees of freedom including polarization, spatial path, frequency mode, temporal bin, and temporal mode encoding [16]. For quantum communication applications, the long decoherence time and limited interaction between photons is a great advantage, though it poses a challenge for photonic quantum computing—where two-qubit interactions are necessary to create universal quantum gates. In 2001, this obstacle was addressed by Knill, Laflamme, and Milburn who set out to develop a scheme for all-optical quantum computing without needing photon-photon interactions [17]. This field, linear optical quantum computing, shows the potential to create a photonic quantum computer using only a source of identical photons, a reconfigurable interferometer, and single photon detectors, replacing two-qubit interactions with probabilistic linear optic interference.

2.1.1 Bits vs. Qubits

Traditional computers process information in bits, which are binary units represented as either 0 or 1. Classical information is represented by strings of bits, and operations in classical computing use boolean logic to manipulate these bit strings. Quantum computers, on the other hand, use quantum bits or qubits. Qubits can exist as superpositions of 0 and 1, allowing for unique utility and the development of new quantum algorithms and computations not possible via classical bits.

Hilbert Space

The advantages of qubits can be seen by discussing the scaling of information stored for bits vs qubits. In quantum mechanics, the state of a physical system is represented by a vector in a Hilbert space, which is a complex vector space with an inner product [1]. For N classical bits, the dimension of this state space scales linearly with N . For qubit systems, on the other hand, the dimension of the state space scales as 2^N , and d -dimensional qubits (called qudits) scale as d^N . For low bit/qubit values, this advantage is small, but as the system scales to hundreds and even thousands of qubits, the benefit is significant. This is one of the advantages of quantum systems—the ability to store exponentially more information (as classical probability amplitudes) for the same number of bits/qubits. The challenge is then to satisfy the DiVincenzo criteria.

Single Qubit States

Figure 2.1 illustrates some examples of photonic qubit systems. In the center, the Bloch sphere is a visual representation of a qubit, with the north and south pole representing the $|0\rangle$ and $|1\rangle$ states. Arbitrary quantum states are represented by points on the surface of the sphere, having the form $\alpha|0\rangle + \beta|1\rangle$ with α and β as complex numbers that represent the probability amplitude of each state. We can measure a bit to determine whether it is a 0 or 1, however for a qubit, we cannot directly measure the values of α and β . Instead, when we measure a qubit, we get result 0 with probability $|\alpha|^2$ and result 1 with probability $|\beta|^2$ where to preserve unity total probability, $\alpha^2 + \beta^2 = 1$. Thus, in order to fully determine the qubit state, numerous measurements are required to distill out the probability amplitude of each state. The superposition of qubit states is counter-intuitive, but many real qubit systems have been established.

The single qubit introduced above ($\alpha|0\rangle + \beta|1\rangle$) can also be written in vector/matrix

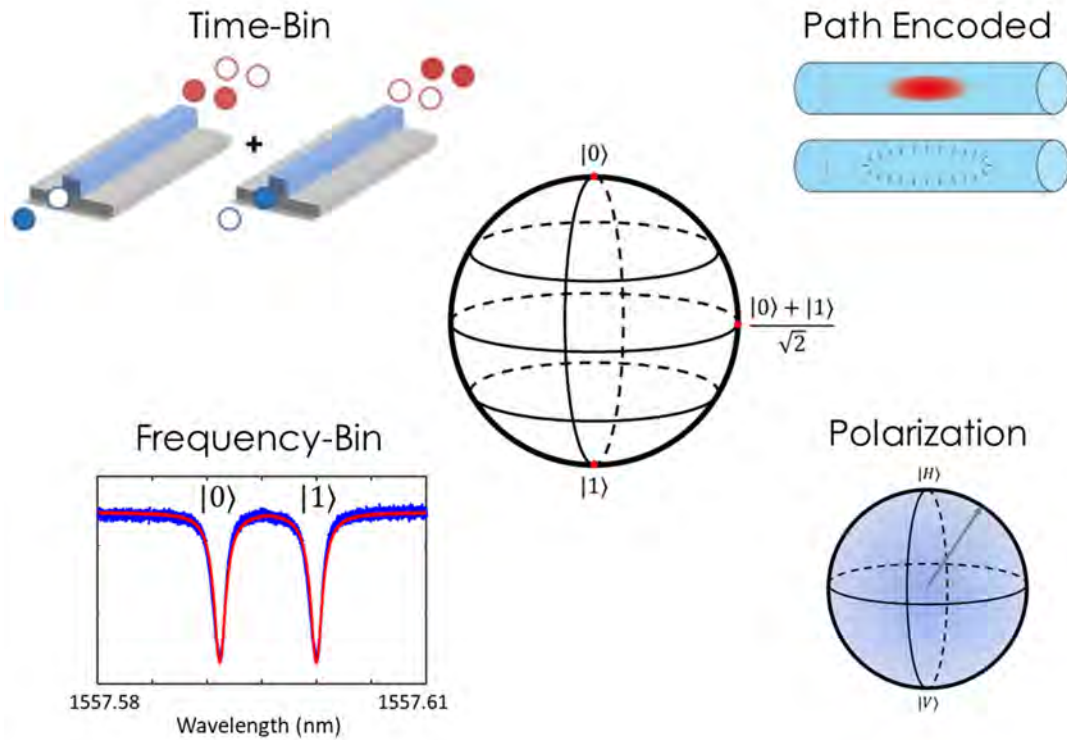


Figure 2.1: Examples of photonic degrees of freedom used as qubits. Time-bin qubits are the superposition of photons in an early or late time window. Path encoding involves photons existing in a state between two paths (commonly waveguides). Frequency-bin qubits are the result of photons existing in a superposition of two different frequencies of light. Polarization qubits involve the superposition of horizontal or vertical polarization. In the center of the picture, the Bloch sphere is illustrated which represents the possible pure qubit states which lie on the surface of the sphere.

notation as $|\psi\rangle = \begin{bmatrix} \alpha \\ \beta \end{bmatrix}$. Now, the top element represents the amplitude of $|0\rangle$ and the bottom entry is the amplitude of $|1\rangle$. This representation can sometimes be useful for the demonstration of operations on the qubit state. For example, a simple NOT gate has the effect of flipping the 0 and 1 bit. The quantum not gate X can be represented by the matrix,

$$X = \begin{bmatrix} 0 & 1 \\ 1 & 0 \end{bmatrix} \quad (2.1)$$

We can express this operation on our arbitrary single qubit state as,

$$X \begin{bmatrix} \alpha \\ \beta \end{bmatrix} = \begin{bmatrix} \beta \\ \alpha \end{bmatrix} \quad (2.2)$$

Quantum gates on a single qubit can be described by two by two matrices [1], and these matrices have constraints to preserve the nature of the quantum state. Recalling the normalization of the probability amplitudes, $|\alpha|^2 + |\beta|^2 = 1$, the output state of a gate must preserve this normalization after the operation. This means that the matrix describing the gate must be *unitary*, meaning that for a matrix U , $U^\dagger U = I$. Here, U^\dagger is the *adjoint* of U which is obtained by taking the transpose of the matrix followed by taking the complex conjugate. I is the two by two identity matrix. For example, the X NOT gate above can easily be shown to be unitary (especially since the adjoint of X is still X),

$$X^\dagger X = \begin{bmatrix} 0 & 1 \\ 1 & 0 \end{bmatrix} \begin{bmatrix} 0 & 1 \\ 1 & 0 \end{bmatrix} = \begin{bmatrix} 1 & 0 \\ 0 & 1 \end{bmatrix} \quad (2.3)$$

Incredibly, the condition that quantum gates be unitary is the *only* constraint on their properties. Another important single qubit gate is the Z gate which leaves $|0\rangle$ unchanged and flips the sign of $|1\rangle$,

$$Z = \begin{bmatrix} 1 & 0 \\ 0 & -1 \end{bmatrix} \quad (2.4)$$

The Hadamard gate is also an important gate that turns $|0\rangle$ into $(|0\rangle + |1\rangle)/\sqrt{2}$ and $|1\rangle$ into $(|0\rangle - |1\rangle)/\sqrt{2}$.

$$H = \frac{1}{\sqrt{2}} \begin{bmatrix} 1 & 1 \\ 1 & -1 \end{bmatrix} \quad (2.5)$$

Mixed States

The previous discussion has been centered on what are known as *pure* states, where the state lies within one superposition state $|\phi\rangle = \alpha|0\rangle + \beta|1\rangle$. In general, a quantum state can exist in one of a number of states $|\psi_i\rangle$ where i is an index and each state has probability p_i . We can express these mixed states as a density matrix $\hat{\rho}$,

$$\hat{\rho} = \sum_i p_i |\psi_i\rangle \langle \psi_i| \quad (2.6)$$

which has purity \mathcal{P}

$$\mathcal{P} = \text{Tr}(\hat{\rho}^2) \quad (2.7)$$

For the pure states discussed in the previous sections, the exact state is known, and the density matrix is simply $\hat{\rho} = |\psi\rangle \langle \psi|$. If the state is not fully known, it exists as a mixed state, which is a mixture of the different pure states in the ensemble for ρ [1]. Mathematically, the purity of a pure state is 1, while a mixed state has $\mathcal{P} < 1$. The purity has values from $1/d$ (fully mixed) to 1 (pure) for states of dimension d . Using the Bloch sphere from the center of Figure 2.1, pure states lie on the outer surface of the sphere, and mixed states lie within the sphere with a fully mixed state at the center of the sphere. Physically, mixed states imply statistical ensembles or probabilistic mixtures of pure states. For a mixed states, the qubits can be thought as having their states pre-defined before any measurement is completed—the mixed state is a statistical summation of two possible states with probabilities. Pure states are coherent superpositions and have corresponding probability amplitudes to exist in two possible states.

Photonic Qubits

For the case of photonic qubits, a qubit can be encoded as a probability amplitude corresponding to the photon occupation of two modes of a specific degree of freedom of the optical field [16]. Table 2.1 lists the generation, manipulation, and detection schemes common for some common degrees of freedom of photons that are used for qubits. One of the most common methods of creating a photonic qubit is to utilize a photon's polarization state where the horizontal polarization can be the $|0\rangle$ state and a vertical polarization can represent the $|1\rangle$ state. Other degrees of freedom can also be utilized to encode a photonic qubit including spatial mode (or path), frequency bin, time bin, and temporal mode. Surrounding the Bloch sphere in Figure 2.1 are four examples of photonic qubits. Time-bin qubits are comprised of a photon in either an early or late arrival time bin. Time delays and interferometers can be used to prepare different quantum states based on the arrival time of a particular photon. Path encoded qubits are defined based on the photon occupation of a particular path (commonly waveguides). Beamsplitters and phase shifters can be used to manipulate the path a photon travels. Frequency-bin encoding utilizes the frequency (wavelength) of the photon to define a $|0\rangle$ and $|1\rangle$ bin. Modulators can be used to mix frequency-bin states, and along with spectral pulse shapers can be used for quantum information processing and computing [18]. Perhaps the most common (and intuitive) photonic qubit is the polarization qubit where the polarization of a photon encodes the quantum information. A great advantage of using photonic qubits compared to other qubit systems is the ability to encode quantum information in multiple of these degrees of freedom simultaneously, enabling one photonic qubit to act as multiple qubits simultaneously. Many of the degrees of freedom listed can also be manipulated to more than two levels, allowing for the creation of qudits and providing advantages to scaling photonic systems.

Degree of Freedom	Generation	Manipulation	Detection
Time-Bin	Unbalanced interferometers	Delay lines, interferometers	Time Correlated SPDs
Path-Encoding	Beamsplitters	Beamsplitters, interferometers	SPDs for each path
Frequency-Bin	Frequency combs	Modulators, pulse shapers	WDMs and SPDs
Polarization	Birefringent materials	Waveplates	PBS and SPDs

Table 2.1: Examples of degrees of freedom used for photonic qubit systems and their generation, manipulation, and detection schemes. **SPD**-single photon detector, **WDM**-wavelength division multiplexer, **PBS**-polarization beamsplitter

Single qubit operations like manipulating the photon population of the two modes or applying a phase shift between them can be readily implemented using interferometers. Two-qubit operations require the ability to apply a π phase shift rotation on one of the qubits depending on the state of the other qubit [1]. Since photons interact very weakly via nonlinear processes, these operations are much more difficult to implement. An alternative method is to mimic nonlinear interactions using linear optics and measurement that creates a probabilistic gate that provides the correct result after post-selection [19]. The most well-known implementation of this concept is the scheme detailed by Knill, Laflamme, and Millburn (KLM) [17]. This method only requires beam splitters, phase shifters, single photon sources and photodetectors to create an efficient quantum computer. The use of non-deterministic gates for the multi-qubit gate requires the input of ancilla photons to herald a successful operation. Thus, although this method circumvents the extremely low efficiency of nonlinear photon interactions, it brings with it a large overhead of ancillary photons required to herald successful operations.

Going back to the DiVincenzo criteria, photonic qubits (along with KLM or linear optic quantum computing protocols) have the potential to meet all of the requirements for a quantum computing system. Photonic systems can be incredibly scalable (using

semiconductor foundries). The photons can be initialized to a desired state using interferometers and phase shifters. Prepared states have long decoherence times (fundamental property of photons). With linear optics, a universal gate set has been established. Finally, the measurement of the qubit state can be completed using single photon detectors. There are still considerable challenges that hinder the current utility of photonic qubit systems. Mainly, the photon generation and gates for standard nonlinear sources are both probabilistic, so achieving larger systems reaches a bottleneck as these probabilities multiply. For example, a standard photonic implementation of a controlled-NOT gate (one of the building blocks for a universal quantum computing gateset) has probability $1/9$ [20], so cascading many of these gates drastically reduces the rate of qubit information processed. Significant work is being done to implement deterministic gates [21] and sources [22] that can overcome these limitations to the scaling of photonic qubit systems. Even with these obstacles, photonic qubits have already been shown to be incredibly useful for quantum communications due to the well-established telecommunications fiber optic network [23, 24]. Quantum communications can leverage the infrastructure already established to rapidly advance and create interconnected quantum networks.

Multiple Qubit States

States of multiple qubits can be represented in a similar way to classical bits. For example, two classical bits exist in one of four possible states $|00\rangle$, $|01\rangle$, $|10\rangle$, $|11\rangle$. Again, we can express this pure state as a superposition of the possible permutations of the two bits $|\psi\rangle = \alpha|00\rangle + \beta|01\rangle + \gamma|10\rangle + \delta|11\rangle$. Each of the individual states is a tensor product of the two single qubit states: $|ij\rangle = |i\rangle \otimes |j\rangle$. Following the matrix notation above, if we have two qubits $|\psi_1\rangle = \begin{bmatrix} \alpha \\ \beta \end{bmatrix}$ and $|\psi_2\rangle = \begin{bmatrix} \gamma \\ \delta \end{bmatrix}$, the total state of the two qubit system

can be described as,

$$|\psi\rangle = |\psi_1\rangle \otimes |\psi_2\rangle = \begin{bmatrix} \alpha \\ \beta \end{bmatrix} \otimes \begin{bmatrix} \gamma \\ \delta \end{bmatrix} = \begin{bmatrix} \alpha\gamma \\ \alpha\delta \\ \beta\gamma \\ \beta\delta \end{bmatrix} \quad (2.8)$$

2.1.2 Entanglement

An interesting and very useful two qubit state is the Bell state which is also known as an EPR pair [25], $\frac{|00\rangle + |11\rangle}{\sqrt{2}}$, named after Einstein, Podolsky, and Rosen . The implications of this state are incredibly useful for quantum teleportation and communications since the result of a measurement on the second qubit will always yield the same outcome as the measurement of the first qubit. This means that the measurements are correlated. This combined state cannot be written independently, measuring one qubit immediately indicates the state of the other qubit, so the state is said to be entangled. A few examples of pure qubit states with maximal correlations, also known as maximally entangled states are listed below. All of the states are normalized, but for the sake of simplicity, the normalization factors are omitted [26].

- Bell states (2 qubits): $|\Phi^\pm\rangle \equiv |00\rangle \pm |11\rangle$ and $|\Psi^\pm\rangle \equiv |01\rangle \pm |10\rangle$
- Greenberger-Horne-Zeilinger states: $|GHZ_N\rangle \equiv |0\rangle^{\otimes N} + |1\rangle^{\otimes N}$
- $N00N$ -states: $|N0\rangle + |0N\rangle$

Another important class of entangled states are known as graph states. These states can be represented as a graph with qubits as the nodes and entanglement between qubits as edges. Overall, entanglement plays a pivotal role in the development of quantum technologies, and the generation of a few of these entangled states will be discussed in

further detail in the following chapters. Specifically, the generation of time-bin entangled photon pairs is demonstrated using a Franson interferometry experiment in Chapter 3, and Chapter 6 shows how a relatively simple integrated photonic circuit can be used to create two of the four maximally entangled Bell states. The entanglement of two photons generated via nonlinear optical processes is furthermore used in Chapter 5 to serve as a source of qubits for quantum key distribution.

2.1.3 Quantum Interference

One of the interesting effects of a quantum description of light is that non-classical interference can be observed. The first measured quantum interference was observed by Hong, Ou and Mandel in 1987 [27, 28] and almost simultaneously by Rarity and Tapster [29]. Both groups sent indistinguishable photons into a balanced beamsplitter (shown in Figure 2.2). They adjusted the time delay of one of the photons to introduce a source of distinguishability in the experiment. What they found was that when the relative delay was set to 0 (meaning the photons were perfectly indistinguishable), the photons experienced quantum interference—bunching and exiting through the same output port.

Using the labeling in Figure 2.2, we can express the beamsplitter unitary as,

$$\hat{U}_{BS} = \begin{bmatrix} r_{ac} & t_{bc} \\ t_{ad} & r_{bd} \end{bmatrix} \quad (2.9)$$

where r_{ij} is the reflectance and t_{ij} is the transmittance for the different input $i = a, b$ and output ports $j = c, d$. Constraints on the physical system and this unitary operator require that $|r_{ac}|^2 + |t_{ad}|^2 = 1$ and $|r_{bd}|^2 + |t_{bc}|^2 = 1$. Additionally, $r_{ac}t_{bc}^* + t_{ad}r_{bd}^* = 0$ where $*$ is the complex conjugate. For an ideal 50/50 beamsplitter, the unitary simply

becomes,

$$\hat{U}_{BS} = \frac{1}{\sqrt{2}} \begin{bmatrix} 1 & 1 \\ 1 & -1 \end{bmatrix} \quad (2.10)$$

Note that this matrix has already been introduced as the Hadamard gate. This unitary beamsplitter acts on the two input states E_a and E_b to give electric field amplitudes E_c and E_d at the output ports (see Figure 2.2 for the port definitions).

$$\begin{bmatrix} E_c \\ E_d \end{bmatrix} = \hat{U}_{BS} \begin{bmatrix} E_a \\ E_b \end{bmatrix} = \frac{1}{\sqrt{2}} \begin{bmatrix} 1 & 1 \\ 1 & -1 \end{bmatrix} \begin{bmatrix} E_a \\ E_b \end{bmatrix} \quad (2.11)$$

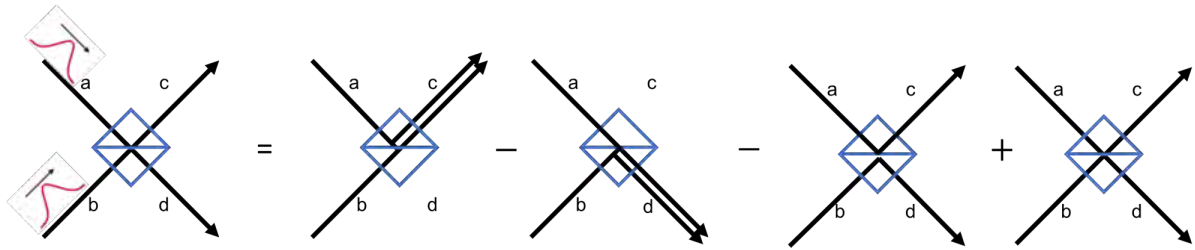


Figure 2.2: The Hong Ou Mandel effect involves two photons impinging on a 50/50 beamsplitter. Classically, the photons can exit in any of the four possible output port configurations. If the photons are indistinguishable, a quantum interference effect causes the two photons to always exit the same port.

Turning to a quantum mechanical description, each of the four ports can be expressed by a photon number state, also known as a Fock state, $|n\rangle$ where n photons occupy the particular state. For example, $|0\rangle$ represents the vacuum state, $|1\rangle$ represents a single photon in the mode, and so on. We can now use the creation and annihilation operators from quantum mechanics [2] to describe the same beamsplitter operation. Here, the creation operator $\hat{a}^\dagger |n\rangle = \sqrt{n+1} |n+1\rangle$, and the annihilation operator $\hat{a} |n\rangle = \sqrt{n} |n-1\rangle$. The creation operator can be thought as increasing the photon number state in a particular mode. We can write the same beamsplitter in terms of the creation operators for the different ports (where we have used the port label to denote which

annihilation operator is being used),

$$\begin{bmatrix} \hat{c}^\dagger \\ \hat{d}^\dagger \end{bmatrix} = \hat{U}_{BS} \begin{bmatrix} \hat{a}^\dagger \\ \hat{b}^\dagger \end{bmatrix} = \frac{1}{\sqrt{2}} \begin{bmatrix} 1 & 1 \\ 1 & -1 \end{bmatrix} \begin{bmatrix} \hat{a}^\dagger \\ \hat{b}^\dagger \end{bmatrix} \quad (2.12)$$

where again the 50/50 beamsplitter unitary has been substituted for the values of r and t . This form is equivalent to saying that if we start from the vacuum state and add a photon into port a , we have an input state

$$|\psi_{in}\rangle = \hat{a}^\dagger |00\rangle_{ab} = |10\rangle_{ab} \quad (2.13)$$

which produces an output state,

$$|\psi_{out}\rangle_a = (\hat{c}_a^\dagger + \hat{d}_a^\dagger) |00\rangle_{cd} = \frac{1}{\sqrt{2}} (|10\rangle_{cd} + |01\rangle_{cd}) \quad (2.14)$$

where we have added a subscript a to the creation operators to note that the contribution is from a photon input into port a . We can write the same expression for a photon input into port b ,

$$|\psi_{out}\rangle_b = (\hat{c}_b^\dagger - \hat{d}_b^\dagger) |00\rangle_{cd} = \frac{1}{\sqrt{2}} (|10\rangle_{cd} - |01\rangle_{cd}) \quad (2.15)$$

Now, if we look at the output state from two arbitrary photons entering the beamsplitter (one into a and one into b), we get an output state described by the tensor product of the two photon output states,

$$|\psi_{out}\rangle_{ab} = \frac{1}{2} \left(\hat{c}_a^\dagger \hat{c}_b^\dagger - \hat{d}_a^\dagger \hat{d}_b^\dagger - \hat{c}_a^\dagger \hat{d}_b^\dagger + \hat{d}_a^\dagger \hat{c}_b^\dagger \right) |00\rangle_{cd} \quad (2.16)$$

where we have reordered the terms of this result to match the right half of Figure 2.2. The subscripts indicate the input port photon, and the operators \hat{c} and \hat{d} represent the

photon output at port c and d , respectively. The characteristic quantum interference effect stems from this simple description. If photons a and b are perfectly indistinguishable, then the terms $\hat{c}_a^\dagger \hat{d}_b^\dagger$ and $\hat{d}_a^\dagger \hat{c}_b^\dagger$ are identical, and the negative sign results in destructive interference of these terms. Thus, for indistinguishable photons, only the first two terms of the expression are observed—where both photons exit the same port. If detectors are placed on ports c and d , a 'dip' in the recorded coincidences between the two detectors will be observed at zero time delay. This dip is commonly referred to as the HOM dip (after Hong, Ou, and Mandel [27]). Thus, the indistinguishability of two photons can be determined by measuring how close to ideal the photons interfere in such a setup.

The HOM interference experiment can be used to determine indistinguishability of multiple sources of photonic qubits—an important characteristic required to scale photonic quantum technologies. Along with high quality sources of indistinguishable photons, a quantum photonic platform needs a few other critical components like large, high fidelity interferometers to implement linear optic quantum gates, high efficiency single photon detectors, and corresponding fast electronics and switches to feed-forward settings to the circuit. This thesis will explore some of these components as well as discuss some promising initial applications of photonic qubit systems with the motivation of creating an integrated photonic circuit capable of both quantum computation and quantum communication tasks.

2.2 Integrated Photonics

As technologies advance, there is a desire to take all of the individual components and put them together on a common platform in order to reduce the size, weight, power, and cost (SWaP-C). Electronic circuits have rapidly advanced due to this integration starting in the late 1950s, resulting in enhanced speed, complexity, and reliability. The same

motivation drives the development of photonic integrated circuits (PICs), ever since the initial proposal by Miller in 1969 [30–32]. With the advent of the semiconductor laser and the increased interest in optical fiber communications, the integrated photonics field exploded, rapidly developing into the leading field for communications and revolutionizing data transmission. As the field expanded, waveguide technologies advanced past one-dimensional slab waveguides and into two-dimensional confinement that allowed for compact routing, bends, and improved losses. Waveguide technologies have largely been focused on the 1.3 μm and 1.55 μm wavelength ranges since it was aligned with the dispersion and loss minima of silica fiber, respectively.

Integrated photonics seeks to manipulate photonic circuits in a similar way that electronic circuits manipulate electrons. Components like splitters, filters, combiners, crossers, and detectors are all necessary to create a photonic integrated circuit (PIC). The following sections will describe some of the basics of photonic waveguides and ring resonators, and Chapter 4 will discuss the other fundamental building blocks that were designed for the AlGaAsOI material platform.

2.2.1 Waveguides

One of the most fundamental concepts required to create PICs is waveguiding. Simply put, a waveguide is a structure designed to guide and manipulate light without altering its shape (i.e. without diffraction). Waveguides are defined via a core material where most of the light propagates and a cladding that surrounds the core (see Figure 2.3b). The selection of a core material depends on numerous considerations, with the most basic being the wavelength of light used. The waveguiding material can only act as a waveguide if it does not absorb all of the light that is propagating within. On a basic level, the material can absorb single photons that have enough energy (larger than the

bandgap) to excite an electron from the valence band to the conduction band. Higher order absorption is also possible where two or three photons can cause this excitation. These contributions are nonlinear with the electric field intensity, and at low powers their effect is small. Thus, selecting a material with a large enough bandgap to minimize these absorption mechanisms for a particular wavelength of light can significantly improve its utility for PICs.

Refractive Index

The refractive index of a material is the ratio of the speed of light in a vacuum (c) to the speed of light within the material (v), $n = c/v$. Since light preferentially propagates in higher refractive index materials, the core material of a waveguide must have a higher refractive index than the surrounding cladding. The cladding is commonly made with materials like SiO_2 or air which have low refractive indices ($n_{\text{SiO}_2}=1.44$ and $n_{\text{air}} = 1.0003$ at 1550nm wavelength). Thus, many material options exist that can be used to create waveguide cores. State-of-the-art waveguides are made with silicon cores which have $n_{\text{Si}} = 3.48$, and the materials studied in this dissertation have similar refractive indices $n_{\text{InGaP}} = 3.12$ and $n_{\text{AlGaAs}} = 3.3$ at 1550nm wavelength. Figure 2.3a) shows the refractive indices of InGaP and AlGaAs as a function of wavelength. The model used to describe the wavelength dependence of AlGaAs follows from Reference [33] and for InGaP from Reference [34].

Electromagnetic Modes

Light within a waveguide propagates in one or more spatial electromagnetic ‘modes’ that travel with a characteristic velocity (with a corresponding effective refractive index, n_{eff}) and maintain confinement as they propagate. Figure 2.3c) shows the fundamental transverse electric mode for a 600nm wide by 400nm thick AlGaAs-on-insulator waveguide.

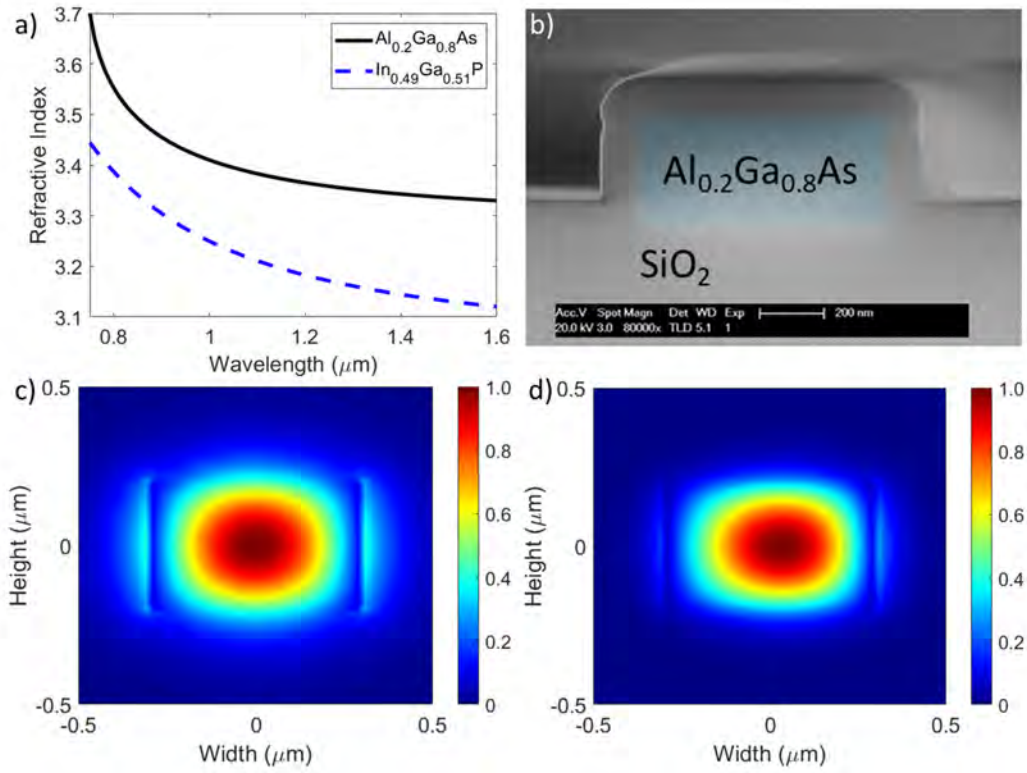


Figure 2.3: a) Real component of refractive index versus wavelength for bulk AlGaAs and InGaP. b) AlGaAs on insulator waveguide structure shown via false-colored SEM image. The AlGaAs core is surrounded by 1 μm thick SiO₂ cladding. c) TE mode profile for a 600nm wide, 400nm thick Al_{0.2}Ga_{0.8}AsOI waveguide. d) TE mode profile for a 10 μm bend, showing the mode get pushed toward the right waveguide wall.

uide, and d) shows the same waveguide mode in a bent geometry with 10 μm bend radius. The introduction of a bend in the waveguide has the effect of pushing the mode toward the outer wall. For high refractive index contrast materials, the mode remains mostly inside of the core material and thus tight bends can be achieved with low loss. For materials with lower contrast, a small bend can cause the light to scatter out of the core and into to the surrounding cladding material.

There are several different waveguide geometries commonly used to confine light within an optical waveguide. The simplest waveguide design is a slab waveguide which only confines light in the vertical dimension. Rib waveguides utilize a partial etch step

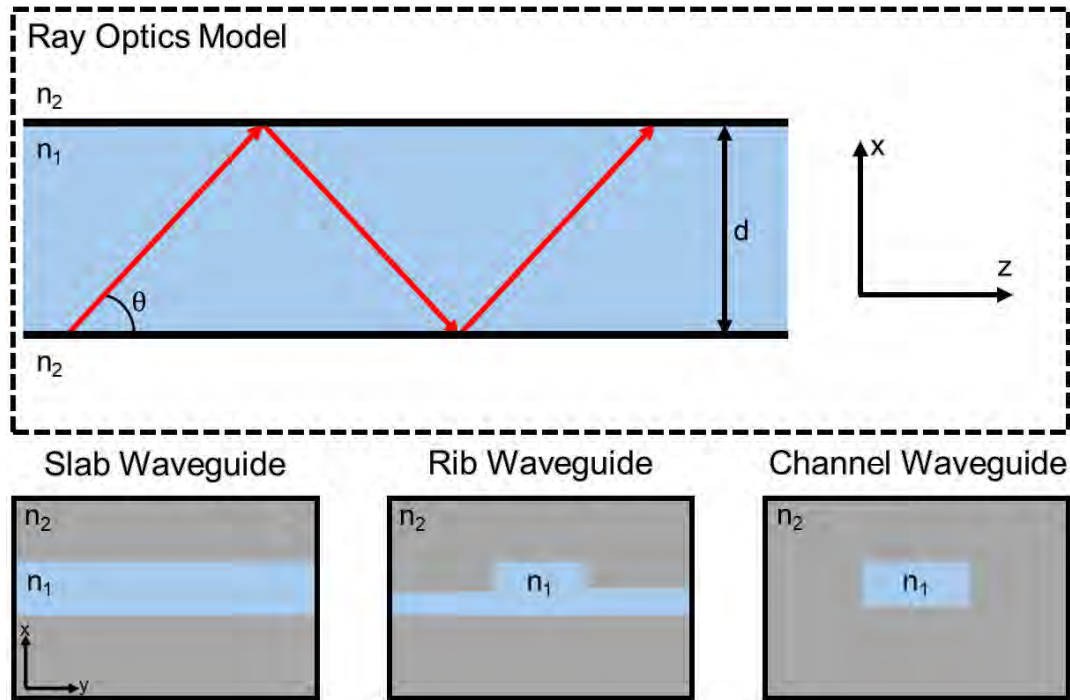


Figure 2.4: Ray optics picture of total internal reflectance for a waveguide. Light reflects at the interface between the two materials at an angle θ . The bottom panels show the different waveguide structures that can confine light.

to add some additional confinement in the lateral dimension, and fully etched waveguides (as the one shown in Figure 2.3b) are known as strip or channel waveguides and confine light fully in two dimensions. Figure 2.4 illustrates these three basic waveguide structures for a core material with refractive index n_1 surrounded by a cladding with refractive index n_2 .

Waveguide Propagation

In a basic, ray optics picture (see the top of Figure 2.4), light is confined in a waveguide if the light is traveling at an angle to the boundary that is larger than the angle of total internal reflection. For a waveguide core with index n_1 and cladding with index n_2 , this condition is $\theta_c = \sin^{-1}(n_2/n_1)$. Light with $\theta > \theta_c$ will propagate within the waveguide without escaping. Along with the angle of incidence requirement, light propagating

in the waveguide must constructively interfere as it reflects internally. Starting (for simplicity) with a slab waveguide (infinite width) having thickness d , the light reflects at the core/cladding boundary as it propagates in the z -direction. After two reflections, the light interferes with itself, and unless these wavefronts are in phase, the initial light and reflected light will destructively interfere. Only certain angles allow for this constructive interference in the waveguide. The light in the core travels with propagation constant $k_1 = 2\pi n_1/\lambda_0$, and using basic geometry, the total distance traveled by the light is $2d\cos\theta$. At the two points of reflection, a phase, ϕ , is accumulated, so the wave propagation requirement is

$$k_1(2d\cos\theta) - 2\phi = m(2\pi) \quad (2.17)$$

allowing for constructive interference if the phase accumulation from the reflections is an integer (m known as the mode number) of 2π . Only certain combinations of θ and ϕ allow for a solution. The phase change ϕ depends on θ and the polarization of the wave, so for each m there is only one allowed angle θ_m and one corresponding ϕ_m . This leads to the waveguide condition [35],

$$\left[\frac{2\pi n_1 d}{\lambda} \right] \cos\theta_m - \phi_m = m\pi \quad (2.18)$$

This condition specifies the allowed values of θ_m which must still meet the requirement for total internal reflection. This limits the total number of modes allowed in a waveguide such that,

$$m \leq \frac{2V - \phi}{\pi} \quad (2.19)$$

where

$$V = \frac{2\pi d}{\lambda} \sqrt{n_1^2 - n_2^2} \quad (2.20)$$

is the normalized thickness. The value of V can be used to determine the threshold where

only a single waveguide mode exists ($m=0$). From the definition above, this condition is met when $V < \pi/2$, and the value of λ that satisfies this relation is known as the cutoff wavelength. For symmetric waveguides, above the cutoff wavelength, only one mode, the fundamental mode, will propagate. Real waveguides are not always vertically symmetric which changes the analysis, and in some cases no guided modes exist. For simplicity, the symmetric waveguide is discussed here. The single-mode waveguiding condition is important for many systems as coupling into higher order modes can add additional loss in the system and reduce the spatial overlap of two different interacting modes.

The ray optics approach above is useful to gain a simple understanding of light propagation in waveguides, but now we will explore a more complete description: how the wave equation can be derived from Maxwell's equations. As an approximation, we can begin with a description assuming the light propagates in a dielectric, non-magnetic, isotropic, and linear medium, Maxwell's equations are reduced to the relations below. If the medium is not linear (like AlGaAs and InGaP), it is necessary to include additional terms involving power expansions of the electric and magnetic fields. An anisotropic medium must also use the optical constants as tensors instead of scalar quantities [36]. Again, for simplicity, we follow the derivation within a dielectric, non-magnetic, isotropic, and linear medium.

$$\nabla E = -\mu_0 \frac{\partial H}{\partial t} \quad (2.21)$$

$$\nabla H = \epsilon_0 n^2 \frac{\partial E}{\partial t} \quad (2.22)$$

with electric and magnetic fields, E and H , μ_0 is the free space permeability, ϵ_0 is the free space permittivity, and n is the refractive index. The wave equations describing the propagation of the light in the medium are the Helmholtz equations,

$$\nabla E + k_0 n^2(r) E = 0 \quad (2.23)$$

$$\nabla H + k_0 n^2(r) H = 0 \quad (2.24)$$

For light propagating in the z -direction of a slab waveguide (and thus the refractive index $n = n(x)$, as shown in the bottom box of Figure 2.4), the solutions for the wave equations above have the form,

$$E(r, t) = E(x) e^{i(\omega t - \beta z)} \quad (2.25)$$

$$H(r, t) = H(x) e^{i(\omega t - \beta z)} \quad (2.26)$$

for angular frequency ω and propagation constant β . The solutions of the Helmholtz equations can be found for two different polarization cases, transverse electric (TE) where the field only has E_y nonzero, and transverse magnetic (TM) where the field only has E_x nonzero. Starting with the TE case, Maxwell's equations with the substitution of solutions 2.25 and 2.26,

$$H_x = -\frac{\beta}{\omega \mu_0} E_y \quad (2.27)$$

$$H_y = 0 \quad (2.28)$$

$$H_z = \frac{i}{\omega \mu_0} \frac{dE_y}{dx} \quad (2.29)$$

$$\frac{d^2 E_y(x)}{dx^2} + [k_0^2 n^2(x) - \beta^2] E_y(x) = 0 \quad (2.30)$$

This final, differential equation gives the amplitude profile for the TE propagating modes, and the solutions are eigenvectors that must also satisfy the boundary conditions which require continuity of E_y and H_z at the interface. The eigenvalues of these solutions are β , and the n th eigenvalue represents the n th mode of the structure. The eigenvalues have a characteristic effective index n_{eff} that satisfies $\beta = k_0 n_{eff}$ and $n_{cladding} < n_{eff} < n_{core}$ in order for the mode to be confined in the structure. In the case of a planar, slab

waveguide, it is possible to independently solve the equations for the three regions (core, upper and lower claddings). The relation can be combined into a single equation [36],

$$\tan(V\sqrt{1-b}) = \frac{1\sqrt{\frac{b}{1-b}}}{1 - \frac{b}{1-b}} \quad (2.31)$$

where V is the normalized thickness defined in the ray optics picture, and b is the normalized mode index,

$$b = \frac{n_{eff}^2 - n_{cladding}^2}{n_{core}^2 - n_{cladding}^2} \quad (2.32)$$

For confined modes, $n_{cladding} < n_{eff} < n_{core}$ so $0 < b < 1$. As in the ray optics picture, there are a finite number of solutions to the transcendental equation 2.31, and thus a finite number of modes can be guided in a particular waveguide geometry. Once the propagation constant of the mode has been calculated, the electric field profile in the three regions can be completely determined. The electric field profile decays exponentially in the cladding region and has a sinusoidal dependence within the core which is expected for a confined mode. The solution for TM modes follows a similar formulation, where now the differential equation, Equation 2.30, is established as a function of the magnetic field instead of electric field.

Channel Waveguides

The mode solutions of a channel waveguide such as that shown in Figure 2.3c) are determined via a similar means to the slab waveguide case with the important distinction that the solutions **cannot** be obtained analytically even for the most basic structures. There are two widely used methods to approximate the mode solutions of a channel waveguide: Marcatili's method and the effective index method. The effective index method approximates the solution by converting the two-dimensional waveguide into

two, one-dimensional slabs and following the same treatment described in the previous section to determine the effective index of one of the slabs which is used to calculate the the effective index in the other. With the recent boom in integrated photonics, softwares such as Lumerical and COMSOL have been established that allow for the numerical approximation of the mode solutions using finite difference mode solvers or finite element eigenmode solvers. These solvers create a mesh and solve Maxwell's equations at each grid point to approximate the total electric field profile in the waveguide material.

Another distinction between the channel and slab waveguides is that for the case of light propagation in a slab waveguide, the light can be grouped in terms of orthogonal polarizations leading to TE and TM modes. However, for the case of channel waveguides, there is no pure TE or TM mode, and the modes instead exist as TEM modes with a stronger polarization along one axis and are said to be quasi-TE or quasi-TM modes. In the discussion of waveguide modes in the following chapters, the "quasi-" is dropped from the conventional, but it is important to note that the channel waveguide modes are not purely TE or TM.

Polarization Fraction

There are a few characteristic properties of waveguide modes that are useful to describe the modes within a waveguide. Since channel waveguide modes are quasi-TE (TM) modes, it is sometimes useful to describe the polarization fraction of a mode which distinguishes the ratio of TE/TM polarization. For particular applications that are polarization sensitive, this metric can be important since only the portion of the light in the correct polarization can interact in the desired fashion.

Effective Mode Area

Another metric that will be used often in the following chapters is the effective mode area for nonlinear interactions. Since some of the mode propagates in the cladding material and not in the nonlinear material, an effective area that describes the overlap of the mode with the nonlinear region is used,

$$A = \frac{\iint_{\infty} |E|^2 dx dy \iint_{NL} dx dy}{\iint_{NL} |E|^2 dx dy} \quad (2.33)$$

Propagation loss

In real systems, light travels with some attenuation in the waveguide due to sources of scattering or absorption. Materials with high refractive index contrast have significant electric field intensity at the core to cladding interface, so scattering loss is commonly the leading factor in propagation loss [37]. The propagation loss is defined using the attenuation constant, $\alpha_{1/km}$ which describes how an input power P_0 attenuates across a length, L (in units of kilometers). The propagation constant incorporates all loss mechanisms with the main contributors being from absorption and scattering loss.

$$\frac{P}{P_0} = e^{-\alpha_{1/km} L} \quad (2.34)$$

The units of α are more commonly expressed in dB/length,

$$\frac{P}{P_0} = 10^{-\alpha_{dB/km} L/10} \quad (2.35)$$

where

$$\alpha_{1/km} = \alpha_{dB/km} * \frac{\ln(10)}{10} \quad (2.36)$$

Propagation constants for high index contrast materials like silicon and AlGaAs are currently experimentally determined to be on the order of 0.2-1 dB/cm [38, 39] while lower index contrast materials like silicon nitride have demonstrated ultra-low loss propagation of a few dB/m owing to the mode being primarily in the surrounding cladding [40].

Group Index

As described above, the effective index of a material relates the speed of wavefront propagation in the medium relative to the speed of light in a vacuum. In the absence of any dispersion, all frequencies travel with this characteristic effective velocity. However, for real materials, the dispersion is non-zero, and thus light at different frequencies travel at different velocities. The group index of a mode describes this effect by indicating the linear variation of the effective index with respect to frequency,

$$n_g = n_{eff} + \omega \frac{dn_{eff}}{d\omega} \quad (2.37)$$

The group index can be obtained directly from the mode field profiles.

Dispersion

Another important metric of waveguide modes is the higher order dispersion parameters that help to fully describe how the propagation speed varies as a function of frequency. The first order dispersion, $\beta_1 = c/n_g$ comes directly from the linear group index dependence, and in general the i th order dispersion relates to the i th order derivative of the propagation constant with respect to frequency. Dispersion parameters describe the variations in the propagation speed via Taylor expansion. In general, this allows us to express the wavenumber k near ω_0 as a summation of the different dispersion contri-

butions,

$$k(\omega) = n(\omega)\omega_c = \sum_{i=0}^{\infty} \frac{\beta_i}{i!} (\omega - \omega_0)^i \quad (2.38)$$

In terms of propagation within a dispersive material, the effect of dispersion causes pulse broadening since the different frequency components of a pulse travel at different velocities. For long waveguides or structures with significant dispersion, this difference can result in destructive interference as certain frequency components become out of phase. For nonlinear quantum light generation, dispersion is a significant consideration in the design of waveguide structures.

One particularly important dispersion parameter which will be used to achieve phase matching in nonlinear photonics is the group velocity dispersion, $\beta_2 = d^2k/d\omega^2$. When the refractive index increases with increasing frequency (meaning $\beta_2 > 0$), the dispersion is said to be *normal*. For the opposite case, the dispersion is said to be *anomalous*. The group velocity dispersion is commonly expressed in terms of the dispersion parameter, D ,

$$D = -\frac{2\pi c}{\lambda^2} \beta_2 \quad (2.39)$$

Chapter 3 will illustrate how the dispersion of waveguides can be manipulated to enable broadband phase matching of generated quantum states of light as well as how different operating regimes can be achieved by adjusting the waveguide dimensions. Standard mode solvers can be used to approximate the values of all of the parameters discussed above (with the exception of propagation loss from scattering and absorption which is fabrication-dependent). The calculation of these mode properties is crucial in determining the waveguide geometry to use for a particular application.

2.2.2 Ring Resonators

One of the most important PIC components utilized in this dissertation is the ring resonator, an optical cavity that enhances nonlinear interactions and enables efficient quantum light generation. Ring resonators are incredibly useful for many PIC applications acting as laser cavities, fast optical switches, integrated filters, modulators, and sensors. In the most basic case, a ring resonator is a circular waveguide that is brought close to a straight waveguide which can supply an electric field into the ring via evanescent coupling or multimode interference coupling. When one waveguide (called the "bus") is present, the resonator is in what is known as an all-pass configuration, and if two waveguides are present, the waveguide is an add-drop resonator (shown in the dashed box of Figure 2.5). The add-drop resonator can be used as a channel dropping filter, and the all-pass resonator serves as a notch filter. Starting with an all-pass resonator as shown in Figure 2.5 and assuming light travels in the bus waveguide from left to right, the output electric field amplitudes $E_{t(1,2)}$ can be described by the transmission and coupling coefficients t, k [41],

$$\begin{bmatrix} E_{t1} \\ E_{t2} \end{bmatrix} = \begin{bmatrix} t & \kappa \\ -\kappa^* & t^* \end{bmatrix} \begin{bmatrix} E_{i1} \\ E_{i2} \end{bmatrix} \quad (2.40)$$

The values of the coupling coefficients are dictated by the mechanism used. For example, in the most basic case, coupling occurs at a single point where the waveguide and ring are nearest each other. κ can be modeled using numerical mode solvers or finite difference time domain solvers to approximate the power transfer between the two waveguides. The next section will discuss a different coupling scheme known as a pulley coupler where the bus waveguide bends and follows the ring for a portion of the arc in order to increase the overall coupling possible for high confinement waveguides with large

gaps between the ring and bus.

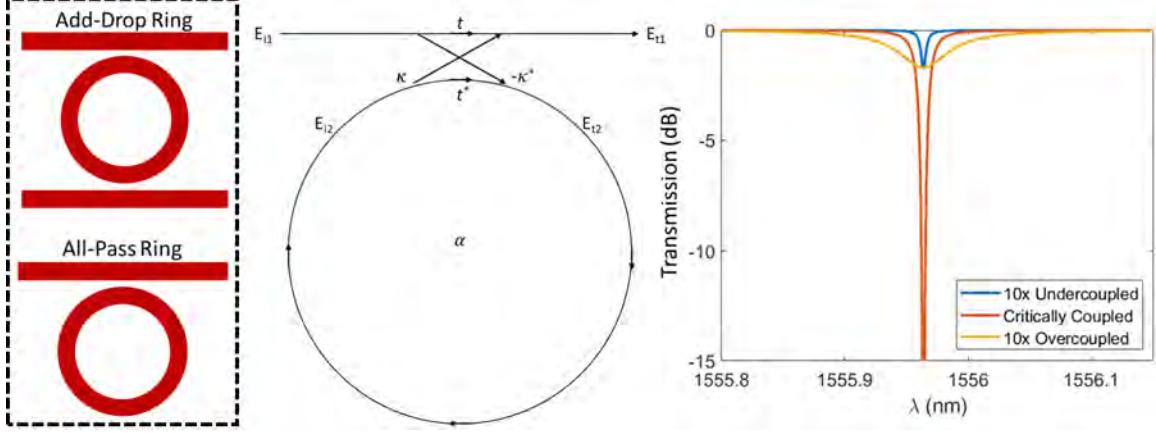


Figure 2.5: Schematic of an add-drop and all-pass ring resonator. The relevant coupling and transmission coefficients for an all-pass ring resonator are shown in the central panel. The different coupling regimes are illustrated in the simulated transmission spectra of an all-pass ring resonator that is 10x undercoupled, critically coupled, and 10x overcoupled.

Regardless of the coupling mechanism and assuming the coupler is lossless, the values of κ and t must follow symmetry such that $|\kappa^2| + |t|^2 = 1$. E_{i1} is chosen to be normalized and equal to 1 to further simplify the system. For one round trip with loss coefficient α , the field at $E_{i2} = \alpha e^{j\theta} E_{t2}$. Here $\theta = kn_{eff}L$ for a ring circumference of $L = 2\pi R$ and a vacuum wavenumber $k = 2\pi/\lambda_0$. Substituting these values,

$$\theta = kn_{eff}L = 4\pi^2 n_{eff} \frac{R}{\lambda_0} \quad (2.41)$$

We can use the matrix formulation from Equation 2.40 to express the output field,

$$E_{t1} = \frac{-\alpha + te^{-j\theta}}{-\alpha t^* + e^{-j\theta}} \quad (2.42)$$

corresponding to a transmitted power,

$$P_{t1} = |E_{t1}|^2 = \frac{\alpha^2 + |t|^2 - 2\alpha|t|\cos(\theta + \phi_t)}{1 + \alpha^2|t|^2 - 2\alpha|t|\cos(\theta + \phi_t)} \quad (2.43)$$

where $t = |t|exp(j\phi_t)$ illustrates the coupling losses and phase of the coupler.

The resonance condition is met when the optical cavity length ($n_{eff}L$) is an integer multiple (m) of the wavelength, i.e. $2\pi R = m\lambda_0/n_{eff}$. On resonance, $(\theta + \phi_t) = 2\pi m$, and Equation 2.43 becomes,

$$P_{t1} = \frac{(\alpha - |t|)^2}{(1 - \alpha|t|)^2} \quad (2.44)$$

As evident in this equation, a special case happens when $\alpha = |t|$ (or in terms of the coupling coefficient $|\kappa|^2 = 1 - e^{-\alpha L}$), which is known as critical coupling. Here, the internal losses are equal to the coupling losses, and the transmitted power becomes zero in the bus output from destructive interference between the incident field and the light coupled out of the ring after one round trip. Figure 2.5 shows critical coupling where the transmitted power goes to zero. When the intrinsic cavity loss exceeds the coupling loss, the cavity is said to be undercoupled, and the resonance has a reduced extinction ratio (shown in Figure 2.5 for 10 times undercoupled). When the intrinsic cavity loss is less than the coupling loss, the resonator is overcoupled, and the resonance is broadened with a reduced extinction ratio.

Another important metric of a ring resonator is the free spectral range, which describes the spacing between adjacent resonance wavelengths.

$$FSR = \frac{\lambda_0^2}{Ln_g} \quad (2.45)$$

where n_g is the group index as described in the waveguide section above (section 2.2.1).

Estimation of Loss

Since the resonance linewidth is related to the coupling regime (and therefore the intrinsic cavity loss), it is possible to use resonators to determine the propagation loss, bending loss, and dominant loss mechanisms in a waveguide platform. For example,

the cavity loss for resonators of varying waveguide widths can indicate the influence of sidewall roughness on the propagation loss, and a group of resonators with different radii can indicate how much bending loss contributes to the overall propagation loss. The quality factor, Q , of a resonator relates the stored energy in the ring divided by the power lost per optical cycle and is a measure of the sharpness of a resonance.

$$Q_{total} = \frac{\omega}{\Delta\omega} \quad (2.46)$$

For the case described above (and shown in Figure 2.5), the total loss in the system can be decomposed into two factors: coupling loss and intrinsic cavity loss (or propagation loss). Thus, the total quality factor (also called loaded quality factor) has contributions from both of these sources of loss.

$$\frac{1}{Q_{tot}} = \frac{1}{Q_0} + \frac{1}{Q_c} \quad (2.47)$$

with $Q_0 = \omega_0\tau_{rt}/\alpha_{1/km}L$ as the intrinsic quality factor and $Q_c = \omega_0\tau_{rt}/|\kappa|^2$ as the coupling quality factor for a round trip time $\tau_{rt} = n_gL/c$. For critical coupling, $Q_c = Q_0$ and the total quality factor is one half the intrinsic quality factor.

Interestingly, from a measurement of the total quality factor and the extinction ratio (magnitude of the resonance dip relative to the off-resonance power), it is possible to estimate the intrinsic quality factor (and thus the coupling quality factor using the expression above) of a ring resonator [42] using the expression

$$Q_0 = \frac{2Q_{tot}}{1 \pm \sqrt{\frac{min}{max}}}, \quad (2.48)$$

where the + case corresponds to undercoupling and the – to overcoupling, and *min* represents the minimum power at the resonance dip and *max* represents the off-resonance

power such that min/max is the extinction ratio of the resonance. With a given coupling regime determined, the Q_0 can be determined using the above equation. From the relationship $1/Q_{tot} = 1/Q_0 + 1/Q_c$ this also allows us to determine the coupling quality factor. To find which coupling regime a particular device is in, the equation above can be assessed for a broad wavelength range (plotting both the + and - cases together). Since the coupling into the resonator has a strong wavelength dependence, it is expected that Q_c will be wavelength dependent. Q_0 , on the other hand, should be less sensitive to wavelength and remain consistent throughout the wavelength scan. With these expected trends, the coupling regime can be approximated. Another method to distinguish coupling and intrinsic Q is to sweep the coupling gap with all other values constant. Tracking the values of the above equation as a function of gap should again show a trend in the Q_c with a consistent Q_0 . Thus, by fitting the resonances of a fabricated device, it is possible to estimate important waveguide parameters like propagation loss. The mechanism of this loss can also be determined (whether the loss is absorption or scattering limited) as is done in Reference [43], though this study is outside the scope of this dissertation.

Pulley-Coupler Design

One of the benefits of using a material platform with a large refractive index like silicon ($n \sim 3.4$ at $1.55\mu m$) or AlGaAs (also $n \sim 3.4$ at $1.55\mu m$) is that waveguides of these materials have high refractive index contrast compared to the commonly used SiO₂ cladding ($n = 1.44$ at $1.55\mu m$). This large contrast enables the design of waveguides with high mode confinement which enhances the nonlinear interaction and allows for more compact structures to be created since the tight confinement results in low loss bends $< 20\mu m$ in radius. On the other hand, this tight confinement can sometimes make it difficult to efficiently couple light from one waveguide to another in a short distance. Thus, in the design of ring resonators, a simple straight waveguide placed next to a

ring may not transfer enough power into the ring for efficient nonlinear quantum light generation. The design of pulley couplers, where the waveguide and ring bend together for a portion of the ring, can allow for more power to be transferred into the ring. Figure 2.6a) illustrates a pulley coupler for a ring with radius R , coupling angle θ , and gap G .

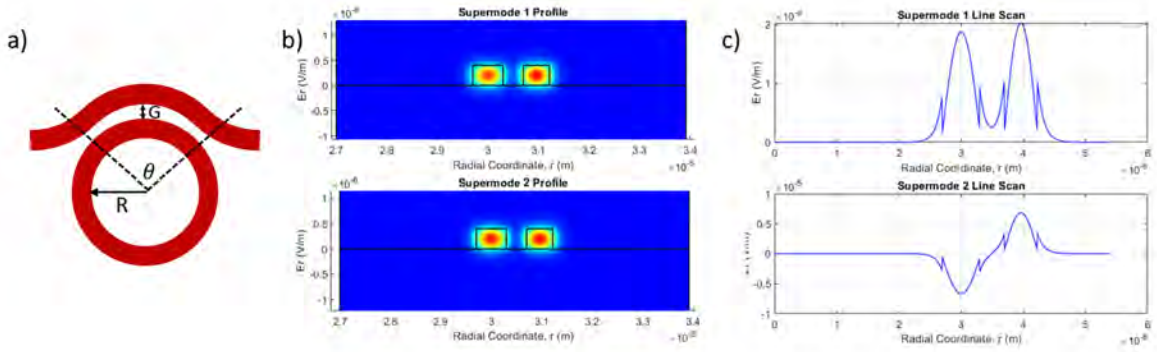


Figure 2.6: a) Schematic of a pulley coupler designed to couple light from a bus waveguide to a ring resonator. b) Mode profiles of the two TE supermodes of a 520 nm wide $\text{Al}_{0.2}\text{Ga}_{0.8}\text{As}$ bus waveguide coupling to a 600 nm wide ring waveguide with a 400 nm gap and a radius of 30 μm solved via Lumerical EME. c) Linear plot showing the electric field profile across the two coupled modes at the center of the waveguide.

The design of a pulley coupler follows coupled mode theory based on the existence of supermodes when two waveguides are brought in close proximity. Figure 2.6b) illustrates the two supermodes that exist between a 520nm wide AlGaAs bus waveguide and 600nm wide ring waveguide with a radius of 30 μm and a coupling gap of 400nm. The AlGaAs waveguide thickness is 400nm, and here the coupling is illustrated for the TE polarized modes. Starting with the simple case of two straight waveguides separated by a gap G , we can model the interaction of light initially traveling in the bus waveguide and coupling into the ring such that the fraction of power coupled into the ring is,

$$\kappa^2 = \frac{P_{ring}}{P_0} = \sin^2(C \cdot L) \quad (2.49)$$

where P_0 is the initial power, P_{ring} is the power transferred to the ring, L is the coupling

length, and C is the coupling coefficient [44–46]. To obtain the coupling coefficient, a numerical calculation of the two supermode effective indices is completed using Lumerical eigenmode expansion (EME) mode solver. Figure 2.6 shows these modes and calculates their effective indices. The coupling coefficient is calculated from,

$$C = \frac{\pi \Delta n}{\lambda} \quad (2.50)$$

where Δn is the different in the effective index of supermode 1 and 2. For the case of a pulley coupler, this method holds with the coupling length now expressed based on the arc length $L = \theta R$, and the supermodes are solved using a bent waveguide model in the EME solver. It is also useful to express the coupling in terms of the difference between the two modes' angular propagation constants,

$$\beta_{1,2} = \frac{2\pi n_{1,2}}{\lambda} \quad (2.51)$$

where the subscript 1, 2 corresponds to the first and second supermode. For the example modes shown in Figure 2.6, the difference in propagation constants between the two supermodes is small 0.1002 rad^{-1} , indicating that the two modes travel with little phase mismatch. Comparing the value of $\Delta\beta_{\text{supermodes}}$ with $\Delta\beta_{\text{uncoupled}}$, the coupling rate between the two waveguides can be calculated $\kappa^2 = (\Delta\beta_{\text{supermodes}})^2 - (\Delta\beta_{\text{uncoupled}})^2$. Note that here, the formula incorporates $\Delta\beta_{\text{uncoupled}}$ since the ring and the bus waveguides have different dimensions. The maximum transmitted power in this system (ignoring the limitations of $< 360^\circ$ coupling angle) is $P_{\text{max}} = \kappa^2 / (\Delta\beta_{\text{supermodes}})$. For the system above, $P_{\text{max}} = 0.9993$ indicating that almost all of the light could (in theory) be transferred from the bus waveguide to the ring. Depending on the desired system, a coupling value κ^2 may be desired anywhere from ~ 0 to 1. Using the methods above, we can estimate

the coupling for a particular ring design,

$$\kappa^2 = P_{max} \sin^2(\theta \Delta \beta_{supermodes}) \quad (2.52)$$

Ring resonators with pulley couplers form the basis of most of this work, so the necessary background information was described in considerable detail in this background chapter. Other fundamental PIC components are left for Chapter 4 which details our work on developing a full toolbox of components for the AlGaAsOI material platform.

2.3 Nonlinear Photonics

The generation of quantum light using nonlinear materials stems from either the second or third order nonlinearity which arise from the polarizability of a dielectric medium. When an electric field is applied on the medium, the material polarization can be described by the sum of electric fields E_j ($j=1,2,3,\dots$) [47, 48],

$$P = \epsilon_0(\chi^{(1)} E_1 + \chi^{(2)} E_1 E_2 + \chi^{(3)} E_1 E_2 E_3 + \dots) \quad (2.53)$$

where ϵ_0 is the electric permittivity of free space, $\chi^{(1)}$ is the linear susceptibility and $\chi^{(2)}$, $\chi^{(3)}$, ... are the nonlinear susceptibilities of the medium. The second order nonlinearity, $\chi^{(2)}$, enables three-wave mixing processes like second harmonic generation and spontaneous parametric down conversion (SPDC) while the third order nonlinearity enables four-wave mixing processes like spontaneous four-wave mixing (SFWM). The nature of these nonlinearities is related to the crystal structure of the dielectric medium. For crystals that are non-centrosymmetric, a $\chi^{(2)}$ nonlinearity exists, and all crystals have a $\chi^{(3)}$ nonlinearity. The strength of these nonlinearities varies based on the crystal structure, and materials with stronger asymmetries tend to have larger nonlinearities. For example,

bulk silicon has a diamond crystal structures that is centro-symmetric; thus, bulk silicon does not have a $\chi^{(2)}$ response due to symmetry arguments. Materials like AlGaAs, on the other hand, have a zinc blende crystal structure with varying atom sizes on the different coordinate points, resulting in a large $\chi^{(2)}$ nonlinearity. In general, the second order nonlinearity is much stronger than the third order nonlinearity. For condensed matter, $\chi^{(2)}$ is on the order of $1/E_{at}$ or $\sim 1.9 \times 10^{-12}$ m/V while $\chi^{(3)}$ is typically on the order of $1/E_{at}^2$ or $\sim 3.8 \times 10^{-24}$ m²/V² where E_{at} is the atomic electric field strength [48]. Table 2.2 shows the values of a few commonly used nonlinear material systems. The reason why polarization (as described in Equation 2.53) is important in the description of nonlinear optical phenomena is that a time-varying polarization can act as a source of new components of the electromagnetic field. We can see this through Maxwell's equations with polarization included,

$$\nabla \times \nabla E + \frac{a}{c^2} \frac{\partial^2 E}{\partial t^2} = -\mu_0 \frac{\partial^2 P}{\partial t^2} \quad (2.54)$$

The final term, $\frac{\partial^2 P}{\partial t^2}$, is a measure of the acceleration of the charges in the medium and is consistent with Larmor's theorem of electromagnetism, which states that accelerated charges generate electromagnetic radiation.

First-Order Processes

The first-order susceptibility coefficient $\chi^{(1)}$ is related to the refractive index of a material $n^2 = \chi^{(1)} + 1$, with the real part contributing to the refractive index and the imaginary part describing loss (or gain). The basis of $\chi^{(1)}$ is dipole excitations induced by a single photon [49]. Semiconductors like silicon see contributions from the effect of free carriers that modify both the real and imaginary components of the $\chi^{(1)}$ susceptibility giving rise to free carrier absorption and dispersion. The complex refractive index for

these materials can be written as [49–51],

$$n(\lambda, N_e, N_h) = n_0(\lambda) + \delta n_{FC}(N_e, N_h) + i \frac{\lambda}{4\pi} [\alpha_0(\lambda) + \delta \alpha_{FC}(N_e, N_h)] \quad (2.55)$$

where $n_0(\lambda)$ and $\alpha_0(\lambda)$ express the wavelength dependence of refractive index and absorption, and δn_{FC} and $\delta \alpha_{FC}$ are the free-carrier index change and absorption which depend on the electron and hole densities ($N_{e,h}$).

Second-Order Processes

As briefly discussed, materials like silicon with inversion symmetry do not possess a second order nonlinear susceptibility, though it is possible to induce second-order effects by disrupting this symmetry [49, 52]. Focusing on materials that inherently possess a second-order nonlinearity like AlGaAs and InGaP, these effects can be evaluated by representing a propagating electric field as a superposition of two waves E_1 and E_2 with frequencies $\omega_{1,2}$. Writing the total field,

$$E(r, t) = \sum_{n=1}^2 [E_n(r, \omega_n) e^{-j\omega_n t} + c.c.] \quad (2.56)$$

and using the second order polarizability from Equation 2.53,

$$P^{(2)}(r, t) = \epsilon_0 \chi^{(2)} E_1 E_2 \quad (2.57)$$

$$\begin{aligned} P^{(2)}(r, t) = & [E_1^2(r, \omega_1) e^{-j2\omega_1 t} + E_2^2(r, \omega_2) e^{-j2\omega_2 t} \\ & + 2E_1(r, \omega_1) E_2(r, \omega_2) e^{-j(\omega_1 + \omega_2)t} + 2E_1(r, \omega_1) E_2^*(r, \omega_2) e^{-j(\omega_1 - \omega_2)t} \\ & + E_1(r, \omega_1) E_1^*(r, \omega_1) + E_2(r, \omega_2) E_2^*(r, \omega_2)] \end{aligned} \quad (2.58)$$

The first two terms correspond to second harmonic generation where a photon at $2\omega_1$ is generated from two photons at ω_1 . The third and fourth terms correspond to sum frequency generation and difference frequency generation, respectively. Here, a photon is generated with frequency $\omega_1 \pm \omega_2$. The last terms contribute a DC component to the polarization vector [52]. Interestingly, if one of the frequencies ($\omega_{1,2}$) is much lower than the other, or if a DC field is applied, the sum and difference frequency generation components oscillate at the high frequency signal, resulting in a refractive index which depends on the amplitude of the low-frequency field. This effect is the linear electro-optic effect or the Pockels effect.

Third-Order Processes

In a similar approach to the second-order process, we can describe the electric field as a sum of three waves $E_{1,2,3}$ such that the third order polarizability becomes,

$$P^{(3)}(r, t) = \epsilon_0 \chi^{(3)} E_1 E_2 E_3 \quad (2.59)$$

$$\begin{aligned} P^{(3)}(r, t) = & [E_1^3(r, \omega_1) e^{-j3\omega_1 t} \\ & + 3E_1^2(r, \omega_1) E_2(r, \omega_2) e^{-j(2\omega_1 + \omega_2)t} \\ & + 3E_1^2(r, \omega_1) E_2^*(r, \omega_2) e^{-j(2\omega_1 - \omega_2)t} \\ & + 6E_1(r, \omega_1) E_2(r, \omega_2) E_3(r, \omega_3) e^{-j(\omega_1 + \omega_2 + \omega_3)t} \\ & + 6E_1(r, \omega_1) E_2(r, \omega_2) E_3^*(r, \omega_3) e^{-j(\omega_1 + \omega_2 - \omega_3)t} \\ & + 3|E_1(r, \omega_1)|^2 E_1(r, \omega_1) e^{-j\omega_1 t} \\ & + 6|E_2(r, \omega_2)|^2 E_1(r, \omega_1) e^{-j\omega_1 t}] \end{aligned} \quad (2.60)$$

For simplicity, the permutations of photon indices have been grouped into like terms, though the complete expression would explicitly include each of these contributions. In a similar fashion to the second-order process, each term in this equation corresponds to a different nonlinear interaction process. The first term is related to third harmonic generation where three photons at ω_1 generate a single photon at $3\omega_1$. The middle terms (second, third, fourth, and fifth) are responsible for four-wave mixing where two photons annihilate and generate two photons at different frequencies (signal and idler photons). The sixth term is responsible for self-phase modulation and two-photon absorption. The real part of $\chi^{(3)}$ describes the self-phase modulation while the imaginary term describes two-photon absorption.

The sixth term is important as it describes the intensity-dependent perturbations of the refractive index and absorption coefficient [52],

$$n = n_0 + n_2 I - j \frac{\lambda}{4\pi} (\alpha_0 + \alpha_2 I) \quad (2.61)$$

Note that this has a similar form to the refractive index change from free carrier absorption Equation 2.55, but now there is an intensity (I) dependence, and the Kerr coefficient (n_2) and two-photon absorption coefficient (α_2) show how the sixth term of Equation 2.60 contribute to the refractive index. The coefficients

$$n_2 = \frac{3}{4\epsilon_0 c n^2} \mathcal{R}(\chi_{eff}^{(3)}) \quad (2.62)$$

and

$$\alpha_2 = \frac{3\omega}{2\epsilon_0 c^2 n^2} \mathcal{I}(\chi_{eff}^{(3)}) \quad (2.63)$$

relating the real and imaginary parts of the effective third-order nonlinearity to the Kerr and two-photon absorption coefficient, respectively. Physically, two-photon absorption

can be seen as the absorption of two photons whose energy is large enough to excite an electron from the valence to the conduction band. This process is an important limitation on nonlinear processes in silicon near the telecom c-band (1550nm) since the sum of the energy of two photons at 1550nm is larger than the silicon bandgap. For material systems that are explored in this dissertation like InGaP and AlGaAs, the bandgap is large enough that two-photon absorption does not impact the performance.

The final term in Equation 2.60 represents the process of cross-phase modulation. This effect is still related to the intensity-dependent refractive index, but here the signal at ω_2 influences the propagation of the ω_1 signal. The leading coefficient shows that cross-phase modulation is twice the strength of self-phase modulation.

This discussion only includes the effects of electronic contributions to the nonlinear susceptibility, though in general, the contributions of phonons should also be considered. The third-order susceptibility can be decomposed into the electronic and Raman (or phonon-mediated) contributions $\chi^{(3)} = \chi_e^{(3)} + \chi_R^{(3)}$. For the scope of this work, phonon-based nonlinear interactions are disregarded.

Further discussion of the second and third order nonlinearity are left for Chapter 3 which describes the generation of quantum states of light using these nonlinear interactions. A summary of some of the material systems used for nonlinear integrated photonics and their relevant parameters is included in the next section.

Material Platforms

The developments of integrated photonic material platforms over the past decade have enabled many new opportunities for chip-scale nonlinear photonics. A review of these platforms and some of the applications that these materials can be used for is found in Reference [53]. One of the driving forces for these platforms is the significant improvement in fabrication techniques that have reduced the waveguide propagation

loss. Advances in the material growth, defect passivation, and microfabrication (reducing sidewall roughness) have brought integrated platforms into the regime where they can compete with their bulk counterparts. The overall improvement in these fabrication systems has also expanded the potential materials that can be used. A list of integrated nonlinear material platforms is included in Table 2.2, and the following sections will highlight the properties of some of the more commonly used material systems. Based on these high-performing nonlinear platforms, quantum photonic devices and system-level demonstrations have been realized.

Silicon: Owing largely to the boom of research surrounding the electronics industry, silicon photonics has seen explosive growth, and is widely considered the state-of-the-art material system for high-speed classical and quantum telecommunications [54]. Many of the properties that make silicon the leading system for electronics are the same qualities that make it a leading material for photonics. Silicon is abundant, has great thermal conductivity, can be grown with incredible purity, can be doped, and has an intrinsic oxide that forms high quality interfaces (and can be used to naturally form a cladding for an optical waveguide). Along with these characteristics, the strong $\chi^{(3)}$ Kerr nonlinearity, thermo-optic effect and transparency in the telecom c-band make it a great material for photonic integrated circuits (PICs) for both classical and quantum applications. The core platform for silicon photonics is silicon-on-insulator (SOI) where the optical waveguides are defined by etching silicon and surrounding it with SiO_2 which serves as the cladding. Many of the essential photonic building blocks required for splitting, modulating, filtering, and generating photons via nonlinear interactions have been demonstrated on the SOI platform [55, 56]. The widespread use of SOI in classical photonics has also enabled rapid advances in chip-based quantum technologies, owing at least in part to the established infrastructure [57, 58].

In terms of quantum light generation, SOI has high refractive index contrast which

enhances the nonlinear effect, and allows for dispersion engineering to optimize the conversion bandwidth. The large Kerr nonlinearity enables efficient spontaneous four-wave mixing from both straight waveguide sources and resonator-based systems [59–61]. Perhaps the most important factor is, again, the scalability, reliability, and precision of the complementary metal oxide semiconductor (CMOS) foundry process which results in a high yield, reproducible, and accessible material platform. Unlike some of the other materials discussed, SOI foundries enable researchers without access to their own nanofabrication facility to create quantum (or classical) PICs. The SOI platform, however, does have some limitations that hinder the ubiquity for large scale QPICs. Besides the well-known fact that silicon has an indirect bandgap which prevents the direct integration of efficient photon emitters for light sources, it also suffers from high nonlinear losses (see Section 2.3) like two-photon absorption and free carrier absorption at telecom wavelengths [62] which restricts the achievable quantum light generation rate. Additionally, since state-of-the-art single photon detectors utilize superconducting nanowire single photon detectors (SNSPDs) [63–65], the lack of electro-optic tuning capability (since silicon does not have a second-order nonlinearity) restricts full-scale implementation of SOI QPICs since thermo-optic tuning does not work at the cryogenic temperatures required. Alternative routes to tune circuit components in SOI involve doping to create a PN-junction which enables operation at lower temperatures, but further increase nonlinear losses from free carrier absorption [66].

Silicon nitride (SiN): SiN is another CMOS-compatible material with great promise for QPICs. Compared to the SOI platform, SiN offers much lower propagation loss and a larger bandgap that enables visible-light applications and eliminates nonlinear losses for light at the telecom c-band. Similar to SOI, one of the main motivations for the SiN platform is its foundry-compatible fabrication which enables high yield, reproducible, and scalable demonstrations. Advances in the fabrication of SiN waveguides has enabled

thick SiN with < 1.0 dB/m propagation loss, corresponding to ring resonator quality factors > 30 million [67]. In fact, > 670 million quality factors have been recorded using a high aspect ratio silicon nitride waveguide [68]. These waveguides, however, push most of the mode into the cladding, making them less useful for nonlinear photonics (since the core has the strong nonlinearity). The low loss of the SiN platform is important as quantum circuits begin to scale to thousands of components. The broad bandgap enables visible quantum light generation and entanglement distribution that can interact with atomic or ion transitions [69, 70].

Similar to SOI, the SiN platform lacks an inherent $\chi^{(2)}$ nonlinearity (though researchers are exploring photo-galvanic induced second-order nonlinear interactions [71]) which limits full-scale integration. The refractive index of SiN (~ 2.2) at telecom wavelengths results in large mode areas requiring large bend radii to prevent scattering loss. This results in a lower device density and increases the size of circuits on the platform. The main limitation, however, is the relatively weak Kerr nonlinearity that reduces the efficiency of nonlinear processes.

Lithium niobate (LN): LN has a large second-order nonlinearity, and thus has been historically used for high-speed electro-optic modulators [72]. LN also has a large bandgap which expands the operating ranges of PICs on the platform, and advances in fabrication maintain relatively low-loss throughout the visible and telecom windows [73]. Along with the large second-order nonlinearity which can be used for quantum light generation via parametric down conversion, the large third-order nonlinearity enables four-wave mixing for frequency comb generation [74] and quantum light generation. Compared to the SOI and SiN discussed in the last two sections, LN can be tuned at cryogenic temperatures via the electro-optic effect. The crystal structure also allows for periodic poling which can be used to create long, quasi-phase matched waveguides that allow for broadband light generation [75]. One of the main limitations of the platform compared to SOI and

SiN is the cost and manufacturability. Wafers of LN can be purchased commercially, but are expensive, and the fabrication process is not nearly as scalable as technologies like SOI and SiN.

IIIV semiconductors: Emerging platforms for integrated nonlinear photonics are based on III-V semiconductors including In(Ga)P, InAs, AlGaAs, GaN, AlN, and InSb. These materials have orders of magnitude larger nonlinear coefficients than silicon and SiN which makes them attractive candidates for nonlinear photonics. Along with the high nonlinearities, the direct bandgap of these platforms opens the potential for integration of chip-scale laser sources, and thus many of these platforms have been integrated with silicon and SiN waveguides for light sources [76–78]. Additionally, waveguide-integrated SNSPDs have been demonstrated [79] which, along with the necessary passive and active components, offers promise for a fully integrated material platform for QPICs. Previously, these materials have had significant propagation loss that has prevented the scaling of purely III-V circuits. Initially, AlN [80] and GaN [81] were developed for nonlinear photonics, followed soon after by materials with exceptionally large nonlinearities like AlGaAs [82–84] and GaP [85, 86]. These highly nonlinear materials are the focus of this thesis, and offer great promise for efficient, scalable, fully integrated nonlinear quantum photonics systems.

A key turning point for the AlGaAsOI platform (which is the main material system explored in this thesis) was the demonstration of low-loss ($< 0.2\text{dB/cm}$) waveguides in 2020 [39, 87]. This result was achieved through advancements in the fabrication process that improved the sidewall roughness and improvements in the surface passivation that reduced the absorption loss from defects on the surface. This result motivated much of the work in this dissertation and led to the demonstration of ultra-bright entangled photon pair generation from AlGaAsOI ring resonators [83] (see Chapter 3).

Currently, one limitation for the IIIV-on-insulator platform is the relatively high prop-

agation loss at short wavelengths, particularly below 1 μm , which is mainly associated with surface defects [88]. Another challenge for these platforms, compared to Si or SiN platforms, is the lack of well-developed components, which currently is limiting system-level demonstrations. This hurdle was recently addressed for AlGaAsOI as described in Chapter 4, but additional development is necessary for other III-V material platforms. Additionally, AlGaAsOI and InGaPOI are capable of relatively inexpensive and high-volume production with potential cost advantages over other novel nonlinear platforms, such as LNOI.

Material	$\chi^{(2)}$ [pm/V]	$\chi^{(3)}$ [cm ² /W]	n at 1550nm	Bandgap [nm]	Scalability [mm]	Reference
SOI	-	6.5×10^{-14}	~ 3.4	1100	300	[89]
SiNOI	-	2.5×10^{-15}	~ 2	238	300	[67]
LNOI	26	5.3×10^{-15}	~ 2.14	310	150	[90]
AlGaAsOI	180	2.6×10^{-13}	~ 3.4	625	200	[87]
GaNOI	9	1.2×10^{-14}	~ 2.3	365	-	[81]
InGaPOI	263	1.1×10^{-13}	~ 3.2	650	200	[86]
AlN-OI	1	2.3×10^{-15}	~ 2	205	300	[80]
SiC-OI	12	1×10^{-14}	~ 2.7	383	100	[91]

Table 2.2: Comparison of nonlinearity, refractive index, bandgap, and scalability of nonlinear material platforms

A summary of the materials discussed in the preceding sections is included in Table 2.2. As discussed, each of the prominent material platforms have their pros and cons. SOI and SiN are incredibly scalable, allowing for large-scale implementations at low cost, but have restrictions on the nonlinear efficiencies from either parasitic effects (like two-photon absorption in SOI) or weak nonlinearities (like SiN). LN is relatively low-loss and has large nonlinearities but is expensive to use for fully integrated circuits. III-V semiconductors are not nearly as scalable as some of these other materials, but offer the possibility of full-scale integration with active components, light sources, and single photon detectors. The recent improvements to AlGaAsOI and InGaP have motivated their use for nonlinear quantum light generation which is the focus of this thesis.

Bibliography

- [1] M. A. Nielsen and I. L. Chuang, *Quantum Computation and Quantum Information*. Cambridge University Press, 2011.
- [2] D. J. Griffiths and D. F. Schroeter, *Introduction to quantum mechanics*. Cambridge University Press, 2018.
- [3] M. Smit, K. Williams, and J. Van Der Tol, *Past, present, and future of InP-based photonic integration*, *APL Photonics* **4** (5, 2019) 050901.
- [4] C. Zhang, M. A. Tran, Z. Zhang, *et. al.*, *Integrated photonics beyond communications*, *Applied Physics Letters* **123** (12, 2023) 230501.
- [5] G. Moody, V. J. Sorger, D. J. Blumenthal, *et. al.*, *2022 Roadmap on integrated quantum photonics*, *Journal of Physics: Photonics* **4** (2022), no. 1 12501.
- [6] T. D. Ladd, F. Jelezko, R. Laflamme, *et. al.*, *Quantum computers*, *Nature* **464** (2010), no. 7285 45–53.
- [7] D. P. DiVincenzo, *The physical implementation of quantum computation*, 2000.
- [8] F. Arute, K. Arya, R. Babbush, *et. al.*, *Quantum supremacy using a programmable superconducting processor*, *Nature* **574** (10, 2019) 505–510.
- [9] H. S. Zhong, H. Wang, Y. H. Deng, *et. al.*, *Quantum computational advantage using photons*, *Science* **370** (12, 2020) 1460–1463.
- [10] E. Togan, Y. Chu, A. S. Trifonov, *et. al.*, *Quantum entanglement between an optical photon and a solid-state spin qubit*, *Nature* **466** (8, 2010) 730–734.
- [11] R. Riedinger, A. Wallucks, I. Marinković, *et. al.*, *Remote quantum entanglement between two micromechanical oscillators*, *Nature* **556** (4, 2018) 473–477.
- [12] A. A. Houck, H. E. Türeci, and J. Koch, *On-chip quantum simulation with superconducting circuits*, *Nature Physics* **8** (4, 2012) 292–299.

BIBLIOGRAPHY

- [13] D. L. Moehring, P. Maunz, S. Olmschenk, *et. al.*, *Entanglement of single-atom quantum bits at a distance*, *Nature* **449** (9, 2007) 68–71.
- [14] S. Choe, *Quantum computing overview: discrete vs. continuous variable models*, .
- [15] D. Jaksch, J. J. García-Ripoll, J. I. Cirac, and P. Zoller, *Quantum Computing with Cold Ions and Atoms: Theory*, *Quantum Information* (4, 2016) 483–517.
- [16] S. Slussarenko and G. J. Pryde, *Photonic quantum information processing: A concise review*, 10, 2019.
- [17] E. Knill, R. Laflamme, and G. J. Milburn, *A scheme for efficient quantum computation with linear optics*, *Nature* **409** (1, 2001) 46–52.
- [18] H.-H. Lu, E. M. Simmerman, P. Lougovski, *et. al.*, *Fully Arbitrary Control of Frequency-Bin Qubits*, *Physical Review Letters* **125** (2020).
- [19] P. Kok, W. J. Munro, K. Nemoto, *et. al.*, *Linear optical quantum computing with photonic qubits*, *Rev. Mod. Phys.* **79** (2007) 135.
- [20] J. Zeuner, A. N. Sharma, M. Tillmann, *et. al.*, *Integrated-optics heralded controlled-NOT gate for polarization-encoded qubits*, *npj Quantum Information* **4** (2018), no. 1 13.
- [21] S. Slussarenko and G. J. Pryde, *Photonic quantum information processing: A concise review*, *Applied Physics Reviews* **6** (12, 2019) 41303.
- [22] S. Scheel, Scheel, and Stefan, *Single-photon sources-an introduction*, *JMOp* **56** (1, 2009) 141–160.
- [23] J. P. Chen, C. Zhang, Y. Liu, *et. al.*, *Twin-field quantum key distribution over a 511km optical fibre linking two distant metropolitan areas*, *Nature Photonics* **2021** *15:8* **15** (6, 2021) 570–575.
- [24] F. Xu, X. Ma, Q. Zhang, *et. al.*, *Secure quantum key distribution with realistic devices*, *Reviews of Modern Physics* **92** (6, 2020) 025002.
- [25] A. Einstein, B. Podolsky, and N. Rosen, *Can quantum-mechanical description of physical reality be considered complete?*, *Physical Review* **47** (5, 1935) 777–780.
- [26] R. Horodecki, P. Horodecki, M. Horodecki, and K. Horodecki, *Quantum entanglement*, *Reviews of Modern Physics* **81** (2009), no. 2 865–942.
- [27] C. K. Hong, Z. Y. Ou, and L. Mandel, *Measurement of subpicosecond time intervals between two photons by interference*, *Physical Review Letters* **59** (11, 1987) 2044.
- [28] F. Bouchard, A. Sit, Y. Zhang, *et. al.*, *Two-photon interference: the HongOuMandel effect*, *Reports on Progress in Physics* **84** (12, 2020) 012402.

BIBLIOGRAPHY

- [29] J. G. Rarity, P. R. Tapster, and E. Jakeman, *Observation of sub-poissonian light in parametric downconversion*, *Optics Communications* **62** (5, 1987) 201–206.
- [30] MILLER SE, *INTEGRATED OPTICS. INTRODUCTION*, *Bell System Tech J* **48** (1969), no. 7 2059–2069.
- [31] E. A. Marcatili, *Bends in Optical Dielectric Guides*, *Bell System Technical Journal* **48** (9, 1969) 2103–2132.
- [32] E. A. Marcatili, *Dielectric Rectangular Waveguide and Directional Coupler for Integrated Optics*, *Bell System Technical Journal* **48** (1969), no. 7 2071–2102.
- [33] S. Adachi, *GaAs, AlAs, and Al_xGa_{1-x}As: Material parameters for use in research and device applications*, *Journal of Applied Physics* **58** (8, 1985) R1–R29.
- [34] H. Tanaka, Y. Kawamura, and H. Asahi, *Refractive indices of In_{0.49}Ga_{0.51x}Al_xP lattice matched to GaAs*, *Journal of Applied Physics* **59** (2, 1986) 985–986.
- [35] S. O. Kasap, *Optoelectronics and photonics: principles and practices*. Pearson, 2 ed., 2012.
- [36] G. Lifante, *Integrated Photonics: Fundamentals*, *Integrated Photonics: Fundamentals* (1, 2003).
- [37] L. Chang, W. Xie, H. Shu, *et. al.*, *Ultra-efficient frequency comb generation in AlGaAs-on-insulator microresonators*, .
- [38] L. Chang, A. Boes, P. Pintus, *et. al.*, *Low loss (Al)GaAs on an insulator waveguide platform*, *Optics Letters* **44** (8, 2019) 4075.
- [39] W. Chang and M. Zhang, *Silicon-based multimode waveguide crossings*, *JPhys Photonics* **2** (4, 2020) 022002.
- [40] J. Liu, G. Huang, R. N. Wang, *et. al.*, *High-yield, wafer-scale fabrication of ultralow-loss, dispersion-engineered silicon nitride photonic circuits*, *Nature Communications* **12** (4, 2021) 1–9.
- [41] D. Rabus, *Integrated Ring Resonators: The Compendium*, vol. 127. Springer, 2007.
- [42] P. E. Barclay, K. Srinivasan, O. Painter, *et. al.*, *Nonlinear response of silicon photonic crystal microresonators excited via an integrated waveguide and fiber taper*, *Optics Express, Vol. 13, Issue 3, pp. 801-820* **13** (2, 2005) 801–820.
- [43] M. Gao, Q. F. Yang, Q. X. Ji, *et. al.*, *Probing material absorption and optical nonlinearity of integrated photonic materials*, *Nature Communications* **13** (6, 2022) 1–8.

BIBLIOGRAPHY

- [44] A. Yariv, *Coupled-Mode theory for guided-wave optics*, *IEEE Journal of Quantum Electronics* **9** (1973), no. 9 919–933.
- [45] A. Yariv and P. Yeh, *Photonics: optical electronics in modern communications*, *Chapter Four* (2007), no. November 849.
- [46] L. Chrostowski and M. Hochberg, *Silicon photonics design*, *Silicon Photonics Design* (1, 2015) 1–418.
- [47] A. Anwar, C. Perumangatt, F. Steinlechner, *et. al.*, *Entangled photon-pair sources based on three-wave mixing in bulk crystals*, *Review of Scientific Instruments* **92** (4, 2021) 41101.
- [48] R. W. Boyd, *Nonlinear Optics, Third Edition*, *Nonlinear Optics, Third Edition* (1, 2008) 1–613.
- [49] J. Leuthold, C. Koos, and W. Freude, *Nonlinear silicon photonics*, *Nature Photonics* *2010 4:8* **4** (7, 2010) 535–544.
- [50] Q. Lin, O. J. Painter, G. P. Agrawal, *et. al.*, *Nonlinear optical phenomena in silicon waveguides: Modeling and applications*, *Optics Express, Vol. 15, Issue 25*, pp. 16604–16644 **15** (12, 2007) 16604–16644.
- [51] R. M. Osgood, N. C. Panoiu, J. I. Dadap, *et. al.*, *Engineering nonlinearities in nanoscale optical systems: physics and applications in dispersion-engineered silicon nanophotonic wires*, *Advances in Optics and Photonics* **1** (1, 2009) 162–235.
- [52] M. Borghi, C. Castellan, S. Signorini, *et. al.*, *Nonlinear silicon photonics*, *Journal of Optics* **19** (8, 2017) 093002.
- [53] G. Moody, L. Chang, T. J. Steiner, and J. E. Bowers, *Chip-Scale Nonlinear Photonics for Quantum Light Generation*, *AVS Quantum Science* **2** (12, 2020) 041702.
- [54] D. Thomson, A. Zilkie, J. E. Bowers, *et. al.*, *Roadmap on silicon photonics*, *Journal of Optics (United Kingdom)* **18** (6, 2016) 073003.
- [55] M. Tran, D. Huang, T. Komljenovic, *et. al.*, *Ultra-Low-Loss Silicon Waveguides for Heterogeneously Integrated Silicon/III-V Photonics*, *Applied Sciences* **8** (7, 2018) 1139.
- [56] S. Paesani, M. Borghi, S. Signorini, *et. al.*, *Near-ideal spontaneous photon sources in silicon quantum photonics*, *Nature Communications* **11** (5, 2020) 1–6.
- [57] J. Wang, S. Paesani, Y. Ding, *et. al.*, *Multidimensional quantum entanglement with large-scale integrated optics*, *Science* **360** (4, 2018) 285–291.

BIBLIOGRAPHY

- [58] X. Qiang, X. Zhou, J. Wang, *et. al.*, *Large-scale silicon quantum photonics implementing arbitrary two-qubit processing*, *Nature Photonics* **12** (2018), no. 9 534–539.
- [59] J. Rong Ong, S. Mookherjea, A. Furusawa, *et. al.*, *Quantum light generation on a silicon chip using waveguides and resonators*, *Optics Express* **21** (2, 2013) 5171–5181.
- [60] C. Reimer, L. Caspani, M. Clerici, *et. al.*, *Integrated frequency comb source of heralded single photons*, *Optics Express* **22** (3, 2014) 6535.
- [61] C. Ma, X. Wang, V. Anant, *et. al.*, *Silicon photonic entangled photon-pair and heralded single photon generation with CAR ζ 12,000 and $g(2)(0)$ \approx 0.006*, *Optics Express* **25** (2017), no. 26 32995–33006.
- [62] C. Xiang, W. Jin, J. Guo, *et. al.*, *Effects of nonlinear loss in high-Q Si ring resonators for narrow-linewidth III-V/Si heterogeneously integrated tunable lasers*, *Optics Express* **28** (6, 2020) 19926–19936.
- [63] B. Korzh, Q. Y. Zhao, J. P. Allmaras, *et. al.*, *Demonstration of sub-3 ps temporal resolution with a superconducting nanowire single-photon detector*, *Nature Photonics* **14** (2020), no. 4 250–255.
- [64] E. A. Dauler, M. E. Grein, A. J. Kerman, *et. al.*, *Review of superconducting nanowire single-photon detector system design options and demonstrated performance*, *Optical Engineering* **53** (2014), no. 8 081907.
- [65] V. B. Verma, B. Korzh, F. Bussi eres, *et. al.*, *High-efficiency WSi superconducting nanowire single-photon detectors operating at 2.5K*, *Applied Physics Letters* **105** (9, 2014) 122601.
- [66] G. T. Reed, G. Mashanovich, F. Y. Gardes, and D. J. Thomson, *Silicon optical modulators*, *Nature Photonics* **4** (8, 2010) 518–526.
- [67] X. Ji, F. A. S. Barbosa, S. P. Roberts, *et. al.*, *Ultra-low-loss on-chip resonators with sub-milliwatt parametric oscillation threshold*, *Optica* **4** (6, 2017) 619.
- [68] H. Lee, T. Chen, J. Li, *et. al.*, *Ultra-low-loss optical delay line on a silicon chip*, *Nature Communications* **3** (5, 2012) 1–7.
- [69] C. Monroe and J. Kim, *Scaling the Ion Trap Quantum Processor*, *Science* **339** (3, 2013) 1164 LP – 1169.
- [70] X. Lu, Q. Li, D. A. Westly, *et. al.*, *Chip-integrated visible-telecom entangled photon pair source for quantum communication*, *Nature Physics* **15** (2019), no. 4 373–381.

BIBLIOGRAPHY

- [71] J. Hu, E. Nitiss, J. He, *et. al.*, *Photo-induced cascaded harmonic and comb generation in silicon nitride microresonators*, *Science Advances* **8** (12, 2022).
- [72] E. L. Wooten, K. M. Kissa, A. Yi-Yan, *et. al.*, *Review of lithium niobate modulators for fiber-optic communications systems*, *IEEE Journal on Selected Topics in Quantum Electronics* **6** (1, 2000) 69–82.
- [73] B. Desiatov, A. Shams-Ansari, M. Zhang, *et. al.*, *Ultra-low-loss integrated visible photonics using thin-film lithium niobate*, *Optica* **6** (3, 2019) 380.
- [74] Y. He, Q.-F. Yang, J. Ling, *et. al.*, *Self-starting bi-chromatic LiNbO₃ soliton microcomb*, *Optica* **6** (9, 2019) 1138.
- [75] C. Wang, C. Langrock, A. Marandi, *et. al.*, *Ultrahigh-efficiency wavelength conversion in nanophotonic periodically poled lithium niobate waveguides*, *Optica* **5** (11, 2018) 1438.
- [76] J. C. Norman, D. Jung, Z. Zhang, *et. al.*, *A review of high-performance quantum dot lasers on silicon*, 2019.
- [77] A. W. Fang, H. Park, O. Cohen, *et. al.*, *Electrically pumped hybrid AlGaInAs-silicon evanescent laser*, *Optics Express* **14** (2006), no. 20 9203.
- [78] A. Y. Liu and J. Bowers, *Photonic integration with epitaxial III-V on silicon*, *IEEE Journal of Selected Topics in Quantum Electronics* **24** (2018), no. 6 1–12.
- [79] C. McDonald, G. Moody, S. W. Nam, *et. al.*, *III-V photonic integrated circuit with waveguide-coupled light-emitting diodes and WSi superconducting single-photon detectors*, *Applied Physics Letters* **115** (8, 2019).
- [80] C. Xiong, W. H. Pernice, and H. X. Tang, *Low-loss, silicon integrated, aluminum nitride photonic circuits and their use for electro-optic signal processing*, *Nano Letters* **12** (7, 2012) 3562–3568.
- [81] C. Xiong, W. Pernice, K. K. Ryu, *et. al.*, *Integrated GaN photonic circuits on silicon (100) for second harmonic generation*, *Optics Express* **19** (5, 2011) 10462.
- [82] E. J. Stanton, J. Chiles, N. Nader, *et. al.*, *Efficient second harmonic generation in nanophotonic GaAs-on-insulator waveguides*, *Optics Express* **28** (3, 2020) 9521.
- [83] T. J. Steiner, J. E. Castro, L. Chang, *et. al.*, *Ultra-bright entangled-photon pair generation from an AlGaAs-on-insulator microring resonator*, *PRX Quantum* **2** (9, 2021) 010337.
- [84] M. Pu, L. Ottaviano, E. Semenova, and K. Yvind, *Efficient frequency comb generation in AlGaAs-on-insulator*, *Optica* **3** (8, 2016) 823.

BIBLIOGRAPHY

- [85] D. J. Wilson, K. Schneider, S. Hönl, *et. al.*, *Integrated gallium phosphide nonlinear photonics*, *Nature Photonics* **14** (1, 2020) 57–62.
- [86] M. Zhao and K. Fang, *InGaP quantum nanophotonic integrated circuits with 1.5% nonlinearity-to-loss ratio*, *Optica* **9** (2, 2022) 258.
- [87] W. Xie, L. Chang, H. Shu, *et. al.*, *Ultrahigh-Q AlGaAs-on-insulator microresonators for integrated nonlinear photonics*, *Optics Express* **28** (4, 2020) 32894.
- [88] L. Chang, A. Boes, X. Guo, *et. al.*, *Heterogeneously Integrated GaAs Waveguides on Insulator for Efficient Frequency Conversion*, *Laser and Photonics Reviews* **12** (10, 2018) 1800149.
- [89] A. Biberman, M. J. Shaw, E. Timurdogan, *et. al.*, *Ultralow-loss silicon ring resonators*, *Optics Letters* **37** (10, 2012) 4236.
- [90] M. Zhang, C. Wang, R. Cheng, *et. al.*, *Monolithic ultra-high-Q lithium niobate microring resonator*, *Optica* **4** (12, 2017) 1536.
- [91] D. M. Lukin, C. Dory, M. A. Guidry, *et. al.*, *4H-silicon-carbide-on-insulator for integrated quantum and nonlinear photonics*, *Nature Photonics* **14** (12, 2019) 330–334.

Chapter 3

Quantum Light Sources

The goal of integrated quantum photonics is to create an ideal source of nonclassical light (such as single photons, photon pairs, photon-number states, or continuous variable squeezed states of light) that can be utilized as a resource of quantum information. Many applications including quantum communications (see Chapter 5), quantum information processing [1, 2], quantum computing [3], quantum networking [4], and quantum metrology [5] require quantum photonic resource states with high brightness, purity, and indistinguishability, and thus, the exploration of material systems that can improve upon the current state-of-the-art single photon sources is an important field of research to expand the scale of quantum systems. As is the motivation for most chip-scale technologies, the miniaturization of these quantum light sources to the chip-scale is driven by low size, weight, power and cost (SWaP-C). There are two main categories of chip-scale quantum light sources: deterministic sources, relying on single-quantum emitters like self-assembled quantum dots (QDs), and probabilistic sources, utilizing nonlinear interactions like spontaneous parametric down conversion (SPDC) and spontaneous four-wave mixing (SFWM) [6]. While SPDC sources have long been seen as cutting-edge for producing heralded single and entangled photons, recent advancements in III-V micro-

fabrication have led to high-quality QD-based sources for quantum applications off-chip, as demonstrated by ground-to-satellite quantum key distribution [7] and 20-photon, 60-mode Boson sampling [8]. Development of single-photon emitters is an active research area with extensive research into the creation and engineering of emitters in several material platforms, including silicon, silicon carbide, diamond, and 2D materials [9, 10]; however, each of these emitter platforms are still at a technology readiness level that prevents large-scale implementation for quantum applications. Some challenges for semiconductor QD development, for example, include limited control over their spatial and spectral properties, difficulties in efficiently guiding emitted light on a chip, and the need for cryogenic operating temperatures. On the other hand, SPDC and SFWM sources offer notable advantages in terms of scalability, boasting arrays of up to 18 indistinguishable heralded sources that can be monolithically integrated onto a silicon photonic chip [11]. Progress in improving the brightness of these sources in recent years has also now led to probabilistic sources comparable to the best single QD sources [12].

In the previous chapter, the concept on nonlinear optics was introduced along with a classical description of SFWM and SPDC. This discussion emphasized some of the characteristics of a material system that could be optimized to increase the interaction strength of this nonlinearity. The ultimate goal of this work with nonlinear integrated photonics is to utilize these nonlinear interactions to generate nonclassical states of light that can be manipulated and utilized for quantum communications and computation applications. This chapter focuses on the generation of quantum states of light from nonlinear materials, with an emphasis on cavity-based integrated sources of quantum light. In the classical picture, the FWM process is stimulated with a seed laser source. Moving to the quantum picture, we will discuss how vacuum fluctuations "seed" the nonlinear interactions in the absence of this stimulated source. This description will be utilized to model the generation rate of entangled photon pairs from both $\chi^{(2)}$ and

$\chi^{(3)}$ nonlinear materials, describing the spontaneous analog to classical four-wave mixing (FWM) and parametric down conversion (PDC). Operating these sources in the low power regime, we will characterize the photon pair generation rate and heralded single photon quality. In the higher power regime, these sources can act as sources of quadrature squeezed light which has many applications in quantum metrology [5] and continuous-variable quantum information [13].

3.1 Photon Pair Sources

Photon pair sources are valuable in various quantum applications due to the correlations that exist between the generated photon pairs. These pairs of photons exhibit inherent connections such that the measurement of one of the photons results in a correlated measurement of the other photon. Figure 3.1 summarizes the key concepts of nonlinear photon-pair generation [6]. In SPDC (a $\chi^{(2)}$ nonlinear process), a single pump photon at frequency ω_p gets annihilated, creating a pair of signal and idler photons at frequencies ω_s and ω_i respectively, where $\omega_p = \omega_s + \omega_i$. In contrast, SFWM (a $\chi^{(3)}$ nonlinear process) generates photon pairs by annihilating two pump photons while conserving energy and momentum ($2\omega_p = \omega_s + \omega_i$). SPDC tends to be more efficient due to the larger $\chi^{(2)}$ nonlinearity; however, SFWM allows for quasi-degenerate or degenerate pump, signal, and idler photon frequencies, providing advantages in relaxed dispersion engineering requirements in photonic waveguides and resonators. For both types of nonlinear sources, two methods for generating photon pairs exist, through linear or spiral waveguides and through microring resonators or photonic crystal cavities (optical cavities) [14]. Waveguides can efficiently produce photon pairs using periodic poling [15, 16] or geometry tailoring [17], enabling phase matching between the photons over longer propagation distances. However, these structures often necessitate millimeter- or centimeter-long

waveguides to generate substantial signal and idler photon flux. Microresonators, on the other hand, offer advantages as the longer cavity lifetime enhances the effective nonlinearity, enabling efficient pair generation in micrometer-scale devices and reducing the impact of fabrication nonuniformity on the phase-matching condition. Chip-scale sources of entangled pairs have been integrated with various photonic platforms, including silicon [18], nitrides [19], indium phosphide [20], and lithium niobate [21], but each has fundamental limitations that restrict the photon-pair brightness and quality, including weak optical nonlinearity or high waveguide loss. Our work focuses on two relatively new integrated photonic material platforms: aluminum gallium arsenide (AlGaAs) and indium gallium phosphide (InGaP). As discussed in the previous Chapter 2, these materials have large nonlinear coefficients, can be integrated with active components, and as of recently can be manufactured on the wafer scale. Improvements to the fabrication process have enabled these platforms to support low loss waveguides and high quality factor microring resonators.

3.1.1 Properties

In order to design a useful source of photon pairs, it is important to identify the metrics that characterize an ideal photon pair source. A description and analysis of the measurements of such photon pair properties constitutes the final sections of this chapter, illustrating some of the fundamental trade-offs between these qualities. Here, we introduce these concepts. First, the ideal photon pair source produces entangled photon pairs that are bright (many pairs generated for a given pump power input) for high rates in a given optical mode, indistinguishable (such that different photons from the same or different sources are in the same quantum state and can be interfered), and pure (such that only the desired photon state is produced). For the creation of larger

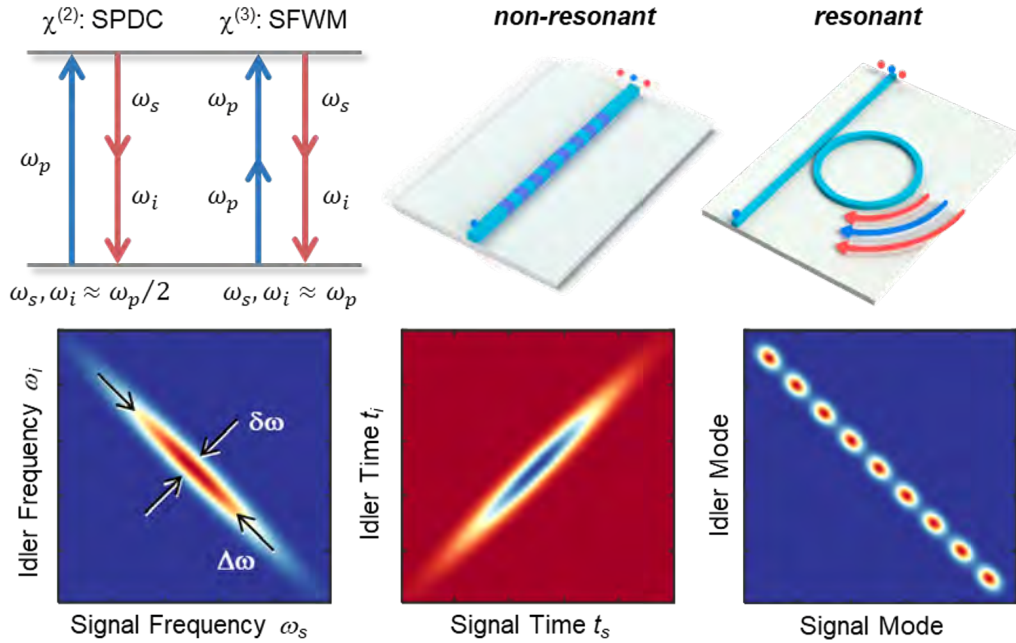


Figure 3.1: Generation of entangled photon pairs using nonlinear materials. The energy conservation of $\chi^{(2)}$ SPDC and $\chi^{(3)}$ SFWM processes is indicated where one (two) pump photon annihilates to generate a signal and idler photon pair for SPDC (SFWM). The generated signal and idler frequencies are correlated as shown in the joint spectral intensity plots. For resonant excitation schemes, the resonance modes are correlated while off-resonant frequencies do not enter the resonator and thus do not generate photon pairs.

qubit systems (for example a system with two or more sources of nominally identical photons), it is also desirable to have photon pairs that are separable such that they are indistinguishable.

Brightness

The photon pair brightness is a common figure of merit that essentially describes the efficiency of the photon pair source in terms of pairs $\text{s}^{-1} \text{mW}^{-1}$ for SPDC (pairs $\text{s}^{-1} \text{mW}^{-2}$ for SFWM). The most basic requirement of a source is that it produces a high photon pair rate with a small amount of input power. Enhanced source efficiency reduces the requirements of the pump power and pump rejection filters, reducing the

system loss (fewer filters typically means lower loss) and enabling larger applications to be explored. The brightness is typically measured using single photon detectors and demultiplexers to record the single photon counts for the signal and idler photon pairs generated from the source. Time correlated single photon counting modules allow for the coincidence count rate of the source to be recorded. Accounting for the loss from the source to detectors, it is possible to estimate the on-chip photon pair brightness using either the single photon counts or the coincidence count rates. Just looking at the collected single photon counts, the brightness of the source on chip can be estimated by taking the collected singles counts, subtracting the accidental/background counts and then accounting for the loss the single photons experience. We can measure the single photon counts as a function of power, and use a fit of N_{raw} vs. P (or P^2 for SFWM sources). The total rate of on-chip photons generated should be $R_{chip} = (N_{raw(s,i)} - N_{background})/\eta_{s,i}$. This approach should yield the same value as using the coincidence counts of the signal and idler photons (CC). Again, the slope of the linear (or quadratic) dependence on power is used to determine the average number of coincidences as a function of power, and $R_{chip} = (CC_{raw} - CC_{acc})/(\eta_i\eta_s)$. In practical applications, the raw (uncorrected) brightness is used since the usable photon rate includes the attenuation caused by system losses, thus encouraging low-loss photonic testbeds. Oftentimes, the brightness is also normalized to the bandwidth across which the pairs can be generated (total bandwidth for a spiral or waveguide source, or mode linewidth for a resonator source). This can provide a better comparison between different types of sources and their usable brightness in a given bandwidth (say, of an optical filter for experimentation).

Coincidence to Accidental Ratio

The photon pairs generated from a nonlinear quantum light source should be temporally correlated meaning that the generated signal and idler photon pair should arrive

at their respective detectors within a time bin the size of the two-photon coherence time (discussed below in Section 3.1.1). This coincidence event should be much brighter than any background noise in the system. The coincidence to accidental ratio (CAR) is a metric that quantifies the ratio of the coincidences from the photon pair source to the background accidental counts. Accidentals are from lost photon pairs, pump leakage into the detectors, dark counts from the detectors, and any other sources of non-correlated photon pairs (like the room lights). A large CAR indicates a good signal to noise of the detected photons, which can be useful to minimize errors in quantum communications or computing applications. There is typically an inverse relationship between photon pair flux and CAR because at higher powers, multi-pair emission events begin to contribute additional uncorrelated accidental coincidence counts.

Indistinguishability

Once a bright source of photon pairs is established, another important property is the indistinguishability of the photons generated from the source. This is important because it dictates the interference expected from pairs of the same source and can limit how two (or more) sources' photons interfere with each other. In order for photons to be indistinguishable, they must be identical in all degrees of freedom: arrival time, transverse mode shape, temporal shape, polarization, and frequency. The use of integrated systems like waveguides and ring resonators eases some of the requirements since the waveguide can be engineered to support one transverse mode and maintain the polarization state. To measure the indistinguishability of a source, a measurement of the interference visibility can be completed. One such measurement is completed using a Franson interferometer [22] where the photon stream is split into two paths, one with a time delay relative to the other. This system measures the time-energy entanglement visibility because the two-photon states can interfere (see Section 3.1.5). If the photons generated from

the source are indistinguishable, the visibility will be 100%. Any degradation in the visibility indicates either a limitation from the measurement or from the quality of the source. Indistinguishability between two (or more) nominally identical pair sources can be determined through Hong Ou Mandel interferometry, which is described in Chapter 6.

Purity

It is also important the photons generated from the source are pure (defined here as the source producing a *single* pair of photons, ignoring the vacuum component due to optical loss and $< 100\%$ pair generation efficiency). The purity of a source can be degraded if, for example, too much power is used and multiple pairs of photons are generated simultaneously in a given time window instead of just one photon pair. To measure the single photon purity, a heralded g^2 measurement is completed where the idler photon is sent directly to a detector and the signal photon is sent through a 50/50 beamsplitter to one of two detectors. A measurement is made based on the three-fold coincidences (which should be zero if only one pair of photons is created). The rate of three-fold coincidences indicates the probability of creating a higher photon number state that degrades the purity of the source.

Coherence Time

The coherence time of a photon is the time duration over which the phase of the wavepacket is stable. It can be related to the linewidth of the photons ($\Delta\omega$) such that $\tau_{coh, single} \approx \frac{1}{\Delta\omega}$ [23]. The coherence time of generated photon pairs will vary based on the pumping scheme due to this relationship. For continuous-wave lasers with narrow linewidths (which can approach 10s of kHz), the coherence time can be quite large ($\sim \mu s$) [24] On the other hand, the use of pulsed lasers results in a broader spectral

linewidth and thus a reduced coherence time of the generated light. When considering nonlinear quantum light sources, the photon pair coherence time (described above) should be distinguished from the coherence of the individual single photons. As described below, both linear waveguides and resonant structures can be used to generate entangled photon pairs. The nature of this generation has a direct impact on the coherence time of the single photons as they propagate. For the case of non-resonant structures, the single photons have coherence times based on the filters used to separate the two single photons. It is common to use standard wavelength division demultiplexers with 100 GHz bandwidths, resulting in single photon coherence times on the order of 10 ps [25]. For the resonator case, the single photons have spectral properties from the resonance, improving the coherence time. A resonance that has a 1 GHz linewidth will result in single photon coherence times on the order of 1 ns [26]. Since the quality factor (as defined in Chapter 2) is $Q = \omega/\Delta\omega$, the coherence time of a photon from a resonator can be estimated as Q/ω .

Both the single photon and photon pair coherence times are important characteristics when considering interference measurements. In order to interfere photon pairs, the time delay τ_d must be below the photon pair coherence time τ_p and above the single photon coherence times τ_s , meaning $\tau_s < \tau_d < \tau_p$. This relation allows the two photons to interfere and prevents the interference between the single photon and itself.

Separability

The last metric impacts the ability to use multiple pairs simultaneously. Separability indicates the state of entanglement that exists between the signal and idler photon pairs. If the pairs are separable, then the signal photon can be measured without providing any information about the state of the idler photon. In the case that the photons are entangled, the measurement of an idler photon will collapse the state of the signal photon,

at least partially disrupting any subsequent interference with photons from other photon pairs. There are continuously varying degrees of separability, so some interference can still occur, but when scaling the dimensionality of entangled photon pair resource states, the separability will fundamentally dictate the interference visibility of different photon pair sources used in parallel.

3.1.2 Waveguide-Based Sources

One of the most straightforward approaches to the chip-scale integration of nonlinear quantum light generation is to utilize a simple straight waveguide. The waveguide approach relies on careful phase matching such that the generated light remains in phase with the injected pump light and gains amplitude as it propagates the length of the waveguide. Provided that this phase-matching requirement is satisfied, the approach is very simple where the SPDC or SFWM signal grows as the modes travel along the waveguide, providing an advantage to longer waveguide lengths (provided the propagation loss is low enough that the additional length does not quench the pump light). However, these longer waveguide geometries also accumulate more phase mismatch due to dispersion, so the enhanced rate comes at the cost of the photon pair generation bandwidth. A consideration often made when designing these systems is the total area required on a fabricated chip. Thus, it is common to utilize spirals that can compactly create long waveguides by looping back around itself instead of requiring a chip that matches that waveguide length. Figure 3.2 shows a microscope image of six spirals with total waveguide lengths of from 3.1 cm to 4.2 cm. In order to fit the same waveguide length in a straight line, the width of the bar would have to be > 10 times larger than used for these devices.

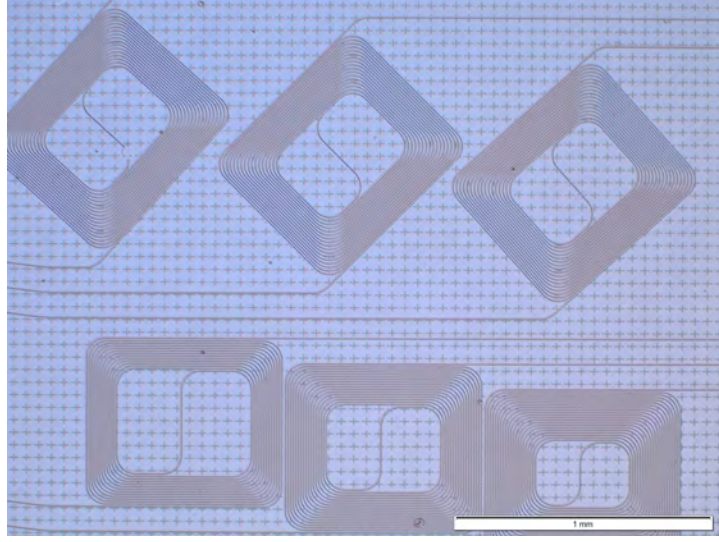


Figure 3.2: Microscope of 400 nm thick $\text{Al}_{0.2}\text{Ga}_{0.8}\text{AsOI}$ waveguide spirals with lengths from 3.1 cm to 4.2 cm.

Second-Order Nonlinearity

Using the classical description of nonlinear interactions established in Chapter 2, we can move into a more quantum description of the states generated via second-order nonlinear interactions in waveguides. Here, we focus on the process of SPDC, but similar derivations can be made for second harmonic generation, sum and difference frequency generation, and other three-wave mixing processes. Starting first with the theory of SPDC in linear waveguides, we can describe the nonlinear Hamiltonian as [15, 27–30],

$$\mathcal{H} = H_L + H_{NL} \quad (3.1)$$

$$\mathcal{H}_L = \int dk \hbar \omega_{Fk} a_{Fk}^\dagger a_{Fk} + \int dk \hbar \omega_{SHk} a_{SHk}^\dagger a_{SHk} \quad (3.2)$$

$$\mathcal{H}_{NL} = - \int dk_1 dk_2 dk S(k_1, k_2, k) a_{Fk_1}^\dagger a_{Fk_2}^\dagger a_{SHk} + H.c. \quad (3.3)$$

where the frequencies are denoted by $\omega_{F,SH}$ for the fundamental and second-harmonic, and the nonlinear coupling coefficient $S(k_1, k_2, k)$ is defined as

$$S(k_1, k_2, k) = \frac{1}{\epsilon_0} \sqrt{\frac{\hbar^3 \omega_{Fk_1} \omega_{Fk_2} \omega_{SHk}}{(4\pi)^3}} \int dr \Gamma_2^{ijk}(r) \times [d_{Fk_1}^i]^* [d_{Fk_2}^j]^* d_{SHk}^k e^{i(\Delta k)z}. \quad (3.4)$$

We can use the linear response of the material to relate $\Gamma_2^{ijk}(r)$ to $\chi^{(2)i,j,k}(r)$.

$$\Gamma_2^{ijk}(r) = \frac{\chi^{(2)i,j,k}(r)}{\epsilon_0 n^2(x, y; \omega_{Fk_1}) n^2(x, y; \omega_{Fk_2}) n^2(x, y; \omega_{SHk})} \quad (3.5)$$

From the form of Equation 3.3, we see that this description is valid for both second-harmonic generation and for down conversion. Following the backward Heisenberg approach [31], the generated state for SPDC can be written as a pump pulse exciting the two-mode squeezed vacuum,

$$|\psi_{gen}\rangle = \exp(\beta C_{II}^\dagger - H.c.) |vac\rangle \quad (3.6)$$

where $|\beta|^2$ is proportional to \mathcal{N}_P , the average number of photons in the pump pulse, and

$$C_{II}^\dagger = \frac{1}{\sqrt{2}} \int d\omega_1 d\omega_2 \phi(\omega_1, \omega_2) a_{F\omega_1}^\dagger a_{F\omega_2}^\dagger \quad (3.7)$$

such that $C_{II}^\dagger |vac\rangle$ is the normalized two-photon state characterized by the biphoton wavefunction $\phi(\omega_1, \omega_2)$ [14]. In the non-depleted pump approximation at low power, the generated state can be approximated as $|\psi_{gen}\rangle \approx |vac\rangle + \beta C_{II}^\dagger |vac\rangle$ indicating that the process mostly generates the $|vac\rangle$ mode with a small conversion into the two-mode state.

Following the work detailed in Ref. [14], we can change this formulation from the general case to the specific case of generating a signal and idler mode from a pump pulse

that is at the second harmonic frequency. We replace the F subscripts with either s or i to indicate the signal and idler modes and replace the SH label with P for the pump mode. We can define a detuning $\Omega = \omega_1 - \omega_P/2$ and utilize the characteristic power of a $\chi^{(2)}$ material, $\mathcal{P} = 8\epsilon_0\bar{n}^6\nu_s\nu_i\nu_P/(\bar{\chi}^{(2)}\omega_P)^2$. Considering a quasi-continuous pump with average power P_P , we can express the average generated power associated with one photon of the pair as,

$$P_i = \frac{\hbar\omega_i P_P L^2}{\mathcal{T}\mathcal{P}\mathcal{A}} \quad (3.8)$$

with

$$\mathcal{T} = \frac{2\pi}{\int_0^{\omega_P/2} d\Omega [1 - (2\Omega/\omega_P)^2] \text{sinc}^2 [L/2[k_i(\omega_P/2 + \Omega) + k_s(\omega_P/2 - \Omega) - k_P(\omega_P)]]} \quad (3.9)$$

and \mathcal{A} is the effective area with the $\chi^{(2)}$ nonlinearity [31]. As evident, the efficiency of SPDC (for a fixed pump power in a given material) can be enhanced by improving the effective nonlinearity, reducing the effective mode area, and increasing the length. The form of this equation follows the well-known result for the stimulated process [14, 32],

$$P_i = P_s \frac{P_p L^2}{\mathcal{P}\mathcal{A}} \text{sinc}^2 \left([k_s(\omega_s) + k_i(\omega_p - \omega_s) - k_p(\omega_p)] \frac{L}{2} \right) \quad (3.10)$$

where in the spontaneous case, the signal seed power is replaced by $\hbar\omega_i/\mathcal{T}$, the average energy of one downconverted photon in a time \mathcal{T} .

Third-Order Nonlinearity

The method used to estimate the generated power of the SPDC photons can be utilized for the case of a third-order nonlinear material (here we assume the material does not have a second-order nonlinear interaction for simplicity, though the addition of the second-order process can be seen by adding Equation 3.3 into the third-order

Hamiltonian below).

$$\mathcal{H}_3 = \mathcal{H}_L + \mathcal{H}_{NL} \quad (3.11)$$

with

$$\mathcal{H}_L = \int dk \hbar \omega_k a_k^\dagger a_k \quad (3.12)$$

and

$$\mathcal{H}_{NL} = - \int dk_1 dk_2 dk_3 dk_4 S(k_1, k_2, k_3, k_4) a_{k_1}^\dagger a_{k_2}^\dagger a_{k_3} a_{k_4} \quad (3.13)$$

describing the annihilation of two photons (one with wavenumber k_3 and one with k_4) to generate two new photons with wavenumbers $k_{1,2}$. Following the backward Heisenberg picture approach as in Section 3.1.2, we can find the average power associated with one of the generated photons as,

$$P_i = \frac{\hbar \omega_P}{\mathcal{T}} (\gamma P_P L)^2 \quad (3.14)$$

where $\gamma = 2\pi n_2 / (\lambda A_{eff})$ is the commonly used nonlinear parameter for a third-order nonlinear material with nonlinear index n_2 . Again, this form matches the classical FWM result with the substitution of $\hbar \omega_P / \mathcal{T}$ for the classical seed power,

$$P_i = P_s (\gamma P_P L)^2 \text{sinc}^2 ([2k_P(\omega_p) - k_s(\omega_s) - k_i(2\omega_P - \omega_s)]L/2) \quad (3.15)$$

As an example, we can utilize the Equation 3.14 to model an 800nm wide, 400nm thick $\text{Al}_{0.2}\text{Ga}_{0.8}\text{As}$ waveguide used to generate entangled photon pairs via SFWM. Here we convert from the idler power P_i to the number of photons through the relation $P_i = \hbar \omega_i \mathcal{N}_D / (2T)$ where T is time the pump is on and \mathcal{N}_D / T is the photon flux in counts per second. Figure 3.3 shows the generation of a linear $\text{Al}_{0.2}\text{Ga}_{0.8}\text{As}$ waveguide with varying lengths. Lumerical Mode simulations are utilized to model the waveguide mode at a pump

wavelength of $1.55 \mu\text{m}$, and the dispersion of the mode is used to determine the values of $k_{s,i}$ as the frequency is swept about the pump wavelength. The waveguide width of 800nm is near the zero-dispersion width, which enables a relatively large $> 20\text{THz}$ SFWM bandwidth (see more details in the next section). The length dependence on the generated photon pair flux is quadratic as expected, and the phase matching bandwidth reduces for longer waveguide lengths (shown by the narrowing of the FWHM on marked with x's).

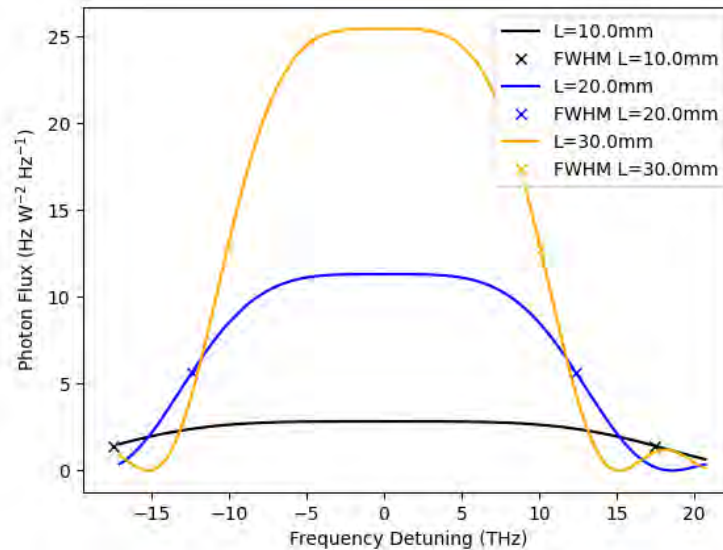


Figure 3.3: Model of SFWM in a 400nm thick $\text{Al}_{0.2}\text{Ga}_{0.8}\text{AsOI}$ waveguide with a 800nm width. The different colors show varying waveguide lengths, and the x's indicate the full width at half maximum.

Phase Matching

In both of the formulations for the SPDC and SFWM generation rates, there is a term of the form $\text{sinc}^2[\dots]$ which dictates the generation bandwidth of the source. This function is known as the phase matching function and limits the generation rate to cases where the wavenumbers (k) of the pump, signal and idler wavelengths yield values for

(SPDC) $\Delta k = k_P - k_s - k_i$ or (SFWM) $\Delta k = 2k_P - k_s - k_i$ that are small (close to 0) such that the sinc^2 function has a maximum. As seen in Figure 3.3, the mismatch in k wavenumbers accumulates phase mismatch for longer waveguide lengths, resulting in a narrower bandwidth as the waveguide length is increased. For materials with significant dispersion (meaning the $k_{P,i,s}$ are very different), the bandwidth can ultimately limit the utility of the source. The photon pairs must fundamentally be separated from the pump light in order to be useful, and it is desirable to use standard wavelength division demultiplexers (which are typically 100 GHz in bandwidth). Thus, a photon pair flux with < 100 GHz bandwidth will be challenging to implement for useful applications unless custom, narrowband filters are used. When designing a source, it is therefore useful to consider a geometry where the wavenumbers of the signal, idler and pump photons result in $\Delta k \approx 0$.

This practice of dispersion engineering can be useful for many applications. For the lithium niobate material platform, this engineering becomes especially useful, as an example, since the crystal structure can be poled in opposite orientations to create a "quasi-phase matched" crystal. Accumulated phase can be reverted by flipping the crystal axis, enabling long waveguides to be created that maintain high photon pair bandwidth [33]. For other systems, the dispersion must be engineered via the waveguide geometry. This dispersion management is especially necessary for SPDC sources where the pump wavelength is $\sim 1/2$ the generated wavelength. Let's start first with the dispersion engineering of an SPDC source.

Using a Type-I SPDC source, the pump light is orthogonally polarized to the generated signal and idler photon pairs. We can utilize this orthogonal polarization to strategically design a waveguide with approximately the same effective indices for the pump, signal and idler modes. If all modes were the same polarization (Type-0), this method would not work because the pump mode is much more confined in the wave-

uide than the longer wavelength signal and idler modes and thus the pump effective index would be much larger than the signal and idler indices. Again, the goal of SPDC phase matching is to design the waveguide such that the $n_{eff,P} \approx n_{eff,(s,i)}$ such that $n_{eff,P}\omega_p - n_{eff,i}\omega_i - n_{eff,s}\omega_s \approx 0$ (or, alternatively, $\Delta k \approx 0$). Using InGaP as an example, this can be achieved by using a thin but wide waveguide along with a TM polarized pump mode (and therefore TE polarized signal and idler modes). Since the material is thin, the TM polarized pump mode is pushed into the cladding, lowering the effective index. The wide waveguide width increases the confinement of the long wavelength modes, allowing for close matching to be achieved. Figure 3.4 shows the method of determine the optimal waveguide geometry for phase matching. On the left panel, the effective indices of the pump TM mode are shown with dashed lines while the generated signal and idler TE modes are shown in solid lines. The location where the solid and dashed lines of the same color cross indicates phase matching for this system (plotted on the right panel of Figure 3.4).

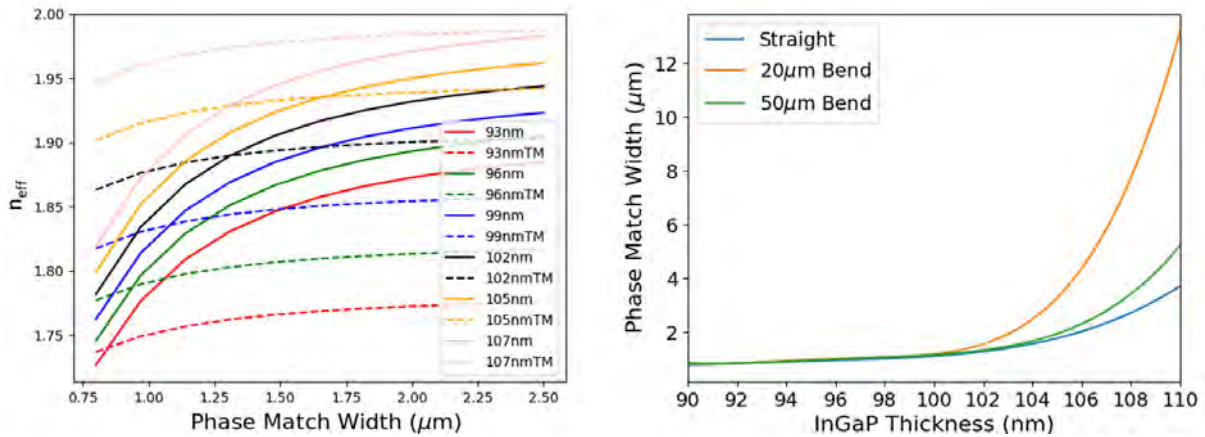


Figure 3.4: Phase matching for SPDC in InGaP waveguides. The pump light is TM polarized (dashed lines) while the generated light is TE polarized (solid). The different colors indicate different waveguide thicknesses, and the location where the TE and TM lines cross indicates the width where phase matching is achieved. On the right panel, this width is plotted as a function of the waveguide thickness for the straight waveguide (left panel) as well as for bent waveguides.

For the SFWM case, the phase matching design becomes more straightforward since the pump, signal, and idler modes are all approximately the same wavelength. Since the material dispersion is typically normal dispersion (longer wavelengths have lower refractive index), it is desirable to make a waveguide have slight anomalous dispersion to compete with the material dispersion. The broadest SFWM spectrum can be achieved when the waveguides have close to zero dispersion at the pump wavelength. Figure 3.5 shows how the dispersion of a 400nm thick $\text{Al}_{0.2}\text{Ga}_{0.8}\text{As}$ waveguide changes for various waveguide widths. At $1.55 \mu\text{m}$ the dispersion is approximately 0 ps/nm/km for a 800nm wide waveguide. Thus, the largest photon pair generation bandwidth can be achieved with waveguides of approximately this width. Sufficiently large bandwidths can still be achieved for some non-zero dispersion for SFWM sources, making it less of a factor in the design of SFWM sources compared to SPDC sources.

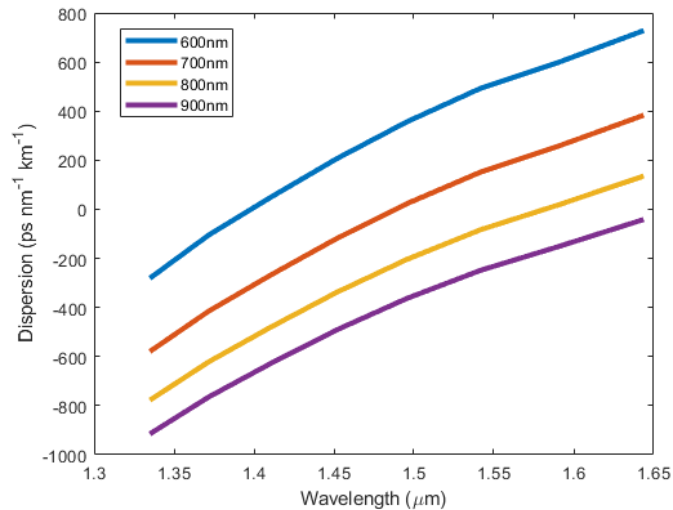


Figure 3.5: Dispersion of 400nm thick $\text{Al}_{0.2}\text{Ga}_{0.8}\text{As}$ waveguides with various widths. For $1.55 \mu\text{m}$ wavelength, the zero dispersion width is approximately 800nm.

3.1.3 Broadband Entanglement Generation

Another interesting use of dispersion engineering is the design of SFWM sources to generate a signal and idler photon at very different wavelengths. Quantum photonics has many great advantages, including room temperature operation, limited environmental interaction, and the ability to leverage already designed fiber-optic telecommunications systems. However, there are other quantum technologies that are better suited for interactions and quantum memory/storage [34]. Many of the systems that are best suited for quantum memories operate with photons in the visible or near-infrared wavelength ranges. The transmission of photons through silica optical fiber at these wavelengths is extremely lossy, so it is impossible to connect these systems across very large distances. In the creation of a global quantum network, these platforms need to be interfaced with telecom-wavelength systems to allow for this large scale implementation. One route for this technology is to use entanglement swapping or quantum teleportation [35–37] to transfer the quantum information from the visible/near-infrared photon to a telecom photon that is compatible with low-loss data transmission. With this motivation, SFWM can actually serve as a great option to create this interconnect. By tailoring the phase matching of the waveguide (via changes in the cross-section), it is possible to expand a SFWM source such that it can generate one photon in the visible and the other in the telecom wavelength range. This method has been explored in silicon nitride waveguides which have a relatively weak nonlinearity; however, the results are quite impressive showing the creation of a photon at 668.4nm wavelength that is entangled with a photon at 1550nm wavelength with photon pair brightness exceeding 2.5 MHz/mW^2 [36].

With hopes to improve upon the efficiency, we explore different materials with higher optical nonlinearity and model the frequency mismatch of a system of SFWM with a pump at 1033nm, signal at 775nm, and idler at 1550nm. The frequency mismatch is

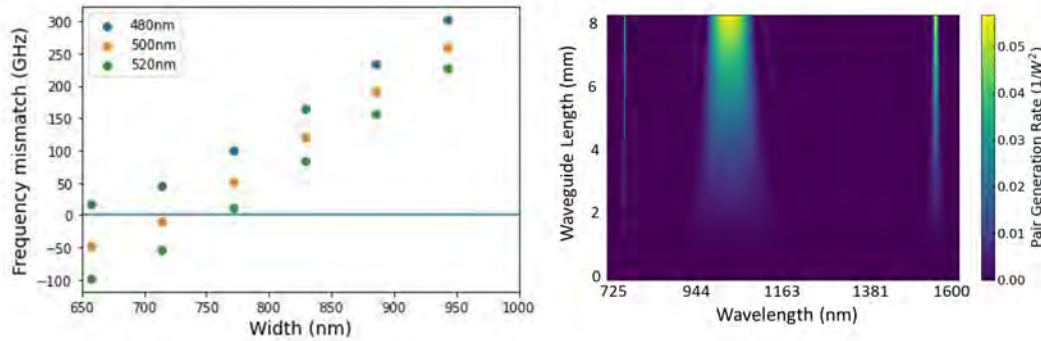


Figure 3.6: Model of phase matching to show a waveguide geometry that can be used to generate visible-telecom entangled photon pairs. a) Frequency mismatch versus the waveguide width for different thicknesses of GaN waveguides. b) Entangled photon pair flux for a 500 nm thick, 725 nm wide GaN waveguide showing the generation of a signal at 775nm and idler at 1550nm.

defined as $\Delta\omega = [(n_s\omega_s + n_i\omega_i)/(2n_p)] - \omega_p$ where $n_{p,s,i}$ are the effective mode indices for the modes with frequencies $\omega_{p,s,i}$. This is the same calculation described in the phase matching section. However, since it is impossible for such a broad wavelength range to have the same effective index, here a specific amount of dispersion is desired to balance the wide range in frequencies used. When a waveguide dimension is selected that falls on the $\Delta\omega = 0$ line, the desired phase matching is achieved. In Figure 3.6, panel a) show the frequency mismatch for different waveguide geometries of GaN, and the photon pairs are generated at the desired wavelengths (see plots in Figure 3.6b). For a linear waveguide, the generation of these telecom-visible entangled photon pairs can be seen by the bright strips in the plots b) at 775nm and 1550nm wavelengths. As described in the previous section, photon pairs will also be generated in a bandwidth near the pump wavelength since the dispersion is relatively small near the pump.

Unfortunately, for the InGaP and AlGaAs material platforms, the refractive index grows exponentially near the 775 nm (see the refractive index plots introduced in Chapter 2). This sharp increase in the refractive index along with the improved confinement of the 775 nm mode makes it impossible to get phase matching between the 775 nm and

1550 nm mode with a 1033 nm pump. Materials like SiN and GaN have more gradual and almost linear index changes with wavelength which allow for phase matching to be achieved (as shown in Figure 3.6). More unique approaches must be utilized to improve the generation bandwidth of InGaP and AlGaAs. For example, using an orthogonal pump scheme (where the pump light is TM polarized and the signal and idler are TE) could enable phase matching when properly designed. This approach is being explored, but it will have reduced efficiency since the nonlinearity for this orthogonal generation scheme is roughly 2-3 times lower than for the same polarization.

3.1.4 Resonator Sources

Second-Order Nonlinearity

Many of the considerations made above for linear waveguides hold true for resonator-based systems. We will now expand the theoretical basis for SPDC and SFWM for the case of a single ring resonator coupled to a waveguide. Owing to the constructive interference and electromagnetic build-up in an optical cavity, a ring resonator can amplify the nonlinear effect significantly [38]. The enhancement of these nonlinear interactions results in a large improvement to the conversion efficiency, requiring less pump power to generate a comparable photon pair flux.

The treatment of a resonator source follows closely to the linear waveguide case with the inclusion of a few additional terms describing the resonant field enhancement. The full description can be found in References [14, 31], and leads to a very similar relation describing the generated power of one photon of the pair,

$$P_i = \frac{\hbar\omega_{\mu_i}}{\mathcal{T}} \frac{P_p L^2}{\mathcal{P}\mathcal{A}} |F_{\mu_P}(\omega_{\mu_P})|^2 \quad (3.16)$$

where now $L = 2\pi R$ (ring round-trip length), ω_{μ_P} represents the frequency of the resonance mode μ with $k_\mu \cdot R = N$, and

$$F_\mu(\omega) = \frac{i[2(1 - \sigma_m u)]^{1/2}}{(1 - \sigma_\mu) - i(\omega - \omega_\mu)L/\nu_\mu} \quad (3.17)$$

representing the field enhancement factor with σ_μ as the "self-coupling" constant [31]. When the frequency is a resonance frequency, this field enhancement can be expressed in terms of the quality factor of the ring

$$F_\mu(\omega_\mu) = 2i\sqrt{\frac{Q_\mu\nu_\mu}{\omega_\mu L}} \quad (3.18)$$

The generation bandwidth time also changes from Section 3.1.2 to include enhancement of the signal and idler modes,

$$\mathcal{T} = \frac{2\pi}{\int d\omega |F_{\mu_i}(\omega_P/2 - \omega)|^2 |F_{\mu_s}(\omega_P/2 + \omega)|^2} \quad (3.19)$$

Third-Order Nonlinearity

In the same fashion, the power associated with one photon from the pair for a SFWM source can be described by,

$$P_i = \frac{\hbar\omega_{\mu_P}}{\mathcal{T}} (\gamma P_P L)^2 |F_{\mu_P}(\omega_{\mu_P})|^4 \quad (3.20)$$

where we assume that we are looking near to the pump wavelength such that $\nu_{\mu_s} \approx \nu_{\mu_i} \approx \nu_{\mu_P}$ and the field enhancements, frequencies, and nonlinearities are approximately equal. The generation bandwidth time for this system is,

$$\mathcal{T} = \frac{2\pi}{\int d\omega |F_{\mu_p}(\omega_{\mu_P} - \omega)|^2 |F_{\mu_p}(\omega_{\mu_P} + \omega)|^2} \quad (3.21)$$

Utilizing the quality factor in place of the field enhancement factors [14],

$$P_i = \hbar(\gamma P_P)^2 \frac{8V_{\mu P}^4}{\pi^2 \omega_{\mu P}^3} \left(\frac{Q_{\mu P}^3}{R^2} \right) \quad (3.22)$$

which emphasizes the enhancement of the nonlinear process due to the resonator quality factor. The final term is a very important consideration in the design of these systems as it encourages low-loss (high quality factor) resonators with small radii which is typically contradictory. Thus, a balance must be found to maximize the ratio of Q^3/R^2 . This consideration is made during our initial testing of devices for SFWM using AlGaAsOI resonators.

3.1.5 Characterization of an AlGaAsOI Entangled Photon Pair Source

With all of the considerations mentioned in the previous sections (including the ring resonator coupling design in Chapter 2, waveguide phase matching, and optimal dimensions for low loss with high nonlinearity), a set of > 100 Al_{0.2}Ga_{0.8}AsOI microring resonators were designed and fabricated using the UCSB nanofabrication facilities. These devices were screened for the quality factor and ranked based on the ratio of Q^3/R^2 (splits of different coupling designs, waveguide dimensions and ring radii were included to find the ideal source of entangled photon pairs). A subset of 39 microring resonators were selected based on the coupling design (as discussed in Section 2.2.2) which was either close to critically coupled or overcoupled. The maximum quality factor (between 1510nm and 1600nm wavelengths) of these samples is plotted versus the sample number in Figure 3.7. The 29th ring was selected for an in depth study as it had a small radius (13.91 μm) and a large quality factor (1.24 million) for its resonance near 1557 nm. The last four rings tested (rings 36-39) shown on the plot had larger quality factors, but were also

much larger with radii $> 50\mu\text{m}$. The pair generation rate for another resonator, ring 24 is included in Table 3.1. This ring had a lower quality factor of 0.91 million, and the same radius as ring 29. The measured pair generation rate of ring 24 follows the expected behavior accounting for the lower quality factor of this resonator. Overall, the data in Figure 3.7 illustrates a relatively consistent fabrication quality across the 20mm bar that was screened indicating that the fabrication of AlGaAsOI resonators can reliably produce > 1 million Q.

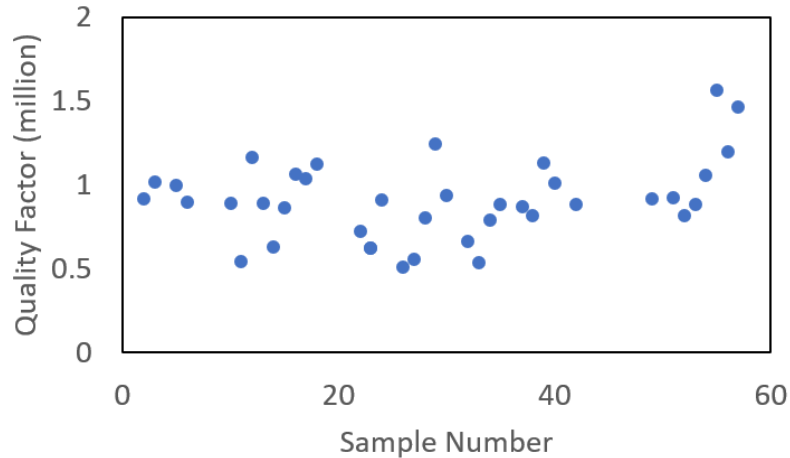


Figure 3.7: The first set of devices used in the quantum experiments with AlGaAsOI were fabricated by Weiqiang Xie in Prof. Bowers group. Here, the quality factor of the devices screened for quantum experiments are shown. This plot lists the maximum quality factor found in a wavelength range from 1510 nm to 1600 nm.

The screening of the devices allowed for the selection of the most promising device to yield a high rate of entangled photon pairs. This device was not only used for this initial work demonstrating an ultra-efficient photon pair source, but was also used for the quantum key distribution demonstration detailed in Chapter 5 and ultimately was the motivation to pursue the AlGaAsOI platform more thoroughly (leading to the development of a photonic component library detailed in Chapter 4). Thus, this thorough, initial assessment of the resonator source forms the foundation for most of this dissertation.

Fabrication of AlGaAsOI microring Resonators

Before beginning the discussion of the efficient, high-quality entangled photon pairs generated from the AlGaAsOI material platform, it is important to briefly discuss how the devices were fabricated. This work began with researchers in Prof. John Bowers group [39–43] and, independently, researchers at the National Institute of Standards and Technology [44, 45] several years ago and has since been adapted, modified and improved by my colleagues Joshua Castro and Lillian Thiel in Prof. John Bowers and Prof. Galan Moody’s groups.

The AlGaAs photonic layer was grown by Molecular-Beam Epitaxy (MBE). Its layer structure from top to substrate is: a [001] orientated 400-nm-thick $\text{Al}_{0.2}\text{Ga}_{0.8}\text{As}$ film on a 500-nm-thick $\text{Al}_{0.8}\text{Ga}_{0.2}\text{As}$ layer on a GaAs substrate. A 5-nm-thick Al_2O_3 film was deposited on the epi-layer by Atomic Layer Deposition (ALD) as an adhesive layer for bonding. The wafer was then bonded on to a 3- μm -thick thermal SiO_2 buffer layer on a Si substrate. The thermal SiO_2 layer was pre-patterned by Inductively Coupled Plasma (ICP) etch. The surfaces of both chips were treated by atmospheric plasma before bonding to activate the surface. After initial contact, the bonded sample was placed in an oven at 100 °C for 12 hours under 1 MPa pressure to enhance the bonding strength.

Initially, the removal of the GaAs substrate was done using mechanical polishing, but now a wet chemical etch approach is employed. This chemical removal of the GaAs substrate was performed in three steps. First, mechanical polishing was applied to lap the GaAs substrate down to $\sim 70 \mu\text{m}$. Then the remaining substrate was removed by $\text{H}_2\text{O}_2:\text{NH}_4\text{OH}$ (30:1) wet etch. Finally, the $\text{Al}_{0.8}\text{Ga}_{0.2}\text{As}$ buffer layer was selectively etched by diluted hydrofluoric ($\sim 2.5\%$) acid, leaving only the $\text{Al}_{0.2}\text{Ga}_{0.8}\text{As}$ photonic layer on the carrier wafer.

After substrate removal, a 5-nm ALD Al_2O_3 layer was deposited on $\text{Al}_{0.2}\text{Ga}_{0.8}\text{As}$ for surface passivation, followed by a 100-nm SiO_2 layer deposition as a hardmask. The wafer was then patterned by a deep ultraviolet (DUV) stepper using a photoresist (UV6-0.8). Prior to the photoresist coating, an anti-reflective (AR) coating (DUV-42P) was used to suppress the backreflection during photolithography. After exposure and development of the resist, a thermal reflow process was applied to the wafer at 155 °C on a hotplate for 2 minutes. ICP etches using O_2 and $\text{CHF}_3/\text{CF}_4/\text{O}_2$ gases were used to remove the AR coating and define the hardmask, respectively, followed by another ICP etch using Cl_2/N_2 gases to pattern the $\text{Al}_{0.2}\text{Ga}_{0.8}\text{As}$ layer. After the etch, the sample was passivated by 5-nm Al_2O_3 layer by ALD and finally clad with 1.5- μm thick SiO_2 by PECVD. For thermal tuners, an additional metal lift-off step is added to define the heating elements. A photoresist is patterned to define the electrodes, and 100 nm thick titanium is deposited followed by 10 nm of platinum. The titanium layer promotes adhesion to the top cladding.

After the metal lift-off, the wafer is singulated using either dicing and polishing or facet etching and dicing. Initial fabrication runs were completed via dicing and polishing, where a mechanical dicing saw was used to separate the individual bars. Since the blade left a rough facet, an additional polishing step was completed to smooth the facets and reduce the input/output coupling loss. Although this process resulted in relatively low facet loss, the dicing blade occasionally chipped the edge of the bar, resulting in reduced yield and inconsistent coupling loss. To address this challenge, an etched facet process was developed. When the wafer is ready for singulation, a thick SPR220-7.0 photoresist is spun and developed, leaving only the region between bars exposed. A CHF_3 etch removes the 1 μm top cladding, 400 nm thick AlGaAs waveguide layer, and the 3 μm bottom cladding to define a smooth facet. The etched region width is selected to leave 5-10 μm of gap on both sides of a ~ 50 μm dicing channel (the width of the dicing saw). After removing the photoresist, the bars are diced. Since the dicing blade does not come

in contact with the facet, the roughness is only defined by the etch (which is improved compared to the polished facet roughness). The transition from dicing and polishing to etching and dicing has shown significant improvement in the facet uniformity and yield. Another benefit of the etched facet process is that the input/output couplers no longer require a buffer region since the dicing channel is defined lithographically.

Two key innovations in the fabrication process have enabled low loss waveguides and microring resonators. First, a thin layer of Al_2O_3 following the etch steps (substrate removal and waveguide etch). Second, the photoresist used for the DUV photolithography goes through a thermal reflow process. The thin alumina layer has been shown to passivate the surface defect states caused by the aggressive etch [46]. These defect states form mid-bandgap states that can absorb the light and cause excess loss in the waveguide. The photoresist reflow process significantly improves the sidewall roughness, therefore reducing the scattering loss [42, 47]. The combination of these two improvements has enabled up to 3 million quality factor resonators and losses < 0.2 dB/cm [42].

Brightness and On-Chip Generation Rate

As emphasized at the beginning of this chapter, one of the most important metrics of an entangled photon pair source is the brightness. If a photon pair source cannot reliably produce a high rate of pairs, it has limited utility (not to mention characterizing such a source would prove quite challenging). Thus, the first characterization of a photon pair source is to measure the photon pair brightness and coincidence rate. Ring 29 was selected for this thorough testing, and Figure 3.8a) illustrates the process of SFWM that generates a signal and idler photon pair. This process only occurs at the resonances of the microring resonator in which quasi-phase matching between the pump, signal, and idler is attained. A demonstrative microscope image of a $30\ \mu\text{m}$ -radius AlGaAsOI microring resonator and pulley waveguide is shown in Figure 3.8b. The microring resonator studied

in the following experiment had a radius of $13.91 \mu\text{m}$. The width of the bus waveguide was $0.48 \mu\text{m}$, and the ring waveguide was $0.69 \mu\text{m}$ wide. The gap between the waveguide and the ring was $0.48 \mu\text{m}$, and the AlGaAs layer was $0.4 \mu\text{m}$ thick. The transmission spectrum of the ring resonator is shown in Figure 3.8c). The sharp dips indicate resonance wavelengths of the microring resonator separated by the free spectral range (FSR). A high-resolution sweep of the pump comb line is shown by the blue trace in Figure 3.8d. The resonance is fit with a Lorentzian function to determine the quality factor Q of the cavity, which is proportional to the ratio of the full-width at half-maximum (FWHM) of the transmission resonance to the FSR. In comparison to other microring resonators utilized for entangled-pair generation, the $Q = 1.24 \times 10^6$ measured for this device is a factor of 100 larger than InP, a factor of ~ 10 larger than AlN and silicon-on-insulator (SOI), and is comparable to Si_3N_4 , as shown in Table 3.1.

By pumping the resonator at one of these resonance wavelengths, entangled-photon pairs are generated spontaneously at adjacent resonances through SFWM. In the experiments presented here, and shown by the dashed box in Figure 3.8c, the pump wavelength is set to be resonant with 1557.59 nm , as this resonance peak had the highest quality factor for the selected ring. As we have shown in Section 3.1.4, the SFWM process is proportional to Q^3/R^2 and should show a quadratic power dependence. In our experiments, the second nearest neighbor resonances highlighted in blue and orange in Figure 3.8c are selected as the signal and idler photons, since this provided additional pump rejection through the bandpass optical filters before the single-photon detectors. Using measured and calculated properties of our AlGaAsOI microresonators, we expected a $PGR = 10^{10}$ pairs $\text{sec}^{-1} \text{ mW}^{-2}$.

The experimental setup is depicted in Figure 3.9. For the measurement of the singles and coincidence counts, the interferometer shown in Figure 3.9 (the short and long arm with the piezo-electric phase shifter) is bypassed. Other than this change for the singles

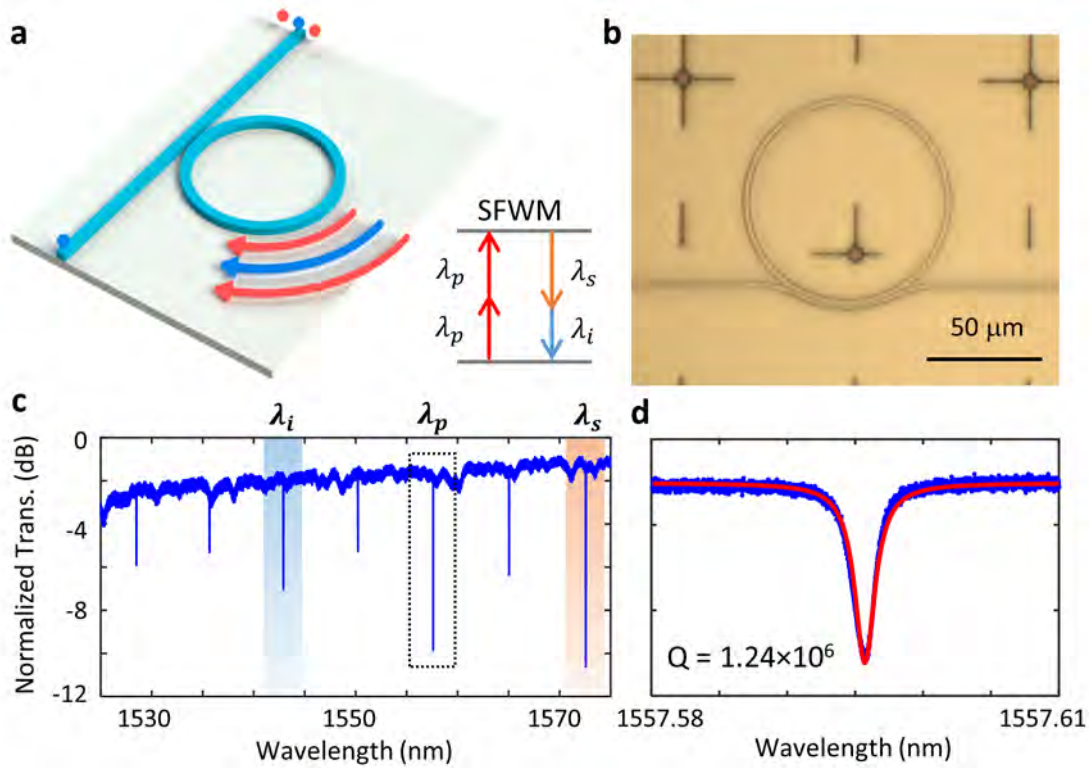


Figure 3.8: a) Schematic illustration of entangled-photon pair generation from a photonic microring resonator. Pump photons (λ_p) are coupled into the waveguide bus and ring and are converted into signal (λ_s) and idler (λ_i) photons via spontaneous four-wave mixing (SFWM). b) Optical microscope image of a representative AlGaAs-OI ring resonator pulley with $30\ \mu\text{m}$ radius. c) Resonator transmission spectrum with signal ($1572\ \text{nm}$) and idler ($1542\ \text{nm}$) wavelengths two free-spectral ranges away from the pump ($1557\ \text{nm}$) resonance. d) Resonator transmission spectrum of the pump resonance (blue-trace). A $Q = 1.24 \times 10^6$ is determined from the superimposed Lorentzian fit (red-trace).

and coincidence measurements, the rest of the experimental design remains consistent. A continuous-wave Koshin Kogaku LS601A (recent measurements have been completed using a Toptica CTL 1550 laser) precision tunable laser source was stepped from approximately $0.1\ \text{nm}$ below the resonance wavelength of the microring resonator to the resonance wavelength. The laser sweep starts below the actual resonance wavelength because the ring resonance red-shifts due to local heating of the resonator as the wavelength approaches the resonance and more pump power is coupled into the resonator. The laser

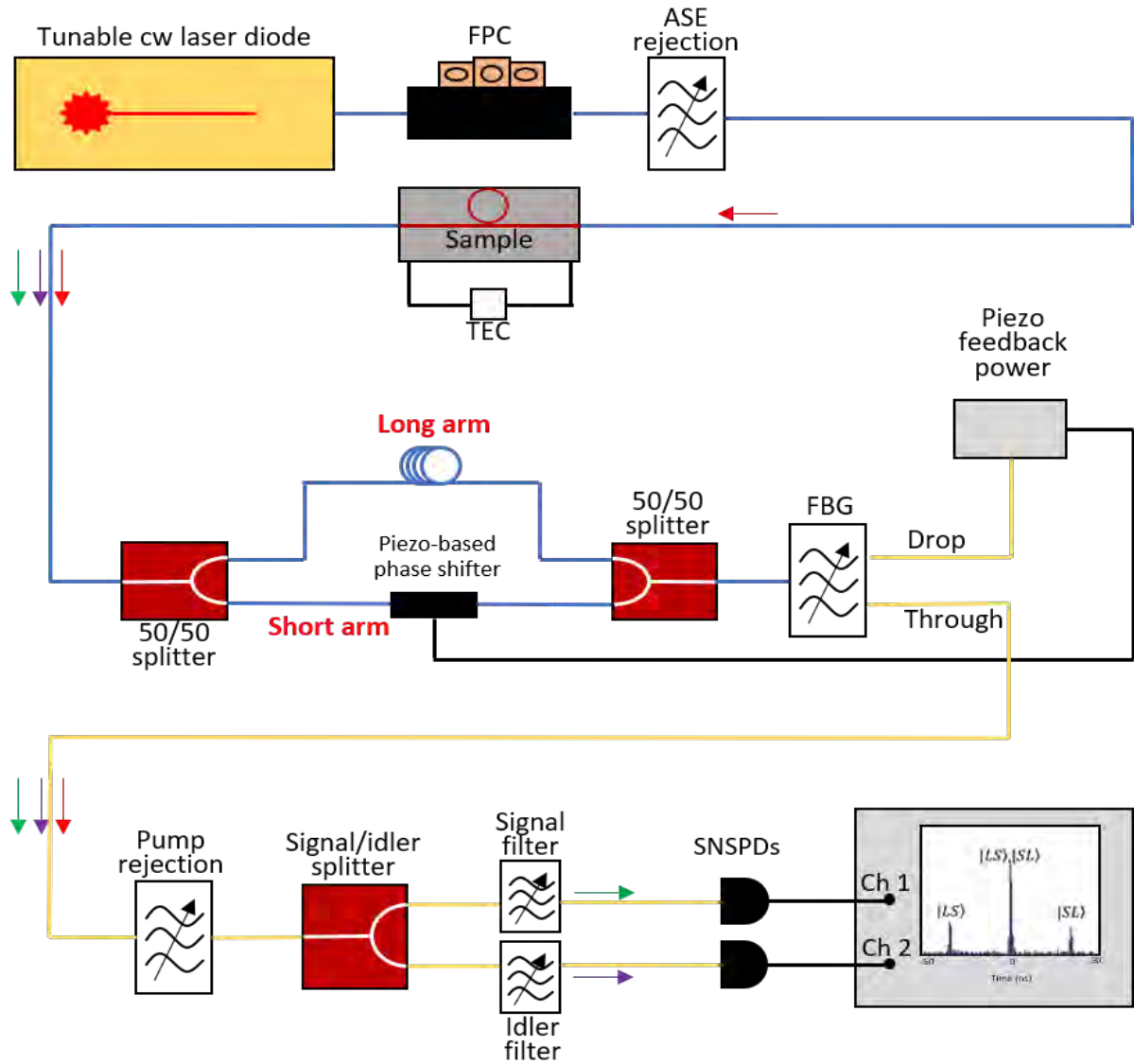


Figure 3.9: Schematic of the experimental setup for a fiber-based folded Franson-type interferometer. The tunable CW laser diode is swept and held at the resonance wavelength of the microring resonator. The laser is sent through ASE rejection filters and coupled via lensed fiber onto and off of the photonic chip. The light is split into a short and long arm of an interferometer. A piezo-based phase shifter is used to modify the phase of the photons that travel through the long arm. The pump photons are removed via an FBG and filters on the signal and idler channels. The signal and idler channels are coupled to SNSPDs to determine the count rates.

was set to its maximum output power of 2.0 dBm (15.8 mW) and sent through a variable optical attenuator (VOA) to allow for adjustment of the input power into the chip.

Etalon-based tunable fiber optic filters were placed after the VOA to provide sideband filtering of the laser to minimize the amplified spontaneous emission (ASE) overlapping with the generated signal and idler modes. After the filters, a 99/1 fiber-based splitter was used to monitor the input power onto the chip. A lensed fiber with a spot size of $2.5\mu\text{m}$ was used to couple the light onto and off of the photonic chip. The coupling loss was approximately 5 dB per facet and was documented for each experiment. The lensed fiber was oriented such that the incoming light was in the transverse electric mode. The temperature of the chip was maintained using a thermo-electric cooler that was set to 20°C . A fiber Bragg grating (FBG) was used after the chip for pump rejection with the drop channel used to monitor the power output from the chip during the experiment. The remaining light from the FBG was split using a 3 dB fiber-based beamsplitter and sent to the signal and idler filter channels. An array of four etalon-based tunable fiber optical filters were used for a total pump suppression of over 150 dB. The singles counts were monitored using superconducting nanowire single photon detectors (SNSPDs) from PhotonSpot operating at 0.77 K. Using a time-correlated single-photon counting (TCSPC) module, the signal and idler counts were recorded for 10 minutes and averaged. The scan was started with the laser set to a slightly off-resonance wavelength to determine the background counts on the detectors (from both the dark counts of the system and any pump photons that reach the detector). An example scan is included in Section A1.

After collecting the raw count data from the TCSPC module, the count rates were corrected to account for the filter losses present in each channel as well as the background counts present before the laser reached the resonance wavelength. The background counts were taken as the one minute average of the counts on each detector before the laser sweep began. To assess the loss at each filter, the laser was set to the wavelength of the signal (idler) and each of the filters on the signal (idler) channel was assessed for the loss at

that wavelength. In our initial experiments, the total loss from all of the filtering and the 3 dB beamsplitters was 19.4 dB for the idler channel and 13.6 dB for the signal channel (in addition to the ~ 5 dB facet loss). This variation is due to the different losses in the etalon-based filters. The singles counts of both the signal and the idler are fitted on a quadratic scale as shown in the main text. We note that since these experiments, system losses have been further reduced to typically < 10 dB for each channel through improved DWDM filtering.

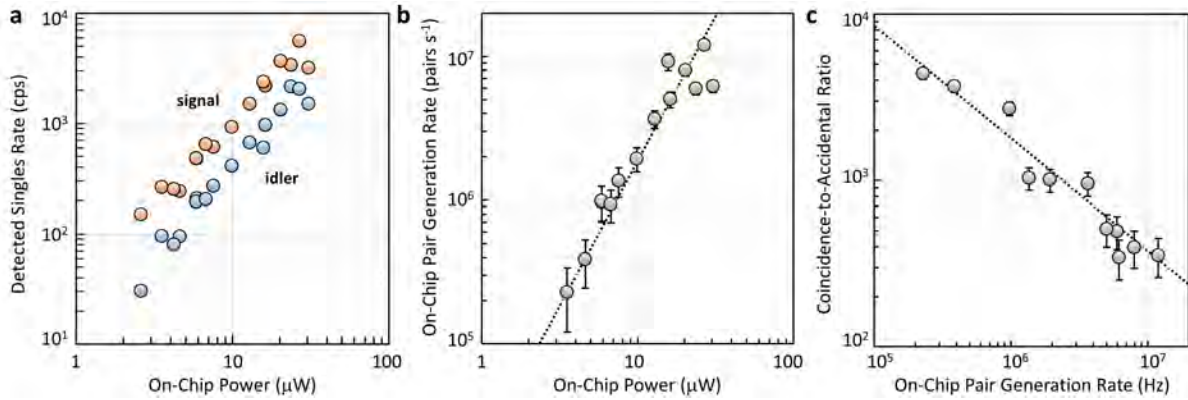


Figure 3.10: (a) Corrected detected singles rates versus on-chip pump power. The difference in the generated singles rates is due to the difference in the filter loss in the two channels (19.4 dB for the idler and 13.6 dB for the signal). (b) On-chip pair generation rate versus on-chip pump power. The dashed line is a fit to the data, yielding a pair generation rate of 20×10^9 pairs $\text{sec}^{-1} \text{mW}^{-2}$ (c) Coincidence-to-accidental ratio (CAR) versus on-chip pair generation rate.

We next measure the coincidence counts by recording two-photon correlation histograms using a TCSPC. The TCSPC module was set to trigger when a photon arrived on the signal channel and measure the difference in arrival time on the idler channel. The data was collected with integration times between 10 and 180 minutes dependent on the on-chip power. Larger integration times were required for lower optical powers as the coincidence-to-accidental calculation requires nonzero accidental counts. Contributors to the accidental counts include lost pairs, dark counts, and excess pump photons. Since almost zero pump photons reach the detectors at low input powers, the accidental counts

are very low and require long integration times. From these measurements, the on-chip PGR is determined by dividing the time-averaged value of the measured coincidence counts, N_c , by the total loss from chip to the SNSPDs. These quantities were measured by separate calibration procedures. The on-chip PGR for various on-chip pump powers is shown in Figure 3.10b. Unlike InP and silicon-based microresonators, we do not observe any saturation of the curve due to two-photon absorption (TPA) as expected, since the AlGaAs bandgap wavelength is shorter than 775 nm. The black dashed line fitted to the data illustrates the P_p^2 behavior as expected. From this fit we determine a slope of 20×10^9 pairs $\text{sec}^{-1} \text{mW}^{-2}$. To the best of our knowledge, this value is over 100-times higher than any previously reported PGR from a ring resonator or spiral-based SFWM source to date, as shown in Table 3.1. By normalizing the PGR to the FWHM of the emission resonance (~ 1 pm), we obtained the entangled-pair brightness $B = 2 \times 10^{11}$ pairs $\text{sec}^{-1} \text{GHz}^{-1}$ (normalized to 1 mW on-chip power), which is more than a 500-fold improvement upon previous state-of-the-art microresonators based on Si_3N_4 [19] and more than 1000-times brighter than SOI [18].

CAR

Another important metric of entangled-photon pair sources is the coincidence-to-accidentals ratio (CAR). An example histogram utilized to determine the CAR is shown in the Appendix (Figure A2). The CAR versus the PGR is shown in Figure 3.10c. The CAR is calculated as the FWHM of the signal-idler coincidence histogram measured as a function of the inter-channel delay divided by the background counts across a similar time window away from the coincidence peak. The highest CAR we measure is 4389 when the PGR is 2.3×10^5 pairs sec^{-1} . At the highest PGR measured here (12×10^6 pairs sec^{-1}), the CAR is equal to 353. The CAR decreases with increasing pump power as P_p^{-1} as expected and shown by the dashed line in Figure 3.10c. We were not able to

measure higher CAR at lower on-chip pump power, since the majority of the histogram time bins had zero registered background counts from our SNSPDs at these powers even for integration times up to 1.5 hours. For comparison, CAR values for an on-chip $PGR = 10^6$ pairs sec^{-1} are shown in Table 1 for various photonic entangled-pair sources. Our reported value is a factor of 4 larger than the next highest reported value at this PGR (LiNbO₃ periodically poled waveguide).

Single Photon Purity

Heralded $g_H^{(2)}$ measurements are performed via three-fold coincidence detection with a third detector. The signal photons are sent to one SNSPD as the herald. The idler photons are sent into a 3 dB fiber beam splitter with the outputs connected to the other SNSPD and a single-photon avalanche diode (SPAD). Using the TCSPC module, we record singles counts from the heralding detector (N_A), coincidence counts between the heralding detector and each of idler detectors (N_{AB} and N_{AC}), and the three-fold coincidence counts N_{ABC} . A coincidence window of 1 ns is used as determined from the two-fold coincidence histogram width. The timing between the channels was calibrated with separate coincidence measurements and the delays adjusted accordingly. The three-fold coincidences between the channels are recorded for > 100 seconds, and the heralded g^2 is calculated through $g_h^2 = \frac{N_{ABC}N_A}{N_{AB}N_{AC}}$. Since the nonlinear process generates a single signal and idler photon pair (in the low power regime), a dip at zero time delay appears where there are very few threefold coincidence events. The magnitude of this dip relative to the background counts characterizes the single photon purity. Figure 3.11 illustrates a measurement of 95% single photon purity for an on-chip power of 108 μW . At lower powers, heralded single photon purities exceed 99%.

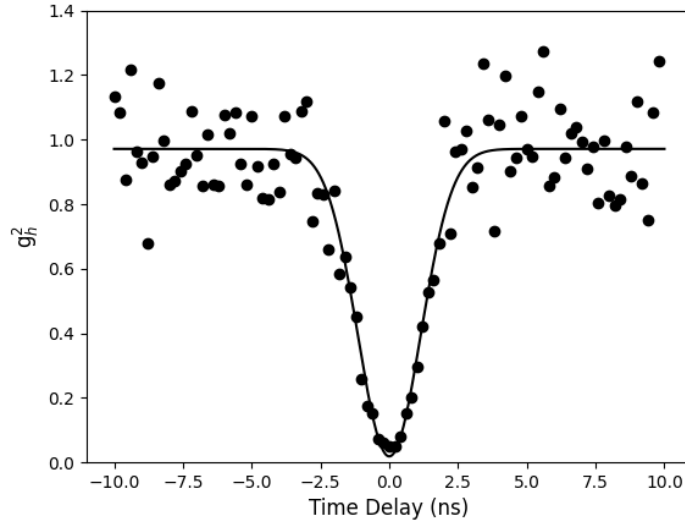


Figure 3.11: Example trace of the heralded g^2 for the second adjacent resonance with an on-chip power of $108 \mu\text{W}$. The dip at zero time delay illustrates $>95\%$ single photon purity.

Indistinguishability

The generated signal-idler pair is expected to exhibit time-energy entanglement [48, 49], which can be measured through a Franson-type two-photon interference experiment as depicted in Figure 3.12a [22, 50]. Signal and idler photons travel through the unbalanced Mach-Zehnder interferometer and then are separated by a 3 dB splitter and bandpass filters before arriving at the SNSPDs. The interferometer path length difference is set such that the propagation delay $\Delta t = 40 \text{ ns}$ is longer than the single-photon coherence time $\tau_c \approx 1 \text{ ns}$ in order to avoid single-photon interference at the detectors, but shorter than the laser coherence time τ_L . In this case, the signal and idler photons can travel along either the short [S] or long [L] paths, allowing a total of four possible permutations.

The differences in photon arrival times between the two paths are illustrated in Figure 3.12b. We can express the two-photon state as a summation over $|ij\rangle$, where the i (j)

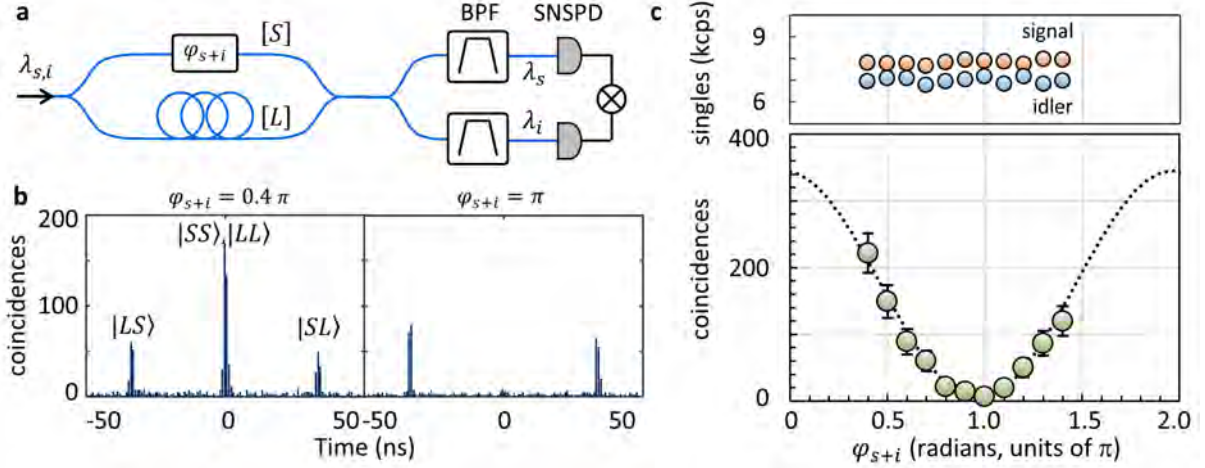


Figure 3.12: (a) Schematic illustration of the setup for the two-photon interference experiment using a fiber-based folded Franson interferometer. BPF = bandpass filter; [S] ([L]) denotes the short (long) interferometer path; SNSPD = superconducting nanowire single-photon detector. (b) Coincidence histograms for different interferometric phase $\phi_{s+i} = 0.4\pi$ and π , respectively. (c) Singles counts (top) measured with the interferometer setup simultaneously with the two-photon interference (bottom). Visibility of the raw (fitted) data yields 95% (97.1%).

index is the path the signal (idler) photon travels, with $i, j = [S, L]$; however, post-selection allows for the different states to be distinguished. The side peaks arise from photons travelling along the $|LS\rangle$ or $|SL\rangle$ paths and are offset from zero delay by Δt . The central peak at zero delay is due to both photons taking the same paths, $|SS\rangle$ or $|LL\rangle$. Because these states are indistinguishable, the two-photon state is expressed as $\frac{1}{\sqrt{2}}(|SS\rangle + \exp(i\phi_{i+s})|LL\rangle)$. By inserting a voltage-controlled fiber phase shifter into the short path and sweeping the phase, two-photon interference is observed as shown in Figure 3.12b for two different phases $\phi_{s+i} = 0.4\pi$ and π . The coincidence counts versus phase is shown in the bottom panel of Figure 3.12c. Proof of photon entanglement requires the Clauser-Horne interference pattern visibility $V \geq 70.7\%$ [51, 52]. Calculated from the raw data (fitted data), we obtain $V = 95\%$ ($V = 97.1\%$), measured when the on-chip PGR was approximately 1×10^6 pairs sec^{-1} . For on-chip powers of $\sim 5 \mu W$ (PGR of $\sim 4 \times 10^5$ pairs sec^{-1}) and $\sim 15 \mu W$ (PGR of $\sim 4 \times 10^6$ pairs sec^{-1}) we measure raw

visibilities of 96% and 94%, respectively. We expect the visibility may further increase with a reduction in pump power, but the goal was to demonstrate the maximum visibility and the highest pump powers (*e.g.* pair generation rate) as possible. In this case, we did not examine higher pump powers in order to avoid reaching the lasing threshold of the microresonator, which would result in uncorrelated background counts that would reduce the entanglement visibility. These measurements confirm the high quality of the time-energy entangled-pair source, as illustrated by the variation of the two-photon coincidences and the constant signal and idler singles rates versus applied phase shift indicating the absence of single-photon interference.

3.1.6 Ultra-Bright Entangled Photon Pair Generation

Platform	Type	Q	PGR [GHz]	Brightness [pairs s ⁻¹ GHz ⁻¹]	CAR	Visibility	$g_H^{(2)}$	Ref.
AlGaAsOI	SFWM	1.2×10^6	20	2×10^{11}	2697 ± 260	$97.1 \pm 0.6\%$	0.004 ± 0.01	[12]
AlGaAsOI	SFWM	0.91×10^6	2.65	2.65×10^{10}	-	-	-	[12]
SOI	SFWM	$\sim 10^5$	0.149	7.1×10^7	532 ± 35	$98.9 \pm 0.6\%$	0.0053 ± 0.021	[18]
InP	SFWM	4×10^4	0.145	3.1×10^7	277	$78.4 \pm 2\%$	-	[20]
Si ₃ N ₄	SFWM	2×10^6	0.004	4.3×10^8	~ 10	$90 \pm 7\%$	-	[19]
LiNbO ₃	SPDC	1.0×10^5	2.7	2.7×10^9	> 100	-	0.097	[53]
AlN	SPDC	1.1×10^5	0.006	5.3×10^6	-	-	0.088 ± 0.004	[54]
InGaP	SPDC	1.1×10^5	27.5	2.7×10^{10}	~ 80	-	-	[55]

Table 3.1: All values are reported for microring resonators. The CAR, visibility, and $g_H^{(2)}(0)$ are shown for 1 MHz PGR. Brightness and PGR shown are normalized to 1 mW on-chip pump power. Data from this dissertation is highlighted in red.

Strategies to improve on-chip entangled-photon pair generation have typically focused on improving the quality factor of microcavities while simultaneously reducing the cavity length. Exploring new material platforms with higher nonlinear coefficients has been limited by the attainable quality factor of these materials. By leveraging our recent advances in compound semiconductor nanofabrication [42], we achieve ultralow waveguide loss (< 0.4 dB/cm) and high microring resonator quality factor ($Q > 1$ million). The high Q and large third-order nonlinearity of AlGaAs lead to more than a 500-fold improve-

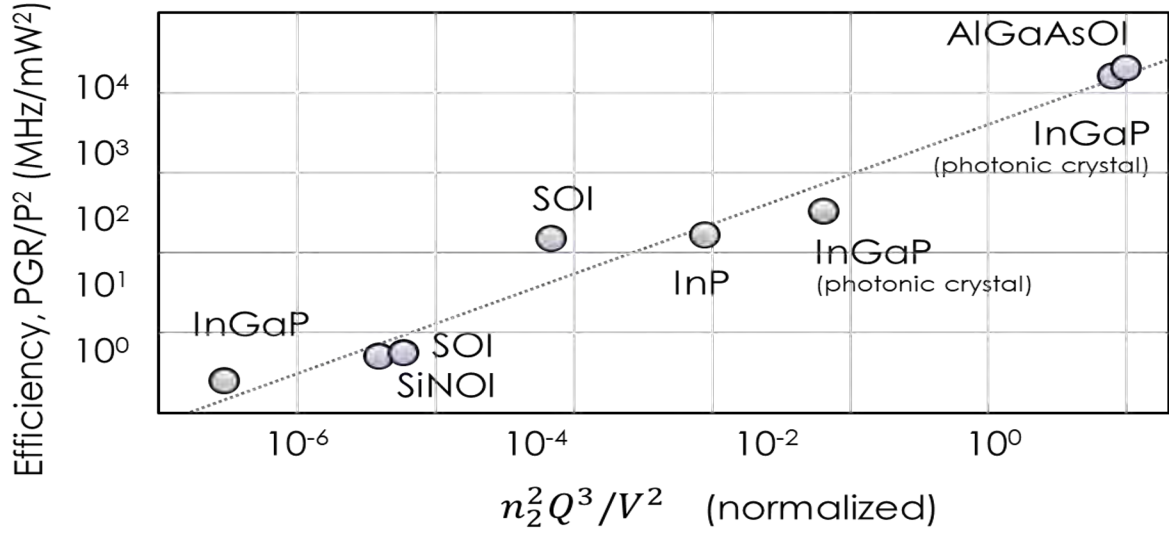


Figure 3.13: Entangled photon pair brightness for various material platforms, illustrating the performance of the AlGaAsOI material platform.

ment of the on-chip pair brightness compared to all other waveguide and resonator-based photonic platforms as shown in Figure 3.13. Recent advances in the creation of InGaP photonic crystal cavities have shown comparable photon pair brightness [56]. The nonlinearity of InGaP is comparable to AlGaAs, and through the creation of high confinement crystal cavities, the mode volume can be significantly reduced (while maintaining moderate to high Qs). The effective nonlinearity of these cavities is therefore similar to the AlGaAsOI resonators discussed in this chapter. For our entangled photon pair source, the photon quality also remains exceptional with a Bell-state violation measurement revealing a $97.1 \pm 0.6\%$ visibility, coincidence-to-accidental ratio of more than 4350 limited by the loss in our optical setup, and a heralded single-photon $g_H^{(2)}(0) = 0.004 \pm 0.01$. Collectively, these values yield an ultra-high quality entangled- and heralded-photon source that surpasses sources from all other integrated photonic platforms, as shown in Table 3.1.

3.2 Squeezed Light Sources

To this point, the focus has been on generating entangled photon pairs using the optical nonlinearity of semiconductor materials like InGaP and AlGaAs. Simulations and modeling of SPDC and SFWM have enabled designs of optical microresonators, and initial results from SFWM show 1000-fold improvement in the entangled photon pair brightness compared to SOI state-of-the-art sources. Another useful quantum state of light is squeezed light, a continuous-variable analog to the discrete variable photon pair generation. Whereas entangled photon pairs are used to generate single quanta, squeezed light refers to light that has a reduced uncertainty in one of the field quadratures relative to the Standard Quantum Limit (SQL). The utilization of squeezed light has already been shown to enhance the sensitivity of gravitational wave detectors in advanced LIGO [57]. Other applications of squeezed light include quantum-optical state engineering and continuous-variable quantum information and computing. For example, an arbitrary superposition of the zero-, one-, and two-photon states can be created utilizing the creation of a two-mode squeezed vacuum to generate heralded single photons [58–60]. Companies like Xanadu have also demonstrated the promise of squeezed light for photonic quantum computing [61]. Since squeezed states of light can be generated using the same nonlinear materials used for photon pair generation, it is desirable to explore the generation of squeezed states of light using the platforms we have established for record-high entangled photon pair generation from.

Heisenberg’s uncertainty principle imposes a lower limit on the achievable uncertainty associated with two observables,

$$\sqrt{\langle \Delta \hat{A}^2 \rangle \langle \Delta \hat{B}^2 \rangle} \geq \frac{1}{2} |[\hat{A}, \hat{B}]| \quad (3.23)$$

where $[\hat{A}, \hat{B}]$ indicates the commutator of the observables \hat{A} and \hat{B} .

When discussing the uncertainty of measuring specific observables of a light source, it is useful to start with a general quantum mechanical description of the electromagnetic field. A particular mode of the electrical field can be described by the oscillation of the two electric field quadratures, \hat{Q}_1 and \hat{P}_1 .

$$E = E_0(\hat{Q}_1 \cos \omega t + \hat{P}_1 \sin \omega t) \quad (3.24)$$

where E_0 indicates the electric field amplitude and ω is the frequency. The variance in the field quadrature operators for a minimum-uncertainty state obeys the Heisenberg uncertainty principle with,

$$\Delta \hat{Q}_1 \Delta \hat{P}_1 = 1/4 \quad (3.25)$$

For coherent states of light (such as a single-mode laser source), the variance on each quadrature is equal. This can be visualized as done in Figure 3.14. When the variance is equal ($\Delta Q = \Delta P$), the state can be seen as a perfect circle in $Q - P$ space, assuming the coherent source is in a minimum-uncertainty state. Minimum-uncertainty squeezed states of light, on the other hand, do not have an equal distribution of uncertainty across each of the quadratures. Instead, one of the variances is reduced—thus, implying that the other variance is increased in order to preserve Heisenberg’s uncertainty principle (Equation 3.25). This can be visualized as the circle shown in Figure 3.14 transforming into an ellipse with a major and minor axis corresponding to the anti-squeezed and squeezed quadratures, respectively.

The generation of such minimum-uncertainty squeezed states follows much of the same formulation as the generation of entangled photon pairs, but here the pump power is no longer in the low power regime. In fact, for the case of resonators, the pump power is near

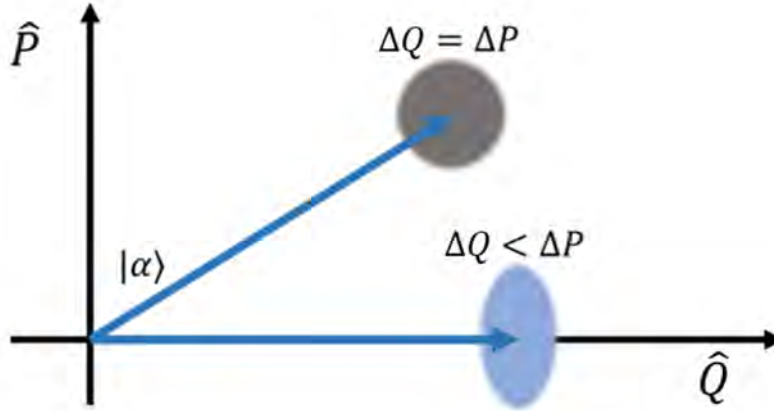


Figure 3.14: Illustration of the uncertainty distribution for a coherent state $\Delta Q = \Delta P$ and a squeezed state $\Delta Q < \Delta P$ of light. The grey circle and blue ellipse illustrate the uncertainty of the particular state.

the optical parametric oscillator (OPO) threshold to maximize squeezing. For simplicity, we can look at the case of squeezed light generated via the $\chi^{(2)}$ nonlinearity (parametric down conversion). For a $\chi^{(2)}$ OPO with threshold P_{thres} , the squeezed vacuum noise (V^-) and anti-squeezed noise (V^+) is [62],

$$V^\pm(\Omega) = 1 \mp \eta_d \eta_c \frac{4\sqrt{P/P_{thres}}}{(1 \pm \sqrt{P/P_{thres}})^2 + \Omega^2/\gamma^2} \quad (3.26)$$

η_c is the coupling efficiency of the resonator at 1550nm, η_d is the overall coefficient of loss until detection, including propagation loss, facet loss, homodyne overlap, and quantum efficiency of the detector, P/P_{thres} is the normalized pump power, and Ω/γ is the measurement frequency normalized by cavity linewidth.

The threshold power for this system can be expressed using the intrinsic quality factors ($Q_{p,i,s}$) and coupling quality factor of the pump ($Q_{p,1}$) with,

$$P_{thres} = \frac{\hbar\omega_s\omega_i\omega_p^2}{64g^2} \frac{Q_{p,1}}{Q_s Q_i Q_p^2} \quad (3.27)$$

where g is the nonlinear mode coupling coefficient between the mode pumped at ω_2 and the downconverted light near ω_1 such that $\omega_2 \approx 2\omega_1$ [55, 63] and is given by

$$g = \sqrt{\frac{\hbar\omega_1^2\omega_2}{8\epsilon_0\tilde{\epsilon}_1^2\tilde{\epsilon}_2}} \frac{\chi_{ijk}^{(2)}\zeta_{ijk}}{\sqrt{V_{eff}}}. \quad (3.28)$$

Here, ζ_{ijk} represents the mode overlap factor, and V_{eff} is the effective mode volume $V_{eff} = (V_1^2 V_2)^{1/3}$.

It can be seen that a large coupling rate, g , and a high quality factor resonator enables low-threshold pump power and thus squeezing at low pump power. The coupling rate is dependent on the nonlinearity of the material, and the modal overlap factor allows for waveguide engineering to maximize the overlap. The squeezed vacuum noise, Equation 3.26, for an InGaP parametric down conversion source with a $5\mu\text{m}$ radius, with 97.5% escape efficiency from the resonator, and loaded quality factor for the pump $Q_{775\text{nm}}=700,000$ is shown in Figure 3.15 as a function of the pump power at 775nm and intrinsic quality factor of the generated photon pairs at 1550nm wavelength. The maximum squeezing occurs when the pump power reaches threshold, and the limit on the squeezing is from the escape efficiency of the resonator ($\sim 97.5\%$ which is -16 dB). In the system shown in Figure 3.14 using Equation 3.26, the collection efficiency is assumed to be unity. System loss (including propagation loss, detection efficiency, coupling efficiency, and detector quantum efficiency), will degrade the magnitude of squeezing that can be detected, thus motivating fully integrated systems or systems with ultra-low loss components. This trend is illustrated in Figure 3.16 for a SFWM squeezed light source, but follows for a SPDC source.

Squeezed light can also be generated from a SFWM photon pair source using the

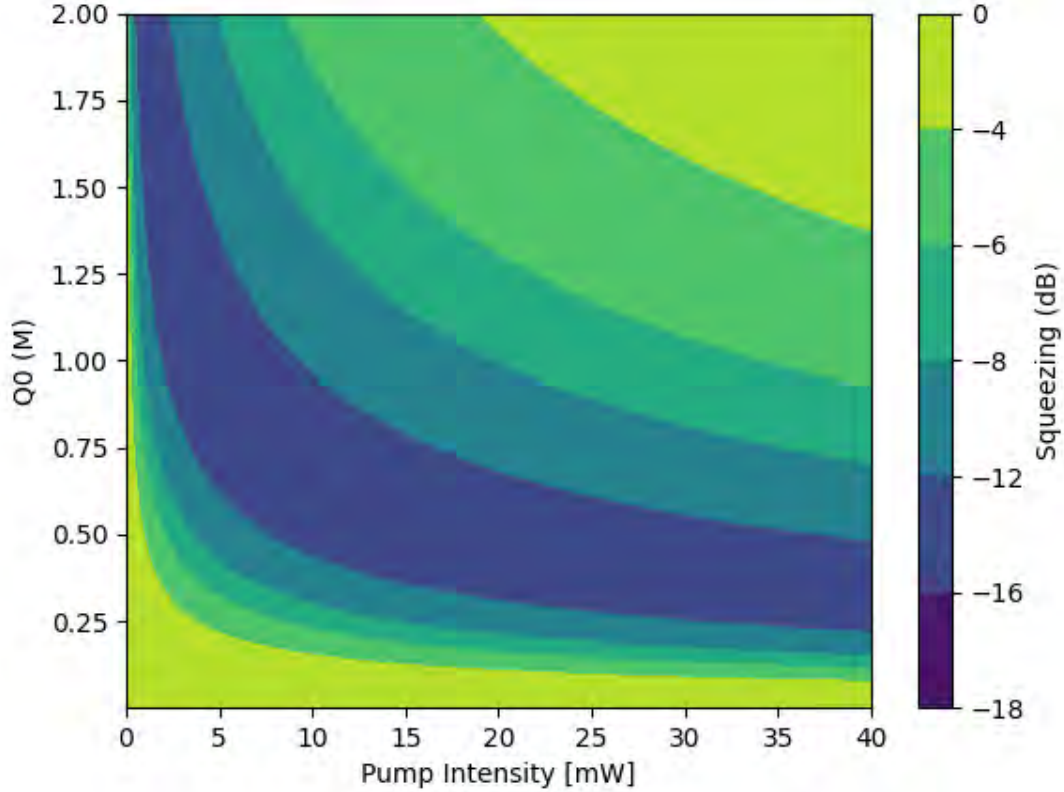


Figure 3.15: Squeezed light generated from an InGaP ring resonator source using the second-order nonlinear interaction when pumped at 775nm and light is generated at 1550nm. The plot shows the squeezing output as a function of the intrinsic quality factor of the 1550nm light and the pump power at 775nm. The source is an InGaP resonator with a $5\mu\text{m}$ radius, with 97.5% escape efficiency from the resonator, and loaded quality factor for the pump $Q_{775\text{nm}}=700,000$

third-order nonlinearity. The vacuum noise variance for such a source can be modeled as [64],

$$V^{\pm} = 1 + 4\eta g(2g \mp \sqrt{1 + 4g^2}) \quad (3.29)$$

where η is the net collection efficiency (now including the resonator escape efficiency), and $g = \Lambda |\bar{\beta}_P|^2 / \bar{\Gamma}$ with $\bar{\Gamma} \approx \omega / (2Q)$ dissipation rate of the signal and idler modes, $\bar{\beta}_P$ as the classical pump mode amplitude, and $\Lambda \approx \hbar \bar{\omega} \nu_g^2 \gamma_{NL} / L$. Again, from the form of 3.29, it can be seen that materials with large nonlinearities and high quality factors approach

the maximum squeezing level at lower pump powers. As an example, Figure 3.16 shows a $14\ \mu\text{m}$ AlGaAsOI microring resonator source of SFWM squeezed light. The squeezed variance is plotted for different overall system efficiencies assuming a quality factor of $Q = 500,000$ and a nonlinear coefficient $\gamma_{NL} = 300\ \text{W}^{-1}\text{m}^{-1}$.

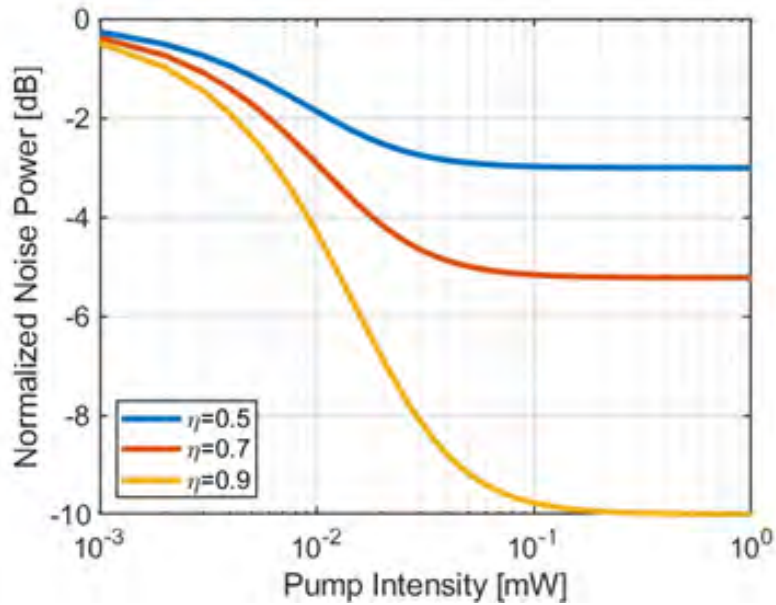


Figure 3.16: Squeezed quadrature variance as a function of the pump power for different system efficiencies. The source is an AlGaAsOI microring resonator with $14\ \mu\text{m}$ radius, $Q = 500,000$, and $\gamma_{NL} = 300\ \text{W}^{-1}\text{m}^{-1}$.

It is important to note that the magnitude of squeezed light generated from nonlinear interactions is generally not material-limited. In other words, if a squeezed light source with 16 dB noise reduction is desired, it is generally possible to use any nonlinear material platform and either SFWM or SPDC to achieve this objective (albeit with much higher pump threshold power for weaker nonlinearity and mode overlap). Instead, the overall system efficiency is what limits the maximum squeezing output (illustrated in Figure 3.16). Thus, advancements in the magnitude of squeezing have been focused on minimizing these system losses (instead of maximizing the nonlinear interactions). One such breakthrough is the creation of coupled resonator photonic molecules which result in split

resonances that remove parasitic nonlinear effects [65]. This design has demonstrated the record on-chip squeezing with 8 dB squeezing inferred on the chip for continuous-wave pumping. Photonic molecules similar to this structure have been designed on the AlGaAsOI and InGaPOI material platforms, though no experimental characterization of these devices has yet been completed at this time.

3.3 Conclusion and Outlook

Overall, the advantages of III-V semiconductor materials for quantum light source development are clear. The enhanced optical nonlinearity and recent improvements to fabrication enable low-loss, high Q resonators to be developed for both SFWM and SPDC quantum light sources of both squeezed light and photon pairs. The main experimental result of this work was to demonstrate an ultra-bright source of entangled photon pairs using an integrated AlGaAsOI source with an internal brightness exceeding 20×10^9 pairs $\text{sec}^{-1} \text{mW}^{-2}$ that emits near 1550 nm, produces heralded single photons with $> 99\%$ purity, and violates Bells inequality by more than 40 standard deviations with visibility $> 97\%$. This source motivates further study into the AlGaAsOI material platform for applications and the development of an integrated quantum photonic circuit platform. In the development of this platform, the InGaPOI material system was also explored, specifically for SPDC. The bandgap of InGaP is larger than that of AlGaAs, suggesting lower loss for a pump wavelength near the visible wavelength range (775nm). Both the AlGaAs and InGaP platforms are modeled to find phase matching for SPDC (and similarly second harmonic generation). Many of the components for these new light sources have been developed, and experimental testing is expected in the near future.

Regarding the future of these platforms, AlGaAsOI and InGaPOI have remarkable potential for all-on-chip quantum photonic integrated circuit (QPIC) development com-

pared to existing platforms. First, the on-chip integration of tunable excitation laser sources can be naturally incorporated into the epitaxial growth process of the photonic layer [66]. These materials are also distinguished by high index contrast for tight modal confinement [67], have negligible two-photon absorption at 1550 nm (with proper Al portion for AlGaAs [68]), exhibit a large $\chi^{(2)}$ nonlinearity for high-speed electro-optic modulation [69], strong piezo-optic effect for optomechanic cavities [70], and ultra-quiet superconducting nanowire single-photon detectors (SNSPDs) having already been integrated with GaAs/AlGaAs waveguides [71]. The possible application space is extraordinarily broad, ranging from ground-to-satellite communications and quantum teleportation to all-on-chip quantum information processing and Boson sampling [72–75].

Such high performances dramatically impact the selection of quantum sources in QPICs. In recent years, self-assembled quantum dots (QDs) embedded in optical microcavities have become state-of-the-art in generating quantum light since they are capable of producing entangled-photon pairs and single photons at rates thought impossible for probabilistic nonlinear sources [76]. However, those photon sources have to be operated at cryogenic temperature, and their selective growth is also quite challenging, which hinders their system level scaling. In addition, an InAs QD's emitted photon energy usually lies outside of the telecommunications wavelength (C band), adding considerable inconveniences in information processing and transmission. Some other on-demand quantum photon sources, such as GaN QDs and carbon nanotubes, can be operated at room temperature, and some of them also operate in the C band, however their photon generation rates are so far limited. Therefore, the more than two (four) orders-of-magnitude improvement in the pair generation rate (brightness) enabled by AlGaAsOI makes probabilistic sources significantly more competitive by combining the advantages of room-temperature operation, higher quality of the produced single photons and entangled-photon pairs, and intrinsic scalability afforded by microring resonator structures.

Although the AlGaAsOI platform boasts groundbreaking values in photon-pair generation, much exciting work remains to be done. Brighter entanglement sources require lower on-chip pump power for a given pair generation rate. This relaxes the requirements of on-chip filters for pump rejection. Compared to current state of the art QPICs based on SOI, the lower waveguide loss of AlGaAsOI can significantly reduce the overall system loss, allowing more components to be accommodated for applications requiring system-level integration, such as multi-qubit quantum computation. Another advantage is on the tuning side: AlGaAs has a factor of two larger thermo-optic coefficient than that of Si, which can enable more efficient thermo-tuners. The electro-optic and piezo-optic effects provide a novel tuning scheme for scenarios where high-speed operation or cryogenic temperatures are required. Therefore, AlGaAsOI holds exciting prospects for all-on-chip quantum photonic integrated circuits, where tunable lasers, nonlinear sources, distributed Bragg grating reflectors, Mach-Zehnder interferometers, high-speed electro-optic modulators, demultiplexers, and chip-to-fiber couplers can be monolithically integrated into the same AlGaAsOI platform without the need for complex heterogeneous integration techniques (see Chapter 4 for preliminary results developing the AlGaAsOI material platform).

Bibliography

- [1] A. Weiner, *Frequency bin quantum photonics*, <https://doi.org/10.1117/12.2610696> **11917** (8, 2021) 119170W.
- [2] H.-H. Lu, H.-H. Lu, M. Liscidini, *et. al.*, *Frequency-bin photonic quantum information, Optica, Vol. 10, Issue 12, pp. 1655-1671* **10** (12, 2023) 1655–1671.
- [3] S. Takeda and A. Furusawa, *Toward large-scale fault-tolerant universal photonic quantum computing*, *APL Photonics* **4** (6, 2019) 060902.
- [4] S.-H. Wei, B. Jing, X.-Y. Zhang, *et. al.*, *Towards Real-World Quantum Networks: A Review*, *Laser & Photonics Reviews* **16** (3, 2022) 2100219.
- [5] E. Polino, M. Valeri, N. Spagnolo, and F. Sciarrino, *Photonic quantum metrology*, *AVS Quantum Science* **2** (6, 2020) 024703.
- [6] G. Moody, L. Chang, T. J. Steiner, and J. E. Bowers, *Chip-Scale Nonlinear Photonics for Quantum Light Generation*, *AVS Quantum Science* **2** (12, 2020) 041702.
- [7] T. Heindel, C. A. Kessler, M. Rau, *et. al.*, *Quantum key distribution using quantum dot single-photon emitting diodes in the red and near infrared spectral range*, *New Journal of Physics* **14** (8, 2012) 083001.
- [8] H. Wang, J. Qin, X. Ding, *et. al.*, *Boson Sampling with 20 Input Photons and a 60-Mode Interferometer in a 1014 -Dimensional Hilbert Space*, *Physical Review Letters* **123** (12, 2019) 250503.
- [9] I. Aharonovich, D. Englund, and M. Toth, *Solid-state single-photon emitters*, 2016.
- [10] S. I. Azzam, K. Parto, and G. Moody, *Prospects and challenges of quantum emitters in 2D materials*, *Applied Physics Letters* **118** (6, 2021) 240502.
- [11] J. B. Spring, P. L. Mennea, B. J. Metcalf, *et. al.*, *Chip-based array of near-identical, pure, heralded single-photon sources*, *Optica* **4** (2017), no. 1 90.

BIBLIOGRAPHY

- [12] T. J. Steiner, J. E. Castro, L. Chang, *et. al.*, *Ultra-bright entangled-photon pair generation from an AlGaAs-on-insulator microring resonator*, *PRX Quantum* **2** (9, 2021) 010337.
- [13] L. S. Braunstein and P. Van Loock, *Quantum information with continuous variables*, *Reviews of Modern Physics* **77** (4, 2005) 513–577.
- [14] L. G. Helt, M. Liscidini, and J. E. Sipe, *How does it scale? Comparing quantum and classical nonlinear optical processes in integrated devices*, *Journal of the Optical Society of America B* **29** (8, 2012) 2199.
- [15] M. Fiorentino, S. M. Spillane, R. G. Beausoleil, *et. al.*, *Spontaneous parametric down-conversion in periodically poled KTP waveguides and bulk crystals*, *Optics Express*, Vol. 15, Issue 12, pp. 7479–7488 **15** (6, 2007) 7479–7488.
- [16] J. Zhao, C. Ma, M. Rüsing, and S. Mookherjea, *High Quality Entangled Photon Pair Generation in Periodically Poled Thin-Film Lithium Niobate Waveguides*, *Physical Review Letters* **124** (4, 2020) 163603.
- [17] M. Jankowski, J. Mishra, and M. M. Fejer, *Dispersion-engineered $\chi^{(2)}$ nanophotonics: a flexible tool for nonclassical light*, .
- [18] C. Ma, X. Wang, V. Anant, *et. al.*, *Silicon photonic entangled photon-pair and heralded single photon generation with CAR $\approx 12,000$ and $g(2)(0) \approx 0.006$* , *Optics Express* **25** (2017), no. 26 32995–33006.
- [19] S. Ramelow, A. Farsi, S. Clemmen, *et. al.*, *Silicon-Nitride Platform for Narrowband Entangled Photon Generation*, .
- [20] R. R. Kumar, M. Raevskaia, V. Pogoretskii, *et. al.*, *Entangled photon pair generation from an InP membrane micro-ring resonator*, *Applied Physics Letters* **114** (1, 2019).
- [21] B. Y. Xu, L. K. Chen, J. T. Lin, *et. al.*, *Spectrally multiplexed and bright entangled photon pairs in a lithium niobate microresonator*, *Science China: Physics, Mechanics and Astronomy* **65** (9, 2022) 1–7.
- [22] J. D. Franson, *Bell inequality for position and time*, *Physical Review Letters* **62** (5, 1989) 2205–2208.
- [23] M. Fox, *Quantum Optics*. Oxford: Oxford University Press, 2006.
- [24] Y. J. Lu and Z. Y. Ou, *Optical parametric oscillator far below threshold: Experiment versus theory*, *Physical Review A* **62** (8, 2000) 033804.
- [25] E. Pomaríco, B. Sangulnettl, N. Gisin, *et. al.*, *Waveguide-based OPO source of entangled photon pairs*, *New Journal of Physics* **11** (11, 2009) 113042.

BIBLIOGRAPHY

- [26] T. J. Steiner, M. Shen, J. E. Castro, *et. al.*, *Continuous entanglement distribution from an AlGaAs-on-insulator microcomb for quantum communications*, *Optica Quantum* **1** (12, 2023) 55–62.
- [27] L. Mandel and E. Wolf, *Optical Coherence and Quantum Optics*. Cambridge university press, 1 ed., 1995.
- [28] R. J. Glauber, *The quantum theory of optical coherence*, *Physical Review* **130** (6, 1963) 2529–2539.
- [29] Z. Y. J. Ou, *Multi-photon quantum interference*, *Multi-Photon Quantum Interference* (2007) 1–268.
- [30] S. M. Spillane, M. Fiorentino, R. G. Beausoleil, *et. al.*, *Spontaneous parametric down conversion in a nanophotonic waveguide*, *Optics Express*, Vol. 15, Issue 14, pp. 8770-8780 **15** (7, 2007) 8770–8780.
- [31] Z. Yang, M. Liscidini, and J. E. Sipe, *Spontaneous parametric down-conversion in waveguides: A backward Heisenberg picture approach*, *Physical Review A - Atomic, Molecular, and Optical Physics* **77** (3, 2008) 033808.
- [32] A. Yariv, *Quantum electronics*. John Wiley & Sons, Ltd, 1988.
- [33] T. Kashiwazaki, N. Takanashi, T. Yamashima, *et. al.*, *Continuous-wave 6-dB-squeezed light with 2.5-THz-bandwidth from single-mode PPLN waveguide*, *APL Photonics* **5** (3, 2020) 036104.
- [34] C. Simon, M. Afzelius, J. Appel, *et. al.*, *Quantum memories*, *The European Physical Journal D 2010 58:1* **58** (4, 2010) 1–22.
- [35] B. J. Metcalf, J. B. Spring, P. C. Humphreys, *et. al.*, *Quantum teleportation on a photonic chip*, *Nature Photonics* **8** (2014), no. 10 770–774.
- [36] X. Lu, Q. Li, D. A. Westly, *et. al.*, *Chip-integrated visibletelecom entangled photon pair source for quantum communication*, *Nature Physics* **15** (2019), no. 4 373–381.
- [37] F. Samara, N. Maring, A. Martin, *et. al.*, *Entanglement swapping between independent and asynchronous integrated photon-pair sources*, *Quantum Science and Technology* **6** (2021), no. 4.
- [38] D. Rabus, *Integrated Ring Resonators: The Compendium*, vol. 127. Springer, 2007.
- [39] L. Chang, A. Boes, P. Pintus, *et. al.*, *Low loss (Al)GaAs on an insulator waveguide platform*, *Optics Letters* **44** (8, 2019) 4075.
- [40] L. Chang, A. Boes, P. Pintus, *et. al.*, *High Efficiency SHG in Heterogenous Integrated GaAs Ring Resonators*, in *31st Annual Conference of the IEEE Photonics Society, IPC 2018*, 2018.

BIBLIOGRAPHY

- [41] L. Chang, A. Boes, X. Guo, *et. al.*, *Heterogeneously Integrated GaAs Waveguides on Insulator for Efficient Frequency Conversion*, *Laser and Photonics Reviews* **12** (10, 2018) 1800149.
- [42] W. Xie, L. Chang, H. Shu, *et. al.*, *Ultrahigh-Q AlGaAs-on-insulator microresonators for integrated nonlinear photonics*, *Optics Express* **28** (4, 2020) 32894.
- [43] W. Xie, C. Xiang, L. Chang, *et. al.*, *Silicon-integrated nonlinear III-V photonics*, *Photonics Research* **10** (2, 2022) 535–541.
- [44] E. J. Stanton, J. Chiles, N. Nader, *et. al.*, *Efficient second harmonic generation in nanophotonic GaAs-on-insulator waveguides*, *Optics Express* **28** (3, 2020) 9521.
- [45] J. Chiles, N. Nader, E. J. Stanton, *et. al.*, *Multifunctional integrated photonics in the mid-infrared with suspended AlGaAs on silicon*, *Optica* **6** (2019), no. 9 1246.
- [46] B. Guha, F. Marsault, F. Cadiz, *et. al.*, *Surface-enhanced gallium arsenide photonic resonator with quality factor of 610^6* , *Optica* **4** (2, 2017) 218.
- [47] L. Chang, W. Xie, H. Shu, *et. al.*, *Ultra-efficient frequency comb generation in AlGaAs-on-insulator microresonators*, *Nature Communications* **11** (2020), no. 1 1–8.
- [48] J. Brendel, N. Gisin, W. Tittel, and H. Zbinden, *Pulsed energy-time entangled twin-photon source for quantum communication*, *Physical Review Letters* **82** (3, 1999) 2594–2597.
- [49] R. Wakabayashi, M. Fujiwara, K.-i. Yoshino, *et. al.*, *Time-bin entangled photon pair generation from Si micro-ring resonator*, *Optics Express* **23** (1, 2015) 1103–1113.
- [50] J. D. Franson, *Two-photon interferometry over large distances*, *Physical Review A* **44** (10, 1991) 4552–4555.
- [51] J. F. Clauser and M. A. Horne, *Experimental consequences of objective local theories*, *Physical Review D* **10** (1974), no. 2 526–535.
- [52] J. G. Rarity and P. R. Tapster, *Experimental violation of Bells inequality based on phase and momentum*, *Physical Review Letters* **64** (5, 1990) 2495–2498.
- [53] Z. Ma, J.-Y. Chen, Z. Li, *et. al.*, *Ultra-bright Quantum Photon Sources on Chip*, *Physical Review Letters* **125** (12, 2020) 263602.
- [54] K. Guo, E. N. Christensen, J. B. Christensen, *et. al.*, *High coincidence-to-accidental ratio continuous-wave photon-pair generation in a grating-coupled silicon strip waveguide*, *Applied Physics Express* **10** (5, 2017) 62801.

BIBLIOGRAPHY

- [55] M. Zhao and K. Fang, *InGaP quantum nanophotonic integrated circuits with 1.5% nonlinearity-to-loss ratio*, *Optica* **9** (2, 2022) 258.
- [56] A. Chopin, A. Barone, I. Ghorbel, *et. al.*, *Ultra-efficient generation of time-energy entangled photon pairs in an InGaP photonic crystal cavity*, *Communications Physics* **6:1** **6** (4, 2023) 1–9.
- [57] J. Aasi, J. Abadie, B. P. Abbott, *et. al.*, *Enhanced sensitivity of the LIGO gravitational wave detector by using squeezed states of light*, *Nature Photonics* **7** (8, 2013) 613–619.
- [58] A. I. Lvovsky, H. Hansen, T. Aichele, *et. al.*, *Quantum state reconstruction of the single-photon fock state*, *Physical Review Letters* **87** (7, 2001) 50402–1.
- [59] A. Ourjoumtsev, R. Tualle-Brouiri, and P. Grangier, *Quantum homodyne tomography of a two-photon fock state*, *Physical Review Letters* **96** (6, 2006) 213601.
- [60] F. Dell’Anno, S. De Siena, and F. Illuminati, *Multiphoton quantum optics and quantum state engineering*, *Physics Reports* **428** (5, 2006) 53–168.
- [61] J. M. Arrazola, V. Bergholm, K. Brádler, *et. al.*, *Quantum circuits with many photons on a programmable nanophotonic chip*, *Nature* **2021** *591:7848* **591** (2021), no. 7848 54–60.
- [62] P. K. Lam, T. C. Ralph, B. C. Buchler, *et. al.*, *Optimization and transfer of vacuum squeezing from an optical parametric oscillator*, *Journal of Optics B: Quantum and Semiclassical Optics* **1** (1999), no. 4 469–474.
- [63] R. Luo, Y. He, H. Liang, *et. al.*, *Optical Parametric Generation in a Lithium Niobate Microring with Modal Phase Matching*, *Physical Review Applied* **11** (3, 2019) 034026.
- [64] V. D. Vaidya, B. Morrison, L. G. Helt, *et. al.*, *Broadband quadrature-squeezed vacuum and nonclassical photon number correlations from a nanophotonic device*, *Science advances* **6** (4, 2020).
- [65] Y. Zhang, M. Menotti, K. Tan, *et. al.*, *Squeezed light from a nanophotonic molecule*, *Nature Communications* **2021** *12:1* **12** (4, 2021) 1–6.
- [66] A. Y. Liu and J. Bowers, *Photonic integration with epitaxial III-V on silicon*, *IEEE Journal of Selected Topics in Quantum Electronics* **24** (2018), no. 6 1–12.
- [67] M. Pu, L. Ottaviano, E. Semenova, and K. Yvind, *Efficient frequency comb generation in AlGaAs-on-insulator*, *Optica* **3** (8, 2016) 823.
- [68] S. Adachi, *{GaAs} and Related Materials*. {WORLD} {SCIENTIFIC}, 10, 1994.

BIBLIOGRAPHY

- [69] R. Walker, N. Cameron, Y. Zhou, *et. al.*, *50GHz gallium arsenide electro-optic modulators for spaceborne telecommunications*, in *International Conference on Space Optics* (N. Karafolas, Z. Sodnik, and B. Cugny, eds.), SPIE, 7, 2019.
- [70] M. Forsch, R. Stockill, A. Walluck, *et. al.*, *Microwave-to-optics conversion using a mechanical oscillator in its quantum ground state.*, *Nature Physics* **16** (1, 2020) 69–74.
- [71] C. McDonald, G. Moody, S. W. Nam, *et. al.*, *III-V photonic integrated circuit with waveguide-coupled light-emitting diodes and WSi superconducting single-photon detectors*, *Applied Physics Letters* **115** (8, 2019).
- [72] J. Yin, Y. Cao, Y. H. Li, *et. al.*, *Satellite-based entanglement distribution over 1200 kilometers*, *Science* **356** (6, 2017) 1140–1144.
- [73] S. K. Liao, W. Q. Cai, W. Y. Liu, *et. al.*, *Satellite-to-ground quantum key distribution*, *Nature* **549** (8, 2017) 43–47.
- [74] D. Llewellyn, Y. Ding, I. I. Faruque, *et. al.*, *Chip-to-chip quantum teleportation and multi-photon entanglement in silicon*, 12, 2020.
- [75] J. B. Spring, P. S. Salter, B. J. Metcalf, *et. al.*, *On-chip low loss heralded source of pure single photons*, *Optics Express* **21** (2013), no. 11 13522.
- [76] H. Wang, H. Hu, T. H. Chung, *et. al.*, *On-Demand Semiconductor Source of Entangled Photons Which Simultaneously Has High Fidelity, Efficiency, and Indistinguishability*, *Physical Review Letters* **122** (3, 2019) 113602.

Chapter 4

AlGaAsOI Integrated Quantum Photonics Toolbox

As illustrated in Chapter 3, the AlGaAsOI material platform can be used as an efficient source of quantum states of light. The platform is capable of producing light via both the second and third order nonlinear interactions at the telecommunications C-band (1550nm) wavelength range. Quantum photonic integrated circuit (QPIC) functionality of any complexity also relies on a set of components for on-chip manipulation of quantum states of light, including active modulators and switches as well as passive routing components, beamsplitters, and on/off chip couplers [1].

Figure 4.1 illustrates the motivation of this chapter where an AlGaAsOI microring resonator quantum light source (a) interfaces with AlGaAsOI active and passive components to create QPICs for quantum computing, boson sampling, quantum teleportation or other application demonstrations. The largest demonstrations to date using these components and on-chip photon sources have been realized on silicon [2, 3], whose swift progress as a quantum photonic platform has benefited from its prominence in classical photonics and the complementary metal oxide semiconductor (CMOS) industry. Chap-

ter 2 discusses some of the other material platforms utilized for QPICs, highlighting the pros and cons of each material system. This chapter builds off the impressive, 1000-fold improvement in entangled photon pair brightness from the AlGaAsOI material platform to develop all of the other necessary photonic components to enable larger scale circuits to be created. This chapter will briefly discuss the design and characterization of the key building blocks of a QPIC. Preliminary simulations and results from testing a subset of the necessary components to design a multi-functional QPIC are presented. Once this “Integrated Quantum Photonics Toolbox” is completed, more advanced quantum circuits can be readily assembled (see Chapter 6). Although the main experimental results shown in the chapter are based on the 400 nm thick AlGaAsOI material platform, the methods can easily be adapted to 102 nm thick InGaPOI and 105 nm thick AlGaAsOI components that are compatible with SPDC-based quantum light sources. The components developed here can similarly be designed for the other material platforms (especially material platforms with similar refractive indices) with adjustments to the critical dimensions. The following discussion will show designs and results for only the 400 nm thick $\text{Al}_{0.2}\text{Ga}_{0.8}\text{As}$ material system, so the aluminum and gallium fraction will be dropped for convenience.

4.1 Fiber to Chip Coupling Strategies

During the initial testing process, it is necessary to utilize either fiber-based or free-space optical testing equipment. Thus, one of the first components to design is an efficient method to couple light into/out of the photonic chip. Various strategies have been explored for efficient coupling [4], but many of the methods that achieve ultra-high efficiency require additional fabrication steps, anti-reflection coatings, or a full redesign of the input/output facet structure. For the case of testing individual components, much simpler structures can be used—as long as the fiber-to-chip coupling efficiency can be

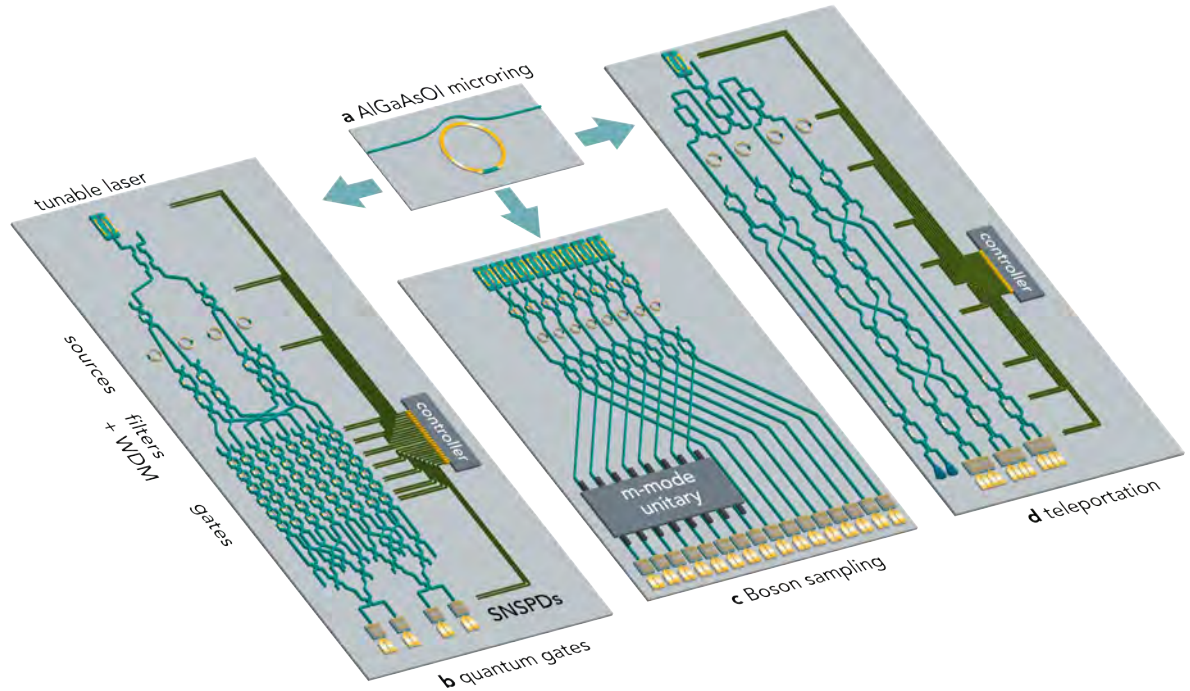


Figure 4.1: a) Tunable AlGaAs-on-insulator (AlGaAsOI) microring resonator entangled-photon pair source. The AlGaAsOI platform enables the large-scale integration of active and passive quantum photonic components, including tunable lasers, nonlinear quantum light sources, filters and wavelength division multiplexing (WDM), superconducting nanowire single-photon detectors (SNSPDs), and microcontrollers. These components can be monolithically integrated for all-on-chip quantum photonic circuits, including b) quantum gates for optical computing, c) m -mode unitary operations for Boson sampling, and d) Bell-state measurements for chip-to-chip teleportation of quantum states.

adequately characterized, any loss due to coupling can be added back to the device performance to estimate its behavior on the chip.

There are two main categories of fiber-to-chip couplers: vertical couplers (based on optical gratings) and edge couplers (also called “in-plane,” “end-fire,” or “butt” couplers). As the name suggests, vertical couplers accept incoming light from the top of the chip (out of plane) while edge couplers couple light impinging from one of the facets of the photonic chip (in plane). Depending on the desired application or testing design, there may be a benefit for utilizing either type of coupler. Vertical couplers are useful for more

compact designs as they do not require waveguides to be routed completely to the edge of the photonic chip. Edge couplers, on the other hand, are easier to design and less sensitive to fabrication variation.

The standard fiber for telecom communication systems is single mode fiber 28 (SMF-28) which has a minimum attenuation of 0.18 dB/km at 1.55 μm wavelength and has a mode field diameter (MFD) of 10.4 μm [4]. The fiber can be made polarization maintaining through the addition of internal stressor rods in the fiber cladding region. When the fiber end is planar-polished, the mode diverges into the air with a 2D Gaussian mode profile and numerical aperture of 0.12. The difficulty of efficient coupling into a photonic structure stems from the divergence, reflection, and the large mode area of the fiber mode relative to the $\sim 100\text{s}$ of nanometer scale mode of the waveguide mode inside a high refractive index contrast waveguide. Chapter 2 introduces the waveguide mode for materials like AlGaAs and InGaP which have large refractive index contrast such that the mode size is very similar to the waveguide structure. Since these materials have thicknesses of 102 nm or 400 nm and widths between 500 nm and 2.5 μm , the mode area is much smaller than the 10.4 μm mode diameter Gaussian mode of the optical fiber. To address this mismatch, several strategies are employed. Namely, the waveguide mode is expanded, and (if possible) lensed fibers are utilized for coupling instead of planar polished fibers. Other strategies like angling the waveguide-to-air facet can reduce the reflection, and for even greater reduction in reflection, an anti-reflection coating can be spun on the facet. For the case of vertical couplers, a different problem arises from the need to angle the optical fiber *and* bring the fiber very close to the vertical coupler. Standard, planar polished fibers will impact the chip when brought too close, so custom angled polished fibers are used when trying to get the best vertical coupling efficiency.

4.1.1 Edge Coupling Strategies

As briefly mentioned above, one of the main limitations to the coupling efficiency into waveguides is the optical mode mismatch. Starting first with in-plane couplers, a basic edge coupling strategy is to gradually reduce the width of the waveguide down to a small tip at the input (output) facet of the photonic chip. As shown in Figure 4.2a) the waveguide width at the facet W_{in} is typically maintained for a short length L_{buffer} to allow for room to polish/dice the facet during singulation of the individual device bars from the wafer. The width is then increased gradually (over L_{taper}) to the final waveguide width w_{wg} to allow for an adiabatic transition to the desired device dimensions. An SEM image of the inverse taper design is shown in Figure 4.2c). This inverse taper design reduces the confinement of the waveguide mode, increasing its effective modal area and decreasing its effective index of refraction. This allows for moderately high coupling efficiencies to a (typically) lensed fiber aligned with the waveguide facet. The overall coupling loss is determined by effects such as reflection at the chip facet (due to refractive index mismatch), fiber-to-waveguide mode mismatch, and mode-conversion within the waveguide taper. Figure 4.2d) illustrates the mode overlap between a $2.5 \mu\text{m}$ diameter spot size lensed fiber (which matches the mode field diameter of commercially available lensed fibers) optical mode and the inverse taper mode for various widths of W_{in} .

For a given Gaussian beam and optical waveguide, the coupling efficiency can be defined by Equation (4.1) [5]. This equation simply states that the coupling efficiency is the normalized mode overlap between the two modes of interest.

$$\eta(z) = \frac{|\int \int_S \vec{E}_1 \cdot \vec{E}_f dx dy|^2}{\int \int_S \vec{E}_1 \cdot \vec{E}_1^* dx dy \int \int_S \vec{E}_f \cdot \vec{E}_f^* dx dy} \quad (4.1)$$

Longer wavelengths have reduced confinement within a given waveguide dimension,

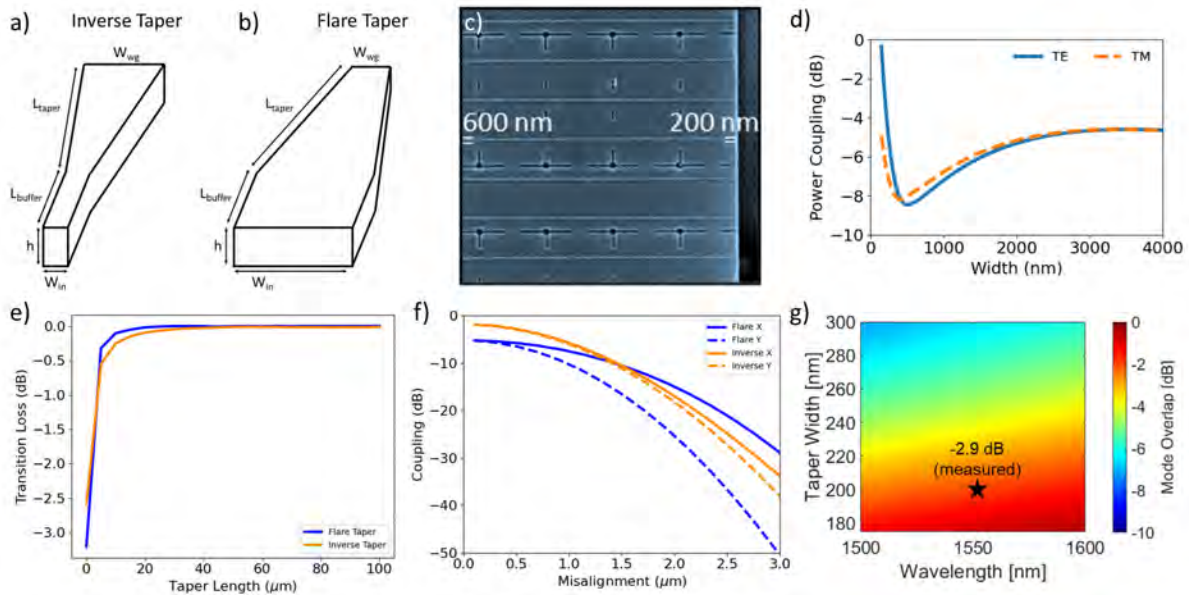


Figure 4.2: a) Design of an inverse taper edge coupler with dimensions labeled. b) Flare taper design. c) Scanning electron microscope (SEM) image of an array of inverse taper edge couplers. d) Simulated mode overlap as a function of taper width for both the TE and TM modes. e) Mode conversion loss in a flare taper of $3\ \mu\text{m}$ width and inverse taper of $200\ \text{nm}$ width as a function of the taper length for the fundamental TE mode. f) Misalignment sensitivity in the x- and y-axes for the flare and inverse taper designs for the TE mode. g) Heat map showing the mode overlap of various inverse taper widths and different wavelengths for the TE mode. The star shows an experimentally obtained value.

resulting in larger modes relative to shorter wavelengths. This trend is illustrated in the simulated mode overlap in Figure 4.2d). Additionally, reducing the waveguide width will push the mode into the cladding, increasing the mode size as well.

Figure 4.2b) illustrates an alternative route to create an edge coupler, sometimes called a “flare” taper or just a standard taper. This design does not push the mode into the cladding, but instead increases the waveguide width to increase the relative mode size within the waveguide. As illustrated by the plot in Figure 4.2d), large waveguide widths can attain moderate mode overlaps on the order of $-5\ \text{dB}$, but are ultimately limited by the vertical dimension (which remains fixed at $400\ \text{nm}$). Thus, flare tapers are less efficient than inverse tapers. Another downside of using flare tapers is the refractive index

mismatch between the flare taper mode and the air at the facet. Since inverse tapers push the mode into the cladding, the effective index of inverse taper modes is close to that of the cladding ($n=1.44$). Flare tapers, on the other hand, maintain confinement within the waveguide material, so the effective index is close to that of the core ($n=3.3$). This mismatch can result in significant reflections at the facet when using flare tapers.

There are, however, a few advantages of using flare tapers. First, the larger waveguide dimension used for a flare taper makes coupling into the structure less sensitive to the fiber alignment (in the x-axis). The sensitivity of the inverse taper and flare taper to fiber misalignment is shown in Figure 4.2f). For both designs, the y-axis misalignment (dashed lines) has the same slope since the vertical dimension is fixed at 400 nm. The x-axis, on the other hand, shows improved stability for the flare taper. Another important thing to note from this simulation is the precision required to obtain maximum coupling into the waveguide. A 2 μm misalignment can result in > 10 dB of excess loss. Thus, careful consideration must be made when creating experimental setups to efficiently couple light into and out of these edge couplers. An additional benefit of using flare tapers is that since the mode is always well-confined within the waveguide, the transition length to the waveguide dimension can be reduced (as illustrated in Figure 4.2e). The inverse taper design must optimize the lengths of L_{buffer} and L_{taper} for both minimization of loss as well as maximum adiabaticity in the conversion of the propagating modes. Longer L_{taper} will more gradually change the mode characteristics, resulting in a smoother transition from the taper dimension to the final waveguide width, but the weakly confined mode will experience increased propagation loss, encouraging a more rapid transition to the strongly confined mode.

For the designs used in all of the devices that follow, a 200 μm taper length is used with hopes of finding a balance between these competing effects. The buffer length is defined based on the singulation process used. For diced and polished facets, a longer

buffer is used ($\sim 200\mu\text{m}$) to account for the width of the dicing blade ($\sim 75\mu\text{m}$) as well as the removal of material during polishing. Improvements to the singulation process have replaced this step with an etched facet. Since the etch is defined lithographically, the buffer length can be set to $0\mu\text{m}$, and the transition can begin immediately at the facet. Regarding the taper width, the fabrication of sub-200-nm features is challenging using the standard photolithography process, so we limit our taper designs to 200 nm or larger. Smaller features than 200 nm will regularly result in delamination of the bonded AlGaAs material from the lower silica cladding. To ensure high yield, the taper dimension is kept at 200 nm.

Experimentally, the measurement of facet loss is straightforward. A continuous-wave laser diode tuned to 1550 nm wavelength is sent through lensed fibers into and out of a straight waveguide with edge couplers on each side. The two fibers are aligned using multi-axis stages to find the maximum power through the straight waveguide. The waveguide length is short ($\sim 2\text{ mm}$) such that propagation loss which is $< 1\text{ dB/cm}$ does not impact the measured loss. Figure 4.2a) illustrates an SEM image of a set of edge coupler devices. Here, the inverse taper width is 200 nm and the waveguide width is 600 nm. Figure 4.2b) shows a star indicating the experimentally obtained facet loss for this design. The measured value was collected by sending 6.95 dBm ($\sim 5\text{ mW}$) of light into a straight waveguide with 200 nm tapers on the input and output facet. The collected power through the waveguide was $1.16\pm 0.23\text{ dBm}$, indicating an approximate loss of 2.9 dB/facet. The measured loss is larger than the simulated mode overlap, which is expected because the measurements also include reflections and mode conversion loss in the taper. The simulated mode overlap acts as an upper bound for the efficiency of the inverse taper. The 2.9 dB/facet of coupling loss in the AlGaAsOI platform is comparable to the sub-3 dB coupling loss expected from standard SOI inverse taper edge coupler designs [6]. The use of narrower taper widths (as shown in Fig. 4.2b)) or an

anti-reflection coating will improve the coupling efficiency further, but ease of fabrication and reliability are prioritized, so for our initial devices, 200 nm inverse tapers are utilized.

4.1.2 Grating Couplers

The second category of coupling strategies is to couple light into the photonic chip vertically. Vertical couplers use constructive interference between distributed scatterers (commonly grating-based structures) to direct light into the vertically aligned fiber. We can use a ray optics model (Figure 4.3a) to illustrate the operating principle of grating couplers. Looking just at the first two corrugations, we have a core waveguide with index n_2 that is etched in a rectangular pattern such that alternating regions of cladding and core are seen by the propagating light (with wavevector k_{mz}). At each corrugation, the light is reflected upward, out of the waveguide and toward the optical fiber. From each corrugation, a ray of light is scattered, and for efficient coupling, the rays must be in phase such that they constructively interfere. That is to say, the optical path lengths must satisfy

$$k_{mz}a - k_1b = 2\pi m \quad (4.2)$$

where m is an integer, and the corrugations are separated by a length a , also called the grating pitch. Substituting the definition of wavevector,

$$\frac{2\pi}{\lambda}n_{eff}a - \frac{2\pi}{\lambda}n_1b = 2\pi m, \quad (4.3)$$

$$n_{eff}a - n_1b = m\lambda, \quad (4.4)$$

$$n_{eff}a - n_1a\sin(\theta) = m\lambda, \quad (4.5)$$

which tells us that the angle of interference is related to the grating pitch, wavelength of light, and effective index of the mode.

$$\sin(\theta) = \frac{n_{eff} - \frac{m\lambda}{a}}{n_1} \quad (4.6)$$

Thus, by tuning these key parameters we can adjust the output angle of the light and try to optimize coupling into a fiber.

Moving away from this simple picture, we can demonstrate the real grating couplers designed for the AlGaAs platform, where now there are additional parameters that can be used to optimize coupling. An example grating coupler cross section is shown in Figure 4.3b). An optical fiber is brought close to the surface of the top silica cladding above the waveguide and grating coupler. The fiber is offset from the start of the grating by x and is tilted at an angle θ . The grating pitch (which was labeled a in the simple picture) has been relabeled as p . The etch length is l_e with depth h_e . The duty cycle is defined as $d = (p - l_e)/p$, and represents the fraction of the grating pitch that is etched. Lastly, there is a bottom cladding of silica before the silicon substrate. With these additional parameters, finding an optimal solution analytically would be quite challenging, so we turn to Lumerical finite difference time domain (FDTD) simulations in conjunction with a swarm optimization protocol to maximize the coupled power to the fiber mode by varying the grating parameters. The principle behind this still follows the equations above, but now there are many ways to manipulate the parameters. For example, both the duty cycle and etch depth can change the effective index in the grating region, and the location of the fiber can change how much of the light is actually coupled into it. There is an effective number of grooves that the light encounters, so the fiber should be aligned over this region to get most of the light into/out of the chip. When light is sent from the fiber, some of it is also reflected off of the substrate interface, and again, if the phase of this light

is $2\pi m$, then it will constructively interfere. Thus, there also exists an optimal lower oxide thickness to satisfy this condition. Overall, doing this without computational software is very difficult, so FDTD simulations are employed which can model the propagation of the light as a function of time. The optimized simulated transmission spectrum for 400 nm thick AlGaAs is shown in Figure 4.3c). The fiber angle θ is fixed to 10 degrees to simplify the simulation parameter space and be compatible with current experimental setups. For the orange dashed plot, the etch depth (h_e) is fixed at 400 nm since the standard etching procedure for the AlGaAs components only includes a full etch (through the 400 nm thick AlGaAs layer). The blue, solid plot allows the etch depth to vary, showing the improved coupling efficiency with this additional degree of freedom. The partial etch reduces the amount of backscattering in the waveguide since the mode does not see a sharp transition from the index of the core to the cladding and thus has improved efficiency compared to the fully etched design.

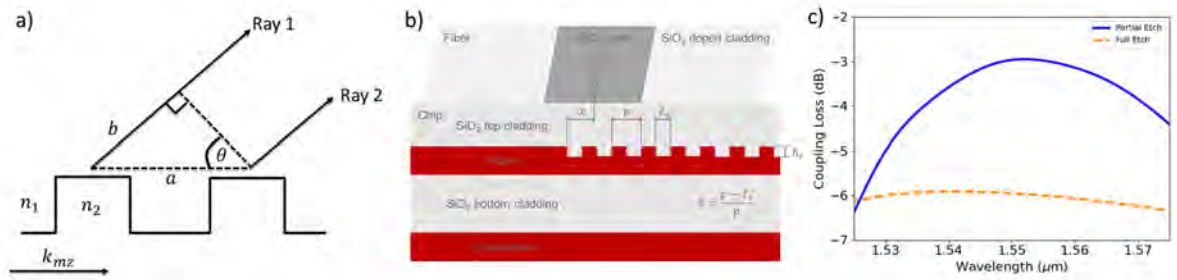


Figure 4.3: a) Schematic showing the operating principle of a grating coupler. b) Schematic illustrating a grating coupler in the AlGaAs platform. c) Simulated transmission efficiency as a function of wavelength for a fully etched AlGaAs grating coupler and one with a partial etch.

In addition to the edge couplers and grating couplers discussed here, there are other approaches that can achieve coupling efficiencies < 1 dB/facet [7] that involve more complex fabrication processes. As far as simple, lithography-based coupling systems, the < 3 dB/facet coupling efficiency demonstrated with inverse tapers, and the simulated

~ 6 dB/facet coupling efficiencies for fully etched grating couplers is efficient enough as to not hinder the measurements performed on the rest of the components detailed in this chapter. Importantly, the coupling efficiency is relatively uniform across the devices, allowing for an estimate of the device-specific loss.

4.2 Waveguide Routing

As QPICs begin to scale, there becomes an increasing need for connectivity between different qubits from different regions of the photonic chip. Simple circuits, for example, may require only interactions between the nearest neighbor photons to perform basic operations. However, for more advanced circuits and experiments, there is a need to interact non-nearest neighbor photons which can be spatially far from each other within a photonic chip. Since the photonic components are all fabricated using the same photonic layer (in the same plane), waveguide crossing designs must be made to route light across the chip. It is important that this crossing does not introduce significant loss or allow for coupling to the orthogonal waveguide that it crosses as this will introduce error in the circuit, reducing the fidelity of any operations. Additionally, scaling to hundreds or thousands of qubits on a single chip may require a significant number of waveguide crossings. For example, in silicon, large-scale QPICs have been designed to implement arbitrary two-qubit processing from photons generated from four silicon spiral sources which requires 18 waveguide crossers [8]. More recent work shows very large-scale integrated quantum photonic circuits with 16 nonlinear quantum light sources, requiring 463 waveguide crossers [9]! It is easy to see how going to much larger scales can require thousands of waveguide crossers.

Several methods have been explored for creating low-loss waveguide crossings including vertical coupling into polymer strip waveguides [10], multi-planar crossings [11],

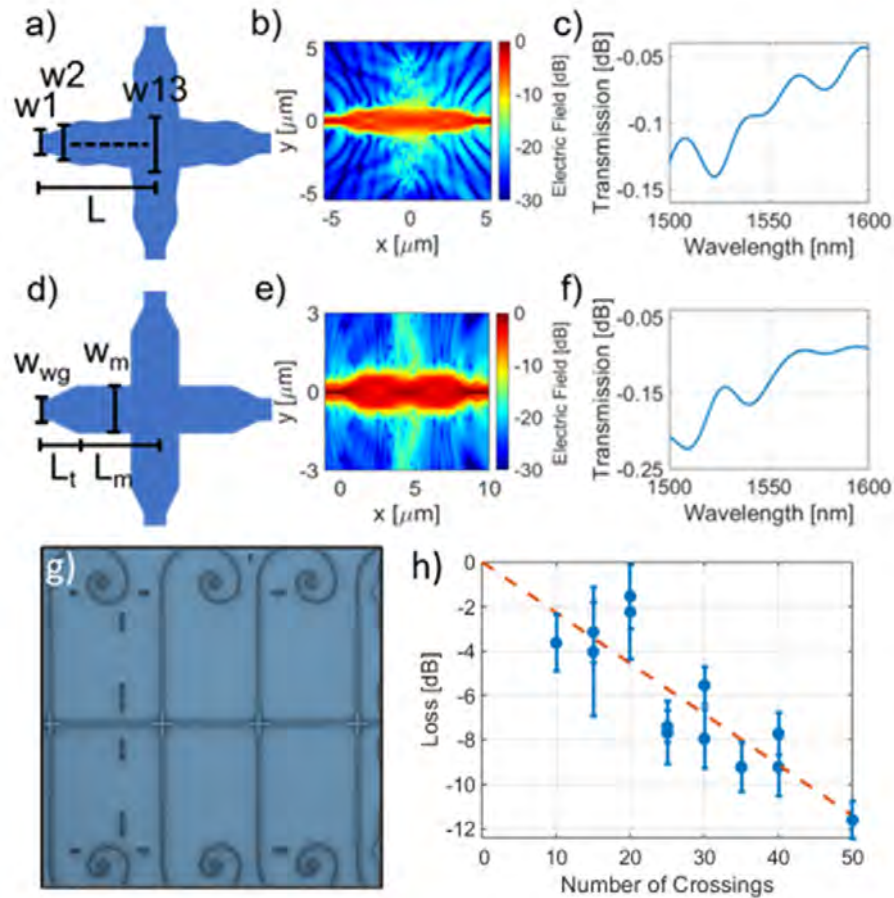


Figure 4.4: a) Schematic image of the simple waveguide crossing design. The relevant design variables are indicated on the image. b) Simulated mode profile for the optimized simple crossing design. The beating between the higher order modes and the fundamental mode results in a maximum electric field intensity in the center of the waveguide at the crossing, which minimizes the coupling to the vertical waveguide. c) Simulated transmission through the simple waveguide crossing as a function of the wavelength. d) Schematic image of the 13-width crossing design where a swarm optimization varies the width of the parabolic taper at 13 locations and minimizes the transmission loss. e) Simulated mode profile of the optimized 13-width crossing. f) Simulated transmission through the 13-width crossing design as a function of wavelength. g) Optical image of cascaded waveguide crossings for loss characterization. h) Normalized waveguide crossing transmission loss at a wavelength of 1550 nm using the cutback method. The orange trend line indicates an insertion loss of 0.23 dB/crossing.

multimode interference-based crossings [12–14], and subwavelength gratings [15]. Many of these methods involve additional fabrication steps that can introduce excess loss and

system design and fabrication challenges. A basic approach for a waveguide crossing relies on tapering an input single-mode waveguide section into a larger waveguide cross section that can support higher-order modes and relies on the beating between the fundamental mode and the higher-order mode to create an electric field maxima that is centered in the waveguide at the crossing location. By focusing the mode into the center of the wide waveguide, evanescent coupling to the perpendicular waveguide is minimized. This design can be completed with a basic linear taper (which will be referred to as a “simple crossing”), or a more complex structure. Here, we consider simulations of both simple and inverse-design crossings and report results from an inverse design approach (which will be referred to as a “13-width crossing”) that utilizes 13 different widths in a parabolic taper that requires no additional fabrication steps and maintains low-loss and high-isolation transmission. This second design utilizes a swarm optimization protocol such that the optical mode is transmitted with minimal coupling to the crossed waveguide.

The simple crossing design is illustrated in Fig. 4.4a) and uses the beating between the fundamental and higher-order mode to create a confined optical mode centered at the location of the crossing. The beat length, L_π , is defined as $L_\pi = \pi/(\beta_0 - \beta_1)$ where $\beta_{(0,1)}$ are the propagation constants of the fundamental and first-order waveguide modes, respectively. For a $1.5 \mu\text{m}$ multimode waveguide width (w_m), the fundamental and first-order TE modes have effective indices of approximately 3.00 and 2.87, respectively, at a wavelength of 1550 nm. Using these effective indices, the beat length is calculated as $5.95 \mu\text{m}$. This approach is similar to the discussion of coupled mode theory for pulley couplers to ring resonators (included in Section 2.2.2). Finite difference time domain (FDTD) simulations were utilized to account for the transition region between the single-mode waveguide and the wider, multimode waveguide as well as allow for a larger bandwidth crossing to be designed where the average loss across a 100 nm bandwidth

is utilized instead of maximizing at a single wavelength. The simulated mode profile for the simple crossing design and the simulated transmission through the device is shown in Fig. 4.4b,c), respectively. From the mode profile simulation, it is clear that the beating between the fundamental and higher order mode create a local maxima at the location of the crossing that minimizes the optical mode scattered into the perpendicularly oriented waveguide. The simulated loss through this structure is 0.15 dB at a wavelength of 1550 nm.

Figure 4.4d) shows the 13-width waveguide crossing with critical dimensions depicted. This design utilizes a swarm optimization protocol in an FDTD solver to optimize the transmission through the crossing by allowing the width to vary at 13 equally spaced sections along the taper. A parabolic interpolation between the 13 widths ensures a smooth transition between the various widths. The 13-width crossing design was also optimized for a bandwidth of 100 nm to maintain low-loss performance of the crossing across a broad bandwidth, which will be compatible with broadband entangled photon pair generation in quantum photonic circuits. Lower loss structures can be made when optimizing for a smaller bandwidth. Starting with an input waveguide width of 400 nm and total crossing length (L) of 9 μm , the optimizer was allowed to vary the widths w_2 - w_{13} between 200 nm and 2000 nm. Figure 4.4e) shows the electric field profile for the optimal crossing design at a wavelength of 1550 nm, and Fig. 4.4f) plots the simulated transmission through the waveguide crossing as a function of the input wavelength. This crossing design has a simulated loss of approximately 0.1 dB at a wavelength of 1550 nm. Since the loss of the 13-width crossing design is smaller than the simple crossing design, the 13-width crossing was fabricated and tested initially.

With the simulated waveguide crossing loss on the order of 0.1 dB, the cutback method [13] is used to measure the loss per crossing to remove coupling-dependent loss and reduce detector sensitivity limitations. For the 13-width crossing, waveguides with

between 10 and 50 crossings were fabricated, and the loss through each line of crossings was measured across eight trials with complete re-alignment of the input and output fibers for each trial to remove any systematic variations due to coupling loss. Figure 4.4g) shows a microscope image of a few of the waveguide crossings in one of the lines. The vertical waveguide channels are terminated with tapered waveguides in a spiral geometry to prevent back-reflections into the crossing. The horizontal spacing of the crossings is varied randomly between $25 \mu\text{m}$ and $35 \mu\text{m}$ to avoid photonic cavity effects. Using the cutback method, the transmission through the crossings was measured at a wavelength of 1550 nm , and the results are shown in Figure 4.4h). The dashed line indicates a linear fit of the loss as a function of the number of crossings, providing an estimated loss of 0.23 dB/crossing . The error bars on the data points indicate the standard deviation of the eight independent measurement trials.

These results for the $13\text{-}\mu\text{m}$ width waveguide crossing (Fig. 4.4h) indicate that the fabricated crossings have slightly higher loss than the simulated loss at a wavelength of 1550 nm . This additional loss is likely due to fabrication variations in the widths along the device; the inverse design is more sensitive to fabrication variation than the use of a simple waveguide crossing. The measured 0.23 dB of loss for the AlGaAsOI $13\text{-}\mu\text{m}$ width crossing is comparable to the 0.2 dB of insertion loss reported from a genetic algorithm-designed SOI waveguide crossing [16] and less than the loss of 0.3 dB from silicon nitride waveguide crossings [17]. Other manuscripts report $\leq 0.1 \text{ dB}$ of insertion loss for elliptical tapers [18] and even on the order of 0.02 dB for sub-wavelength grating-based structures [19]. Reference [14] compares various results of waveguide crossing on the SOI platform.

4.3 Beamsplitters

A standard building block in both classical and quantum PICs is the beamsplitter. The beamsplitter allows for the electromagnetic wave amplitude to be distributed across two (or more) waveguides with a desired splitting ratio. It is also a necessary sub-component of many other fundamental photonics components including interferometers, filters, and ring resonators (as previously introduced in 2.2.2). One of the more common objectives is to split the input signal perfectly in half to two output waveguides, which is known as a 3-dB beamsplitter or 3-dB coupler. In QPICs, 3-dB couplers are utilized to distribute light evenly between two waveguides, to interfere single photons, and to serve as a component for tunable Mach-Zehnder Interferometers (MZIs) for programmable PICs. This places strict requirements on the devices, such as low loss for potential scalability, a large bandwidth to support broadband quantum light generation, and precise splitting ratios to maximize the extinction ratio and minimize cross-talk in MZIs. We explore two designs for creating on-chip 3-dB couplers: directional couplers (DCs) and multimode interferometers (MMIs). The first coupler design based on DCs uses the overlap of evanescent modes between two neighboring waveguides, allowing the mode to fully couple into the adjacent waveguide. The full crossover length relies on the difference in refractive index between the even and odd supermodes created when two waveguides are in close proximity. DCs are straightforward couplers to design and are capable of any splitting ratio by adjusting the coupling length, but they are also more susceptible to fabrication imprecision and errors compared to MMIs. MMIs are based on the self-imaging principle, similar to the aforementioned simple waveguide crossings; however, unlike in the waveguide crossing design, the beat length between the two modes, L_π , is used to calculate the core length necessary to achieve a splitting ratio as close to 3-dB as possible.

4.3.1 Directional Couplers

The basic principles of directional couplers have already been introduced in the section on pulley couplers for ring resonators, Section 2.2.2. Since pulley couplers are a form of directional coupler, the approach to design directional couplers for beamsplitting follows a similar approach. Here, the design is even more straightforward since both waveguides are selected to be the same width, w_{wg} , and without a bend (meaning the propagation constant will be identical in both waveguides and phase matching is trivial). Figure 4.5a) illustrates a common directional coupler design. Symmetric sine bend waveguides on the input and outputs with transverse displacements of x_{off} and y_{off} enable light to propagate into the coupling region. The minimum radius of these sine bends is kept to $20 \mu\text{m}$ to reduce bending loss. The separation between the waveguides in the coupling region where the evanescent modal overlap occurs is w_{gap} , and the coupling length is L_{DC} .

To determine the coupling behavior between two waveguides in a directional coupler, Lumerical Mode simulations are utilized to determine the effective indices of the first and second supermode that exists between the two waveguides. Figure 4.5b) and c) illustrate the first and second TE supermode for two AlGaAs waveguides with 400 nm widths and 400 nm heights separated by a 300 nm gap. Much like the pulley coupler case, we can determine the coupling between the two waveguides with [20, 21],

$$\kappa^2 = \frac{P_{transferred}}{P_0} = \frac{\sin^2 \left(CL\sqrt{1 + (\Delta\beta/2C)^2} \right)}{1 + (\Delta\beta/2C)^2} \quad (4.7)$$

where P_0 is the initial power, $P_{transferred}$ is the power transferred to the other waveguide, L is the coupling length, and C is the coupling coefficient (also defined in the pulley

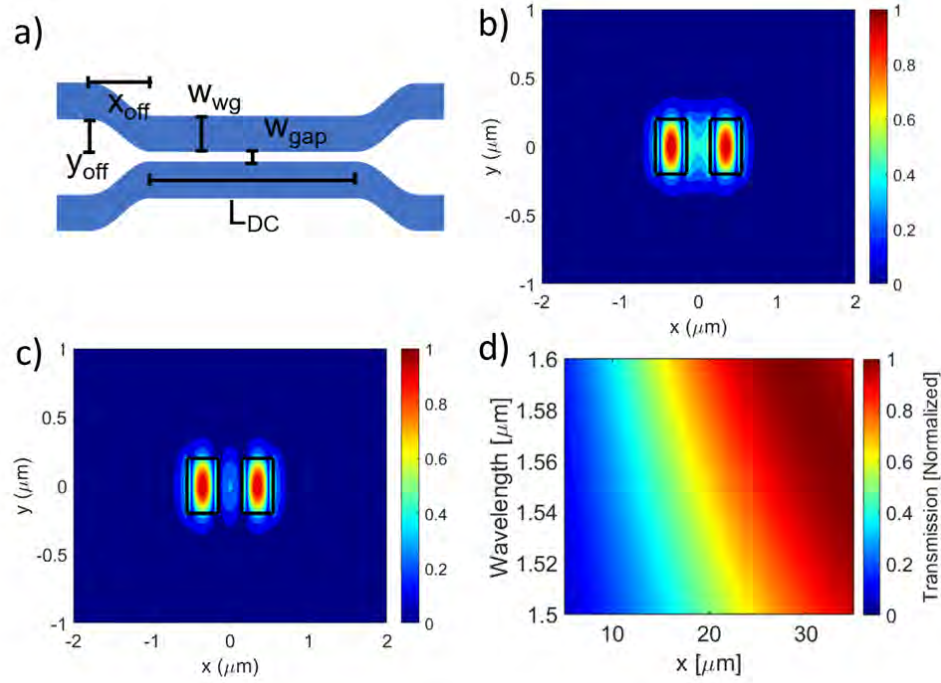


Figure 4.5: a) Directional coupler with relevant design parameters labeled. b) The first TE supermode for a pair of two waveguides with 400 nm width and 400 nm height separated by a 300 nm gap. c) The second TE supermode. d) FDTD simulation of the power transferred to the lower waveguide of the directional coupler including the input/output sine bends.

coupler section 2.2.2) [20–22],

$$C = \frac{\pi \Delta n}{\lambda} \quad (4.8)$$

where Δn is the different in the effective index of supermode 1 and 2.

The form of Equation 4.7 has been expanded to include mismatch between the propagation constants of the two waveguides. However, by selecting identical waveguides, the equation is simplified since $\Delta\beta = 0$,

$$\kappa^2 = \sin^2(CL) \quad (4.9)$$

The power transfer between the two waveguides has a \sin^2 dependence, so the power

oscillates between the two waveguides as a function of length. Thus, by selecting a length where the power is split in half ($\sin^2(CL) = 1/2$), a 3-dB (50/50) directional coupler can be made. The length at which all of the power transfers from the initial waveguide to the secondary waveguide is the crossover length, and can be determined by,

$$L_x = \frac{\lambda}{2\Delta n} \quad (4.10)$$

For the supermodes shown in Figure 4.5b) and c), the effective index difference is 0.0185, indicating that for 1.55 μm wavelength the crossover length is approximately 41.9 μm . Thus, for 3-dB coupling, a length of ~ 21 μm can be used. Reducing the gap between the two waveguides increases the effective coupling rate, allowing for more compact directional couplers to be designed.

In general, the supermode approach can provide a reasonable estimate on the length required for a particular beamsplitting ratio. However, it is important to note that this calculation simplifies the full structure (shown in Figure 4.5a). Since the sine bends into and out of the coupling region are adiabatic and gradual, there is some evanescent coupling that occurs in these regions (in addition to the coupling region). Thus, for a better understanding of the true coupling length for 3-dB splitting, Lumerical FDTD simulations are used. The result of the full structure simulated in FDTD is shown in Figure 4.5d). The addition of these input/output bends reduces the crossover length considerably (to ~ 34 μm from ~ 42 μm using just coupled mode theory). Thus, the actual devices were designed using the results of the FDTD simulation instead of the coupled mode theory results. One important thing to note is that the directional coupler response has a strong wavelength response (as evident in Figure 4.5d), so for broadband applications, alternative structures like adiabatic couplers [23] or multimode interferometers (next section) should be used.

4.3.2 Multimode Interferometers

For applications that require broader bandwidth operation or the creation of devices that are less sensitive to fabrication variation, multimode interferometers (MMIs) can offer a great alternative to directional couplers for beamsplitting. An example MMI schematic is shown in Figure 4.6a). Here, a 2x2 MMI is shown, but other combinations of input/output ports are designed following the same approach. The input waveguide at width, w_1 is tapered gradually to w_2 at the beginning of the core MMI region (width w_{core}). The core length, L_{core} is determined by the desired splitting ratio of the output waveguides. The electric field in the wide core region can exist in many modes, and the interference between these different modes in the core creates the pattern shown in Figure 4.6b) which is calculated using FDTD in Lumerical.

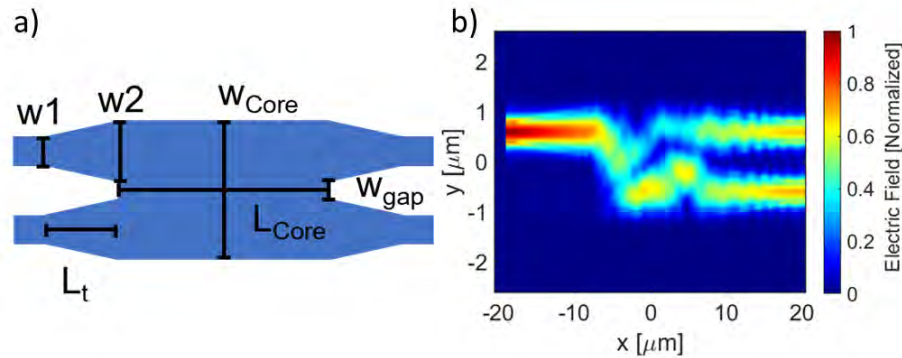


Figure 4.6: a) Schematic illustration of a multimode interferometer with the relevant design parameters. b) Simulated mode profile of an $Al_{0.2}Ga_{0.8}As$ MMI depicting 3-dB coupling behavior with a length near $16.0 \mu m$. Here, the waveguide is tapered from $w_1 = 0.4 \mu m$ to $w_2 = 0.9 \mu m$ in over $L_t = 10 \mu m$. The core width is $2.1 \mu m$, and the length is $18.75 \mu m$.

The operation of MMI couplers is based on the self-imaging effect of multimode interference [24]. The superposition of the many guided modes in a multimode waveguide

leads to a local field distribution ($\Phi(x, z)$) at any position of the core of the MMI [25, 26],

$$\Phi(x, z) = \sum_m c_m \phi_m(x) \exp(-j\beta_m z) \quad (4.11)$$

where c_m is the expansion coefficient for the m -th eigenmode with field ϕ_m and propagation constant β_m .

The beat length L_π (or self-imaging length) is defined by the interference of the 0th and 1st mode,

$$L_\pi = \frac{\pi}{\beta_0 - \beta_1} \approx \frac{4n_r W_e^2}{3\lambda_0} \quad (4.12)$$

where λ_0 and n_r are the free-space wavelength and refractive index of the core, and W_e is the effective width of the core. Because the beat length scales with the MMI core width, a narrow width is often chosen to reduce the component footprint.

For the initial MMIs designed, a core width of $2.1 \mu\text{m}$ was selected. Symmetric input and output tapers expand the mode from a waveguide width of $0.4 \mu\text{m}$ to $0.9 \mu\text{m}$ nearest to the core. A $0.3 \mu\text{m}$ separation leaves no excess core width beyond the dimensions of the tapers in an effort to reduce Fabry-Perot effects due to reflections. The core length design began by first calculating the beat length from mode simulations and multiplying it by a factor of 1.5 (to obtain 3-dB splitting after 1 cycle of self-imaging), resulting in $L_\pi = 18.75 \mu\text{m}$. The full device was then simulated using Lumerical FDTD, and the electric field profile is shown in Figure 4.6b). The FDTD simulations again differ slightly compared to the mode-based calculations due to the presence of the input/output mode tapers which are not considered in the simple beat length calculation. With a combination of the calculated beat length and FDTD simulations, a core length of $17.2 \mu\text{m}$ was chosen for 3-dB splitting.

Both MMIs and directional couplers have their importance in integrated photonic

circuits. Directional couplers are more straightforward to design, and typically can have lower loss than MMIs due to the waveguides remaining unconnected (reducing back-reflections). MMIs are more tolerant to fabrication variation and less sensitive to wavelength, allowing for more consistent performance and broadband operation. Both components could be used for the larger circuits designed in Chapter 6 of this dissertation, but due to the ease of design and fabrication, directional couplers are primarily used.

4.4 Optical Filters

On-chip optical filters and demultiplexers are critical components as they allow for the separation of the signal and idler photons from the initial, uncorrelated pump photons and allow for the manipulation of signal and idler photons independently. This can be especially useful for heralded single photon-based applications as the signal (or idler) photon can be sent directly to a detector for heralding while the idler photon can be sent through a series of quantum gates or operations. There are several strategies that can be used for pump filtering or demultiplexing [27], but here the focus will be on unbalanced MZI filters, coupled resonator optical waveguides (CROW), and ring-based spectral pulse shapers. Additionally, photonic interleavers where a ring resonator is placed into the arm of a MZI are explored as a route to improve the performance of MZIs.

4.4.1 Filter Performance Metrics

The shape of an optical filter is critical in determining which filters to use for particular applications. Common filter shapes include bandpass, low-pass, high-pass, notch, and interference filters. Each type serves a distinct purpose in manipulating the transmission or reflection of light within a specified wavelength range. Bandpass filters allow for a specific range of wavelengths to be transmitted while blocking other wavelengths.

Low-pass filters permit only wavelengths below a threshold wavelength to pass, and high-pass filters permit only wavelengths above a particular wavelength to pass. Notch filters block only a particular band of wavelengths, and transmit other wavelengths. Interference filters rely on the interference of light waves to periodically transmit/block certain wavelengths, commonly resulting in a sinusoidal response as a function of wavelength. Ring resonators in the all-pass configuration (as introduced in Section 2.2.2) can act as narrow notch filters where the resonance wavelengths are blocked from transmission and off-resonance wavelengths are transmitted. Adding a second bus waveguide to the ring resonator creates an add-drop configuration, and the drop port of the resonator will have a bandpass filter response (where the resonant wavelengths are transmitted). High- and low-pass filters can be made using absorption or waveguide engineering to sustain only particular modes. In the following section, Mach-Zehnder interferometers will be introduced which are a very commonly used interference-based optical filter.

Generally, the most important performance metrics of optical filters are the extinction ratio, insertion loss, and bandwidth. The extinction ratio of an optical filter is commonly defined as the ratio of the minimum optical power transmitted to the maximum power transmitted. High quality filters typically have extinction ratios on the order of 30 dB, meaning that 99.9% of the initial signal is blocked. For quantum photonic experiments, single photon detectors are often utilized, requiring extremely high extinction rates to block photons at undesired wavelengths. Since single photon count rates of ~ 10 counts per second at $1.55 \mu\text{m}$ wavelength have ~ -150 dBm of power, full rejection of the pump wavelength to reasonable single photon count rates can typically require > 120 dB extinction. Importantly, this extinction must be met with the lowest amount of loss of the quantum signal as possible. The insertion loss of a filter characterizes how much loss the transmitted light experiences when going through the filter. For chip-scale filters, the biggest contribution to this loss is the fiber-to-chip coupling efficiency, while bulk optics

can experience loss from reflections, connections, or other effects like mode conversion and focusing. Lastly, the filter bandwidth is important in determining which wavelengths are filtered and how sensitive the filter is to misalignment. The filter bandwidth is typically reported at a particular extinction level (for example 10-dB bandwidth). For this work, the optical filters are utilized to separate generated signal and idler photon pairs generated from nonlinear quantum light sources. Since the source is typically a ring resonator, the filters must have bandwidths that are smaller than the free spectral range of the ring resonator (such that only one resonant mode can be transmitted through the filter). The bandwidth should also be large enough that the filter shape can fully cover the (for example) pump spectral shape. If the bandwidth is too narrow, undesired photons can reach the single photon detectors.

4.4.2 Mach-Zehnder Interferometers

As introduced briefly, Mach-Zehnder Interferometers are a form of interference-based filters that are commonly used for on-chip optical filters. Unbalanced MZI-based filters utilize the interference between photons that travel along the two paths (one being longer than the other). The MZI response has a sinusoidal transmission versus wavelength as different wavelengths accumulate different relative phases when traveling the two paths. The length of the imbalance in the two paths provides a means to control the free spectral range (FSR) or spacing between the perfectly constructive interference peaks. Placing a thermo-optic phase shifter on one of the paths (arms) enables the tuning of the peak locations such that they align with a desired frequency mode. An unbalanced MZI can provide high extinction ratio filtering exceeding 30 dB (with cascaded designs exceeding even 60 dB) [28].

Tunable MZIs are a key component in QPICs, playing an important role for numer-

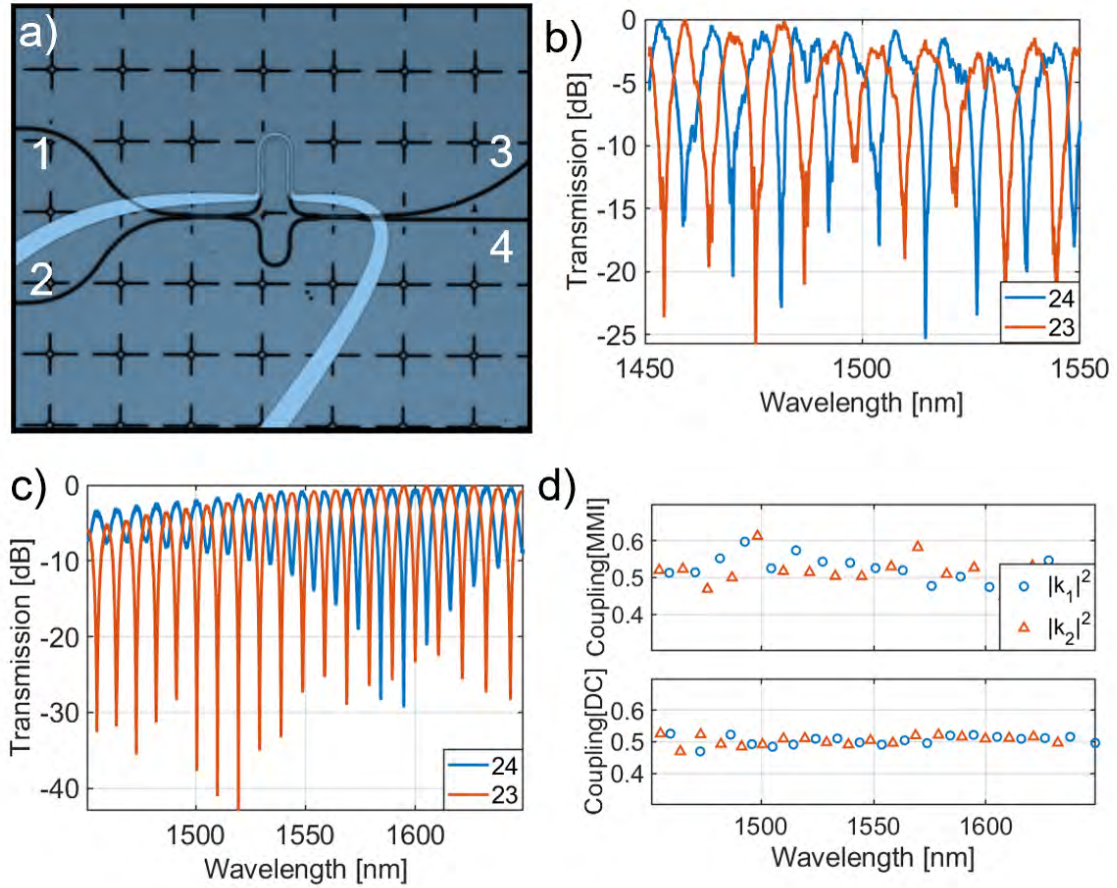


Figure 4.7: a) Optical image of an AlGaAs MZI with DCs and a $45 \mu\text{m}$ path imbalance. b,c) Transmission spectra of the 2-4 and 2-3 port combinations of an MZI with MMIs (b) and DCs (c). The MMIs have parameters matching the simulations in Figure 4.6. The directional couplers consist of 400 nm wide waveguides with a 300 nm coupling gap and a $20.8 \mu\text{m}$ coupling length. d) Extracted coupling coefficients for the DCs and MMIs in the MZIs indicating near-optimal 3-dB coupling.

ous functions, including as reconfigurable postselected entangling gates (R-PEGs) [29], demultiplexers [30], variable beamsplitters [28], filters [31], and single photon quantum logic gates [29]. In an MZI, a 3-dB coupler splits light evenly into two different paths that may be equal (balanced MZI) or unequal (unbalanced MZI) in length, which then recombine with another coupler. Here, we focus on two variations of thermo-optically tunable unbalanced MZIs employing both DCs and MMIs. Figure 4.7a) shows an optical

image of an MZI utilizing DCs as couplers with a 45 μm path imbalance on the top arm with the metal thermal tuner above the 1 μm thick cladding to sweep and control the MZI phase. One advantage of thermo-optic tuning with AlGaAs is its inherent large thermo-optic coefficient, which, for an MZI with a 60 μm path imbalance and a 10.28 nm free spectral range (FSR), allows for a full 2π phase sweep with $20 \text{ mW}/\pi$ efficiency, which is 10 (0.6) times more efficient than silicon nitride [32] (silicon [33]) designed for similar QPIC applications.

These devices were designed using the transfer matrix method [34], where each component of the MZI can be represented by a matrix: two equivalent matrices for the 3-dB couplers, and a standalone matrix representing the path imbalance. The coupler scattering matrices can be represented by,

$$C = \begin{bmatrix} \cos \theta & -j \sin \theta \\ -j \sin \theta & \cos \theta \end{bmatrix} \quad (4.13)$$

where the power coupling and transmission coefficients of the DC (or MMI) are $\kappa^2 = \sin^2 \theta$ and $\tau^2 = \cos^2 \theta$. The path length difference between the two arms, ΔL , results in an accumulation of phase in the longer arm $\phi = \frac{2\pi n_{\text{eff}} \Delta L}{\lambda}$ (here taken as the top arm) [34],

$$T = \begin{bmatrix} \exp(-j\phi) & 0 \\ 0 & 1 \end{bmatrix} \quad (4.14)$$

Thus, the full MZI can be expressed by the transfer matrix $S = CTC$ where we have assumed the input and output couplers are perfectly identical. We can use these matrix formulations to determine the power coupling between the ports. Simplifying for lossless

3-dB couplers, the transfer matrix simplifies to,

$$S = je^{j\phi/2} \begin{bmatrix} \sin \frac{\phi}{2} & \cos \frac{\phi}{2} \\ \cos \frac{\phi}{2} & -\sin \frac{\phi}{2} \end{bmatrix} \quad (4.15)$$

The transmission spectrum of MZIs with MMIs and DCs are shown in Figure 4.7b) and Figure 4.7c), respectively, for two different input/output configurations. We observe an ER above 10 dB across ≥ 100 nm bandwidth for through ports and ≥ 200 nm for cross ports, comparable to silicon MZIs [31, 35]. With the wavelength-dependent ER measurements, the true coupling coefficient κ of each coupler can be extracted [34], as shown in Figure 4.7d). The DC (MMI) couplers exhibit an average coupling coefficient of 0.501 ± 0.03 (0.52 ± 0.11) across a 100 (200) nm bandwidth centered at 1570 (1550) nm. Since many MZIs are required for a complete QPIC, the loss across each device must be minimized, and each coupler should exhibit as close to a 3-dB splitting ratio as possible to achieve a maximum extinction ratio, defined here as the power ratio of neighboring MZI fringes in the transmission spectrum.

4.4.3 CROW Filters

Another strategy to create chip-scale optical filters is the use of coupled resonator optical waveguide (CROW) filters which couple two or more rings in series to create a high extinction ratio, narrowband filter. Single rings act as filters—they allow only resonant wavelengths to be transmitted through the drop port of the resonator. By coupling multiple identical rings, the rings act together to provide additional filtering. Figure 4.8a) shows a schematic of two rings coupled in series to form a CROW filter. The response of this device can be solved using the transfer function method discussed in Section 2.2.2. For a double-ring (or second-order) CROW filter, the transmission

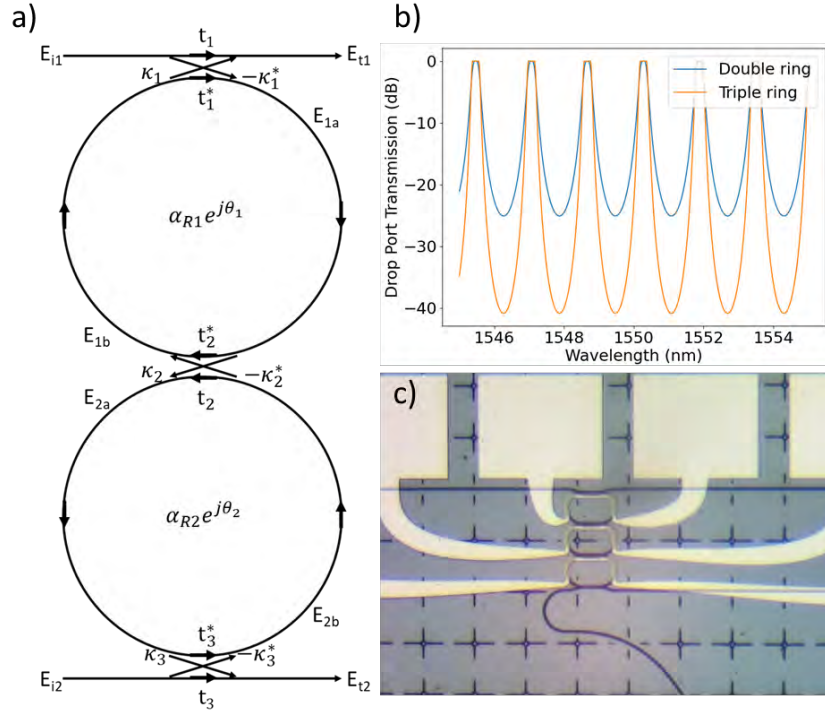


Figure 4.8: a) Schematic of a double-resonator CROW filter with the relevant coupling and transmission coefficients labeled. b) Simulated transmission through the drop port of the coupled resonators. The plot shows the expected trend for two rings and three rings coupled in series. The rings here are designed using 400 nm thick $\text{Al}_{0.2}\text{Ga}_{0.8}\text{As}$ with waveguide widths of 690 nm and radii of 20 μm . The loss is assumed to be 0.4 dB/cm and $\kappa_1^2 = \kappa_3^2 = 0.5$ and $\kappa_2^2 = 0.1$. c) Microscope image showing the fabricated CROW filter device.

response is [36],

$$T = \frac{|\kappa_1^2 \kappa_2 \alpha_1 \alpha_2|^2}{\left| 1 - \sqrt{(1 - \kappa_1^2)(1 - \kappa_2^2)} (\alpha_1 e^{-j2\theta_1} + \alpha_2 e^{-j2\theta_2}) + (1 - \kappa_1^2) \alpha_1 \alpha_2 e^{-j2(\theta_1 + \theta_2)} \right|^2} \quad (4.16)$$

where the parameters are defined in Figure 4.8a) and we have assumed that $\kappa_3 = \kappa_1$, and κ_i are the coupling coefficients, θ_i are the half round-trip phase delay of rings 1 and 2, and α_i are the half round-trip loss coefficients [37]. A full derivation of the transfer functions for the second-order and third order CROW filters can be found in Reference [36].

Figure 4.8b) shows the modeled transmission through the drop port of a second- and

third-order CROW filter on the AlGaAs platform. The drop port response has a flat shape at the transmitted wavelengths and has > 40 dB extinction for the third-order filter. The filter shape is useful in separating entangled photon pairs due to its free spectral range that can be aligned to select pairs of photons generated from a quantum light source. These filters have been employed for quantum photonic circuits in silicon with impressive, 96 dB extinction when two second-order CROWs are cascaded [37]. Figure 4.8c) shows AlGaAs CROW filters designed and fabricated at UCSB. The heaters on each ring can be used to tune the filter such that the maximum extinction ratio is achieved.

4.4.4 Interleavers

In the MZI section above (Section 4.4.2), the behavior of MZIs was introduced for use as an interference-based optical filter. The response which is sinusoidal in nature, is not necessarily ideal for circuits and devices that may have some variation in the exact spacing of signal and idler entangled photon pair frequencies. Instead, it is desirable to have a filter with a flat transmission band such that small variations in the the wavelengths still have maximal transmission through the filter. The previous section showed that CROW filters can have this characteristic, but their performance is quite sensitive to the inter-ring coupling, and thermal crosstalk makes it more difficult to align the rings. An alternative route to achieve a flat, high-extinction filter is to use a ring-assisted Mach-Zehnder interleaver [38]. A microscope image of the device is shown in Figure 4.9a). Following the transfer function approach used for MZIs and ring resonators, the output electric field of the top (port 1) and bottom (port 2) ports of the interleaver can be expressed as,

$$\begin{bmatrix} E_{out,1} \\ E_{out,2} \end{bmatrix} = \begin{bmatrix} t_2 & k_2 \\ -k_2^* & t_2^* \end{bmatrix} \begin{bmatrix} T(\omega)e^{j\phi_1} & 0 \\ 0 & e^{j\phi_2} \end{bmatrix} \begin{bmatrix} t_1 & k_1 \\ -k_1^* & t_1^* \end{bmatrix} \begin{bmatrix} E_{in,1} \\ E_{in,2} \end{bmatrix} \quad (4.17)$$

where $T(\omega)$ is the ring resonator transfer function, ϕ_i is the phase shift of the top ($i = 1$) and bottom arm ($i = 2$), $k = j\sqrt{K}$ is the coupling coefficient, and $t = \sqrt{1-K}$ is the transmission coefficient. The form of this equation is $E_{out} = C_2TC_1E$ which is identical to the MZI transfer function derived above (Section 4.4.2). The only change here is that T now includes the path imbalance as well as the ring resonator transfer function. A full discussion can be found in Reference [38].

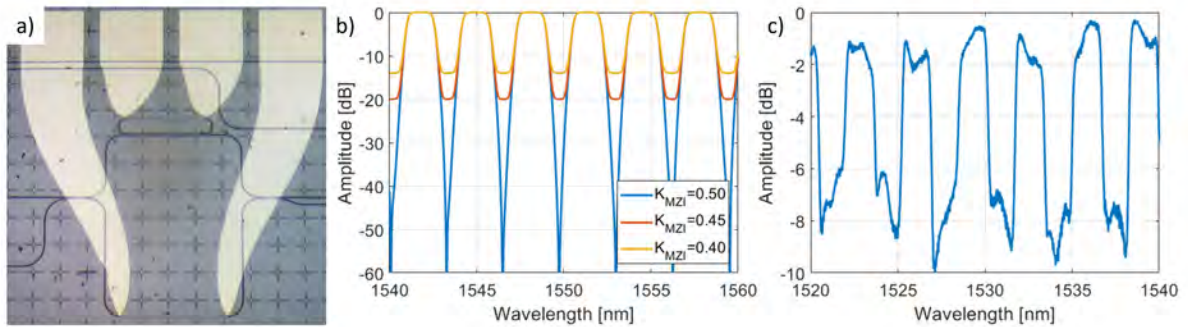


Figure 4.9: a) Microscope image of a ring-assisted Mach-Zehnder interleaver device. b) Simulated transmission through the interleaver as a function of the coupling coefficient of the directional coupler on the input and output of the MZI. The device was designed with a $62 \mu\text{m}$ radius ring, $195 \mu\text{m}$ path imbalance, and waveguide widths of 600 nm . The waveguide to ring coupling was designed using a $140 \mu\text{m}$ coupling length with 275 nm gap. c) Experimental transmission scan showing 10 dB extinction for an interleaver device designed to match the simulation parameters.

Figure 4.9b) shows the simulated transmission of an AlGaAsOI interleaver designed with a $62 \mu\text{m}$ radius ring, $195 \mu\text{m}$ path imbalance and 90% coupling between the bus waveguide in arm 1 and the ring resonator. This resonator coupling is critical in maintaining a flat filter shape. The device optimally works when the input and output directional couplers are perfectly 3-dB splitters (the same is true for MZIs). The different traces in the plot of Figure 4.9b) show how the extinction ratio degrades for imperfect splitting

ratios. This device was fabricated and tested, with the transmission scan shown in Figure 4.9c). The extinction ratio is only 10 dB (much less than the expected 60 dB from the simulation). It is likely that the directional couplers are not perfectly 3-dB splitters, resulting in a reduced extinction ratio for the real device. The transmission, however, is quite flat, indicating that the bus-to-ring coupling is likely close to ideal. Since this extinction ratio is worse than the individual MZIs, a future redesign is needed for these devices to act as viable interleavers. At their current performance, they are both more challenging to use (since the ring resonator has to be tuned along with the phase of the arms) and lower performance than standard MZIs. There is, however, hope that these components can serve as higher extinction, flatter filters for QPICs in the future.

4.4.5 Pulse Shaper

Encoding quantum information in narrow, evenly spaced frequency bins has emerged as a novel scheme for quantum information processing (QIP) as it is compatible with dense spectral multiplexing networks commonly used in telecommunications. One of the key advances in the field was the development of a quantum frequency processor which is a photonic device comprised of an alternating sequence of electro-optic phase modulators (EOMs) and Fourier-transform pulse shapers [39]. An input quantum state of frequency-bin encoded qubits (or qudits) enters the quantum frequency processor where the EOM serves as a frequency mode mixer and the pulse shaper applies a specific phase pattern to get either constructive or destructive interference in the different frequency bins. This technology has been demonstrated to implement numerous quantum gate operations and even simulations [39–42]. Although these demonstrations are exciting, one of the next steps is to create a route toward a scalable, all on-chip quantum frequency processor with integrated biphoton frequency comb sources, EOMs, and pulse shapers. Hopefully,

the improved nonlinear efficiency of AlGaAsOI sources along with the ability to design EOMs and pulse shapers on the platform will enable an integrated demonstration in the next few years. The vision is illustrated in Figure 4.10 where an integrated quantum frequency comb source (ring resonator) is used to generate frequency-bin qubits which are filtered and have phases applied in the pulse shaper before being mixed using a fast electro-optic modulator. The integration of all of these components would significantly reduce the overall system loss and improve the efficiency.

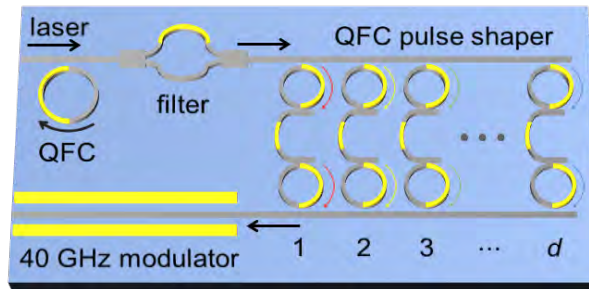


Figure 4.10: Motivation for frequency-bin quantum information processing using electro-optic modulators and pulse shapers. A quantum frequency comb is generated using a microring resonator and sent through an integrated pulse shaper to apply phases to particular frequency modes. The output is mixed using a fast electro-optic modulator.

As a first step, AlGaAsOI pulse shapers with 6 channels were fabricated and tested. A microscope image of the fabricated pulse shaper is shown in Figure 4.11a). Six ring resonators with $31 \mu\text{m}$ radii are aligned using thermo-optic heaters to the desired frequencies of the pulse shaper. The drop port of each ring has a snaking waveguide with a long phase shifter such that up to 2π phase can be applied to the dropped frequency channel. A second ring is used to add the phase shifted signal back to the upload channel. The coupling of rings was designed to be overcoupled such that the resonance linewidth was near 2 GHz. This selection was made to allow for near unity filtering of a quantum frequency comb with 100s of MHz linewidth. Thermal tuners are placed on each ring and the phase shifter to allow for full tuning of the device. The tuning response of each of

the top 6 rings is shown in Figure 4.11b). Since the rings had a $\sim 3.2 \mu\text{m}$ FSR, the full tuning range of the heater enables more than 1 FSR tuning for each ring. This implies full flexibility in the operating frequencies of the pulse shaper.

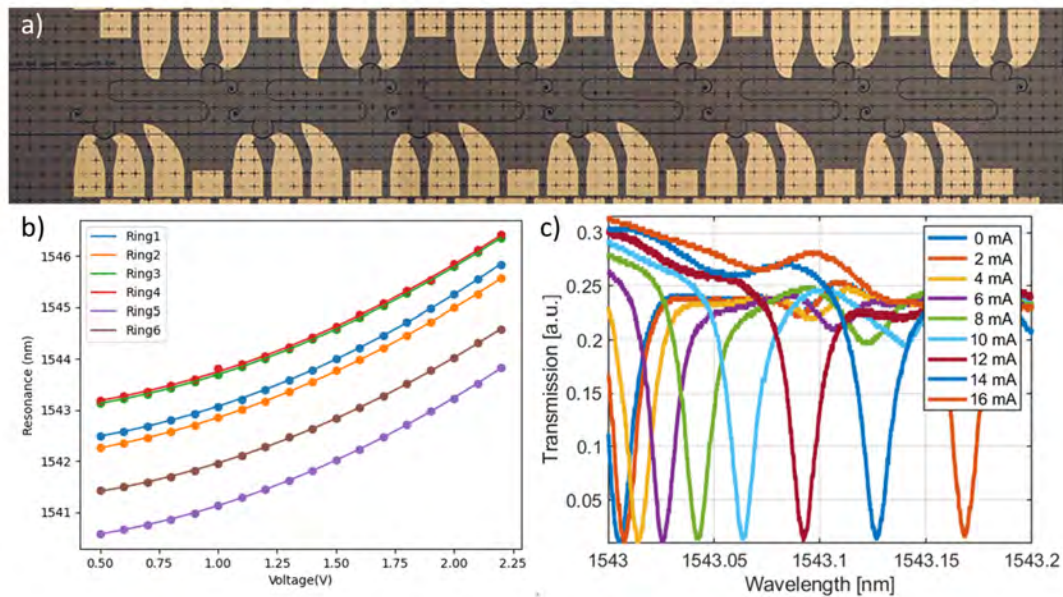


Figure 4.11: a) Microscope image of a 6 channel AlGaAsOI pulse shaper. Each ring had a $31 \mu\text{m}$ radius, 690 nm waveguide width, 350 nm coupling gap, and a coupling angle of 80 degrees. b) Tuning map of the top six rings showing >1 FSR tuning capability ($\sim 3.2 \mu\text{m}$ FSR). c) Thermal crosstalk measurement for the leftmost ring (ring 1) where the resonance location of ring 1 is monitored while the phase shifter in its drop arm is swept.

Since the heating elements are in close proximity, the effect of tuning one phase shifter (or ring) can impact the temperature of a nearby component. To characterize this behavior, traces are made where the adjacent heating elements are tuned and the impact of the resonance shift is recorded. Figure 4.11c) illustrates one of these characterizations where the phase shifter of path 1 is swept while the resonance location of ring 1 is monitored. The impact of this local heating is significant, so the alignment procedure of all channels and phase shifters becomes more complicated. Now, for each heater setting, all adjacent heaters must be adjusted to maintain alignment. An optimization protocol was devel-

oped using the pymoo multi-objective optimizer in python. Initially, four channels were aligned to show the optimization protocol. The laser frequency was set to each desired channel frequency, and the power in the through port was minimized (aligning the top ring resonator). Once the top ring was aligned, the bottom ring was aligned by maximizing the power through the upload output. As additional heaters were adjusted, the initial parameters had to be adjusted to account for thermal crosstalk. The alignment protocol (starting with coarse manual alignment) is completed in roughly 20 minutes, and shows significant improvement to just manual alignment. Figure 4.12a) shows an attempt at manual alignment while the phase shifter on channel 1 is tuned. Since ring 1 is heated via thermal crosstalk, the upload port transmission becomes misaligned, and no power exits the system. In Figure 4.12b), the result of the 20 minute optimizer is shown. The four channels remain aligned even while tuning the phase shifter on the first channel. This improvement is significant and shows the necessity of an optimizer to align the four channels. There are other approaches currently being explored such as injecting a broadband optical source and using an optical spectrum analyzer to align the channels.

One major limitation of the initial pulse shaper design is the high insertion loss of the system. As shown in the optimized transmission scan in Figure 4.12b), even with aligned channel, the uploaded signal is > 20 dB lower than the input signal. This loss can be partially attributed to a lower fabrication quality that resulted in quality factors $< 100,000$. The rings designed for this spectral pulse shaping can be redesigned to have wider waveguide widths (current widths were 700 nm) which has been shown to improve the quality factor significantly.

Even though the loss was quite large, a proof-of-principle quantum experiment was completed. The ring resonator characterized in Chapter 3 was pumped to generate entangled photon pairs. The output light was coupled into the pulse shaper, and two of the channels were tuned to filter out one pair of entangled photons. The schematic of

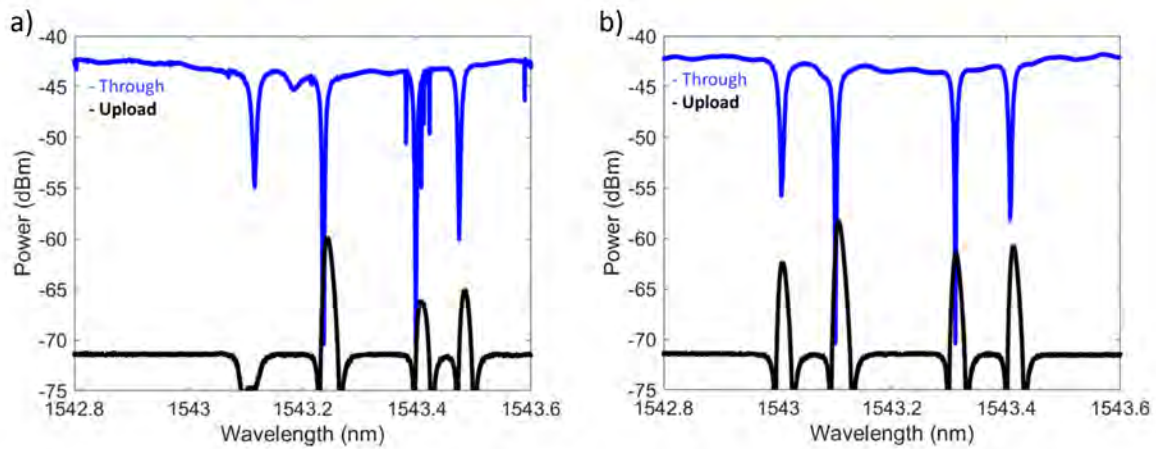


Figure 4.12: a) Manual alignment while tuning the channel 1 phase shifter. The black trace shows the transmission through the upload port and the blue trace shows the through port response. Since ring 1 is shifted due to thermal crosstalk, the upload port becomes misaligned while trying to do manual alignment. b) Optimizer result while tuning the phase shifter. The channels remain aligned as the phase shifter is tuned.

this experiment is shown in Figure 4.13a). The output single photon flux was 0.5 MHz for the idler channel and 1 MHz for the signal channel. After being filtered through the pulse shaper, the recorded flux was 1 kHz for the idler channel and 25 kHz for the signal channel. The facet coupling loss and large (> 20 dB) insertion loss of the pulse shaper justifies this significant reduction in recorded single photon counts. The flux is recorded for 1000 seconds to show the stability of the pulse shaper alignment. As shown in Figure 4.13b), the single photon counts remain consistent through the entire integration time. The coincidence peak demonstrates that the signal and idler photon time correlations are not disrupted after the pulse shaper (shown in Figure 4.13c).

The loss of the initial pulse shaper was too significant to do any novel frequency-bin quantum information processing experiments, so additional redesign and fabrication is needed. Regardless of the loss, a robust optimization protocol was developed to maintain alignment while thermally tuning other components in the pulse shaper system, and a proof-of-principle quantum experiment demonstrated the preservation of photon pair

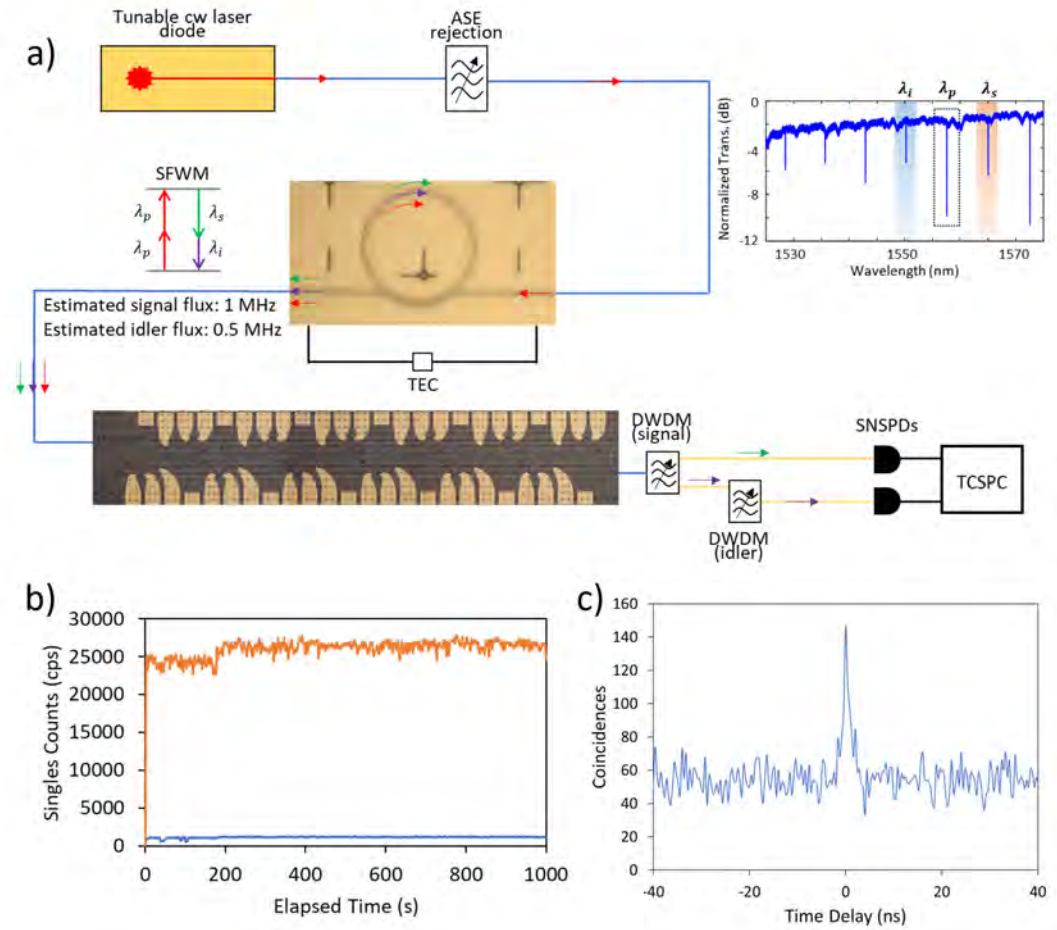


Figure 4.13: a) Experimental design using the pulse shaper to demultiplex signal and idler photon pairs from a ring resonator entangled photon pair source. A CW laser pumps the ring resonance near 1557 nm to generate a signal and idler photon at the adjacent resonances with 1 MHz and 0.5 MHz off-chip photon flux. This light is then coupled into the pulse shaper chip, and the channels are tuned to demultiplex the signal and idler photons. b) Signal photon counts (orange) and idler photon counts (blue) for 1000 seconds, showing robust alignment of the pulse shaper. The idler photon counts experience significant loss and thus are only on the 1 kHz level. c) Coincidence peak over the 1000 second integration showing the time-correlations of the photon pairs is preserved through the pulse shaper.

correlations through the spectral pulse shaper.

Table 4.1: Table comparing the AlGaAsOI platform with SOI and Si₃N₄.

	AlGaAsOI	SOI	Si ₃ N ₄
Inverse Taper Coupling Loss	2.9 dB	< 3 dB [6]	2 – 3 dB [43]
Waveguide Crossing Loss	0.23 dB	0.2 dB [16]	0.3 dB [17]
MZI Extinction Ratio	> 30 dB	> 30 dB [44]	> 40 dB [45]
MZI Bandwidth (> 10 dB ER)	200 nm Cross 90 nm Through	> 40 nm [35]	180 nm [45]
MZI Heater Efficiency	20 mW/ π (10.2 nm FSR)	12 mW/ π [33] (5.8 nm FSR)	200 mW/ π [32] (NA)

4.5 Conclusion and Outlook

In this Chapter, we demonstrate many of the fundamental components necessary to develop fully integrated quantum photonic circuits on AlGaAsOI. With high-quality entangled photon pair sources [46] and the efficient edge couplers, 3 dB splitters, waveguide crossings, and optical filters demonstrated, a plethora of application-oriented integrated quantum circuits become available. Demonstrations of chip-to-chip quantum teleportation [47], multi-photon quantum information processing [29], and other large-scale quantum photonic circuits have already been realized on the SOI platform [48, 49]. The benefits of the AlGaAsOI platform should enable more efficient demonstrations of these circuits at significantly lower optical pump power, reducing the required time to collect useful data and allowing for larger-scale circuits to be created. A summary of a few of the components discussed in this report is shown in Table 4.1 along with the performances of comparable components made on the SOI and Si₃N₄ platforms, which are also commonly used for quantum photonic circuits. It is important to note that the selected device performances were for Si and Si₃N₄ components that follow similar designs to the AlGaAsOI components that are relevant and routinely used for QPICs. For example, edge couplers with 0.35 dB of loss have been fabricated using silicon with silicon nitride,

but these were achieved with multiple layers [50]. Here we compare similar component designs across the three platforms—using only a single photonic layer and standard photolithography to fabricate the devices. Overall, the AlGaAsOI components have similar or better performance to their SOI and Si₃N₄ counterparts, indicating that AlGaAsOI-based photonic circuits will exhibit little-to-no degradation in performance compared to the current state-of-the-art platforms. Although the components detailed in this work were fabricated using a 22 mm by 24 mm bonded AlGaAs chip, wafer-scale bonding with compound-semiconductor-on-insulator is possible [51, 52], enabling larger circuits to be created in the near future. In addition to the components developed here for the 400 nm thick AlGaAsOI platform, the same methods can be used to create components for other material platforms discussed in this manuscript.

Bibliography

- [1] G. Moody, V. J. Sorger, D. J. Blumenthal, *et. al.*, *2022 Roadmap on integrated quantum photonics*, *Journal of Physics: Photonics* **4** (2022), no. 1 12501.
- [2] C. Vigliar, S. Paesani, Y. Ding, *et. al.*, *Error-protected qubits in a silicon photonic chip*, *Nature Physics* *2021 17:10* **17** (2021), no. 10 1137–1143.
- [3] C. Ma, X. Wang, V. Anant, *et. al.*, *Silicon photonic entangled photon-pair and heralded single photon generation with CAR ζ 12,000 and $g(2)(0)$ \approx 0.006*, *Optics Express* **25** (2017), no. 26 32995–33006.
- [4] R. Marchetti, C. Lacava, L. Carroll, *et. al.*, *Coupling strategies for silicon photonics integrated chips [Invited]*, *Photonics Research* **7** (2, 2019) 201.
- [5] G. Ren, S. Chen, Y. Cheng, and Y. Zhai, *Study on inverse taper based mode transformer for low loss coupling between silicon wire waveguide and lensed fiber*, *Optics Communications* **284** (9, 2011) 4782–4788.
- [6] X. Mu, S. Wu, L. Cheng, and H. Y. Fu, *Edge couplers in silicon photonic integrated circuits: A review*, *Applied Sciences (Switzerland)* **10** (2, 2020) 1538.
- [7] G. Son, R. A. Pradono, J.-B. You, *et. al.*, *Highly Efficient Broadband Adiabatic Mode Transformation Between Single-Mode Fibers and Silicon Waveguides*, *Journal of Lightwave Technology* **41** (2023), no. 21 6764–6772.
- [8] X. Qiang, X. Zhou, J. Wang, *et. al.*, *Large-scale silicon quantum photonics implementing arbitrary two-qubit processing*, *Nature Photonics* **12** (2018), no. 9 534–539.
- [9] J. Bao, Z. Fu, T. Pramanik, *et. al.*, *Very-large-scale integrated quantum graph photonics*, *Nature Photonics* **17** (4, 2023) 573–581.
- [10] A. V. Tsarev, *Efficient silicon wire waveguide crossing with negligible loss and crosstalk*, *Optics Express* **19** (7, 2011) 13732.

BIBLIOGRAPHY

- [11] J. Chiles, S. Buckley, N. Nader, *et. al.*, *Multi-planar amorphous silicon photonics with compact interplanar couplers, cross talk mitigation, and low crossing loss*, *APL Photonics* **2** (2017), no. 11 116101.
- [12] W. Chang and M. Zhang, *Silicon-based multimode waveguide crossings*, *JPhys Photonics* **2** (4, 2020) 022002.
- [13] W. Bogaerts, P. Dumon, D. V. Thourhout, and R. Baets, *Low-loss, low-cross-talk crossings for silicon-on-insulator nanophotonic waveguides*, *Optics Letters* **32** (10, 2007) 2801.
- [14] S. Wu, X. Mu, L. Cheng, *et. al.*, *State-of-the-art and perspectives on silicon waveguide crossings: A review*, *Micromachines* **11** (3, 2020) 326.
- [15] P. J. Bock, P. Cheben, J. H. Schmid, *et. al.*, *Subwavelength grating crossings for silicon wire waveguides*, *Optics Express* **18** (7, 2010) 16146.
- [16] P. Sanchis, P. Villalba, F. Cuesta, *et. al.*, *Highly efficient crossing structure for silicon-on-insulator waveguides*, *Optics Letters* **34** (9, 2009) 2760.
- [17] H. Yang, P. Zheng, G. Hu, *et. al.*, *A broadband, low-crosstalk and low polarization dependent silicon nitride waveguide crossing based on the multimode-interference*, *Optics Communications* **450** (11, 2019) 28–33.
- [18] T. Fukazawa, T. Hirano, F. Ohno, and T. Baba, *Low Loss Intersection of Si Photonic Wire Waveguides*, *Japanese Journal of Applied Physics, Part 1: Regular Papers and Short Notes and Review Papers* **43** (2, 2004) 646–647.
- [19] Y. Zhang, A. Hosseini, X. Xu, *et. al.*, *Ultralow-loss silicon waveguide crossing using Bloch modes in index-engineered cascaded multimode-interference couplers*, *Optics Letters* **38** (9, 2013) 3608.
- [20] L. Chrostowski and M. Hochberg, *Silicon photonics design*, *Silicon Photonics Design* (1, 2015) 1–418.
- [21] A. Yariv, *Coupled-Mode theory for guided-wave optics*, *IEEE Journal of Quantum Electronics* **9** (1973), no. 9 919–933.
- [22] A. Yariv and P. Yeh, *Photonics: optical electronics in modern communications*, *Chapter Four* (2007), no. November 849.
- [23] H. Yun, W. Shi, Y. Wang, *et. al.*, *2x2 adiabatic 3-dB coupler on silicon-on-insulator rib waveguides*, *Proc. SPIE 8915, Photonics North 2013* **8915** (10, 2013) 251–256.
- [24] O. Bryngdahl, *Image formation using self-imaging techniques**, *JOSA* **63** (4, 1973) 416–419.

BIBLIOGRAPHY

- [25] L. B. Soldano and E. C. Pennings, *Optical Multi-Mode Interference Devices Based on Self-Imaging: Principles and Applications*, *Journal of Lightwave Technology* (1995).
- [26] A. Maese-Novo, R. Halir, S. Romero-García, *et. al.*, *Wavelength independent multimode interference coupler*, *Optics Express* **21** (3, 2013) 7033–7040.
- [27] D. Liu, H. Xu, Y. Tan, *et. al.*, *Silicon photonic filters*, *Microwave and Optical Technology Letters* **63** (9, 2021) 2252–2268.
- [28] C. M. Wilkes, X. Qiang, J. Wang, *et. al.*, *60 dB high-extinction auto-configured MachZehnder interferometer*, *Optics Letters* **41** (11, 2016) 5318.
- [29] J. C. Adcock, C. Vigliar, R. Santagati, *et. al.*, *Programmable four-photon graph states on a silicon chip*, *Nature Communications* **10** (12, 2019) 1–6.
- [30] F. Horst, W. M. J. Green, S. Assefa, *et. al.*, *Cascaded Mach-Zehnder wavelength filters in silicon photonics for low loss and flat pass-band WDM (de-)multiplexing*, *Optics Express, Vol. 21, Issue 10, pp. 11652-11658* **21** (2013), no. 10 11652–11658.
- [31] M. Piekarek, D. Bonneau, S. Miki, *et. al.*, *Passive High-Extinction Integrated Photonic Filters for Silicon Quantum Photonics*, *Conference on Lasers and Electro-Optics (2016)*, paper FM1N.6 (2016) FM1N.6.
- [32] J. M. Lee, W. J. Lee, M. S. Kim, *et. al.*, *Controlled-NOT operation of SiN-photonic circuit using photon pairs from silicon-photonic circuit*, *Optics Communications* **509** (2022) 127863.
- [33] J.-M. Lee, M.-S. Kim, J. T. Ahn, *et. al.*, *Demonstration and fabrication tolerance study of temperature-insensitive silicon-photonic MZI tunable by a metal heater*, *J. Lightwave Technol.* **35** (11, 2017) 4903–4909.
- [34] M. A. Tran, T. Komljenovic, J. C. Hulme, *et. al.*, *A Robust Method for Characterization of Optical Waveguides and Couplers*, *IEEE Photonics Technology Letters* **28** (2016), no. 14 1517–1520.
- [35] J. M. Lee, W. J. Lee, M. S. Kim, and J. J. Ju, *Noise Filtering for Highly Correlated Photon Pairs from Silicon Waveguides*, *Journal of Lightwave Technology* (2019).
- [36] D. Rabus, *Integrated Ring Resonators: The Compendium*, vol. 127. Springer, 2007.
- [37] R. R. Kumar and H. K. Tsang, *High-extinction CROW filters for scalable quantum photonics*, *Optics Letters* **46** (1, 2021) 134–137.
- [38] J. Song, Q. Fang, S. H. Tao, *et. al.*, *Passive ring-assisted Mach-Zehnder interleaver on silicon-on-insulator*, *Opt. Express* **16** (6, 2008) 8359–8365.

BIBLIOGRAPHY

- [39] H.-H. Lu, E. M. Simmerman, P. Lougovski, *et. al.*, *Fully Arbitrary Control of Frequency-Bin Qubits*, *Physical Review Letters* **125** (2020).
- [40] H.-H. Lu, J. M. Lukens, B. P. Williams, *et. al.*, *A controlled-NOT gate for frequency-bin qubits*, *npj Quantum Information* **2019 5:1** **5** (3, 2019) 1–8.
- [41] H.-H. Lu, J. M. Lukens, N. A. Peters, *et. al.*, *Quantum interference and correlation control of frequency-bin qubits*, *Optica* **5** (11, 2018) 1455.
- [42] H. H. Lu, N. Klco, J. M. Lukens, *et. al.*, *Simulations of subatomic many-body physics on a quantum frequency processor*, *Physical Review A* **100** (7, 2019) 012320.
- [43] S. Ramelow, A. Farsi, S. Clemmen, *et. al.*, *Silicon-Nitride Platform for Narrowband Entangled Photon Generation*, .
- [44] J. Wang, D. Bonneau, M. Villa, *et. al.*, *Chip-to-chip quantum photonic interconnect by path-polarization interconversion*, *Optica* **3** (4, 2016) 407.
- [45] A. Rao, G. Moille, X. Lu, *et. al.*, *Up to 50 dB Extinction in Broadband Single-Stage Thermo-Optic Mach-Zehnder Interferometers for Programmable Low-Loss Silicon Nitride Photonic Circuits*, *Conference on Lasers and Electro-Optics (2021)*, paper SM1A.7 (2021) SM1A.7.
- [46] T. J. Steiner, J. E. Castro, L. Chang, *et. al.*, *Ultra-bright entangled-photon pair generation from an AlGaAs-on-insulator microring resonator*, *PRX Quantum* **2** (9, 2021) 010337.
- [47] D. Llewellyn, Y. Ding, I. I. Faruque, *et. al.*, *Chip-to-chip quantum teleportation and multi-photon entanglement in silicon*, **12**, 2020.
- [48] G. Moody, L. Chang, T. J. Steiner, and J. E. Bowers, *Chip-Scale Nonlinear Photonics for Quantum Light Generation*, *AVS Quantum Science* **2** (12, 2020) 041702.
- [49] L. Lu, X. Zheng, Y. Lu, *et. al.*, *Advances in Chip-Scale Quantum Photonic Technologies*, *Advanced Quantum Technologies* **4** (11, 2021) 2100068.
- [50] X. Wang, X. Quan, M. Liu, and X. Cheng, *Silicon-nitride-assisted edge coupler interfacing with high numerical aperture fiber*, *IEEE Photonics Technology Letters* **31** (3, 2019) 349–352.
- [51] E. J. Stanton, J. Chiles, N. Nader, *et. al.*, *Efficient second harmonic generation in nanophotonic GaAs-on-insulator waveguides*, *Optics Express* **28** (3, 2020) 9521.
- [52] L. Chang, G. D. Cole, G. Moody, and J. E. Bowers, *CSOI: Beyond Silicon-on-Insulator Photonics*, *Optics and Photonics News* **33** (2022) 24–31.

Chapter 5

Quantum Key Distribution

5.1 Introduction

Throughout history, there has been a need to convey secret messages in a form that prevents undesired users from reading the message. One of the most basic examples of this encryption is the substitution cypher where the standard alphabet is replaced by another character (for example replacing "A" with "D" and "B" with "E"). Perhaps the earliest known case of this simple cipher was the implementation by Julius Caesar who communicated secret messages by scrambling the letters via a 4 letter shift [1]. This system is straightforward for a third party to figure out, and state-of-the-art encryption systems rely on several unique methods to establish secure communications between users.. Regardless of the system utilized, the goal of cryptography is simple: establish a means to encode/decode information (known as a cipher), encode a message using the cipher (encryption), transfer the encrypted information (also known as cipher text) to the desired end-user, and decode the message using the cipher (decryption). Variations in strategies for cryptography can modify which users control particular steps of the procedure. For example, in a symmetric key cryptography protocol, the two users (Alice

and Bob) share a secret key that no one else in the system has. Alice encrypts a message with the secret key, and Bob can use the secret to decrypt the message. An alternate route, known as public key or asymmetric key cryptography, involves the use of a public and private key. Alice shares a public key (which can be known by everyone in the system) which Bob uses to encrypt a message. Alice then decrypts the message from Bob using a private key (that is paired with the public key, but only Alice possesses). In both cases, a key is used at both Alice and Bob's location to encrypt or decrypt the message. The key is not sent directly between the two users (since an eavesdropper could intercept and use the key). Thus, only already-encrypted messages travel across a communication channel, and Alice and Bob can communicate in secret as long as they keep their key secure from third-parties.

The creation of a cipher (or protocol for encoding/decoding information) is one of the most important aspects of cryptography, and one of the most widely used systems is RSA encryption—a form of asymmetric key encryption.

RSA Protocol [2]:

1. Alice chooses two large prime numbers p and q and keeps them secret.
2. Alice computes $n = pq$. n is released as part of the public key, and n is used as the modulus for both public and private keys.
3. Compute $\lambda(n)$ where λ is Carmichael's totient function [3]. $\lambda(n) = lcm(p-1, q-1)$ where lcm is the lowest common multiple. $\lambda(n)$ is also kept secret.
4. Choose an integer e such that $2 < e < \lambda(n)$ and e and $\lambda(n)$ are coprime. e is released as part of the public key.
5. Alice calculates $d = e^{-1} \pmod{\lambda(n)}$. d is kept secret as the private key exponent.

From this procedure, a public key that consists of n and e is distributed. Alice maintains the private key elements d , p , q , and $\lambda(n)$. Now Bob can communicate a secure message M to Alice using the public key.

Encryption: Bob computes the ciphertext c of his message using the public key $c = m^e \pmod{n}$. Bob then transmits the ciphertext to Alice.

Decryption: Alice can recover the message by using the private key. $c^d = (m^e)^d = m \pmod{n}$.

RSA derives its security from the difficulty of factoring large integers using a classical computer. The protocol is efficient in one direction: multiplying two large prime numbers p and q is efficient, and easy to do using standard computers, making encryption easy. However, starting from n and determining two large prime factors is incredibly difficult to do. The best approach is a guess and check strategy. For 2048-bit RSA encryption, it is estimated that it will take 300 trillion years to determine the value of p and q using a standard classical computer [4]. Since Alice keeps the values of p and q secret, the prime factorization is the only way for an eavesdropper to determine the private key to decrypt the message. The use of RSA encryption is widespread, and the advancement of quantum technology begins to threaten the security of this encryption technique due to the development of quantum algorithms, specifically Shor's factoring algorithm [5]. Shor's algorithm can be used to find prime factors in polynomial time which, provided a large enough quantum computer could be created, would allow for the RSA encryption protocol to be broken [6]. Figure 5.1 illustrates the current state-of-the-art quantum computer size. Two forms of quantum systems are included— universal quantum computers implemented with superconducting circuits and quantum annealers. It is important to note that quantum annealing is not a universal quantum computer, and **cannot** implement Shor's factorization algorithm. Instead, researchers have approached the factorization as an optimization problem (which can be solved using quantum annealers like D-Wave's

Quantum Computer) [7]. With 89 qubits, quantum annealers have been able to crack a 20-bit number [8] which is still a long way from 2048-bits, but with a Moore's law-like trend of doubling every two years, RSA 2048 can be broken with quantum annealers in less than a decade. Quantum annealers continue to scale with up to 5000 qubits [9], expanding the range of numbers accessible using similar optimization algorithms. On the other hand, IBM currently leads the field with an 1121-qubit universal quantum computer released in late 2023 [10]. Other companies like Google are continuing to push the number of superconducting qubits at a rapid pace, and in conjunction with improvements to Shor's algorithm [11] (shown in red on Figure 5.1), the likelihood of breaking RSA 2048 encryption in the next few decades seems real. It is important to note that although this algorithm has been developed for over 26 years, scaling the algorithm past the few (tens of) qubit level has proven challenging due to the high error rates and noise, and thus there is no immediate threat to RSA encryption [12, 13]. It is currently unclear if physical limitations will prevent Shor's algorithm to fully disrupt classical cryptography, but as quantum computers begin to scale, much of the inherent security of these protocols will be vulnerable. Thus, many research institutions and companies have begun investing in quantum cryptography methods to overcome this potential risk [14]. It is also important to note that the current classical cryptosystems are fragile even now, since eavesdroppers can intercept information and store this encrypted message while waiting for a sufficiently large quantum computer to become available [15]. Thus, there exists an immediate need to update cryptosystems to prevent significant security leaks now and in the future.

Generally, there are two approaches to quantum-safe systems. First, the current, conventional systems are used, but alternative key encryption schemes like hash-based are used. Hash-based encryption derives its security from the unidirectionality of hash functions [16]. These hash functions, unlike RSA prime factorization, are secure against

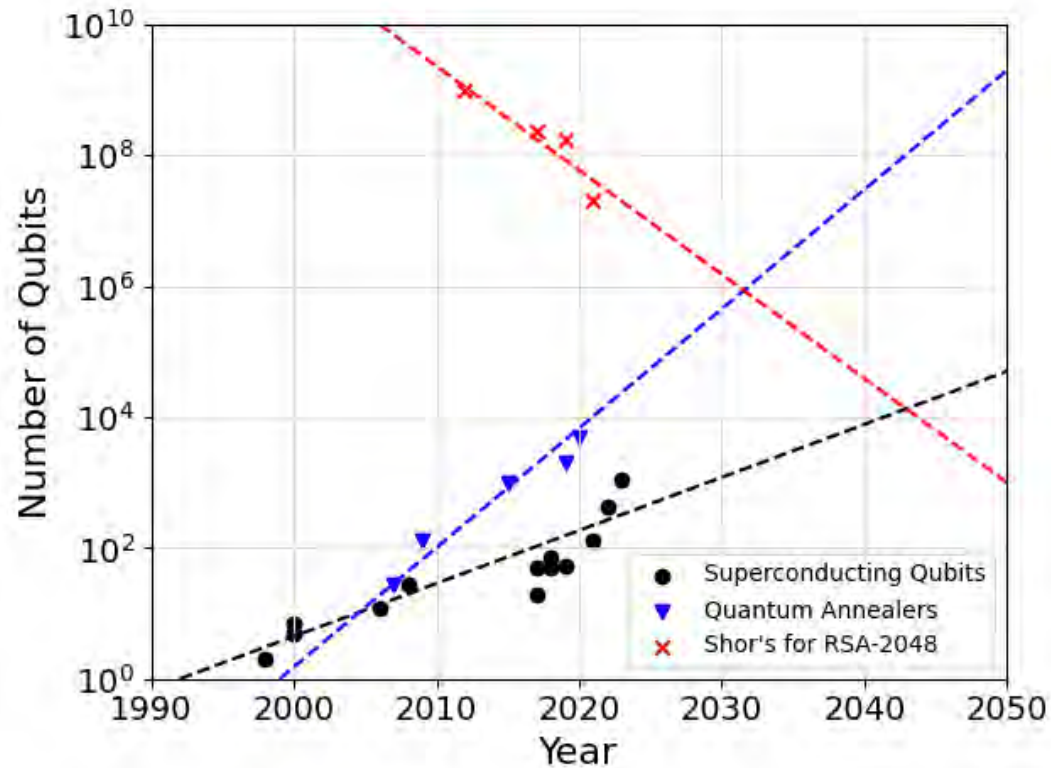


Figure 5.1: Progress on quantum computing and Shor's factorization algorithm. Quantum annealers are **not** universal, and **cannot** implement Shor's algorithm, however they can implement efficient optimization algorithms to factor large numbers, making them a contender to break RSA 2048 encryption. Results for quantum annealers are from D-Wave's system which boasts up to 5000 qubits [9]. Universal quantum computers based on superconducting circuits are also advancing rapidly with up to 1121 qubits demonstrated on IBM's latest quantum computer [10]. Advances in Shor's algorithm have improved the resource requirements, now requiring only 20 million qubits for RSA 2048 [11].

all currently known quantum attacks due to their complex mathematical structure which has been strategically designed to only work in one direction [17]. The other method is to utilize a similarly "quantum" system to establish security. This method, also known as quantum key distribution (QKD), relies on the inherent security of quantum mechanics based on the projection/collapse of quantum states following a measurement and the quantum no-cloning theorem, which states that it is impossible to perfectly clone an unknown quantum state [18].

Quantum no-cloning: Suppose we have an unknown state, $|\psi\rangle$ that we intend to copy to a initially pure target state, $|s\rangle$, resulting in an initial state two-qubit state indicated by

$$|\psi\rangle \otimes |s\rangle. \quad (5.1)$$

Assuming we can apply a unitary operator U that copies the target state to the unknown state:

$$U(|\psi\rangle \otimes |s\rangle) = |\psi\rangle \otimes |\psi\rangle, \quad (5.2)$$

we can use this method to copy two pure states $|\psi\rangle$ and $|\phi\rangle$. Then

$$\begin{aligned} U(|\psi\rangle \otimes |s\rangle) &= |\psi\rangle \otimes |\psi\rangle \\ U(|\phi\rangle \otimes |s\rangle) &= |\phi\rangle \otimes |\phi\rangle. \end{aligned} \quad (5.3)$$

Taking the inner product of these gives

$$\langle\psi|\phi\rangle = (\langle\psi|\phi\rangle)^2 \quad (5.4)$$

which only has solutions when the two states are equal or orthogonal [18]. This very simple proof shows that the creation of a universal cloning unitary is impossible and can only be used to clone orthogonal states, which is not known to be useful for quantum communications. This theorem, in conjugation with the collapse of the quantum state from measurement, is foundational for many quantum communication systems. Simply put, the transmission of a quantum state is secure because an eavesdropper cannot perfectly clone the state, and if the eavesdropper attempts to measure one of the properties, the quantum states collapse. The desired users of the quantum information can observe the eavesdropper's presence by simply checking a subset of the transmitted information

to check for errors in the transmission of the quantum states (see Table 5.1).

When establishing a secure key using quantum information, there exists several properties necessary for the security of the key established by Claude Shannon in 1949 [19, 20].

1. The key has to be truly random, meaning the individual bits are uncorrelated.
2. The key has to be at least as long as the message.
3. The key can never be reused in whole or partly.
4. The key must be completely secret.

Provided a QKD protocol can establish a key with all of these properties, the key can be used to securely encrypt a message. As discussed above, quantum information provides inherent secrecy (meeting the fourth requirement), allowing for the ability to detect if some of the information was intercepted by a third party. Through the use of probabilistic components (like beamsplitters) for measurements, the first metric can also be easily met. The second and third metrics simply require the user to send enough information such that the key is established in whole with no redundancy and of sufficient length. Thus, we continue the discussion by focusing on a few different QKD protocols and the security of these approaches.

As discussed in the background section 2.1.1, orthogonal degrees of freedom of a photonic state can be utilized as a basis for the transmission of information. The most straightforward example of this encoding is using the polarization state of a photon such that a horizontal polarization corresponds to a 0-bit and a vertical polarization corresponds to a 1-bit. Similar basis definitions can be made for the other degrees of freedom of a photon, but the example of polarization will be used as it is the most intuitive and commonly used in real-world demonstrations and commercialized systems. With this basis definition, it is possible to encrypt a message using a string of polarized

photon states to establish a secure key between two users. The encrypted message will be sent over classical communication channels, with the two users encrypting/decrypting the message using the key established from the sent/received photon polarizations. In this case, we can envision a user, Alice, sending this string of photons to a second user, Bob. Alice can prepare a particular sequence of photon polarizations and send the secure key to Bob who can use a birefringent polarization beam splitter to separate each photon to one of two detectors (see Figure 5.2). This process does not have an inherent security since an eavesdropper, Eve, could simply tap into the fiber optic or free-space optical channel and measure the polarization state received from Alice and transmit the same polarization to Bob. Eve would be undetected, and could ascertain all of the information Alice intended to send to Bob. In 1984, Bennett and Brassard proposed a protocol (BB84) using a prepare-and-measure scheme that would allow for the secure transmission of information with only a few modifications to this simple initial system [21]. Alice now sends photons in one of four initial states that she randomly selects (shown in Alice's box of Figure 5.2): horizontal polarization (\leftrightarrow), vertical polarization (\updownarrow), or $\pm 45^\circ$ (\swarrow or \nwarrow). Now, the horizontal polarization and $+45^\circ$ represent 0-bits, and the vertical polarization and -45° represent 1-bits. Bob now randomly selects to measure the polarization of the photon in either the rectilinear ($+$ shown in green in Figure 5.2) or circular (\times shown in grey in Figure 5.2) basis. When Bob measures in the same basis that Alice prepared her state in, they receive the same result. For example, Alice sends a horizontal photon and Bob measures in the rectilinear basis (photon 1 in the table of Figure 5.2). Since Bob randomly measures in the compatible basis, he detects the horizontal polarization. If instead Bob were to measure in the circular basis (photon 2 in the table of Figure 5.2), Bob would randomly detect this photon in either the diagonal or antidiagonal bin (with 50% probability resulting in a 50% error rate). This behavior follows for the remaining combinations of Alice's state preparations and Bob's measurements. The next step of

the procedure is for Alice and Bob to classically communicate which basis was used for each of the photons they detected. When both Alice and Bob use the same basis, the measurement is kept in their key, and when they use opposite bases, the measurement is thrown out. This process, known as sifting, is used to establish the final sifted key between Alice and Bob. Figure 5.2 demonstrates this protocol for a few different photon preparation and measurement configurations. In this case, Alice sends Bob 10 photons, of which half of them are measured in the same basis, so the sifted key is 5 photons in length. This protocol can be completed as long as necessary to establish a key that is the length of the intended message.

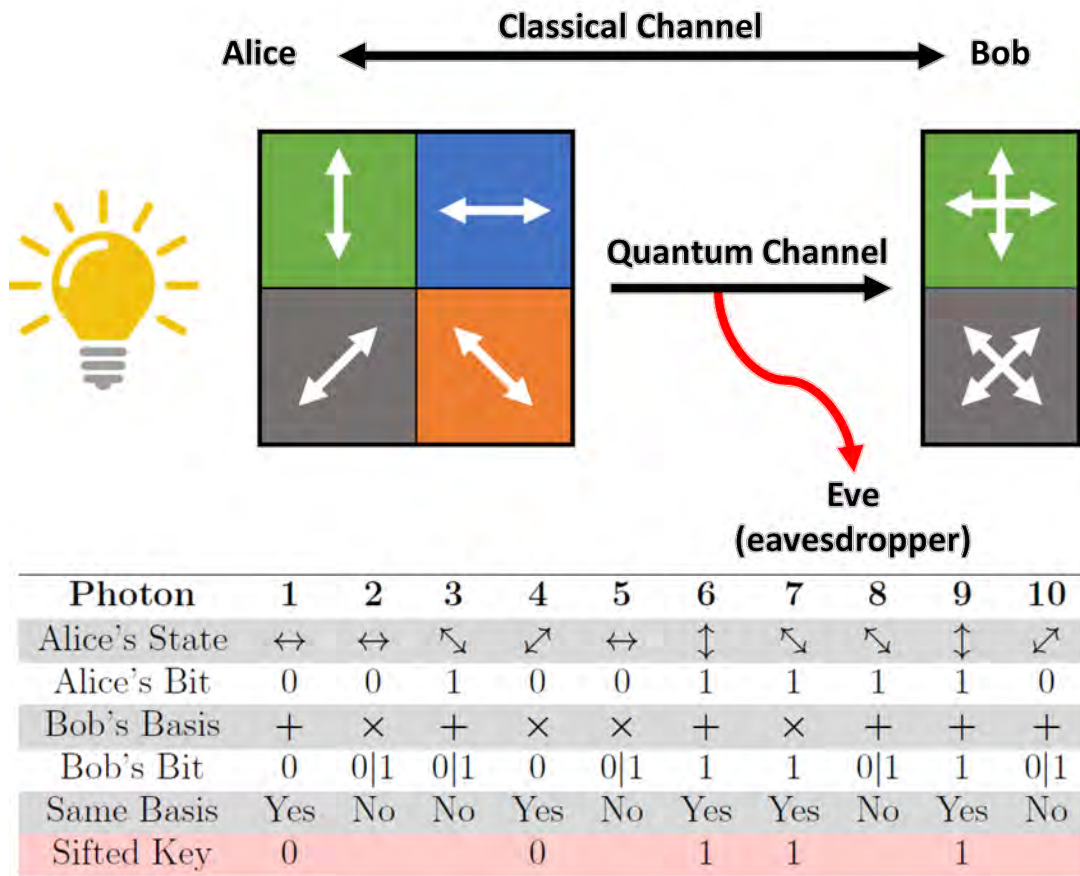


Figure 5.2: BB84 Quantum Key Distribution Protocol

In order to guarantee the security of the protocol, Alice and Bob will compare a subset

of the results of their measurements to be sure that a third party did not interfere with the protocol. Let's say that an eavesdropper, Eve, intercepts the quantum information and decides to randomly measure the photon polarization in the rectilinear or circular basis (using the same methods as Bob) and then resend the result of her measurement to Bob as a new photon with the encoded polarization. This is illustrated in Table 5.1. When Eve measures in the same basis as the state prepared by Alice, she will receive the correct bit value. If Bob also chooses to measure in this basis, all three users will have the same bit value, and Eve's presence is undetected. As an example (see the 9th photon in Table 5.1), let's say Alice prepares a vertically polarized photon (\uparrow) and Eve measures in the rectilinear basis, getting the result of vertical polarization. If Bob also measures in the rectilinear basis, he will measure vertical as well, and there is no apparent error. However, if Eve randomly chooses incorrectly and measures in the circular basis (like for the 6th photon in Table 5.1), she will randomly get $+45^\circ$ or -45° and send the result to Bob. When Bob measures in the rectilinear basis, he will now randomly get either horizontal or vertical polarization (instead of the horizontal polarization that Alice sent). To detect Eve's presence, Alice and Bob must simply share the results of a subset of the total measurements (sufficiently large that probabilities can approach their average values). When Eve is present in the system, a 25% error rate will be observed, and Alice and Bob will know that the communication channel has been compromised. Table 5.1 uses the same measurement settings for Alice and Bob with added rows showing the effect Eve has on the protocol. Now, when Alice and Bob use the same basis, but Eve uses an alternative basis, Bob has a 50% probability of getting the correct result (compared to the 100% in the eavesdropper-free case). Bob's sifted key will have $> 25\%$ error, indicating the presence of an eavesdropper.

The BB84 protocol does not actually require the single photons to share any entanglement with each other, and can be completed using both single photon emitters and even

Photon	1	2	3	4	5	6	7	8	9	10
Alice's State	\leftrightarrow	\leftrightarrow	\nearrow	\swarrow	\leftrightarrow	\updownarrow	\nearrow	\nearrow	\updownarrow	\swarrow
Alice's Bit	0	0	1	0	0	1	1	1	1	0
Eve's Basis	\times	$+$	$+$	$+$	$+$	\times	$+$	\times	$+$	\times
Eve's Result	\swarrow	\leftrightarrow	\updownarrow	\leftrightarrow	\leftrightarrow	\nearrow	\updownarrow	\nearrow	\updownarrow	\swarrow
Bob's Basis	$+$	\times	$+$	\times	\times	$+$	\times	$+$	$+$	$+$
Bob's Bit	0 1	0 1	1	0 1	0 1	0 1	0 1	0 1	1	0 1
Same Basis	Yes	No	No	Yes	No	Yes	Yes	No	Yes	No
Bob's Sifted Key	0 1			0 1		0 1	0 1		1	

Table 5.1: **Eavesdropper:** BB84 quantum key distribution protocol with eavesdropping.

using weakly attenuated laser pulses (with additional requirements necessary to ensure security through, e.g. intensity modulated decoy states) [22, 23]. With over 40 years of research, many implementations of the BB84 protocol have been demonstrated using real systems [24]. Along with the advancement of this protocol, and the corresponding security proofs [25], many other QKD protocols have been developed that can either provide additional security, ease of use, or enhanced key rates. Of interest to this work are the systems that implement entanglement-based QKD. Not only can the distribution of entangled states be used to establish secure keys, but this entanglement distribution can also provide routes toward quantum interconnects and a system of quantum networks via quantum teleportation and entanglement swapping [26]. A brief discussion of this quantum networking approach is included in Section 3.1.3. The BB84 protocol described above is an end-to-end system where one user, Alice, communicates the key directly to the second user, Bob. This limits the ability to expand the network since adding users would require additional unique connections made between the users. Entanglement-based systems can have a center-out approach where the source of the key is distinct from Alice/Bob's system. This means that pairs of users can tap into the entangled resource from the central source and establish secure keys between themselves to create a larger network of users. The security of these entanglement-based systems is also im-

proved due to the quantum no-cloning theorem and the correlations inherent to entangled particles. In 1992, shortly after the proposal of the BB84 protocol, Bennett, Brassard, and Mermin proposed the first entanglement-based system for QKD (BBM92) [27]. In the BBM92 protocol, a central source produces entangled photon pairs, sending one photon from each pair to Alice and the other to Bob. Let's say, as an example, the source produces entangled photon pairs in the $|\psi^-\rangle$ Bell state (any of the Bell states would suffice). Thus, the output of the source are of the form $|HV\rangle - |VH\rangle$ which is equivalent to $|DA\rangle - |AD\rangle$. This example is shown in Table 5.2. Alice and Bob now each randomly measure in the rectilinear or circular basis. They compare the measurement bases using a classical channel and sift their key to only include the instances when they both measured in the same basis. Here, the entanglement between Alice's photon and Bob's photon yields correlated results when measured in the same basis (When Alice measures a horizontal polarization, Bob measures a vertical polarization) [28]. Thus, in a similar way to the BB84 protocol (only now there is a central source of entangled photons), the BBM92 protocol can establish a secure key for encryption. Following the table in 5.2, Alice and Bob both randomly select bases. For the case of a source producing $|\psi^-\rangle$ photon pairs, their results are inversely related, so an additional step is added where Bob inverts all of his bit values to match the result of Alice. Again, sifting is completed by communicating through a classical channel the basis used for each photon measurement.

Another important advantage of the BBM92 protocol is that the entanglement established in the photon pairs removes the requirement for a modulator at the source. In BB84, a modulator is required to randomly pick the basis that Alice uses (sending in either the rectilinear or circular basis). However, through the inherent entanglement of the photon pairs such that $|HV\rangle - |VH\rangle = |DA\rangle - |AD\rangle$, this basis selection is not necessary since it is built into the source.

Many of the initial and current QKD protocols utilize polarization states of photons

Input state: $ HV\rangle - VH\rangle = DA\rangle - AD\rangle$										
Photon	1	2	3	4	5	6	7	8	9	10
Alice's Basis	+	+	×	×	×	×	+	+	+	×
Alice's Result	\leftrightarrow	\updownarrow	$\nearrow\searrow$	$\swarrow\searrow$	$\swarrow\searrow$	$\swarrow\searrow$	\leftrightarrow	\updownarrow	\updownarrow	$\nearrow\searrow$
Alice's Bit	0	1	1	0	0	1	0	1	1	1
Bob's Basis	+	×	+	×	×	+	×	+	+	+
Bob's Result	\updownarrow	$\swarrow\searrow$	\updownarrow	$\swarrow\searrow$	$\swarrow\searrow$	\leftrightarrow	$\swarrow\searrow$	\leftrightarrow	\leftrightarrow	\updownarrow
Bob's Bit	1	0	1	1	1	0	1	0	0	1
Bob's Inversion	0	1	0	0	0	1	0	1	1	0
Same Basis	Yes	No	No	Yes	Yes	No	No	Yes	Yes	No
Sifted Key	0			1	0			1	1	

Table 5.2: BBM92 entanglement-based quantum key distribution protocol.

to encode the qubits, as they can readily be prepared, are easily manipulated, and can be measured using standard components like polarization beamsplitters and single photon detectors. Entangled photons and single-photon states can also be prepared in one or multiple other degrees of freedom of a photon [29]. Some of the most common implementations, in addition to polarization, include time-bin encoding and frequency-bin encoding. For nonlinear entangled photon pairs sources, the generation process of the entangled photon pairs is spontaneous and simultaneous. The latter attribute means that—provided the photons travel the same distance—the photon pairs will arrive to the detectors at the same time (or a careful calibration can determine the relative time delay between the independent paths of each photon from the pair). This time-bin correlation can be exploited through several methods. Alice and Bob will now define their 0-bit and 1-bit based on an early and late time bin established by sending the photons through a short and a long path to detectors, where the paths/time-bins are defined at Alice and Bob. Time-bin protocols, especially when photons are traversing optical fibers, are often more robust to environmental noise compared to polarization states [30] and are generally compatible with already established optical fiber (whereas polarization-based systems would need polarization maintaining fiber or polarization compensation). As

a brief aside, it is important to note that resonator-based entangled photon pairs have longer two-photon correlation times due to an extended lifetime in the cavity which results in a broader time-bin correlation compared to waveguide or bulk crystal sources (see Section 3.1.1 for a discussion of the coherence time). Another benefit of this time-bin encoding is the ability to expand into higher dimensions (provided the detectors and coincidence electronics are sufficiently fast). This high-dimensional encoding, sometimes called large alphabet encoding, allows for each detected photon to carry multiple bits of information by segmenting into many small (~ 200 ps) bins. These protocols boast some of the fastest secure key rate transmissions with up to 2.7 Mbps shown at 20 km [31].

In the past decade, there have been very promising results from research groups across the world with system-level demonstrations of up to 830 km of deployed optical fiber [32] and satellite-based QKD exceeding 1,200 km [33, 34]. Other groups are working on creating quantum interconnects and networks that can interface other quantum platforms like superconducting qubits, trapped ions, and neutral atoms [35]. Much of the pioneering work is done using bulk and/or commercial laser sources, detectors, modulators, and nonlinear crystals (for entanglement-based systems) [17, 36]. As source and detector technologies continue to advance, however, there has been a push for low-SWaP approaches relying on chip-scale implementations that take advantage of existing semiconductor and photonic manufacturing techniques (see Reference [37] for a summary of recent advancements in chip-based QKD technologies).

5.2 QKD Using AlGaAsOI microcombs

Several chip-scale platforms have been developed to generate and distribute entanglement, many of which operate near the telecommunications C-band which has a minimum loss for optical fiber [38]. Among these, one of the most promising is aluminum gallium

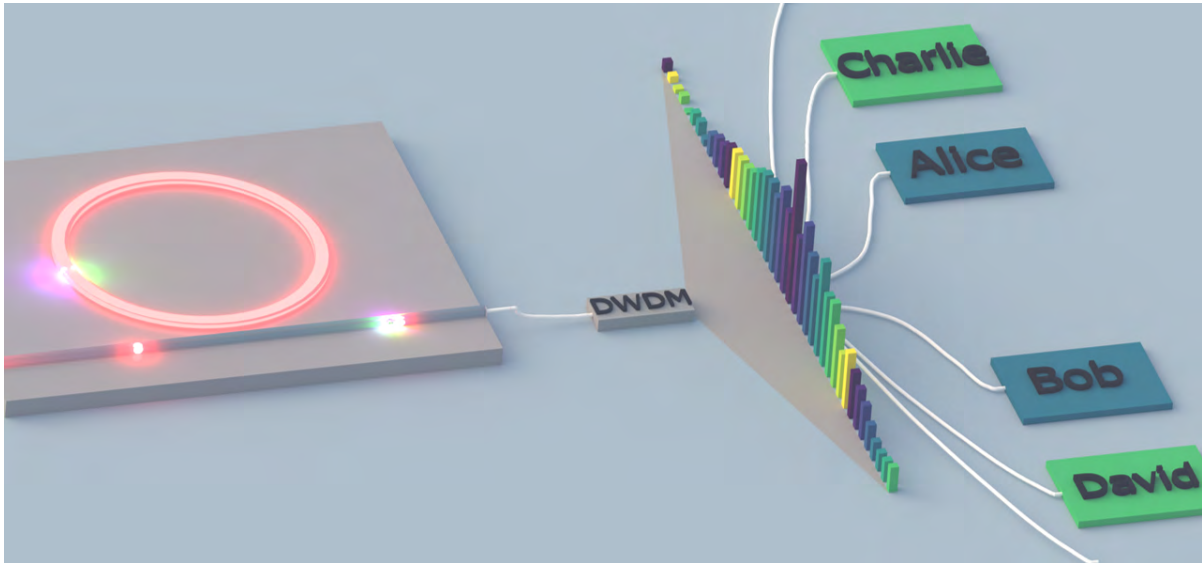


Figure 5.3: AlGaAsOI quantum optical microcomb enabling multi-user entanglement distribution. A microring resonator generates pairs of entangled photons across many spectral modes that can be distributed to various users over long distances using low-loss telecommunication optical fibers. The frequency comb spectrum shown is from the device characterized in this work and shows the ability to create a user network with more than 20 nodes with ultrabright entanglement generation requiring $< 100 \mu\text{W}$ on-chip power. In this illustration, Alice and Bob each receive a photon from one set of modes, and Charlie and David each receive a photon from a different set.

arsenide-on-insulator (AlGaAsOI), which, as discussed in the preceding chapters, has been used to demonstrate ultra-bright, high-quality entangled-photon pairs from a spontaneous four wave mixing (SFWM) process in a microring resonator [39]. In conjunction with a low-loss photonic testbed consisting of double-pass dense wavelength division multiplexers (DWDMs from Fiberdyne Labs), this source can be used as an efficient source of a quantum key. The AlGaAsOI resonator generates a broad spectrum spanning $> 300 \text{ nm}$ ($> 40 \text{ THz}$) of entangled-photon pairs with larger free-spectral range for simple DWDM, which can be used to either spectrally multiplex for higher secure key distribution rates or used to send different pairs to numerous users, creating a multi-user connected quantum information network as demonstrated in Figure 5.3 [40].

The goal of this work was to expand on the efficient source of entangled photon pairs

established using a high Q AlGaAs resonator to show its utility in a quantum application [39]. One of the major improvements made to the system compared with the initial demonstration as detailed in Chapter 3 is the reduction of system loss to less than 10 dB per channel (including off-chip coupling, pump rejection, and signal/idler demultiplexing). Table 5.3 characterizes the individual component losses for a basic experiment where the generated entangled photon pairs are sent through two pairs of DWDMs to demultiplex the signal and idler photons before being sent directly to the detectors. The characterization of the system losses follows a very straightforward approach where the laser is tuned to the signal (idler) resonance wavelength and sent through the DWDMs, recording the initial input power and the power that exits the DWDMs. To get more than sufficient pump extinction, two sets of identical DWDMs are used. To measure the coupling loss, the laser is sent through the chip with a slight detuning from the resonance wavelength (to avoid any loss from power coupling into the resonator). The loss is assumed to be roughly symmetric (input coupling and output coupling loss identical), so the total fiber-to-chip-to-fiber loss is simply divided by a factor of two. The detector loss is based on the vendor specifications boasting a $> 85\%$ efficiency.

	Idler Channel	Signal Channel
Off-chip Coupling (dB)	3.5	3.5
DWDM Loss (dB)	3.4	4.0
Detector Loss (dB)	<0.7	<0.7
Total Loss (dB)	7.6	8.2

Table 5.3: System losses for the measurement of entangled photon pairs generated from a high-Q AlGaAsOI microring resonator.

An example transmission scan of one of the demultiplexing DWDMs is shown in Figure 5.4. The filter has exceptional performance through the transmission port, showing > 50 dB extinction outside of the 100 GHz bandwidth. It is important to note that for this scan, the power reaches the instrument limit, and other characterization indicates

that the true extinction ratio is close to 100 dB. The insertion loss of the transmission channel is also quite small < 2 dB. The reflection channel has < 0.6 dB insertion loss and almost 30 dB of extinction. The use of such a low-loss, high extinction ratio is critical for the implementation of efficient QKD protocols since system loss reduce the overall single photon flux along with introducing additional errors. Thus, the DWDM filters shown here are a great improvement to the system, enabling a high flux, low error rate system for QKD. Combined with efficient chip-to-fiber coupling and high quality single photon detectors, the generated entangled photon pair flux from the ring resonator source can be collected with high rates, exceeding 1 million counts per second.

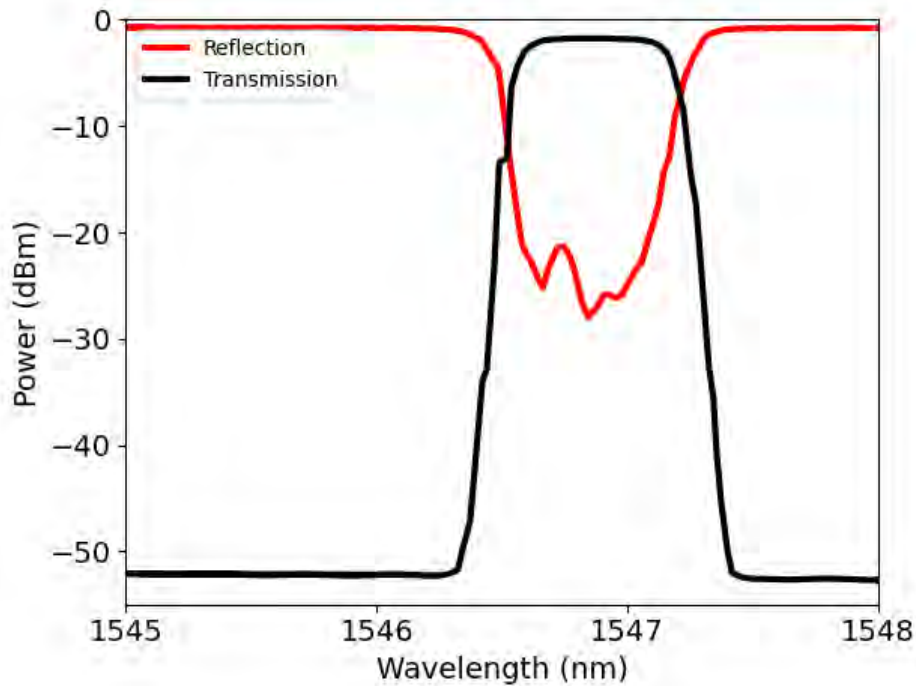


Figure 5.4: Filter characterization illustrating the insertion loss, extinction ratio, and filter bandwidth of one set of fixed-wavelength DWDMs. The transmission measurement is limited by the power meter sensitivity, with additional characterization showing > 100 dB extinction.

5.2.1 Three-Detector Time-Bin Protocol

As described in Chapter 3, AlGaAsOI ring resonators have been used to efficiently generate entangled photon pairs. The goal of this next project was to utilize these ultra-bright sources for a real application, namely QKD. Since the source can produce high rates of entangled photons (with low pump power) using a continuous-wave pump, time-bin QKD protocols were explored. Importantly, through the use of a continuous-wave laser pump and time bins defined at Alice and Bob, there is no need for timing synchronization. Time-bin protocols are robust to environmental interactions and compatible with already deployed fiber near the UCSB campus, motivating this approach. We follow a three-detector QKD protocol recently developed using bulk nonlinear crystals to obtain a miniaturized, more efficient quantum light source that is compatible with this protocol [41]. The protocol also enhances the secure key rate by a factor of 2 by requiring one fewer detector than similar implementations [42], which enabled 7 kbps sifted key rates using a bulk SPDC source [41]. Here, we expand on this demonstration through the use of a SFWM chip-scale source that reduces the input optical power while maintaining high key rates.

The protocol is illustrated in Figure 5.5. A tunable continuous wave (cw) laser source enters tunable etalon-based bandpass filters to remove amplified spontaneous emission (ASE) at the signal and idler frequencies used for the protocol. The pump light is coupled into/out of an AlGaAsOI ring resonator designed for a 1 THz free-spectral range using lensed optical fibers. SFWM generates entangled-photon pairs in sets of spectral modes adjacent to the pump. In Figure 5.5, the inset shows the energy conservation of the SFWM process, where λ_p , λ_i , and λ_s correspond to the pump, idler, and signal photons [43]. Once the photon pair is generated, the signal and idler photons are demultiplexed using double-pass 100 GHz DWDMs (as shown in Figure 5.4 and Table 5.3) to provide

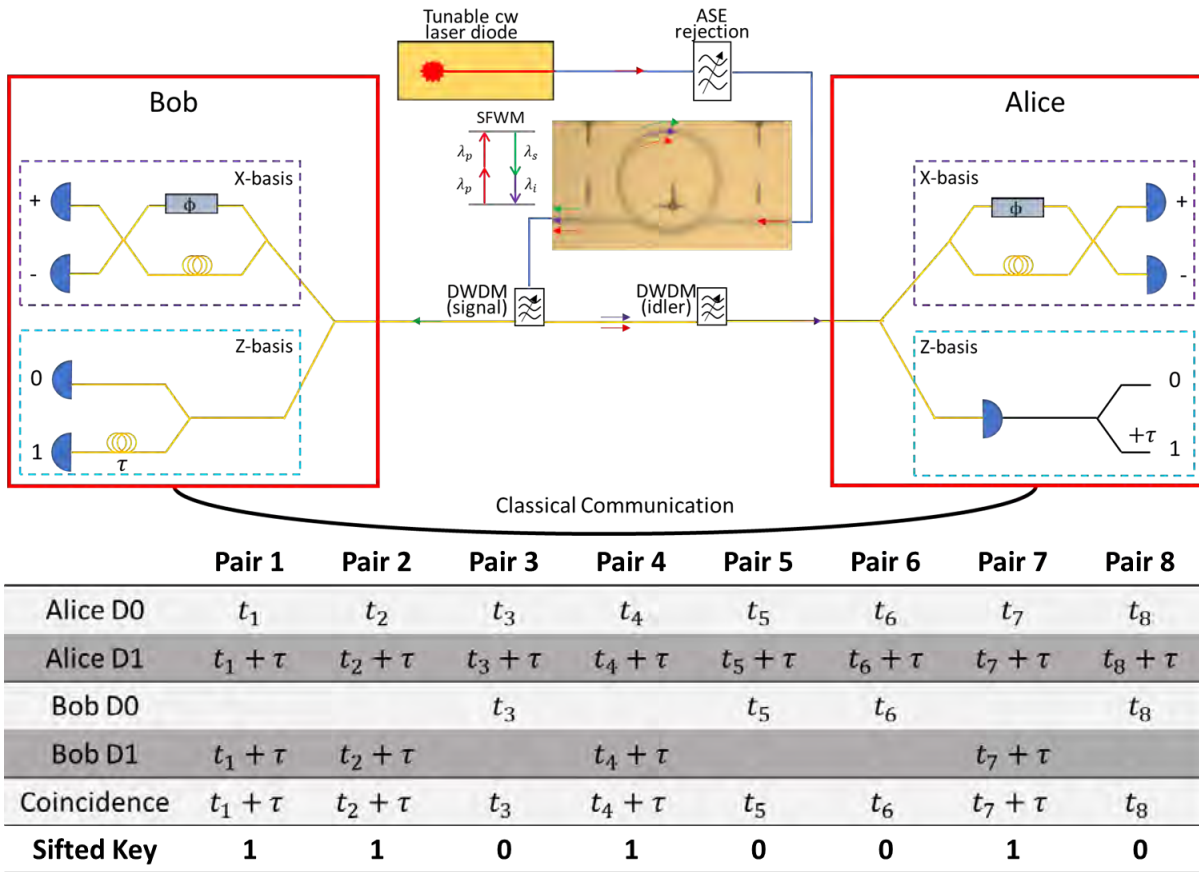


Figure 5.5: Experimental design for a three-detector time-bin QKD protocol. A tunable continuous wave (CW) laser source pumps the resonator source after passing through amplified spontaneous emission (ASE) filters. The pump light, along with the entangled photon pairs generated via spontaneous four wave mixing (SFWM) couple from the chip to lensed optical fibers and enter dense wavelength division demultiplexer (DWDM) filters. The signal photon travels to Bob’s measurement setup, and the idler photon travels to Alice. Alice and Bob establish visibility measurements in the X basis via locked Franson interferometry. Alice has a tunable phase shifter and sweeps the relative phase between the short and long path to show two-photon interference of the $\frac{1}{\sqrt{2}}(|SS\rangle + \exp(i\phi)|LL\rangle)$ state. In the Z basis, Alice uses a single superconducting nanowire single photon detector (SNSPD) and collects the single photon arrival times as well as an electronically delayed channel (black lines). Bob splits his signal photons into two paths using a fiber-based 3-dB splitter. Each path has an SNSPD, and Bob records detection events in either the "0" time bin (short path) or "1" time bin (long path). The table shows how a sifted key is established.

sufficient extinction of the pump light and to separate the signal and idler photons into respective fiber channels. The signal photons are sent to Bob while the idler photons are

sent to Alice. Both Alice and Bob utilize a beamsplitter to send their stream of photons to either the X or the Z basis; the Z basis is used to generate the key and measures the photon arrival time in one of two time bins separated by a user-defined, fixed delay τ . The X basis monitors the signal-idler two-photon interference visibility to determine the security of the key, where a visibility $> 50\%$ surpasses the classical limit and $> 70.7\%$ violates the Clauser-Horne visibility [44, 45].

A key innovation for continuous-wave time-bin QKD introduced by Pelet *et al.* is that Alice and Bob have unique Z basis measurement systems [41]. The table in Figure 5.5 shows an example of 8 sets of photon pairs arriving to Alice and Bob's Z bases. Bob's Z basis measurement consists of a 3-dB beamsplitter to randomly send the signal photons along one of two optical paths corresponding to a 0-bit (short optical path with time t_n in the table in Figure 5.5) or a 1-bit (long optical path with time $t_n + \tau$). Bob uses two superconducting nanowire single photon detectors (SNSPDs) to measure the photon's arrival time within 100 ps time-bins and $> 85\%$ detector efficiency. Contrary to Bob, Alice utilizes a *single* SNSPD to detect the arrival time of the idler photons. With her arrival times, she creates a second, electronically delayed channel with a delay equal to Bob's long fiber path delay, τ . Alice thus records a detection event at t_n and $t_n + \tau$ for each detected idler photon from the source. Using a classical channel, Bob only communicates to Alice the arrival time of photons at his detector without sharing any path information. By comparing the arrival times and looking for coincidences within a 1 ns window (which is set based on the bi-photon cavity lifetime of the source), Alice is able to determine whether Bob detected the photon in his 0- or 1-bit path. Alice sends the coincidence event information back to Bob over the classical channel, only communicating the arrival time. Bob determines whether this event corresponds to the 0- or 1-bit by finding the detector that received the corresponding click. Through this post-selection scheme, Alice and Bob establish their sifted key based on the photon coincidence with

Bob's 0-bit or 1-bit detector. The table in Figure 5.5 illustrates the protocol with eight exemplary measurement outcomes and the corresponding sifted key. Common time-bin protocols utilize a pulsed laser for synchronization and a 3-dB splitter on both Alice and Bob's Z basis measurement, which limits the secure key rate to 25% of the generated coincidence count rate [42]. Here, the raw coincidence count rate usage is improved to 50% by removing the choice of two paths on Alice's side.

The X basis monitors the entanglement visibility via Franson interferometry [46]. Importantly, since the Z basis simply monitors the arrival times of the photons, the X basis is essential to monitor the security of the protocol. Without a continuous measurement of the two-photon entanglement visibility, Eve could simply recreate Alice's measurement system and resend photons with the same time-bin spacing. The X basis (which also requires the single photons to be entangled) allows for Alice and Bob to monitor the security of the key throughout the protocol. Each photon enters an unbalanced Mach-Zehnder interferometer separating the photon coincidences into three distinct time bins: an early bin when the idler takes the short path and the signal takes the long path, a late time bin when the idler takes the long path and the signal takes the short path, and a central bin when both photons take the same path (see Figure S2). This central bin corresponds to the photon state: $\frac{1}{\sqrt{2}}(|SS\rangle + \exp(i\phi)|LL\rangle)$ where the phase ϕ is set by a tunable phase shifter in the short arm. To maximize the two-photon interference visibility, the delay of the interferometers must follow the relations: $\tau_s^c < \tau_{a,b} < \tau_p^c$, and $|\tau_a - \tau_b| \ll \tau_s^c$ where $\tau_{a(b)}$ are the delays in Alice's (Bob's) interferometer, and τ_s^c and τ_p^c are the coherence times of the single photons and the photon pairs [41]. Using a continuous wave laser, τ_p^c is larger than 1 μ s (the two-photon coherence time is determined by the laser coherence time, since the photon pairs can be created anytime within the laser coherence time). The single photon coherence time is on the order of 1 ns (related to the cavity lifetime of a 1.24 million Q resonator). Thus, in order to obey the first relation, the delay must

be between 1 ns and $1\mu s$. The second relation simply states that the *difference* in the path lengths of Alice and Bob's interferometers should be much smaller than the 1 ns single photon coherence time ($\ll 0.2m$). Thus, selecting a ~ 15 ns delay and verifying the lengths of Alice and Bob's delay are nearly identical can optimize the interference visibility measurement design. Alice's and Bob's interferometers are locked to maintain a consistent relative phase during the measurement, and Alice's voltage controlled phase shifter can be swept to change the phase between the two states. Bob uses the phase shifter in his interferometer to locally stabilize the X-basis to any environmental fluctuations. Since Alice sweeps her phase shifter across the full π range, relative phase drift between Alice and Bob's interferometers do not impact the visibility measurement (provided each interferometer is stable for the duration of a π phase sweep). Importantly, because the time bins are defined at Alice and Bob, only the interferometers at Alice and Bob need to be phase stable, whereas phase fluctuations in the fibers from the source to Alice and Bob do not impact the phase of the time-bin entangled pairs defined once the photons arrive at the nodes.

5.3 QKD Source Characterization

5.3.1 Entangled Photon Pair Flux and Coincidences

The source used to generate entangled photon pairs is the same high-Q AlGaAsOI microring resonator described in Chapter 3 (a microscope image of a comparable source is shown in Figure 5.5). The microring resonator has a radius of $13.91\ \mu m$, the width of the bus waveguide was $0.48\ \mu m$, and the ring waveguide was $0.69\ \mu m$ wide. The gap between the waveguide and the ring was $0.48\ \mu m$, and the AlGaAs layer was $0.4\ \mu m$ thick. The resonator is pumped at the resonance near $1557\ \text{nm}$ to generate a quantum

frequency comb that spans over 300 nm. When pumped with sufficient power (above the optical parametric oscillator threshold), the frequency comb is visible with an optical spectrum analyzer showing the possible generation of >20 pairs of entangled photon pair frequencies, as shown in Figure 5.6a). Above 1650 nm, the optical spectrum analyzer has a limited responsivity and thus exhibits an increasing background that eventually surpasses the generated comb lines. In Figure 5.6a), the adjacent and second nearest resonances are denoted by the blue star and black triangle, respectively. Throughout this work, data collected from both resonances will be presented. Data from the adjacent resonance will be plotted using blue stars, and data from the second nearest resonance will be black triangles. As described in the previous section, the QKD protocol relies on a single pair of photon modes, thus such a large bandwidth can be used for either wavelength multiplexing (enhancing the key rate by a factor of ~ 20) or for multi-user distribution of quantum information.

First, we bypass the beamsplitters that distribute photons to the X and Z basis shown in Figure 5.5 and send the signal and idler photons directly to the SNSPDs to characterize the raw single photon count rate and coincidence count rates. The low-loss system loss of < 8 dB per channel enables efficient collection of signal and idler photons with high coincidence count rates for low pump powers. The pump resonance (near 1557 nm) has a loaded quality factor $Q = 1.24$ million corresponding to a full width at half maximum (FWHM) of 220 MHz while the adjacent resonances (blue stars) have quality factors of 0.67 and 0.39 million corresponding to a FWHM of 340 MHz and 575 MHz, and the second nearest resonances have quality factors of 1.05 million and 1.00 million (black triangles) corresponding to a FWHM of 239 MHz and 279 MHz. The lower quality factors for the nearest resonance modes reduces the entangled-photon pair generation rate, however, even with the nearest modes, over 2.5 MHz detected single photon counts and 30 kHz coincidence counts are recorded (Figure 5.6b,c)) with less than 300 μW of

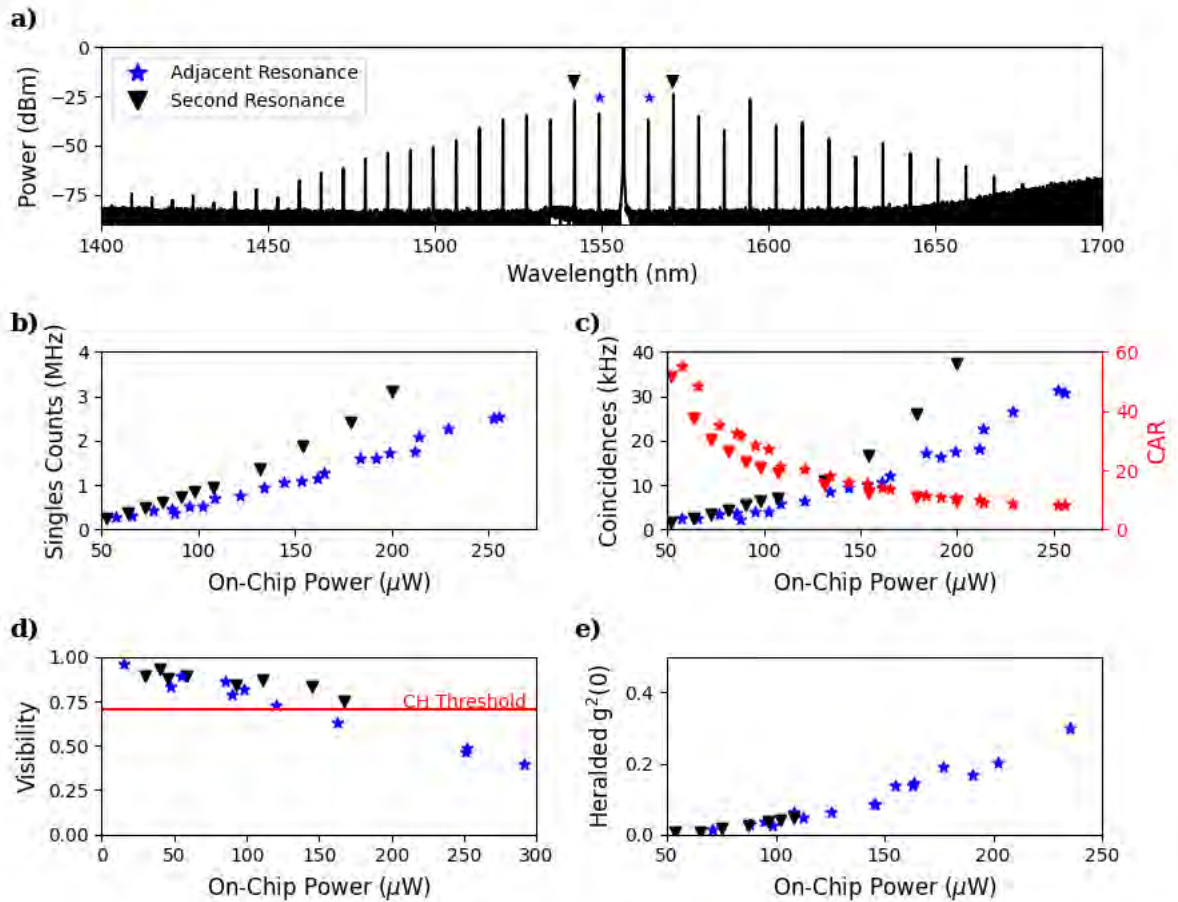


Figure 5.6: Characterization of the entangled photon pair source used for the QKD protocol. a) The frequency comb spectrum from the ring resonator source when pumped with sufficient pump power to generate a frequency comb visible using an optical spectrum analyzer. The blue stars indicate the adjacent resonance and the black triangles indicate the second nearest resonance. b) Collected raw single photon counts as a function of the on-chip pump power. c) Measured coincidence count rate as a function of on-chip power along with the coincidence-to-accidental ratio (CAR). d) Raw (without background subtraction) two-photon interference visibility as a function of the on-chip power. The visibility is largely limited by the pump leakage at higher powers. Figure 5.8 shows the visibility after background subtraction. e) Heralded single photon purity measurement as a function of power.

on-chip pump power. The coincidence to accidental ratio (CAR) of the source remains above 8 at all powers, indicating a high quality, low loss photonic testbed capable of generating a secure key with low errors and high rates. For the second nearest resonance, we measure up to 40 kHz raw coincidences and a measured singles count rate above 4

MHz, which is limited by latching of the SNSPDs.

5.3.2 Visibility Measurement

The security of the protocol relies on measuring the entanglement visibility of the source during operation. Here, the two-photon entanglement visibility is monitored using a folded Franson interferometer where both the signal and idler photon enter the same interferometer before being demultiplexed from each other. In the folded configuration, both the signal and idler photon enter into an unbalanced interferometer with a long and a short path. The resulting two-photon state can be expressed as a summation over $|ij\rangle$, where the i (j) index is the path the signal (idler) photon travels, with $i, j = [S, L]$. Figure 5.7 shows the three distinct peaks that arise from the various path length combinations. The side peaks arise from photons travelling along the $|LS\rangle$ or $|SL\rangle$ paths and are offset from zero by the difference in the long and short path lengths. The central peak at zero delay is due to both photons taking the same paths, $|SS\rangle$ or $|LL\rangle$. Because these states are indistinguishable, the two-photon state is expressed as $\frac{1}{\sqrt{2}}(|SS\rangle + \exp(i\phi_{i+s})|LL\rangle)$. A voltage-controlled phase shifter is used to sweep the relative phase ϕ_{i+s} between the two paths to show interference between the states. Figure 5.7a) shows the difference between the coincidence peaks when a 0.4π phase is applied (blue trace) and π phase (black trace). The central peak shows two-photon interference visibility of 74.9% without background subtraction, and 91% after removing the background counts. This visibility measurement was taken from the second resonance when pumped at $170 \mu\text{W}$. At higher powers, the extinction of our filters is not sufficient to block all of the pump light from reaching the detectors, which degrades the two-photon visibility. As a result, above $120 \mu\text{W}$ of on-chip power, the visibility is below the Clauser-Horne (CH) threshold [44]. We thus keep the on-chip pump power below $140 \mu\text{W}$ during the QKD protocol. The

second resonance has greater pump extinction since the modes are 2 THz from the pump mode, allowing for a higher pump power to be used while maintaining sufficient visibility; however, to keep the data compatible with multiplexed QKD systems, the pump power is limited to $120 \mu\text{W}$ to be well above the CH threshold for both the adjacent and second resonance modes. Figure 5.6d) shows the visibility of the source as a function of on-chip power without background subtraction.

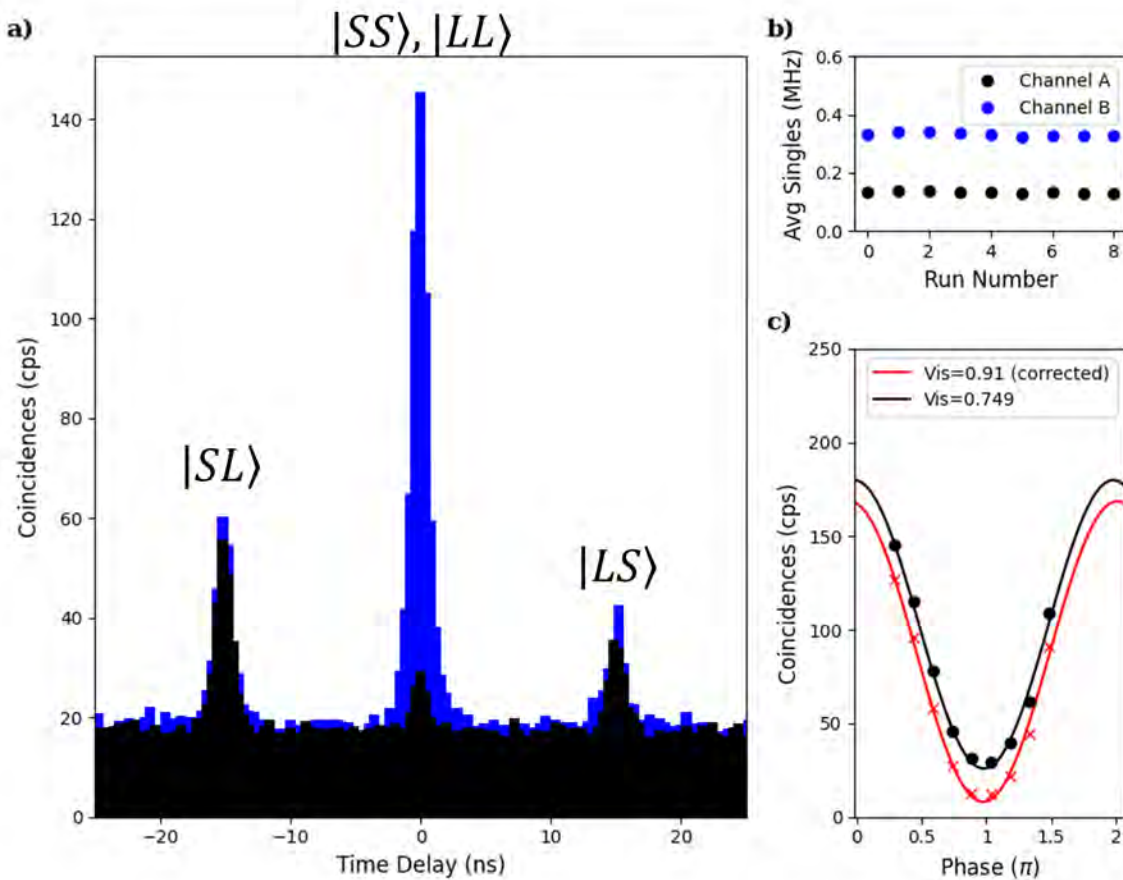


Figure 5.7: a) Coincidence histogram of the two-photon interference at 0.4π (blue) and π (black) relative phase between the long and the short path. b) Single photon flux as the relative phase is swept showing stable flux on both channels. c) Coincidence counts in the central peak as a function of the relative phase along with a sinusoidal fit of the data. The fit shows 74.9% uncorrected two-photon visibility and 91% visibility with background subtraction.

As briefly illustrated in Figure 5.7, the two photon entanglement visibility improves significantly through background subtraction. Figure 5.8 illustrates the same plot from Figure 5.6d) now including both uncorrected (black, blue) and background subtracted data points (red). The visibility still degrades as the power increases, which is expected since the multi-photon pair emission probability increases with power, but the background subtracted data shows the ability to surpass the CH threshold at much higher powers compared to the uncorrected data. The background subtracted data suggests that up to $275 \mu\text{W}$ of pump power can be used while still remaining above the CH threshold. The improvement from the background subtraction suggests the possibility to extend the useful range of the source to higher powers, but there exists a trade-off. In order for the system to function in an analogous state to the background-subtracted case, significantly more pump filtering is required, and therefore there will inevitably be an increase to the overall system loss. Since the coincidence rate increases quadratically with the pump power and the filter loss is a constant value, there is a certain degree of pump filtering that maximizes the useful QKD rate. Due to experimental limitations, this optimum is not explored, though it could be easily studied by simply increasing the number of filters and recording the coincidence count rate and visibility as additional filters are added. Regardless of the number of pump rejection filters used, at large enough powers, the multi-photon pair emission probability begins to contribute considerably, opening up the potential risk of photon-number splitting attacks on the QKD system [47]. A photon-number splitting attack occurs when there is a high probability of multi-photon pair emission such that Eve can collect single photons from the stream without disrupting the number of photons that arrive to Bob. Since this protocol (and most protocols) does not use photon number resolving detectors, Alice and Bob are unaware of the photon distribution at their detectors. Thus, from all practical standpoints, Alice and Bob see the arrival of one photon exactly how they observe the arrival of multiple photons within

the same time interval. In the case of a high probability of multi-photon generation, Eve will go unnoticed because her measurement does not necessarily disrupt the entanglement between the pair of photons that still reach Alice and Bob.

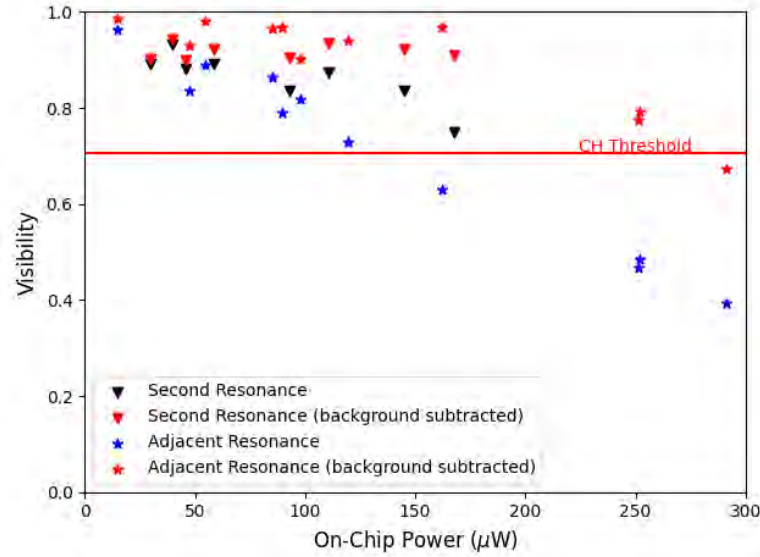


Figure 5.8: Visibility as a function of power for the adjacent and second nearest resonance with and without background subtraction. The red data points indicate the background subtracted results while the blue and black data points indicate the same data as shown in Figure 5.6d).

5.3.3 Heralded Single Photon Purity Measurement

Related to the previous section, another important property of the source is the heralded single-photon purity, which can be used to quantify the probability of generating multiple photon pairs in a given time bin. This characterization is completed using a heralded $g^2(0)$ measurement where the signal photons are detected directly, and the idler photons are sent to a 3-dB splitter before being detected at one of two detectors. Since the nonlinear process generates a single signal and idler photon pair (in the low power regime), a dip at zero time delay appears where there are very few threefold coincidence events. The value of the heralded $g_H^{(2)}(0) = \frac{N_{ABC}N_A}{N_{AB}N_{AC}}$ where N_{ABC} is the

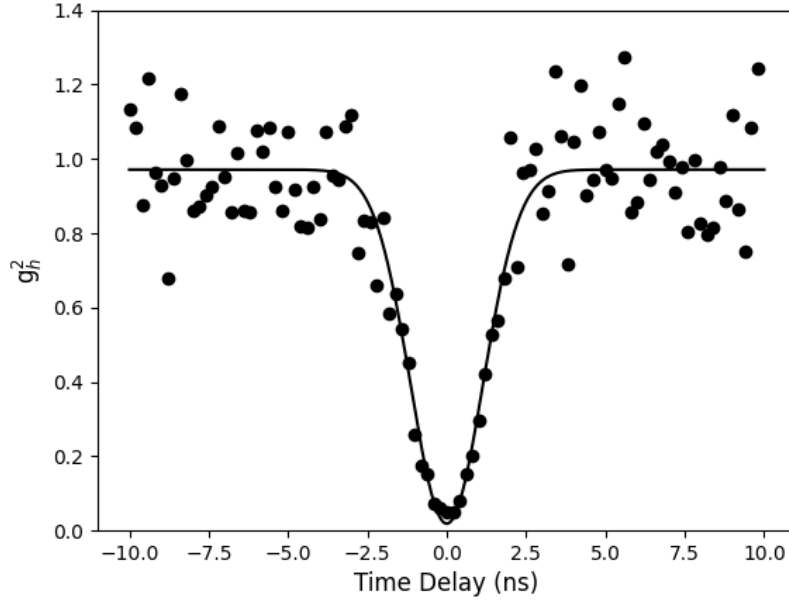


Figure 5.9: Example trace of the heralded g^2 for the second adjacent resonance with an on-chip power of $108 \mu\text{W}$. The dip at zero time delay illustrates $>95\%$ single photon purity.

number of threefold coincidences, N_A is the heralding count rate, and $N_{AB,AC}$ are the twofold coincidences between the heralding channel and one of the two idler channels. The magnitude of this dip relative to the background counts characterizes the single photon purity. An exemplary scan of the heralded $g^2(0)$ for the QKD source is shown in Figure 5.9 with 95% single photon purity. Tracking the heralded single photon purity as a function of power can indicate power regimes that compromise the security of the protocol as discussed in the previous section since multi-photon emission events are susceptible to attacks. Figure 5.6e) shows the heralded $g^2(0)$ as a function of on-chip power. For both sets of modes, the single photon purity remains above 90% when the on-chip power is below $150 \mu\text{W}$.

5.4 Time Bin Quantum Key Distribution

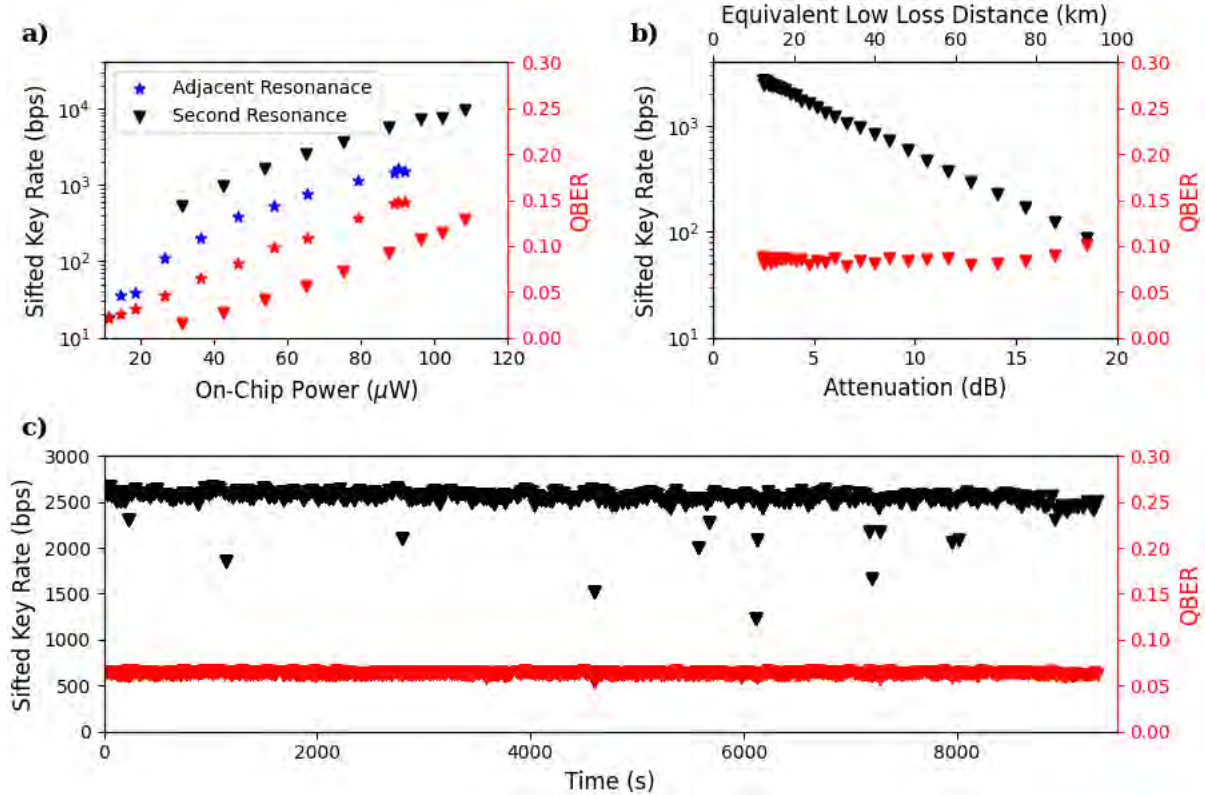


Figure 5.10: a) Sifted key rate and bit error rate as a function of on-chip pump power. The pump power is limited to $<120 \mu\text{W}$ to maintain a visibility above 70.7%. The triangles indicate the adjacent resonance characterization, and the stars indicate the second nearest resonance. b) Sifted key rate and bit error rate of the second nearest resonance as a function of attenuation on Alice’s path. The pump power is maintained at $\sim 90 \mu\text{W}$ while sweeping the voltage on a variable optical attenuator. The equivalent optical fiber distance is calculated and indicated on the top axis. c) Key rate stability measurement. Pumping with $\sim 65 \mu\text{W}$ of on-chip power, the source consistently outputs 2.5 kbps sifted key rate for up to 10,000 seconds (limited by the measurement time of the experiment).

With a bright source of entangled-photon pairs operating in a regime with high visibility and high single-photon purity, the QKD protocol described in Section 5.2.1 can be implemented. We monitor the Z basis (shown in Figure 5.5) to generate a sifted key at various pump powers to assess how the error rates and sifted key rates scale with power. Figure 5.10a) shows the sifted key rates collected for the adjacent and second nearest

resonance of the ring resonator source. As described in the source characterization section, the difference in resonance quality factors between these two pairs of modes creates a difference in the generated entangled photon pair flux, and thus the key rate of the second resonance is ~ 4 times larger than that of the adjacent resonance. Additionally, the pump rejection filters used in this experiment have larger extinction ratios for larger detuning from the pump wavelength, so the error rates of the adjacent resonance are larger than the second nearest resonance due to pump leakage into the detectors. Figure 5.6d) shows the visibility measurement (X basis) for the resonances at different pump powers. Since the Clauser-Horne threshold is surpassed for powers less than $126 \mu\text{W}$, we demonstrate the QKD protocol up to these powers. Without any error correction, sifted key rates with less than 11% error rates of up to 0.6 kbps and 8 kbps are recorded for the adjacent and second nearest resonance, respectively. A binary secure key can be established with up to $\sim 11\%$ error rates at which the Shannon rate $1 - 2H(x)$ reaches 0 (where $H(x) = -x\log_2(x) - (1-x)\log_2(1-x)$ is the binary entropy function) [25, 48–50]. Figure 5.11 plots the Shannon information versus the on-chip power illustrating the upper bound on the usable QKD rate. For the adjacent resonance, the error rate exceeds $\sim 11\%$ for powers above $\sim 70\mu\text{W}$, and for the the second resonance, this bound is $\sim 110\mu\text{W}$. We report the sifted key rates up to this bound to ensure that a secure key can be established. With additional pump filtering for the adjacent resonance, it is expected that the rate can approach 2 kbps.

A comparison of this result with a subset of other entanglement-based QKD demonstrations is included in Table 5.4, and Reference [17] has an extensive review of recent experimental works. For comparable error rates, our source does not outperform all of the demonstrations in this table; however, the efficiency of this source is improved, requiring only $\sim 100 \mu\text{W}$ of optical power to generate a comparable sifted key. For example, when normalizing to the pump power, the sifted key generation efficiency (74 kbps/mW)

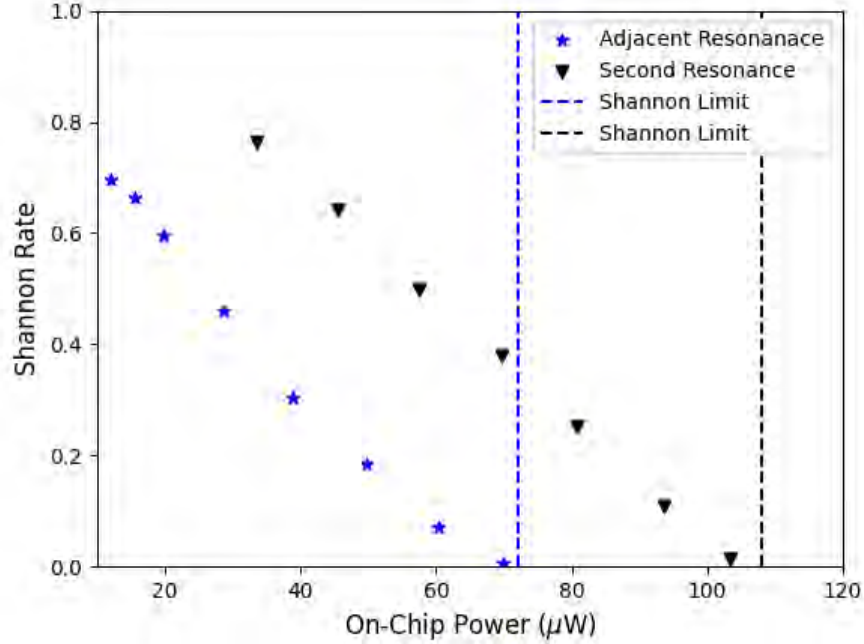


Figure 5.11: The Shannon rate, $1 - 2H(x)$, of the QKD system as a function of the on-chip power. As the error rate approaches $\sim 11\%$, the Shannon rate goes to 0, and no secure key can be established. For the adjacent resonance, this occurs $\sim 70\mu\text{W}$, and for the second resonance this value is at $\sim 108\mu\text{W}$.

is > 60 times higher in this work compared to bulk periodically poled lithium niobate (PPLN) used for the same protocol [41]. Other implementations using polarization encoding using bulk PPLN with > 66 multiplexed modes can generate key rates to > 1 Gbps [51] but require 400 mW of pump power. Comparing efficiencies for low-SWaP applications such as space-based entanglement distribution, the AlGaAsOI PIC single-pair efficiency of 74 kbps/mW (up to 120 μW for the studied device) is higher than these polarization encoding demonstrations with bulk PPLN (45 kbps/mW).

Next, the QKD protocol is extended to artificial distances using a variable optical attenuator placed before Alice's detection setup. Figure 5.10b) shows the sifted key rate and bit error rate as a function of attenuation. The top axis shows the equivalent distance in kilometers for the attenuation assuming low-loss optical fiber with 0.2 dB/km

Platform	Type	Resource	Sifted Key Rate (kbps)	Error Rate	Pump Power (mW)	Reference
AlGaAsOI ring	SFWM	Time-bin	8	0.09	0.108	This work
Bulk PPLN	SPDC	Time-bin	7	0.047	<6	[41]
AlGaAs waveguide	SPDC	Polarization	0.039	0.02		[52]
Bulk PPKTP	SPDC	Polarization	0.109	0.064	2.4	[53]
Bulk PPLN	SPDC	Polarization	0.3	<0.06	1-10	[54]
Si waveguide	SFWM	Dispersive optics	0.04-0.06	0.07-0.08		[37]
Bulk PPLN	SPDC	Polarization	$>100 \times 10^3$	<0.07	422	[42]
Bulk PPLN	SPDC	Polarization	$>1.8 \times 10^4$		400	[51]

Table 5.4: Comparison of entanglement-based QKD protocols. The key rates are adjusted to reflect transmission without attenuation and are reported for a single set of photon pairs (i.e without multiplexing).

attenuation. Since the protocol relies simply on the photon arrival times, photon loss will dominate all contributions to the degradation of the sifted key rate and increase in error rate. Using the second nearest resonance at an attenuation-free sifted key rate of 6 kbps and error rate of approximately 8.5 percent, the attenuator voltage is swept from 2.5 dB of attenuation (the insertion loss of the attenuator) to 18.5 dB of attenuation. The key rate remains above 100 bps for all attenuations, and the error rate remains consistent until approximately 15 dB of attenuation where it gradually increases to ~ 10 percent at the largest attenuation. With this data, we show an effective key rate of 100 bps at an equivalent distance of 92.5 km with error rates below 10%. It is important to note that the coincidence window used by Alice and Bob is 1 ns, which corresponds to the cavity lifetime of the photon pairs, so the effect of chromatic dispersion will be very small, and the use of an optical attenuator to estimate real fiber distance is reasonable. For example, based on our ~ 200 -500 MHz resonance linewidths and an SMF-28 fiber chromatic dispersion (about 18 ps/km/nm), we expect < 10 ps broadening of the wavepackets, which is $< 1\%$ of the 1 ns coincidence bin size for generating the sifted key. During the initialization stage, Alice and Bob can collect coincidence data to determine the optimal coincidence window and settings to reduce the impact of dispersion on the recorded key. The visibility of the link should not be influenced by chromatic dispersion since the relative phase between

the stabilized interferometer arms dictates this effect, and global phase accumulation from the deployed fiber will be stabilized.

To assess the long-term stability of the source, we show in Figure 5.10c) a sifted key and error rate measurement for up to 10,000 seconds. To align the pump laser with the resonance, the laser wavelength is swept from 0.1 nm below the resonance up to the resonance wavelength, allowing for the resonance to thermally shift as power begins to couple into the ring. Since the extinction ratio of the pump resonance is > 3 dB, an external power meter can be used to determine when the laser wavelength and resonance are aligned (showing a > 3 dB dip in the monitored power). During the stability measurement, if the power meter reading increases by > 3 dB, it is indicative of the laser and ring becoming misaligned. The wavelength sweep is repeated, taking < 5 seconds, to realign the pump laser with the ring resonance. The data shown in Figure 5.10c) is sampled every 20 seconds during the stability measurement, and the data points with key rates lower than the others are caused by this realignment process. Other than this monitoring, the operation requires no additional adjustments to the source. The slight reduction in the key rate over time is caused by fiber drift in the experimental setup, which can be mitigated through fiber packaging. Throughout the 10,000 seconds, the error rate is stable at ~ 6 percent.

5.5 Deployed Fiber QKD

To demonstrate the practical utility of the source, we send Alice's photon through a deployed, standard SMF-28 telecom fiber on the University of California Santa Barbara campus. The image in the background of Figure 5.12 shows an illustration of the approximate deployed fiber path with a ~ 2 km fiber loop connecting our research lab with another building on campus which is used to demonstrate the robustness of the

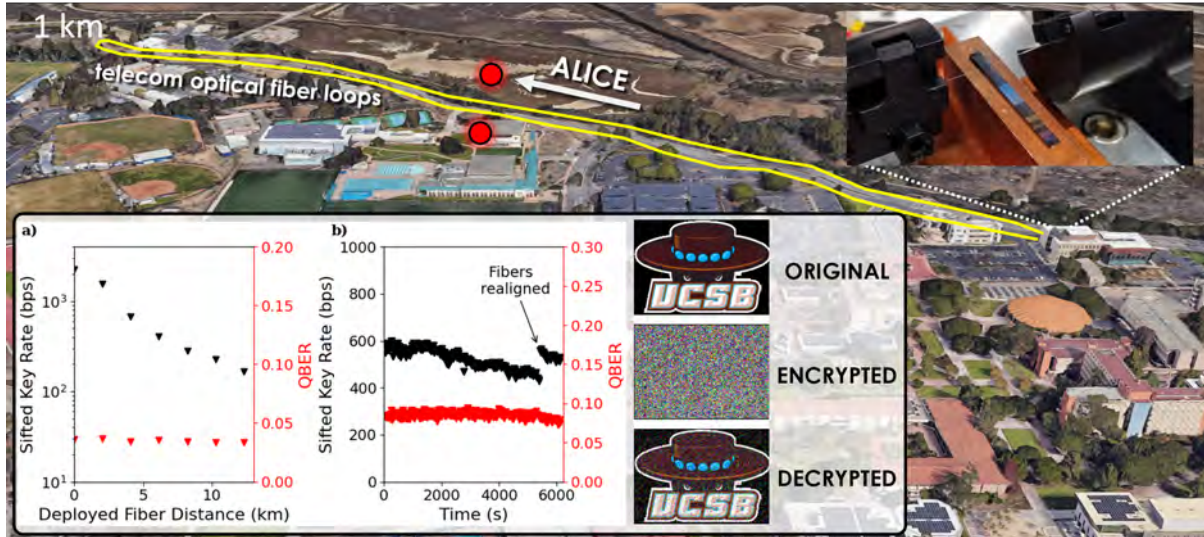


Figure 5.12: Illustration of the deployed fiber experiment conducted on the UCSB campus. Six loops of ~ 2 km fibers are in place between our research lab in Henley Hall and the campus police department building. The yellow lines indicate a rough estimate of the path of the deployed fibers which follow underneath the road connecting these parts of campus. The six independent loops allow for measurements to be completed at different deployed fiber lengths. a) The sifted key rate and error rate of the QKD protocol after sending Alice’s photons through the deployed fiber path. b) The stability of the key rate and error rate at the longest deployed fiber distance of 12.3 km. The chip-to-fiber coupling drift is significant during this measurement, so a realignment is completed at the 5,300 second mark. Using the 12.3 km deployed fiber, the UCSB logo is transmitted and encrypted using the QKD protocol. The image is encrypted with a key transmitted at 600 bps and a 9 percent error rate without any error correction.

protocol to external environmental factors. Six fiber loops are made, allowing for 12 km transmission using real fiber lines. Figure 5.12a) shows the key rate and errors for the second nearest resonance mode with an initial rate of 1 kbps and 3 percent error. The deployed fibers exhibit additional loss due to connectors instead of fiber splices being used to configure the number of fiber loops in the channel, which degrades the secure key rate. However, the error rate remains consistent and low for all fiber loop configurations indicating that the influence of environmental factors is negligible. Additionally, the visibility is monitored and is $> 73.9\%$ at 12.3 km indicating that the state is not impacted through the long distance distribution.

The stability of the system is also monitored for 6,000 seconds to confirm that external factors like vibrations from vehicles on the road above the fiber or temperature fluctuations do not influence the sifted key generation rate stability. As shown in the measurement in Figure 5.12b), fiber drift at the chip-fiber coupling interface is the largest factor in the key rate variation over time. To make sure this variation was from the chip-fiber interface and not a variation in the deployed fiber, a fiber realignment was completed showing that the initial rate can be recaptured and confirming that the deployed fiber does not impact the sifted key rate. With this information, we hypothesize that the attenuation-based demonstration accurately models the impact of deployed fiber length on the error rate and key rate. We therefore predict the ability for > 100 bps key rates with < 10 percent error at 92.5 km without spectral multiplexing.

Finally, we use the deployed 12.3 km fiber to transmit a key to encrypt and decrypt an RGB image as shown in Figure 5.12. Alice and Bob establish their key at 600 bps with an error rate < 9 percent (at the same time as the stability measurement shown in Figure 5.12b)) to communicate the UCSB logo. The right side of the inset of Figure 5.12 shows the original image, encrypted image and decrypted image using the QKD protocol described in this work. Without error correction, the source shows the capability of transmitting a key across the 12.3 km real deployed fiber to securely encrypt/decrypt a 21 kB image.

5.6 Conclusion and Outlook

Using a high-quality AlGaAs-on-insulator microring resonator, we generate a quantum optical microcomb spanning > 300 nm with > 20 time-energy entangled modes that can be easily demultiplexed and filtered using commercial, off-the-shelf telecom fiber components. We demonstrate the ability to demultiplex photon pairs for scalable entan-

lement distribution across standard telecom SMF-28 fiber. As an illustrative example, we demonstrate a continuous-wave time-bin quantum key distribution protocol that does not require pulsed optical excitation for clock synchronization. Requiring only $\sim 120 \mu\text{W}$ of optical power to generate up to 8 kbps sifted key rates with errors < 10 percent, we demonstrate the low SWaP capability and stability of the source and the protocol using a campus-deployed telecom fiber loop. The source operates with > 20 frequency mode pairs allowing for key rates exceeding 100 kbps to be achieved through wavelength multiplexing or a connected > 20 -user quantum photonic network to be established. We record sifted key rates and sifted key efficiencies up to 8 kbps and 74 kbps/mW of pump power (up to $100 \mu\text{W}$ for the studied device), respectively, for a single pair. The efficiency, which surpasses the record efficiency from bulk PPLN [51], is enabled by the tight optical confinement in the highly nonlinear and low-loss microring resonator, demonstrating the advantage of PICs for quantum communication applications that require low-SWaP.

Looking forward, the low SWaP of the source while maintaining ultra-high entanglement distribution rates opens new opportunities for practical quantum networks and communications, such as space-based and long-distance metropolitan channels. While we show here spectral modes spaced by 1 THz across 300 nm of bandwidth, dense spectral multiplexing with high generation rates is possible by cascading arrays of microcombs. For example, our AlGaAsOI chip (shown on the inset to Figure 5.12) has > 100 individual microring resonators, which could each be independently tuned and spectrally aligned to match the 100 GHz telecom ITU grid and pumped with fiber arrays to further enhance the key rates or improve the network user capacity. This could enable $> 1,000$ independent users with a single photonic chip or end-to-end multiplexed entanglement key rates exceeding 10 MHz.

The AlGaAsOI platform offers the potential not just for time-bin QKD protocols, but also for frequency-bin entanglement distribution, polarization encoding, and continuous-

variable protocols. Inherent to ring resonator sources is the broad range of frequency mode pairs generated through the SFWM process. Through the use of modulators, these frequency modes can be inferred to create frequency-bin states that can be used as an entangled resource for quantum communication [55]. Other, more complex systems can create frequency-bin encoded states using a series of ring resonators [56]. Polarization entangled states can be generated using AlGaAs waveguides [52], and additional work has been done to make the material platform compatible with silicon photonic systems [57–59]. Since AlGaAs can also naturally host quantum dots, integration with electrical injection is within reach, allowing for a turnkey generator of polarization entangled photon pairs (using a modified waveguide structure). The material platform (400nm thick AlGaAsOI) focused on in this work can also be adjusted to support both the TE and TM polarizations of light. Provided efficient fiber-to-chip couplers and symmetric ring coupling for both polarizations could be designed, it would be possible to pump the waveguide with a diagonally polarized input, generating both TE and TM polarized photon pairs in a superposition. The most straightforward approach for this would be the use of a symmetric 400nm by 400nm waveguide which would, in theory, meet the requirements. However, the loss in this system would be significant and the benefits of using polarization encoding over time-bin or another type of encoding do not outweigh these additional losses. Moving away from the discrete variable regime, AlGaAs seems promising for squeezed light generation with very low pump power, enabling continuous-variable QKD protocols and entanglement distribution technologies [60, 61]. The system that was the focus of this work can also be explored with pulsed excitation which can create a synchronized signal for Alice and Bob to define coincidence bins over. The use of a pulsed laser would increase the peak electric field intensity in the waveguide and enable a higher effective nonlinearity. The ease of continuous-wave excitation protocols is not to be ignored, and thus was the focus of this initial work. The large nonlinearity

and low loss make an AlGaAs source efficient, regardless of the photon degree of freedom being exploited, producing more entangled photon pairs for a given input power.

Using a simple ring resonator structure, we have been able to demonstrate a large improvement in the efficiency of an entanglement-based QKD source that boasts 74 kbps/mW key efficiencies with error rates $< 10\%$. Integration of this source with on-chip demultiplexers and packaging the optical fiber input/output would allow for a stable, efficient QKD source capable of producing $> \text{kHz}$ of secure key rates with a single set of frequency modes. This source can be explored (without modification) for other QKD systems such as high dimensional time-bin encoding and frequency-bin encoding, showing the flexibility of the platform and the source. This work shows an impressive first demonstration of the capability of the AlGaAs material platform for quantum communications applications.

Bibliography

- [1] J. Holden, *The mathematics of secrets : cryptography from caesar ciphers to digital encryption*. Princeton University Press, 1 ed., 2018.
- [2] A. J. Menezes, P. C. Van Oorschot, and S. A. Vanstone, *Handbook of applied cryptography*. CRC press, 2018.
- [3] R. D. Carmichael, *On Eulers -function*, *Bulletin of the American Mathematical Society* **13** (1907), no. 5 241–243.
- [4] Z. Sun, “Quantum computers may soon breach blockchain cryptography: Report.”
- [5] A. Ekert and R. Jozsa, *Quantum computation and Shor’s factoring algorithm*, *Reviews of Modern Physics* **68** (7, 1996) 733.
- [6] C. H. Ugwuishiwu, U. E. Orji, C. I. Ugwu, and C. N. Asogwa, *An overview of quantum cryptography and shors algorithm*, *Int. J. Adv. Trends Comput. Sci. Eng* **9** (2020), no. 5.
- [7] R. Dridi and H. Alghassi, *Prime factorization using quantum annealing and computational algebraic geometry*, *Scientific Reports* **7** (2, 2017) 1–10.
- [8] W. C. Peng, B. N. Wang, F. Hu, *et. al.*, *Factoring larger integers with fewer qubits via quantum annealing with optimized parameters*, *Science China: Physics, Mechanics and Astronomy* **62** (6, 2019) 1–8.
- [9] A. D. King, J. Raymond, T. Lanting, *et. al.*, *Quantum critical dynamics in a 5,000-qubit programmable spin glass*, *Nature* **617** (4, 2023) 61–66.
- [10] J. Gambetta, “IBM Quantum Computing Blog — The hardware and software for the era of quantum utility is here.”
- [11] C. Gidney and M. Ekerå, *How to factor 2048 bit RSA integers in 8 hours using 20 million noisy qubits*, *Quantum* **5** (4, 2021) 433.
- [12] T. Monz, D. Nigg, E. A. Martinez, *et. al.*, *Realization of a scalable Shor algorithm*, *Science* **351** (3, 2016) 1068–1070.

BIBLIOGRAPHY

- [13] A. Politi, J. C. Matthews, and J. L. O'Brien, *Shor's quantum factoring algorithm on a photonic chip*, *Science* **325** (9, 2009) 1221.
- [14] D. J. Bernstein and T. Lange, *Post-quantum cryptography*, *Nature* **549** (9, 2017) 188–194.
- [15] S. Pirandola, U. L. Andersen, L. Banchi, *et. al.*, *Advances in quantum cryptography*, *Advances in Optics and Photonics* **12** (12, 2020) 1012.
- [16] M. D. Noel, V. O. Waziri, S. M. Abdulhamid, and J. A. Ojieniyi, *Review and analysis of classical algorithms and hash-based post-quantum algorithm*, *Journal of Reliable Intelligent Environments* **8** (12, 2022) 397–414.
- [17] F. Xu, X. Ma, Q. Zhang, *et. al.*, *Secure quantum key distribution with realistic devices*, *Reviews of Modern Physics* **92** (6, 2020) 025002.
- [18] M. A. Nielsen and I. L. Chuang, *Quantum Computation and Quantum Information*. Cambridge University Press, 2011.
- [19] C. E. Shannon, *Communication Theory of Secrecy Systems*, *Bell System Technical Journal* **28** (1949), no. 4 656–715.
- [20] R. Wolf, *Quantum Key Distribution*, vol. 988 of *Lecture Notes in Physics*. Springer International Publishing, Cham, 2021.
- [21] C. H. Bennett and G. Brassard, *Quantum cryptography: Public key distribution and coin tossing*, *Theoretical Computer Science* **560** (12, 2014) 7–11.
- [22] W. Wang and N. Lütkenhaus, *Numerical security proof for the decoy-state BB84 protocol and measurement-device-independent quantum key distribution resistant against large basis misalignment*, *Physical Review Research* **4** (10, 2022) 043097.
- [23] H. K. Lo, X. Ma, and K. Chen, *Decoy state quantum key distribution*, *Physical Review Letters* **94** (6, 2005) 230504.
- [24] A. Kumar and S. Garhwal, *State-of-the-Art Survey of Quantum Cryptography*, *Archives of Computational Methods in Engineering* **28** (4, 2021) 3831–3868.
- [25] P. W. Shor and J. Preskill, *Simple proof of security of the BB84 quantum key distribution protocol*, *Physical Review Letters* **85** (2000), no. 2 441–444.
- [26] S.-H. Wei, B. Jing, X.-Y. Zhang, *et. al.*, *Towards Real-World Quantum Networks: A Review*, *Laser & Photonics Reviews* **16** (3, 2022) 2100219.
- [27] C. H. Bennett, G. Brassard, and N. D. Mermin, *Quantum cryptography without Bell's theorem*, *Physical Review Letters* **68** (2, 1992) 557–559.

BIBLIOGRAPHY

- [28] O. Cangea, C. S. Oprina, and M. O. Dima, *Implementing quantum cryptography algorithms for data security, European Conference on Artificial Intelligence* (2, 2016).
- [29] P. Zhao, M.-Y. Yang, S. Zhu, *et. al.*, *Generation of hyperentangled state encoded in three degrees of freedom, Science China Physics, Mechanics & Astronomy 2023* **66:10** **66** (9, 2023) 1–12.
- [30] B. Korzh, C. C. W. Lim, R. Houlmann, *et. al.*, *Provably secure and practical quantum key distribution over 307km of optical fibre, Nature Photonics* **9** (2, 2015) 163–168.
- [31] T. Zhong, H. Zhou, R. D. Horansky, *et. al.*, *Photon-efficient quantum key distribution using timeenergy entanglement with high-dimensional encoding, New Journal of Physics* **17** (2, 2015) 022002.
- [32] S. Wang, Z. Q. Yin, D. Y. He, *et. al.*, *Twin-field quantum key distribution over 830-km fibre, Nature Photonics* **16** (1, 2022) 154–161.
- [33] S. K. Liao, W. Q. Cai, W. Y. Liu, *et. al.*, *Satellite-to-ground quantum key distribution, Nature* **549** (8, 2017) 43–47.
- [34] R. Bedington, J. M. Arrazola, and A. Ling, *Progress in satellite quantum key distribution, npj Quantum Information* **3** (8, 2017) 1–13.
- [35] X. Lu, Q. Li, D. A. Westly, *et. al.*, *Chip-integrated visibletelecom entangled photon pair source for quantum communication, Nature Physics* **15** (2019), no. 4 373–381.
- [36] S. Cobourne, *Quantum Key Distribution Protocols and Applications*, tech. rep., Surrey TW20 0EX, England, 2011.
- [37] X. Liu, J. Liu, R. Xue, *et. al.*, *40-user fully connected entanglement-based quantum key distribution network without trusted node, Photonix* **3** (12, 2022) 1–15.
- [38] G. Moody, L. Chang, T. J. Steiner, and J. E. Bowers, *Chip-Scale Nonlinear Photonics for Quantum Light Generation, AVS Quantum Science* **2** (12, 2020) 041702.
- [39] T. J. Steiner, J. E. Castro, L. Chang, *et. al.*, *Ultra-bright entangled-photon pair generation from an AlGaAs-on-insulator microring resonator, PRX Quantum* **2** (9, 2021) 010337.
- [40] T. J. Steiner, M. Shen, J. E. Castro, *et. al.*, *Continuous entanglement distribution from an AlGaAs-on-insulator microcomb for quantum communications, Optica Quantum* **1** (12, 2023) 55–62.

BIBLIOGRAPHY

- [41] Y. Pelet, G. Sauder, M. Cohen, *et. al.*, *Operational entanglement-based quantum key distribution over 50 km of field-deployed optical fibers*, *Physical Review Applied* **20** (10, 2023) 044006.
- [42] S. P. Neumann, A. Buchner, L. Bulla, *et. al.*, *Continuous entanglement distribution over a transnational 248 km fiber link*, *Nature Communications* **13** (10, 2022) 1–8.
- [43] L. G. Helt, Z. Yang, M. Liscidini, and J. E. Sipe, *Spontaneous four-wave mixing in microring resonators*, *Optics Letters* **35** (9, 2010) 3006.
- [44] J. F. Clauser and M. A. Horne, *Experimental consequences of objective local theories*, *Physical Review D* **10** (1974), no. 2 526–535.
- [45] J. G. Rarity and P. R. Tapster, *Experimental violation of Bells inequality based on phase and momentum*, *Physical Review Letters* **64** (5, 1990) 2495–2498.
- [46] J. D. Franson, *Bell inequality for position and time*, *Physical Review Letters* **62** (5, 1989) 2205–2208.
- [47] S. Sun and A. Huang, *A Review of Security Evaluation of Practical Quantum Key Distribution System*, *Entropy* **24** (2, 2022) 260.
- [48] S. P. Neumann, T. Scheidl, M. Selimovic, *et. al.*, *Model for optimizing quantum key distribution with continuous-wave pumped entangled-photon sources*, *Physical Review A* **104** (8, 2021) 022406.
- [49] X. Ma, C. H. F. Fung, and H. K. Lo, *Quantum key distribution with entangled photon sources*, *Physical Review A - Atomic, Molecular, and Optical Physics* **76** (7, 2007) 012307.
- [50] E. Waks, A. Zeevi, and Y. Yamamoto, *Security of quantum key distribution with entangled photons against individual attacks*, *Physical Review A - Atomic, Molecular, and Optical Physics* **65** (2002), no. 5 16.
- [51] S. P. Neumann, M. Selimovic, M. Bohmann, and R. Ursin, *Experimental entanglement generation for quantum key distribution beyond 1 Gbit/s*, .
- [52] F. Appas, F. Baboux, M. I. Amanti, *et. al.*, *Flexible entanglement-distribution network with an AlGaAs chip for secure communications*, *npj Quantum Information* **7** (7, 2021) 1–10.
- [53] Y. Shi, S. Moe Thar, H. S. Poh, *et. al.*, *Stable polarization entanglement based quantum key distribution over a deployed metropolitan fiber*, *Applied Physics Letters* **117** (9, 2020) 124002.
- [54] S. K. Joshi, D. Aktas, S. Wengerowsky, *et. al.*, *A trusted node-free eight-user metropolitan quantum communication network*, *Science Advances* **6** (9, 2020).

BIBLIOGRAPHY

- [55] H.-H. Lu, E. M. Simmerman, P. Lougovski, *et. al.*, *Fully Arbitrary Control of Frequency-Bin Qubits*, *Physical Review Letters* **125** (2020).
- [56] M. Clementi, F. A. Sabattoli, M. Borghi, *et. al.*, *Programmable frequency-bin quantum states in a nano-engineered silicon device*, *Nature Communications* **14** (12, 2023).
- [57] J. Schuhmann, L. Lazzari, M. Morassi, *et. al.*, *Hybrid III-V/Silicon photonic circuits embedding generation and routing of entangled photon pairs*, .
- [58] J. M. Ramirez, H. Elfaiki, T. Verolet, *et. al.*, *III-V-on-Silicon Integration: From Hybrid Devices to Heterogeneous Photonic Integrated Circuits*, *IEEE Journal of Selected Topics in Quantum Electronics* **26** (3, 2020).
- [59] W. Xie, C. Xiang, L. Chang, *et. al.*, *Silicon-integrated nonlinear III-V photonics*, *Photonics Research* **10** (2, 2022) 535–541.
- [60] L. S. Braunstein and P. Van Loock, *Quantum information with continuous variables*, *Reviews of Modern Physics* **77** (4, 2005) 513–577.
- [61] H. Yonezawa and A. Furusawa, *Continuous-variable quantum information processing with squeezed states of light*, *Optics and Spectroscopy (English translation of Optika i Spektroskopiya)* **108** (2, 2010) 288–296.

Chapter 6

Integrated Qubit Demultiplexing and Hong-Ou-Mandel Interference

The first 5 chapters of this dissertation served to demonstrate the capabilities of III-V semiconductor material platforms for efficient generation and manipulation of quantum light. Specifically, the AlGaAsOI platform was developed and motivated for fully integrated quantum photonic circuits using entangled photons generated via the third order nonlinearity. Chapter 3 showed record-breaking performance for the entangled photon pair brightness from AlGaAsOI ring resonators, and Chapter 4 demonstrated the ability to create the other low-loss components required for basic quantum photonic circuits including chip-to-fiber couplers, waveguide crossers, optical filters, and interferometers. Using this platform, the next step in advancing the technology is to create some small quantum photonic circuits and characterize their performance. This chapter will highlight two steps toward fully integrated quantum photonic circuits on the AlGaAsOI platform. First, a bright entangled photon pair source was integrated with on-chip optical filters for a chip-scale demultiplexing experiment. The performance of the filter was characterized by monitoring the single photon counts through the signal and idler demultiplexed

channels. After demonstrating this experiment, a more advanced circuit was designed to demonstrate quantum interference between two nominally identical ring resonator sources. This experiment forms the foundation for scaling the AlGaAsOI material platform past the single qubit level. Understanding the intricacies of two photon pair sources will aid in the development of more advanced systems involving four or even more sources such as the impressive demonstrations of photonic graph states in silicon [1].

6.1 Qubit Demultiplexing

To benchmark our platform, we perform a qubit demultiplexing experiment in which entangled signal and idler photons generated from SFWM in a microring resonator are separated on-chip using a tunable unbalanced MZI with an FSR equal to twice the signal/idler mode separation. As discussed in Chapter 4, the unbalanced MZI provides an interference-based filtering that has a sinusoidal transmission dependence as a function of wavelength. By tuning the path length imbalance of the MZI, the sine period can be adjusted to match four times the FSR of the ring resonator photon pair source. Since the entangled photon pairs are generated adjacent to the pump resonance mode (see Figure 6.1b), the MZI period is designed to transmit one of the single photon modes (signal) and block the other mode (idler). This can be achieved by making the MZI period 4-times the ring FSR. Selection of different pairs of modes can also be made by using a different MZI period. Using these design parameters, a series of ring resonators integrated with MZI period. Using these design parameters, a series of ring resonators integrated with MZI optical filters were fabricated and tested. The extinction ratio of the MZIs varied between 10 and 30 dB, and one of the higher extinction ratio devices was selected for the qubit demultiplexing experiment.

The demultiplexing setup schematic is shown in Figure 6.1a). A tunable, narrow-linewidth continuous wave (cw) laser is tuned into resonance with a ring resonator mode

near 1555 nm (labeled λ_p in Figure 6.1b). Tunable fiber etalon-based bandpass filters (3x Agiltron filters with ~ 30 dB extinction ratio and ~ 3 dB insertion loss) are tuned to the pump wavelength and placed immediately after the laser to suppress amplified spontaneous emission at the wavelengths of the signal and idler modes, which helps ensure that pump photons do not reach the single-photon detectors in the experiment. The laser is polarized along the TE mode of the input waveguide, and light is coupled onto the chip with high-numerical aperture lensed fiber. Pump light is coupled into the microring resonator using a pulley coupler (Section 2.2.2), where the time-energy entangled signal and idler photon pairs are generated. The signal, idler, and pump photons are routed through the tunable MZI. When the phase of the MZI is properly tuned (Figure 6.1b), it demultiplexes the signal and idler photons into separate waveguides. Light from one output port is coupled off chip using a lensed polarization-maintaining single-mode fiber. The output is then sent to superconducting nanowire single-photon detectors (SNSPDs). A 100 GHz bandwidth DWDM filter is placed in front of the SNSPDs to ensure that only detector 1 measures signal photons and detector 2 measures idler photons; these are in place for characterizing the chip, but their extinction ratio is > 40 dB and thus they have no impact on the performance of the qubit demultiplexing chip. The DWDM is also necessary since an interference-based optical filter is used for the demultiplexing. Since the filter response is periodic with the wavelength and the entangled photon pair source generates a relatively broadband spectra of photon pairs, every fourth idler (signal) mode will also be transmitted through the demultiplexer. An accurate characterization of the source quality is to look at just one pair of modes, so the DWDM filters all of these unwanted modes out of the detected single photons. Additionally, since the MZI is just used as a demultiplexer (and not a pump rejection filter), a significant portion of the pump light would reach the detectors. In order to make the circuit be free of off-chip filtering, additional pump rejection filters would need to be integrated. These could also

be MZI-based devices, but now the MZI period would be twice the ring FSR such that it transmits both the signal and idler photon but not the pump mode.

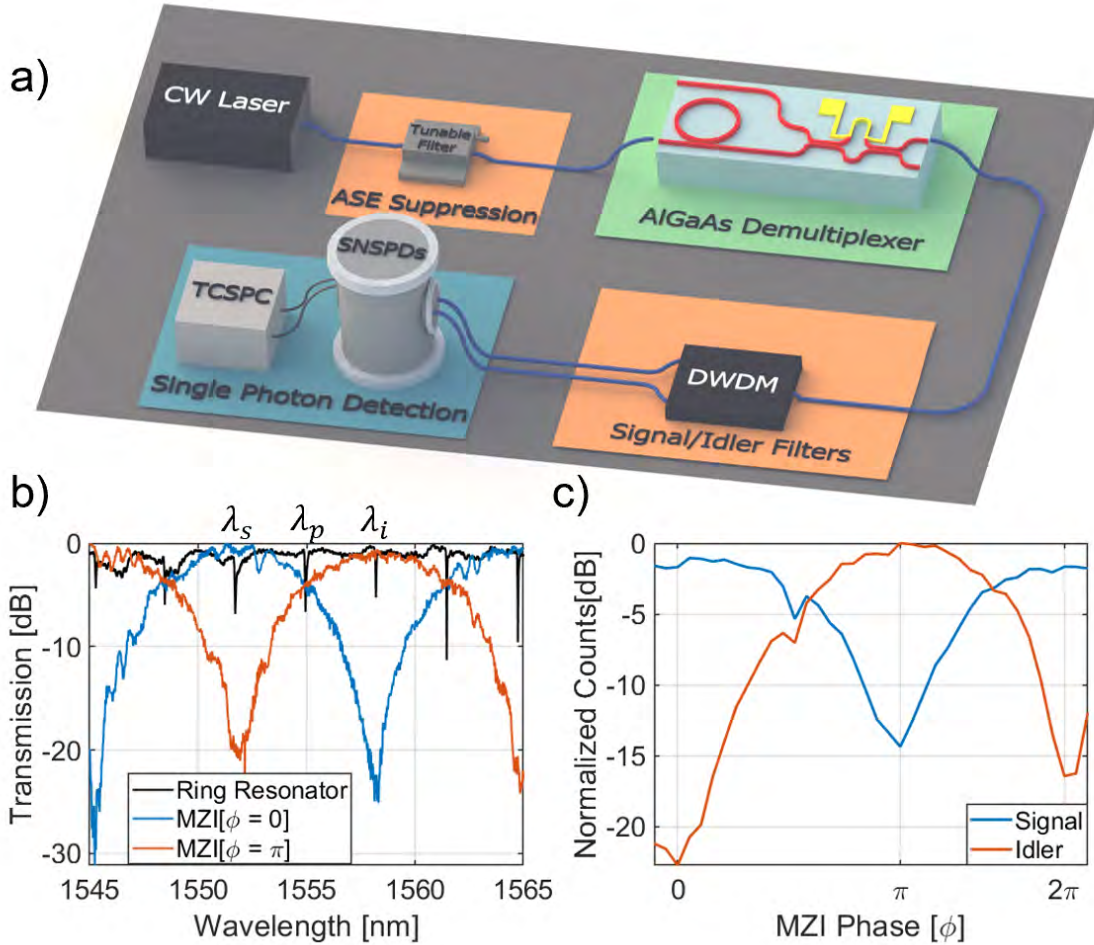


Figure 6.1: a) Experimental schematic of qubit demultiplexing utilizing an 3.2 nm FSR AlGaAs ring resonator source and a 13.0 nm FSR MZI (DC). b) Transmission spectra of a ring resonator and MZI tuned to a relative phase of zero and π radians. The signal, pump, and idler wavelengths are indicated. c) Normalized counts on the SNSPDs after demultiplexing as the MZI phase is swept from 0 to 2π radians.

The chip is designed with an MZI with directional couplers and a $45.4 \mu\text{m}$ path imbalance for these experiments, which results in an MZI FSR that is equal to twice the signal/idler mode spacing of the microring resonator entangled-photon pair source (or four times the ring resonator FSR). Figure 6.1b) shows the transmission spectrum of the

MZI chip when coupling into port 1 and out of port 4 for two different thermo-optic heater voltages corresponding to an interferometer phase $\phi = 0$ and $\phi = \pi$ radians, respectively. The maximum MZI extinction is ~ 23 dB near the signal and idler wavelengths. As the phase is swept from 0 to π , the transmission at a single wavelength sweeps from maximum to minimum. Vertical lines in the plot depict the wavelengths of the pump (1555.0 nm), signal (1551.7 nm), and idler (1558.2 nm) photons from the microring resonator. We next pump the resonator to generate entangled pairs (as shown in Figure 6.1a), which propagate through the MZI for demultiplexing. Normalized counts from the two SNSPDs are shown in Fig. 6.1c) as a function of the MZI phase. We measure an extinction ratio up to ~ 23 dB, which is identical to the measured MZI extinction ratio shown in Fig. 6.1b) obtained from the transmission spectrum.

6.2 Integrated Hong-Ou-Mandel Interferometer

Here, we further advance the AlGaAsOI material platform by combining multiple efficient entangled-pair sources with tunable interferometric circuits to demonstrate two experiments: (1) a tunable Bell state generator that can produce two of the four maximally entangled Bell states, and (2) an integrated Hong-Ou-Mandel interferometer that allows for measurement of heralded two-photon interference on-chip from two resonator sources. In the CW pumping case, it requires $\sim 100 \mu\text{W}$ of input power to achieve comparable photon pair generation rates to the ~ 10 mW input power required for silicon quantum sources, relaxing the demands on filtering and demultiplexing to achieve large coincidence-to-accidental ratios. While only being comprised of ~ 10 components, this circuit demonstrates the efficiency, stability, and manufacturability of AlGaAsOI for larger-scale quantum photonics, including graph-state generators and entangling fusion gates for distributed information processing and communications [2, 3].

6.2.1 Tunable Bell State Generator

The circuit designed for the integrated Hong-Ou-Mandel (HOM) interference experiment was initially designed for the case where both ring resonators generate entangled photon pairs simultaneously; however, when analyzing the evolution of the quantum state in the system, it was also discovered that the circuit can be used to produce a path-encoded photonic Bell-pair that can be tuned using the final interferometer. For low enough pump powers, either the top ring or the bottom ring generates a photon pair (the probability that both sources generate simultaneously is low); thus, either a photon pair exists in the upper two paths $|11\rangle$ or the lower two paths $|00\rangle$, as illustrated in Fig. 6.2. Since the sources are both probabilistic, the likelihood of both sources generating a photon in the same time window (τ) scales with the product of the two sources generation rate $P_{both} \propto R_1 * R_2 / (\tau^2)$. Reducing the generation rate (through using lower pump power) can thus make the simultaneous generation probability near 0. Coincidence measurements between the different combinations of output ports allow for the construction of the bi-photon density matrix for a specific phase setting on the final interferometer. The inset of Figure 6.2 shows simulated density matrices of the initial state after the demultiplexers, in which the two photons are in the $|\Phi^+\rangle = \frac{1}{\sqrt{2}}(|00\rangle + |11\rangle)$ state. Qubit A (B) is defined by the outer (inner) two paths, with state $|1\rangle$ ($|0\rangle$) defined as the top (bottom) path for each qubit.

The bi-photon state evolves into the $|\Psi^+\rangle$ state when the last symmetric MZI has a phase shift $\phi = 0$ or the $|\Phi^-\rangle$ state when the phase shift $\phi = \pi$. This evolution comes from the final balanced MZI which has a tunable phase. The MZI unitary evolution can

be described by (as introduced in Chapter 4 Section 4.4.2),

$$S = je^{-j\phi/2} \begin{bmatrix} \sin \frac{\phi}{2} & \cos \frac{\phi}{2} \\ \cos \frac{\phi}{2} & -\sin \frac{\phi}{2} \end{bmatrix} \quad (6.1)$$

When the initial state, $|\Phi^+\rangle = \frac{1}{\sqrt{2}}(|00\rangle + |11\rangle)$, enters the final MZI, the state evolves as $U(\phi)|\Phi^+\rangle$ which has significant results when $\phi = 0$ and $\phi = \pi$. For these particular phase values, the output can be theoretically tuned to output either the $|\Psi^+\rangle$ or $|\Phi^-\rangle$.

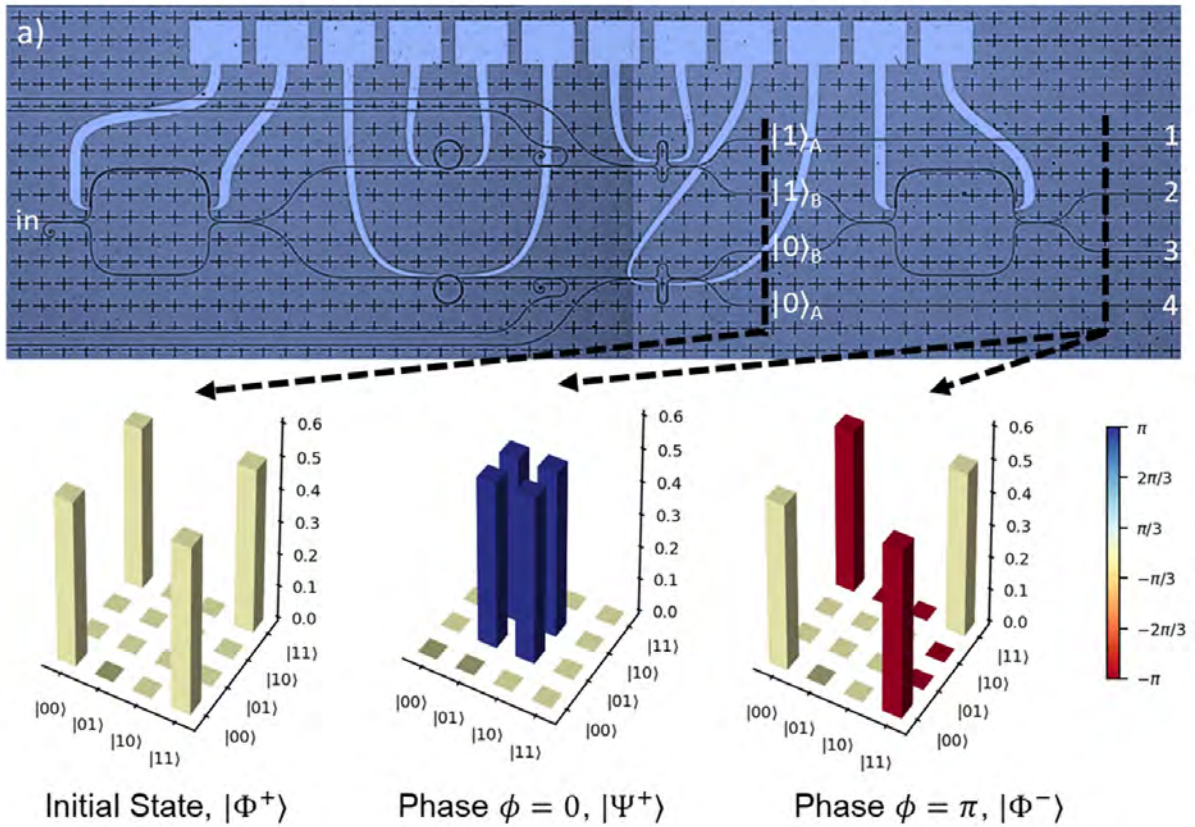


Figure 6.2: a) Microscope image of the AlGaAsOI circuit for HOM and tunable Bell State generation. The ports on the output are labeled 1-4 on the right side of the image. The initial photon state is in $|\Phi^+\rangle$ (shown in the bottom left panel of the inset). After exiting the final interferometer, the unitary MZI operator transforms the initial state into either the $|\Psi^+\rangle$ or $|\Phi^-\rangle$ state when a 0 and π phase shift is applied, respectively.

Unfortunately, full quantum state tomography is not possible with the current circuit design. Since the circuit does not have an integrated interferometer and phase shifter for the heralding arms (paths 1 and 4), only a subset of the necessary stabilizers can be measured, which limits the ability to reconstruct the full quantum state [2]. Thus, the tunable Bell state generator, although theoretically possible with this circuit, cannot be directly verified using the current design. The addition of phase shifters on the heralding paths and an interferometer would enable this measurement. From two-fold coincidences, we can verify that the final MZI can apply the necessary phase shifts and adjust the ratio of photons exiting ports 2 and 3 (which will be done in the next section). This verifies that the circuit works as desired, and therefore should create the predicted states. Through analysis of the indistinguishability of the two sources (described below), the extracted parameters can be used to then model and reconstruct the density matrix.

6.2.2 HOM Interference

At higher input powers such that the probability of generating photon pairs simultaneously in both resonators is high, this circuit can also be utilized to demonstrate the indistinguishability of two microring resonator entangled photon pair sources. The power must remain sufficiently low that the multi-photon pair emission from each source still remains low (the heralded $g^{(2)}(0)$ for each source remains < 0.5). When both resonators generate photon pairs simultaneously and the demultiplexers are aligned, each source supplies an identical idler photon into the final interferometer. The Hong-Ou-Mandel effect describes the behavior of two indistinguishable photons entering a beamsplitter where the two photons always exit the same port due to destructive interference of the states where one photon exits each port [4]. The full mathematical description of this effect is included in Section 2.1.3. A microscope image of the AlGaAsOI quantum pho-

tonic circuit is shown in Figure 6.3. This microscope image is the same as the previous section, but now the critical steps in measuring HOM interference are labeled. The device has two ring resonators with $31.5 \mu\text{m}$ radii, 350 nm coupling gap, 650 nm ring widths, and MZIs with $45.4 \mu\text{m}$ path imbalance. The 3 dB couplers are all $20.8 \mu\text{m}$ in length. If the two sources generate perfectly indistinguishable photons, then there will be zero four-fold coincidences at zero time-delay since both idler photons will exit the same port. By tuning the phase of the final interferometer, the photons can be swept from indistinguishable (with phase $\phi = 0$) to distinguishable (with phase $\phi = \pi$). An off-chip tunable

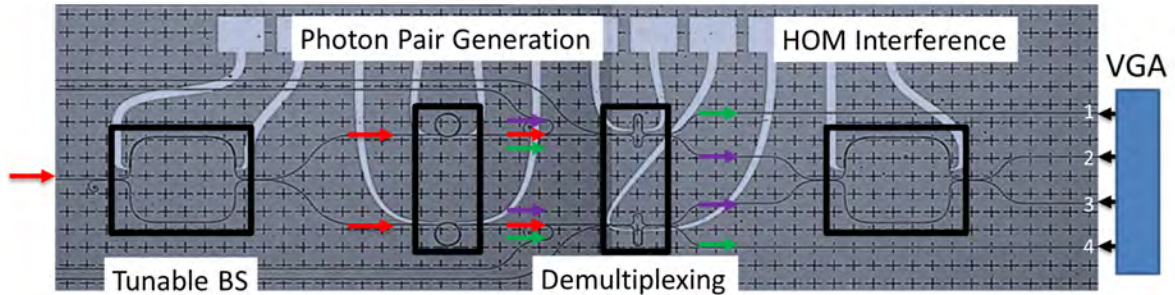


Figure 6.3: Microscope image of the AlGaAsOI circuit for HOM interference. This image is the same as illustrated in Figure 6.2a), but now the different portions of the circuit are highlighted for the HOM interference experiment. Light enters from the left side of the circuit and goes into a symmetric MZI that acts as a tunable beamsplitter (BS) to distribute the input power equally to the two ring sources. The two ring resonators act as sources of entangled photon pairs. Next, two unbalanced MZIs demultiplex the signal and idler photon pairs into two paths. The signal photons exit ports 1 and 4 for heralding, and the idler photons enter the HOM interferometer to show two-photon quantum interference.

continuous wave laser source is input into the central waveguide and enters a tunable symmetric MZI (labeled “Tunable BS”). This MZI acts as a tunable beamsplitter allowing for the ratio of power entering the two rings to be tuned such that they have similar entangled photon-pair generation rates which improves the probability that both sources generate a photon pair at the same time. The light is sent to each of the resonators, which can be thermo-optically tuned to align their resonances. Upon entering the resonators,

there is a probability that two pump photons interact and annihilate through SFWM to generate a pair of correlated photons (labeled “Photon Pair Generation”). After each resonator, an unbalanced MZI serves as a spectral demultiplexer to separate the signal and idler photons (labeled “Demultiplexing”). The signal photon from the top (bottom) ring exits port 1 (4) and is used to herald the presence of an idler photon in the final interferometer. The idler photons enter the final MZI (labeled “HOM Interference”) where a 3-dB directional coupler splits the light into two paths, one of which has a tunable phase shifter. The HOM interference occurs on the final 3-dB directional coupler where both idler photons should exit the same port if they are perfectly indistinguishable. The phase shifter on the upper path enables the distinguishability to be swept from perfectly distinguishable to indistinguishable. Thus, by monitoring the fourfold coincidence counts as a function of the applied phase, the indistinguishability of the idler photons from the two sources can be determined.

6.2.3 Linear Component Characterization

The performance of the individual circuit elements had to be carefully characterized to determine how the entire circuit might function. This characterization follows the linear optical characterization described in Chapter 4. A CW laser is swept continuously from 1510 nm to 1600 nm wavelength and the transmission through the different ports is monitored using a photodiode and oscilloscope. A transmission spectrum of ports 1 and 4 is shown in Figure 6.4a,b). The sinusoidal response shows the behavior of the demultiplexer, which can be tuned to have a minimum at the idler wavelength and a maximum at the signal wavelength to demultiplex the two photons into separate paths. The demultiplexer shown in Figure 6.4 has an extinction ratio > 15 dB for the signal and idler wavelengths studied in this experiment, but devices with > 30 dB extinction

have been demonstrated on the platform [5]. The deeper, narrow transmission dips are caused by the ring resonances. Since port 1 (4) only sees the top (bottom) ring, only that ring's resonances are observed in the transmission scan. The current of the thermal tuners on the rings and demultiplexers are set to align the resonances of the signal and idler photons with the center of a commercial double-pass DWDM filter. This filter is the same detailed in Chapter 5 and has >100 dB extinction with <4 dB of insertion loss. Although the signal and idler photons are demultiplexed on-chip and sent through different ports, the pump light is not filtered, and the periodic behavior of the MZI-based demultiplexers necessitates additional off-chip filters to only observe one pair of signal and idler frequency modes and to remove excess pump light.

In Figure 6.4a,b), the selected signal (orange), pump (blue), and idler (green) photon wavelengths are highlighted. The alignment shown in the transmission scan is done coarsely—such that the resonances of interest are roughly aligned. During the actual experiment, an alignment protocol is utilized to assure that the rings are both being pumped simultaneously. The protocol is described in more detail in the next section. From the initial scans, the three resonances were fit using the ring resonator transfer function (described in Section 2.2.2). A zoom in of the three resonances are shown in Figure 6.4c-e) for the top ring (ring 1) and in Figure 6.4f-h) for the bottom ring (ring 2). Careful inspection of these plots will show a 0.1 nm misalignment between the top and bottom ring. This can easily be corrected by changing the current on the thermal tuners for each ring. The insertion loss of the HOM circuit (including component loss, chip-to-fiber coupling, and propagation loss) was <15 dB for port 1 and <20 dB for port 4. Since the power of the pump laser can be increased to improve the on-chip power, the input coupling loss is not as critical to the device performance. Instead, the losses after the photon pairs are generated will dictate the efficiency of the system. Here, the losses from the photon pair source to the single photon detectors is on the order of 12 dB and

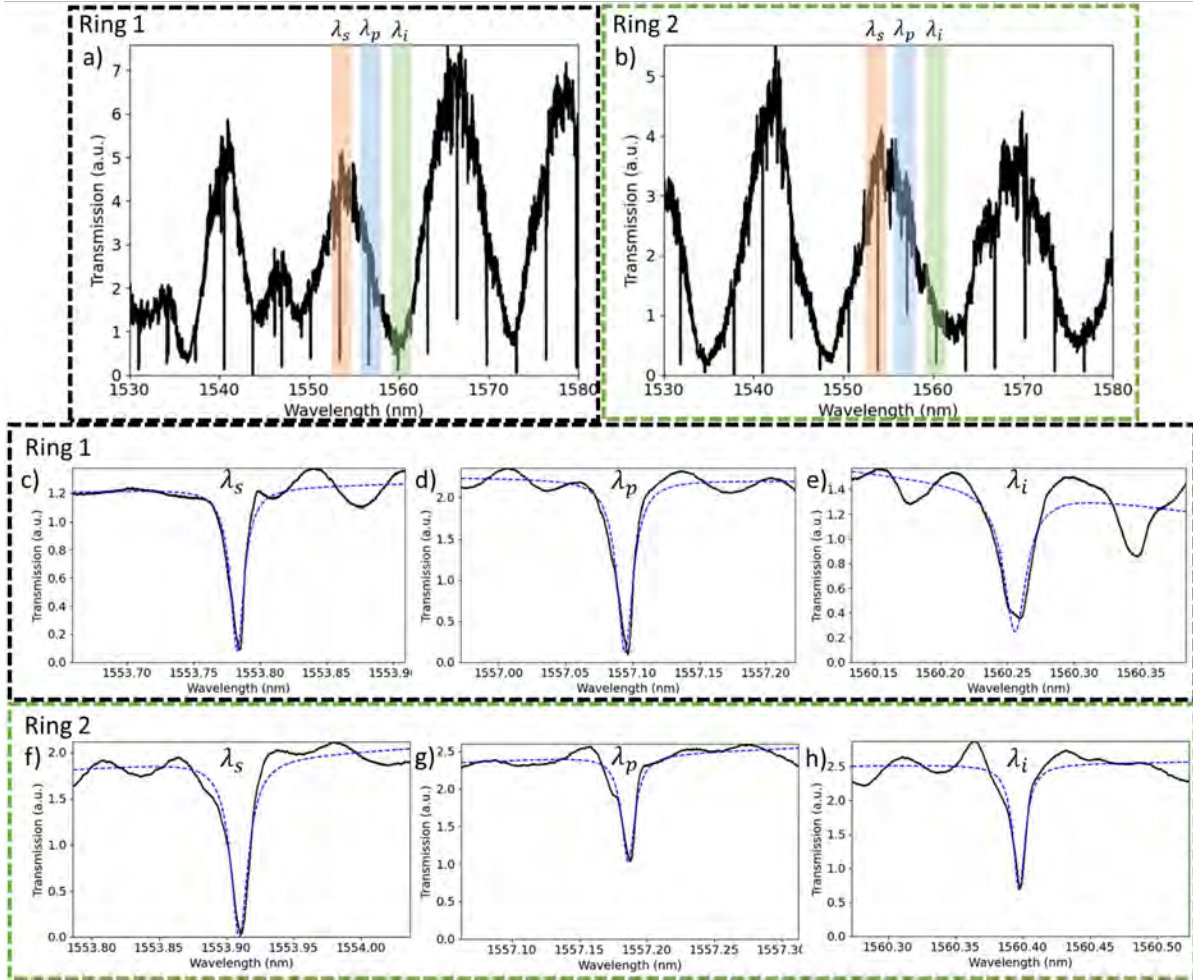


Figure 6.4: a) Transmission scan through ring 1 and exiting through the topmost port (port 1). b) Transmission scan through ring 2 and exiting through the bottommost port (port 4). c) Signal resonance scan for ring 1 showing 1.2×10^5 loaded quality factor. d) Pump resonance scan for ring 1 showing 1.1×10^5 loaded quality factor. e) Idler resonance scan for ring 1 showing 0.7×10^5 loaded quality factor. f) Signal resonance scan for ring 2 showing 0.9×10^5 loaded quality factor. g) Pump resonance scan for ring 2 showing 1.2×10^5 loaded quality factor. h) Idler resonance scan for ring 2 showing 1.4×10^5 loaded quality factor.

16 dB for the top and bottom ring.

6.2.4 Nonlinear Characterization

After completing the linear characterization and selecting the resonance wavelengths for the signal, pump, and idler modes, the quality of each of the ring sources was assessed to determine the expected performance in the HOM experiment. The basic characterization completed in Chapter 3 was repeated with a few modifications. Primarily, since the device has one input that sends the pump laser to both the rings simultaneously, the initial tunable beamsplitter (see Figure 6.4) had to be tuned to send all of the light to only one of the two rings. Figure 6.5a) demonstrates the ratio of power coupled out of the two ring sources through tuning of the initial beamsplitter. At 7 mW of heater power, the first ring receives most of the pump light, and the second ring is at a minimum. Under this beamsplitter condition, the input pump power is swept to track the single photon counts and coincidence counts of the resonator source as a function of power. At the highest power recorded, the first ring outputs almost 2 million single photons a second with a coincidence rate exceeding 4000 counts per second (shown in Figure 6.5b). The second ring has a lower insertion loss (illustrated by the larger power transmitted through the port). Figure 6.5c) shows the performance of the second ring source which is less efficient than the first ring (for higher power, produces fewer single and coincidence photon counts). The source, however, still produces almost 1 million single photons through port 4 and has coincidence rates exceeding 1500 counts per second. Thus, both ring sources can produce high rates of photon pairs through CW pumping.

6.2.5 Alignment

In order to perform the nonlinear characterization above, all of the components had to be aligned to perform the desired role. The initial beamsplitter was aligned through monitoring of the power into each ring such that the two ring sources produced similar

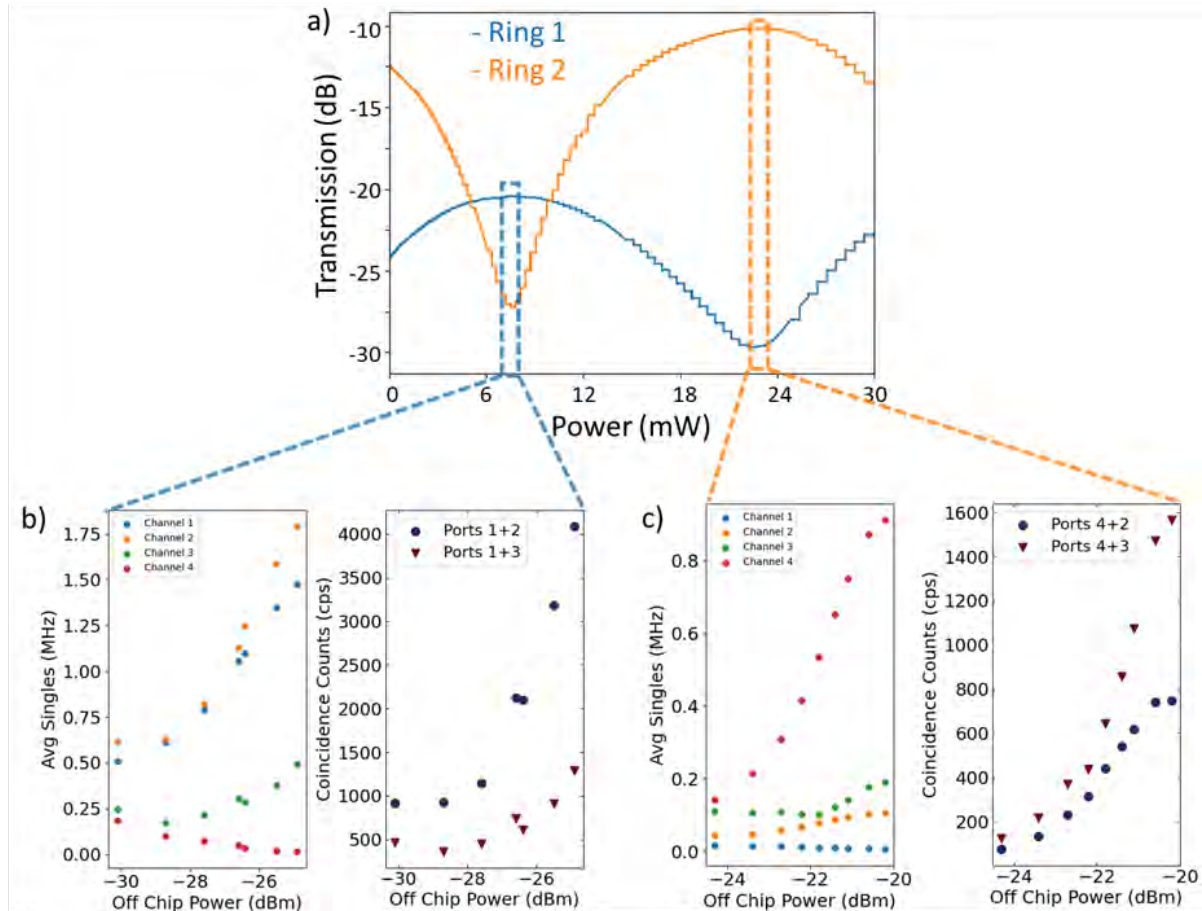


Figure 6.5: a) Tuning of the first tunable beamsplitter of the HOM circuit to adjust the power coupled into each of the two ring sources. b) Single photon counts and coincidence counts for various pump powers of the first ring source. c) Single photon counts and coincidence counts for various CW pump powers of the second ring source.

rates of entangled photon pairs (see Figure 6.5), the rings had to be aligned to generate photon pairs that were centered in the selected DWDM filter channels, and the demultiplexers had to be aligned to send the signal photons through ports 1 and 4 and the idler photons through ports 2 and 3 (and into the HOM interferometer). This alignment procedure could not be done independently since the act of increasing the heater current on one component resulted in thermal crosstalk to adjacent components. Thus, a tuning map had to be made for different heating conditions. Initially, the components were characterized individually (as done in Figure 6.5a) to align them coarsely. After tuning

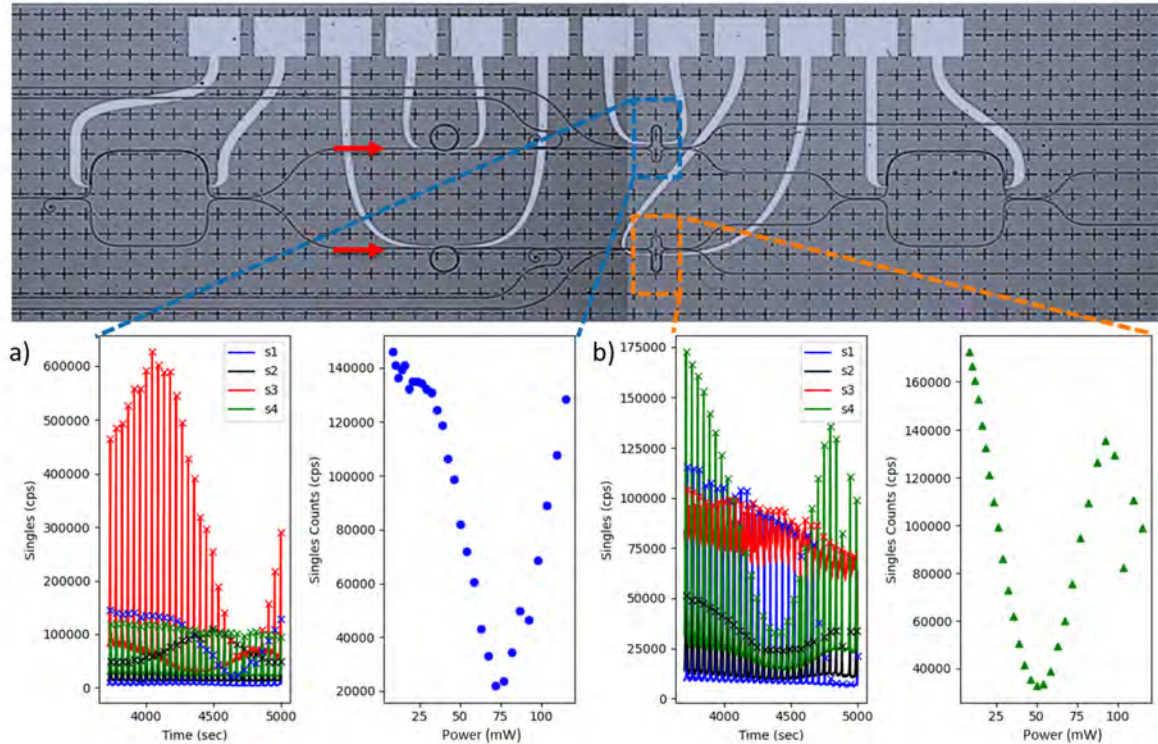


Figure 6.6: The demultiplexers are highlighted on a microscope image of the HOM circuit. a) Single photon counts as the power in the demultiplexer heater is swept. The left panel shows all four SNSPD channels, and the right panel shows just the photons exiting the top port (port 1). b) Same plot as *a* for the second demultiplexer.

all components, fine tuning was completed to get the best alignment of each portion of the circuit. For components like the tunable beamsplitters, the power through the ports was simply monitored as the heater current was swept. For more sensitive components like the demultiplexers, the light was coupled off-chip into fiber-based DWDMs for single photon detection, and the single photon counts at the signal and idler wavelengths was optimized. Figure 6.6 illustrates the single photon counts for ring 1 (a) and ring 2 (b) as the demultiplexer current is swept. For the top demultiplexer, the maximum photon counts occurs at 125 and 0 mW, while for the lower demultiplexer, the maximum occurs at 0 mW and 90 mW. The trace in the right panel of Figure 6.6b) shows the drift of the ring resonance and fibers over time. Although a maxima is reached at both 0 and

90 mW, the 90 mW peak has considerably fewer photon counts. This is due to fiber misalignment as the data is collected.

For the CW HOM testing, integration times exceeding 3 hours were required due to the rare nature of fourfold coincidences (which for silicon were on the order of 1 mHz) [2, 6, 7]. The AlGaAs platform is expected to have more efficient photon pair sources, however, there is a threshold at which the source can be pumped to generate just one photon pair (with minimal multi-pair contributions). Thus, the collected photon pair rates are typically comparable to silicon sources, simply requiring less power to achieve the rates. Considering a count rate on the order of mHz, it is important to collect sufficient data such that the signal to noise on the HOM experiment is sufficient. With noise scaling as \sqrt{N} (where N is the number of counts), collected fourfold coincidence counts >10 are necessary—meaning data collection must occur for more than 3 hours. The experimental setup had to be adapted to enable such long measurement times. The lensed fibers were mounted with additional tape to secure the fibers from drifting, and the length of fiber extending past the fiber mount was reduced to limit drift over time. The chip was secured on a thermoelectric cooling stage to maintain consistent temperature.

Even with all of these modifications, the stability of the system remained a challenge as illustrated in Figure 6.6b) where the drift is noticeable even in 1500 seconds (duration of the scan). During CW testing, the amount of optical power coupled into the ring resonator impacts the location of the resonance wavelength due to the thermal instability of the ring [8]. Since vibrations and fiber drift could change the optical power coupled into the ring, in order to maintain alignment between the two ring resonator sources, an optimizer was developed. The optimizer utilized the two ring heaters to constantly adjust the temperature of each ring to maintain alignment to the pump laser wavelength. First, the power coupled out of ports 1 and 4 (see Figure 6.4) is monitored using a 99:1 fiber beamsplitter. The 1% tap is connected to a power meter, and the remaining 99%

is sent through the rest of the components described in the section below for photon coincidence measurement. The laser is kept at a single wavelength, and the ring heaters are set to an initial setpoint that is close to alignment (as determined by a coarse sweep in the heater setting). Since the resonance extinction ratio is > 10 dB for this particular device, the 1% tap will show a reduction of 10 dB in the recorded power when the ring resonance is aligned with the laser. The individual ring heaters are dithered toward the minimum power on their corresponding port. As the heater oscillates, the power will increase if the ring moves away from the laser wavelength and decrease if the alignment improves. Thus, a small oscillation in the heater power allows for continuous adjustments to small drift in the conditions. Large or fast perturbations in the environment cannot be adjusted for using this method, but slow changes like fiber drift and temperature change can be accommodated. The development of this optimizer enabled the experiment to be free-running without monitoring for up to four hours before the fiber drift was too large.

Further improvements to the system could be made through packaging and wire-bonding to a printed circuit board. The packaged chip would reduce fiber drift, and the wire-bonding would reduce the day-to-day fluctuations in the probe contacts with the metal heaters. The short term solution created by the optimizer was sufficient to collect the necessary HOM data.

6.2.6 HOM Interference

After characterizing the individual component performance and aligning all of the parts of the HOM integrated circuit, the HOM interference could be measured. The experimental setup for the HOM characterization is shown in Figure 6.7a). A Toptica CW tunable laser is set to the pump wavelength (near 1556.6 nm) while the demultiplexer MZIs and ring MZIs are tuned into alignment. The ring alignment optimizer is started

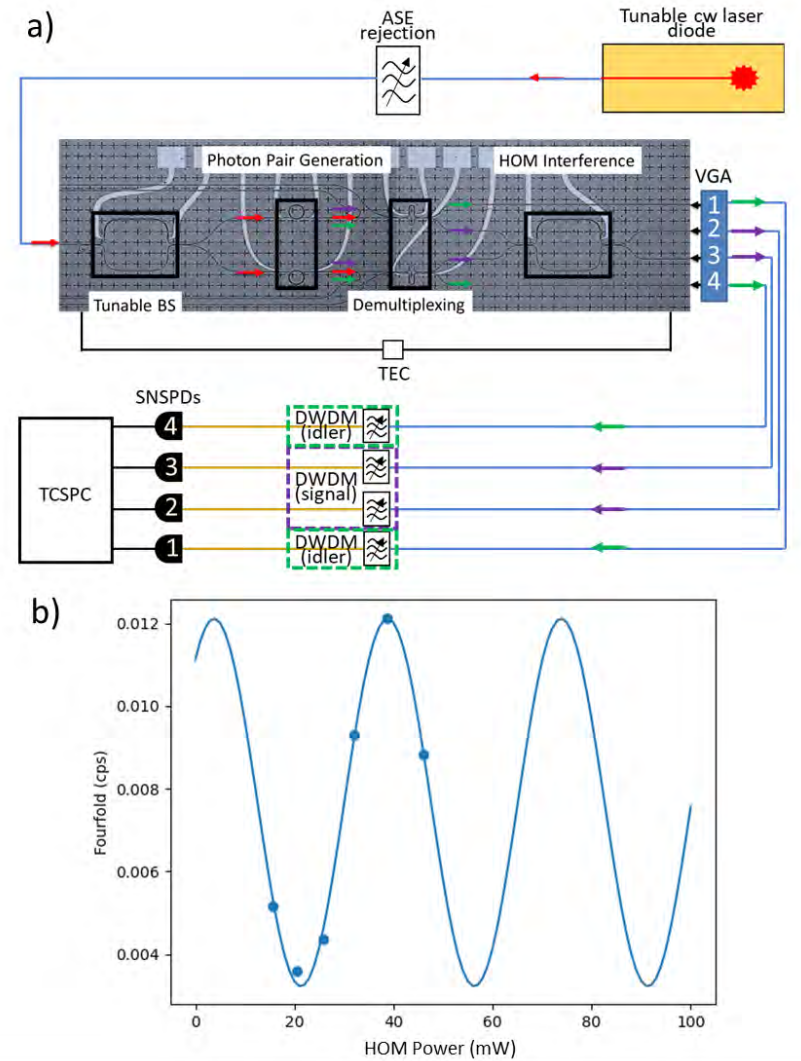


Figure 6.7: a) Experimental setup to measure HOM interference using a tunable CW laser. The laser is filtered through tunable bandpass filters to remove ASE power at the signal and idler wavelengths before being coupled into the chip. The chip performs the HOM experiment when the rings both generate photon pairs simultaneously that can interfere on the final HOM interferometer. A fiber v-groove array couples light from all four output ports of the circuit. Ports 1 and 4 are sent through DWDMs aligned with the idler mode, and ports 2 and 3 are sent through the signal DWDMs. The photons are detected using SNSPDs and time correlations are measured using a time correlated single photon counting module. b) Example interference scan as the HOM interferometer phase heater power is swept.

after setting the initial conditions, and the rings are kept on resonance for the duration of the measurement. Each measurement is taken for longer than 10,000 seconds to

collect sufficient photon counts above the background. During the measurement, a drift of > 3 dB in the fiber alignment necessitated a realignment of the optical fibers using the piezo-electric tuners of the fiber stages. This alignment process took less than 30 seconds in the $> 10,000$ second measurement and thus did not impact the recorded data significantly. The HOM interferometer heater is set to the initial setpoint of the sweep. A v-groove array couples light out of all four ports simultaneously and is aligned using a 6-axis stage. The light from each port is sent through the corresponding signal or idler 100 GHz DWDM filter channel. Since the demultiplexers on-chip are periodic, the off-chip filters are required to suppress the periodic transmission of undesired signal or idler wavelength modes. The filters also suppress the residual pump light to minimize the leakage of pump photons to the detectors. Each channel is sent to a superconducting nanowire single photon detector (SNSPD), and the singles, two-fold coincidences, and fourfold coincidences are recorded for the $> 10,000$ seconds. The coincidence windows are set by the biphoton coherence time to 1 ns. A time-correlated single photon counting module records the photon events, and the data is processed using the saved raw binary files. The post-processing allows for implementation of electronic delays to adjust relative arrival time of the photons on each channel.

The total fourfold coincidence counts in the measurement are divided by the integration time to estimate the fourfold coincidences per second. As the HOM interferometer heater power is swept (sweeping the relative phase of the two paths), the nominally indistinguishable photon pairs become distinguishable. When the relative phase is 0, the photons should be perfectly indistinguishable and display the HOM effect on the final beamsplitter of the HOM interferometer. When there is a phase difference in the paths, the photons are no longer indistinguishable, and the photons can exit either port or the same port. Thus, by sweeping the phase, the interference can be swept from nominally indistinguishable to perfectly distinguishable. Recording the fourfold coincidence counts

as this phase is applied will show an oscillation in the recorded counts (shown in Figure 6.7b). The visibility here is 60 % which shows quantum interference of the photons from the two sources. Small measurement steps near the maximum and minimum of the interference pattern will likely improve this value further. A visibility greater than 50 % shows that the interference is no longer in the classical regime [6, 7, 9, 10]. Future work is focused on improving the data density and sweeping across a wider range of heater powers to populate a better visibility plot. A different device from the third wafer of devices fabricated was characterized using a similar method and showed 72 % interference visibility. The details of this device are included in Appendix A4.

6.3 Conclusion and Outlook

Preliminary results from a HOM interference measurement integrated on a single AlGaAs photonic chip indicate the ability to show quantum interference between two ring resonator sources. The circuit utilizes the fundamental components established in Chapter 4 along with the bright entangled photon pair sources discussed in Chapter 3 to demonstrate a step toward fully integrated quantum photonic circuits. This experiment is a culmination of the efforts made in the initial projects of this dissertation and shows the ability to create chip-scale integrated quantum photonic circuits using a novel, highly nonlinear material—AlGaAsOI. The characterization of this circuit can be advanced through the addition of phase shifters on the waveguides of ports 1 and 4, and interfering the heralding channels will allow for full quantum state tomography of the system. This characterization can verify the existence of two of the four maximally entangled Bell States and allow for the realization of a tunable Bell state generator (which is proposed here via modeling, but not confirmed).

Additionally, the HOM interference visibility can be improved by changing the char-

acteristics of the pump source used for the experiment. To understand this change, a brief discussion of the joint spectral intensity of an entangled photon pair is necessary. The bi-photon state produced by the SFWM and SPDC processes is given by [11],

$$|\psi\rangle \propto \int \int \Theta(\omega_s, \omega_i) \Psi(\omega_s, \omega_i) d\omega_s d\omega_i |1\rangle_s |1\rangle_i \quad (6.2)$$

where Θ is the spectral shape of the pump, $\Psi(\omega_s, \omega_i) = \phi_{pm}(\omega_s, \omega_i)T(\omega_s)T(\omega_i)$ is determined by the phase matching, ϕ_{pm} and the amplitude transmission functions, T , of the component. The phase matching function is discussed in detail in Chapter 2. The joint spectral intensity (JSI) of a photon pair source is defined as $\Theta \times \Psi$. Example JSIs are shown in Figure 6.8a,b). The JSI describes the relationship between the frequencies of signal and idler photons generated. The width along the diagonal (short axis) is given by the pump photon bandwidth $\delta\omega_p$, while the length along the antidiagonal (long axis) is determined by the lesser of the spectral bandwidth of the phase-matching function or the transmission windows. For the case of CW excitation (shown in Figure 6.8a), the pump bandwidth is much smaller than the signal and idler spectral bandwidth, creating an elliptical JSI. Pulsed lasers, on the other hand, have narrow time domain signals (broad spectral bandwidths), resulting in a circular JSI. For the HOM effect, any form of distinguishability can degrade the measured visibility. For the case of the CW pump laser, it is possible that the generated signal and idler photons of the two rings have slightly different frequencies. As shown in Figure 6.8c), the pump laser can generate photon pairs at either the green or the orange location (marked in Figure 6.8a for clarity). Since these frequencies are different, two nominally identical photon pairs sources with CW pumping can still have non-unity HOM visibility. Pulsed excitation, on the other hand, has a circular JSI, meaning that the photons generated have better overlap in the frequency domain and can reach close to unity visibility.

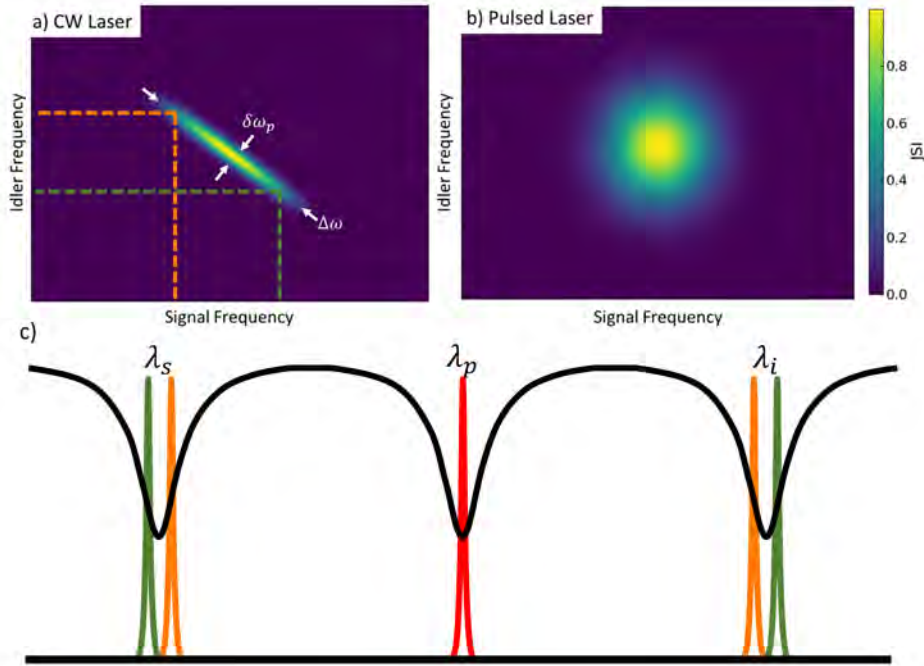


Figure 6.8: a) Joint spectral intensity of a CW ring resonator entangled photon pair source. The main diagonal has width related to the spectral bandwidth of the pump source, and the antidiagonal is set by the lesser of spectral bandwidth of the phase-matching function or the transmission window. b) JSI of a pulsed laser showing the broadening along the main diagonal which results in a separable bi-photon state. c) Illustration of CW pumping with a signal and idler resonance. The pump mode is narrow relative to the resonance linewidth and can thus generate a variety of unique signal and idler frequencies. The green and orange lines in a) are shown in the schematic in c).

Although the results from the CW show the capability of the platform to create quantum photonic integrated circuits, much more exciting work can be done. First, it is expected that changing the pumping scheme from CW to pulsed would further improve the visibility of the HOM circuit utilized for these experiments (as discussed in the previous section). When combining this new pumping scheme with recent improvements to the facet quality via etching instead of polishing, the next generation of HOM circuits is expected to have much better performance. Packaging of the chips and wire-bonding of the heater pads can make the experiment more stable and capable of operating without monitoring or realignment. Lastly, a redesign of the circuit with considerations for

thermal management—such as the inclusion of thermal isolation trenches in between components [12]—and additional phase shifters on the heralding ports 1 and 4 can expand the functionality of the circuit and make experiments more straightforward. With all that being said, the preliminary results from the HOM circuit and integrated qubit demultiplexer experiment illustrate that the necessary components for integrated quantum photonic circuits using III-V semiconductors have been established.

Bibliography

- [1] J. Bao, Z. Fu, T. Pramanik, *et. al.*, *Very-large-scale integrated quantum graph photonics*, *Nature Photonics* **17** (4, 2023) 573–581.
- [2] J. C. Adcock, C. Vigliar, R. Santagati, *et. al.*, *Programmable four-photon graph states on a silicon chip*, *Nature Communications* **10** (12, 2019) 1–6.
- [3] H. Shapourian and A. Shabani, *Modular architectures to deterministically generate graph states*, *Quantum* **7** (6, 2023).
- [4] Z. Y. Ou, C. K. Hong, and L. Mandel, *Relation between input and output states for a beam splitter*, *Optics Communications* **63** (7, 1987) 118–122.
- [5] J. E. Castro, T. J. Steiner, L. Thiel, *et. al.*, *Expanding the quantum photonic toolbox in AlGaAsOI*, *APL Photonics* **7** (9, 2022) 096103.
- [6] I. I. Faruque, G. F. Sinclair, D. Bonneau, *et. al.*, *On-chip quantum interference with heralded photons from two independent micro-ring resonator sources in silicon photonics*, *Optics Express* **26** (8, 2018) 20379.
- [7] A. Baldazzi, L. Pavesi, Y. Sohn, *et. al.*, *Do different kinds of photon-pair sources have the same indistinguishability in quantum silicon photonics?*, *Photonics Research, Vol. 11, Issue 11, pp. 1820-1837* **11** (11, 2023) 1820–1837.
- [8] T. Carmon, L. Yang, and K. J. Vahala., *Dynamical thermal behavior and thermal self-stability of microcavities*, *Optics Express* **12** (10, 2004) 4742–4750.
- [9] K. I. Harada, H. Takesue, H. Fukuda, *et. al.*, *Indistinguishable photon pair generation using two independent silicon wire waveguides*, *New Journal of Physics* **13** (6, 2011) 065005.
- [10] Z. Y. Ou, J. K. Rhee, and L. J. Wang, *Photon bunching and multiphoton interference in parametric down-conversion*, *Physical Review A* **60** (7, 1999) 593.
- [11] G. Moody, L. Chang, T. J. Steiner, and J. E. Bowers, *Chip-Scale Nonlinear Photonics for Quantum Light Generation*, *AVS Quantum Science* **2** (12, 2020) 041702.

BIBLIOGRAPHY

- [12] M. Milanizadeh, D. Aguiar, A. Melloni, and F. Morichetti, *Canceling Thermal Cross-Talk Effects in Photonic Integrated Circuits*, *Journal of Lightwave Technology* **37** (2, 2019) 1325–1332.

Chapter 7

Conclusion and Outlook

This thesis was aimed at establishing the necessary components for integrated quantum photonics using III-V semiconductor materials, including AlGaAsOI and InGaPOI. These materials offer many advantages over other quantum photonic platforms, but should also be developed in parallel and integrated with with foundry-processed silicon-based wafers for scalable quantum photonics. In this work, we established many key steps toward advanced functionality and quantum state engineering with these nonlinear material platforms. The motivation behind this work was to establish quantum light sources that require significantly less pump power to operate with high quality and rates, thus reducing the requirements of pump rejection filters and enabling lower loss implementations of circuits already demonstrated with silicon photonics. The lower loss systems should enable higher collection efficiency and higher heralding rates that can significantly reduce the measurement time for many experiments. Although the progress here is considerable, there is much work to be done. The AlGaAsOI and InGaPOI fabrication device yield is lower than silicon due to a less mature fabrication process and lack of fabrication capabilities in a Tier-1 foundry, which makes the creation of large scale circuits more challenging. Thus, a long-term direction may involve the integration of nonlinear

quantum light sources based on III-V semiconductors with silicon nitride ultra-low-loss waveguides. Since the quantum light is only generated in a small fraction of the entire integrated circuit, one could envision this generation occurring in the nonlinear material, while the rest of the circuit is made using a foundry-compatible platform like silicon or silicon nitride. This integration has already been done for classical applications [1, 2], so it is a logical step toward improving the functionality of quantum photonic circuits using these nonlinear materials.

Additionally, the bulk of the work in this thesis focused on the generation of entangled photon pairs or single photons at 1550 nm, which is motivated by the low-loss transmission in standard silica optical fibers. The platforms discussed here are compatible with various other wavelength ranges that can be explored for new applications. For example, Chapter 5 demonstrated quantum key distribution at 1550 nm using deployed optical fibers. Future work can also generate entangled photon pairs near 775 nm—a transparency window of atmosphere—such that satellite-based and free-space quantum communication systems can be created. Furthermore, broadband entangled-photon pair sources are proposed in Chapter 3 but not implemented. These sources could offer a route toward networking different quantum systems like trapped ions or single photon emitters in diamond and interfacing them with a photon at 1550 nm such that the information can be transmitted in fiber with low loss. This application opens a host of new opportunities for efficient quantum interconnects. Lastly, simulations show the capability of these highly nonlinear platforms to generate 16 dB of squeezing on chip, which has great utility for continuous-variable quantum computing and communication systems. The demonstration of such a large magnitude of squeezing would enable many new applications. The results shown in this thesis are also based on four wave mixing (a third-order nonlinear process), which is less efficient than parametric down conversion (a second-order process). The transition to second-order nonlinear sources (which are

designed in Chapter 3) can offer even more efficient photon pair sources with the added benefit of easier pump filtering since the pump is at twice the frequency of the generated light.

The final route toward expanding the systems developed in this thesis involves integrating more components onto the photonic chip. The circuits discussed in Chapter 6 include most of the critical components, but still have reduced efficiency due to off-chip filtering, detection, and pumping. Packaging of the photonic chips could improve the stability of the circuits and allow for easier measurements, but future work should move toward full-scale implementation to reduce the overall system loss and enhance the scalability. Waveguide integrated single photon detectors have already been demonstrated [3], and higher extinction ratio filters have been designed [4] that could remove the off-chip filter requirement. The integration with single photon detectors adds an additional layer of functionality (and complexity due to the cryogenic temperatures required for superconducting nanowire single photon detectors). Thermal tuning becomes almost impossible at these temperatures, so material systems with electro-optic capabilities will be required — again, motivating the III-V nonlinear semiconductors discussed in this work. Lastly, chip-scale laser integration could enable turnkey quantum circuits and quantum key transmitters.

Thus, although this work demonstrates the benefits of highly nonlinear materials like InGaP and AlGaAs, it is just the starting point for many new interesting quantum photonics demonstrations. The lessons learned through the development of these material platforms can be transferred to other material systems like GaN (which has a much larger bandgap and can be used for UV/visible quantum photonics). The field of integrated quantum photonics has started to grow rapidly, and the demonstrations in the next decade will be at the forefront of quantum technology.

Bibliography

- [1] J. M. Ramirez, H. Elfaiki, T. Verolet, *et. al.*, *III-V-on-Silicon Integration: From Hybrid Devices to Heterogeneous Photonic Integrated Circuits*, *IEEE Journal of Selected Topics in Quantum Electronics* **26** (3, 2020).
- [2] W. Xie, C. Xiang, L. Chang, *et. al.*, *Silicon-integrated nonlinear III-V photonics*, *Photonics Research* **10** (2, 2022) 535–541.
- [3] C. McDonald, G. Moody, S. W. Nam, *et. al.*, *III-V photonic integrated circuit with waveguide-coupled light-emitting diodes and WSi superconducting single-photon detectors*, *Applied Physics Letters* **115** (8, 2019).
- [4] R. R. Kumar and H. K. Tsang, *High-extinction CROW filters for scalable quantum photonics*, *Optics Letters* **46** (1, 2021) 134–137.

Appendix

A1 Example Singles Scan

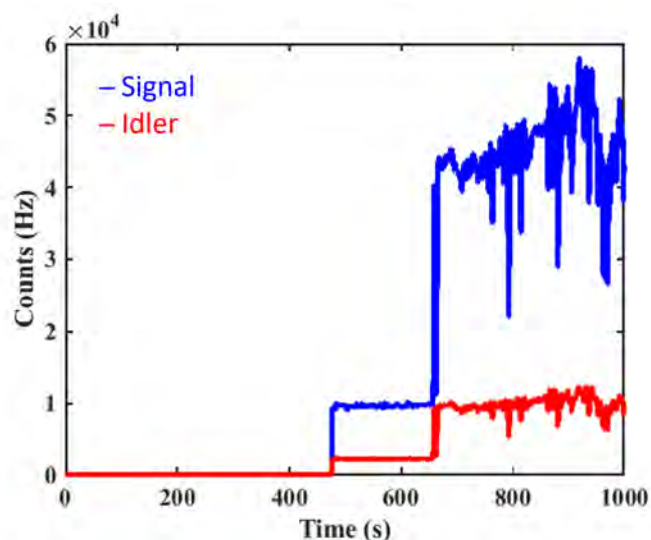


Figure A1: Example singles scan for an on-chip power of -15.14 dBm ($30.6 \mu\text{W}$). The scan begins with the laser set to an off-resonance wavelength (at 430 seconds). The laser is then swept to the resonance wavelength, reaching the resonance wavelength at approximately 630 seconds. The laser is held at this wavelength for 360 seconds to allow for the average singles rate to be determined.

To determine the singles counts for the signal and idler channels, the pump laser was swept from an off-resonance wavelength to the resonance wavelength and held on resonance for > 360 seconds. An example scan for an on-chip power of -15.14 dBm ($30.6 \mu\text{W}$) is shown in Figure A1. The measurement starts at 430 seconds, and the initial

counts represent the off-resonance counts on the detector. Ideally, these counts would be identical to the dark counts of the SNSPDs, but for larger on-chip powers, some of the pump photons still reach the detectors. Starting at the 630 second mark, the laser has reached the resonance wavelength (as shown by the sharp increase in single photon counts). The resonator remains aligned for the remainder of the data collection, with some oscillations due to variations in the fiber-to-chip coupling. The idler channel has lower counts due to a larger filter loss on this channel relative to the signal channel.

A2 Example Coincidence Measurement

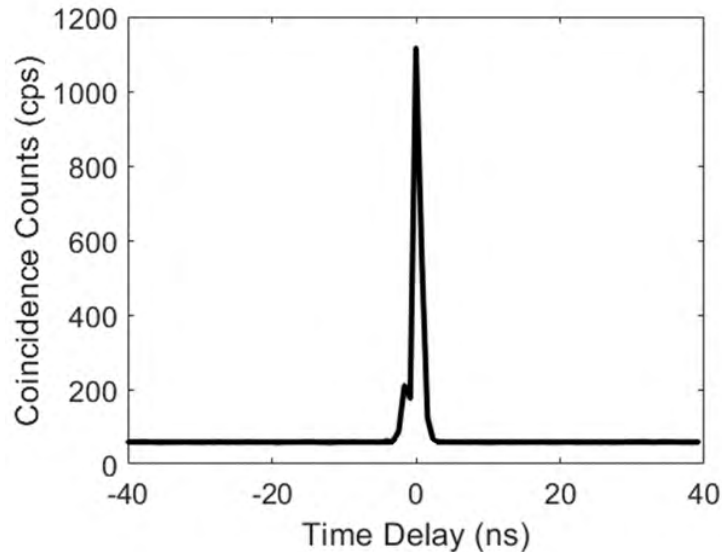


Figure A2: Example histogram showing the normalized coincidence counts (in counts per second) as a function of the time delay. The data is from the device characterized in Chapter 3 with record-high photon pair brightness. Here, -12.2 dBm of power into the ring generates over 1200 coincidences per second.

An example histogram of a coincidence measurement at -12.2 dBm ($60 \mu\text{W}$) is shown in Figure A2. The coincidence counts are collected until the accidental counts average to a nonzero value (longer integration times for lower powers). Here, the coincidence rate

(> 1200 coincidences per second) is sufficient that less than 1 minute of data collection is necessary.

A3 CAR Measurement

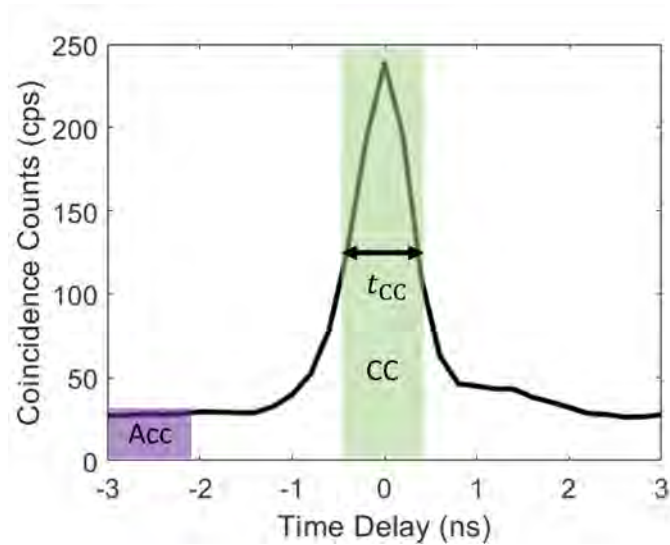


Figure A3: Illustration of the CAR measurement. Here, data from the QKD protocol used in Chapter 5 is used to illustrate the CAR calculation. The coincidence peak is integrated over a roughly 1 ns window (corresponding to the FWHM) and shown in green to collect the total coincidence count rate. The accidental counts are recorded by integrating over the same time window away from the peak (shown in purple). Here, the total coincidence count rate is 861.3 counts per second, and the accidental counts are 105.7 counts per second, corresponding to a CAR of 8.15.

The coincidence to accidental ratio (CAR) of an entangled photon pair source is an important metric describing the quality of both the source and experimental setup. To measure CAR, a coincidence count trace is recorded, and the peak is integrated within the full width at half maximum (FWHM) as shown in green in figure A3. The accidental counts are measured away from the peak and integrated using the same time window. Here, the total coincidence count rate is 861.3 counts per second, and the accidental counts are 105.7 counts per second, corresponding to a CAR of 8.15. Since the coincidence

FWHM is related to the biphoton correlation time (see Chapter 3), for a given source, the same coincidence window can be used for all measurements.

A4 Additional HOM Measurement

Another HOM interferometer device was tested during the characterization of the circuit. A summary of the results for this device is included in Figure A4. The transmission scan of the device while coarsely aligned is shown in Figure A4a). The blue trace shows the output through port 1, and the orange trace shows the output through port 4. The pump wavelength was selected near 1553.3 nm, and the signal and idler wavelengths were selected at 1550.1 nm and 1556.5 nm. In panel b), the single photon and coincidence count rates for the top ring source (ring 1) are shown as a function of the off-chip power. Here, the source is efficient enough to generate > 2 million single photons per second and coincidence count rates exceeding 4 kHz. The source is so efficient, in fact, that the SNSPDs latch and cannot collect data at the powers above -23 dBm off-chip (indicated by the black box). In panel c), the second ring is characterized, showing 300,000 single photon counts per second and 400 coincidences per second. Notably, the second source has much lower efficiency — the off-chip power of the second source is 7 dBm larger than that of the first ring, but the coincidence rate is an order of magnitude lower. This is largely due to a reduced quality factor of the second ring, and was part of the motivation to pursue the device that is fully characterized in Chapter 6. Panel d) illustrates the fourfold coincidence data for the HOM experiment with this device. The raw visibility is 72 %. The fit shows a visibility of almost 90 %.

The device shown in this appendix has lower quality factor resonators $< 100,000 Q$, higher insertion loss < 20 dB per channel, and a greater variation in the performance of the two ring sources. This device was from the Crazy Coral wafer 3 run, and had diced

BIBLIOGRAPHY

facets that were not polished. The device in the main body of this dissertation (from Crazy Coral wafer 0) had much better performance with higher Qs, lower loss, and better uniformity.

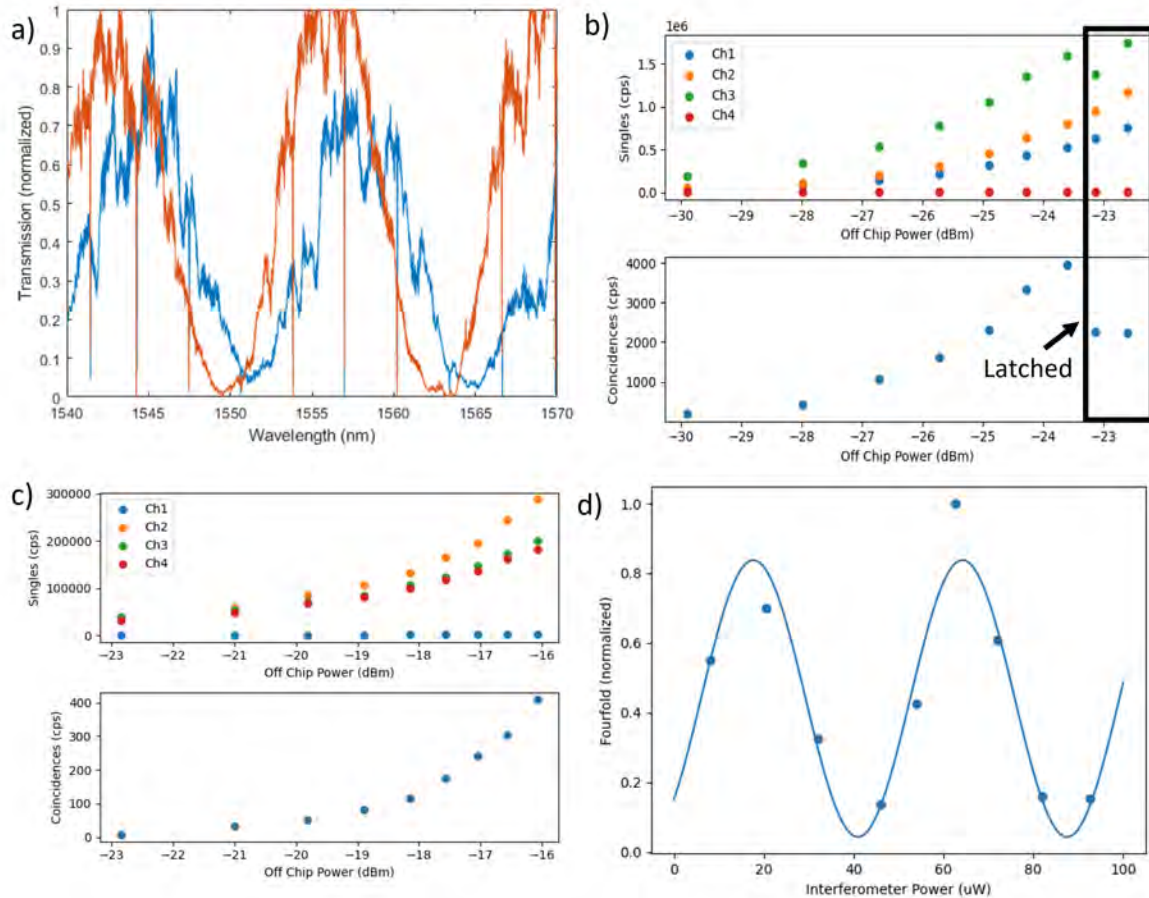


Figure A4: a) Transmission scan of the 8th device of Crazy Coral wafer 3. The blue trace shows the output through port 1, and the orange trace shows the output through port 4. b) The single photon and coincidence count rates for the top ring source (ring 1) are shown as a function of the off-chip power. The source is so efficient that the SNSPDs latch and cannot collect data at the powers above -23 dBm off-chip (indicated by the black box). c) The second ring is characterized, showing 300,000 single photon counts per second and 400 coincidences per second. d) The fourfold coincidence data for the HOM experiment with this device, showing a raw visibility of 72 %.

A5 Device List for Experiments

Here, a list of device names and numbers for the experiments discussed in this thesis is included for convenience and to allow for reproduction of the results.

A5.1 Chapter 3 Devices

Figure 3.7 shows characterization of devices fabricated by Weiqiang Xie and members of John Bowers’s group before 2019. These AlGaAsOI ring resonators were fabricated for classical integrated photonics applications and transferred to Prof. Moody’s group for quantum experiments in 2019. The remaining experimental results of this chapter are from ring 29 of these devices. In table 3.1, results from both ring 29 and ring 24 are shown.

A5.2 Chapter 4 Devices

The edge coupler results in Figure 4.2 are from ring 29 of the initial devices fabricated by Weiqiang Xie. The waveguide crossers (Figure 4.4), and MZIs (Figure 4.7) are from the fabrication run “Ample Abode”. The photonic interleaver results (Figure 4.9) are from the third wafer of the “Bongo Brook” fabrication run. The pulse shaper results (Figure 4.11) are from the “Ample Abode” fabrication run called “AAJP_Jul14” device number 9.

A5.3 Chapter 5 Devices

The results for QKD are all from ring 29 fabricated by Weiqiang Xie. This device was fully characterized in Chapter 3 and used as an ultra-efficient source of entangled photon pairs for the QKD experiment.

A5.4 Chapter 6 Devices

The results for the demultiplexing experiment are from the third wafer of the fabrication run “Crazy Coral”. The HOM experiment used device 2 from the 0th wafer of “Crazy Coral”, and the additional data shown in Appendix A4 is from the third wafer of “Crazy Coral”, device number 8.